NNT/NL : 0000AIXM0000

THÈSE DE DOCTORAT

Soutenue à Aix-Marseille Université
le 17/05/2024 par

Thomas Gianoli

Development of a Lattice-Boltzmann Method for Turbomachinery: Towards S-Duct Simulations

Discipline
Sciences pour l'ingénieur

Spécialité
Mécanique et physique des fluides

École doctorale
ED 353 Sciences pour l'ingénieur: mécanique, physique, micro et nanoélectronique

Laboratoire/Partenaires de recherche
M2P2
CERFACS
Safran Aircraft Engines

Composition du jury

Stéphane AUBERT Professeur, École Centrale de Lyon	Rapporteur
Sofiane KHELLADI Professeur, ENSAM Paris	Rapporteur et président
Jérôme BOUDET Maître de Conférences, École Centrale de Lyon	Examinateur
Marlène SANJOSÉ Professeure, ÉTS, Université du Québec	Examinatrice
Jérôme DE LABORDERIE Ingénieur, Safran Aircraft Engines	Examinateur
Pierre SAGAUT Professeur, Aix-Marseille Université	Directeur de thèse
Jean-François BOUSSUGE Ingénieur de recherche, CERFACS	Invité

Affidavit

Je soussigné, Thomas Gianoli, déclare par la présente que le travail présenté dans ce manuscrit est mon propre travail, réalisé sous la direction scientifique de Pierre Sagaut et Jean-François Boussuge, dans le respect des principes d'honnêteté, d'intégrité et de responsabilité inhérents à la mission de recherche. Les travaux de recherche et la rédaction de ce manuscrit ont été réalisés dans le respect à la fois de la charte nationale de déontologie des métiers de la recherche et de la charte d'Aix-Marseille Université relative à la lutte contre le plagiat.

Ce travail n'a pas été précédemment soumis en France ou à l'étranger dans une version identique ou similaire à un organisme examinateur.

Fait à Toulouse le 05/03/2024

Gianoli

Thomas GIANOLI

List of Publications and Participation at Conferences

Liste des publications et/ou brevets réalisées dans le cadre du projet de thèse:

1. T. Gianoli, J-F. Boussuge, P. Sagaut, J. de Laborderie, "Development and validation of Navier–Stokes characteristic boundary conditions applied to turbomachinery simulations using the lattice Boltzmann method". Int J Numer Meth Fluids. 2022; 1- 29. https://doi.org/10.1002/fld.5160

2. T. Gianoli, J-F. Boussuge, P. Sagaut, J. de Laborderie, "Investigation of an Inter-Compressor S-duct using the Lattice Boltzmann Method". Journal of Turbomachinery. 2023;

Participation aux conférences et écoles d'été au cours de la période de thèse:

1. T. Gianoli, J-F. Boussuge, P. Sagaut, J. de Laborderie, "S-Duct Turbomachinery Simulations using the Lattice Boltzmann Method", 56th Edition of the 3AF International Conference on Applied Aerodynamics, Toulouse, France, (March 2022)
2. T. Gianoli, J-F. Boussuge, P. Sagaut, J. de Laborderie, "Inter-Compressor Annular S-duct Simulations using the Lattice Boltzmann Method", 15th European Conference on Turbomachinery Fluid dynamics & Thermodynamics
ETC15, April 24-28, 2023; Budapest, Hungary

Résumé

Les cols de cygnes sont des passages aérodynamiques utilisés dans l'aviation afin de guider l'écoulement sortant du compresseur basse pression vers le compresseur haute pression. Dans un but d'optimisation du poids et de la taille des moteurs, la longueur de ces cols de cygne à tendance à diminuer au cours des dernières années menant à des designs de plus en plus agressifs. Toutefois, ces nouveaux designs ne doivent pas générer de pertes aérodynamiques supplémentaires qui pourraient venir impacter la performance globale du moteur.

L'utilisation de la mécanique des fluides numériques est une pratique courante afin de concevoir les turbomachines. Cependant, les méthodes traditionnelles sont basées sur les modèles de type RANS (Reynolds-Averaged Navier-Stokes) qui se sont avérés ne pas prédire les niveaux de pertes avec précision. Les approches classiques de Simulation aux Grandes Échelles (SGE) sont quant à elles plus précises mais limitées par leur coût de calcul.

La méthode de Boltzmann sur réseau est alors apparue comme une alternative viable afin de réaliser des calculs (SGE) à un coût satisfaisant. Le cœur de la méthode repose sur un algorithme de collision et propagation, se révélant particulièrement efficace d'un point de vue informatique, ainsi que sur des maillages Cartésien facilement réalisable. Cependant, la LBM a été peu appliquée à la simulation de configurations turbomachines complexes.

L'objectif de cette thèse de doctorat est le développement et la validation de l'approche LBM pour la simulation de cols de cygnes de complexité croissante. La partie de développement concerne l'intégration et la validation de conditions limites caractéristiques d'entrée et de sortie adaptées aux applications turbomachines.

Ces développements ont ensuite permis la simulation d'un col de cygne académique sur laquelle la capacité du code à retrouver les résultats expérimentaux de référence a été démontrée. Ensuite, un col de cygne représentatif d'un cas industriel est simulé et les capacités et limitations du code sont discutées.

Mots clés : Méthode de Lattice-Boltzmann, cols de cygne, mécanique des fluides, turbomachine, pertes aérodynamiques, compresseur.

Abstract

S-ducts are used in aircraft engines as aerodynamic passages to drive the flow from the low-pressure compressor to the high-pressure compressor. To optimize performance, the engine weight and length are progressively reduced, leading to more and more aggressive S-Duct designs. However, these new designs must not generate additional aerodynamic losses that could impact the global performance of the engine.

Computational Fluid Dynamics (CFD) is a common practice in the field of turbomachinery design. However, traditional approaches are based on Reynolds-Averaged Navier Stokes models which were shown not to predict accurately losses. The Large Eddy Simulation (LES) approach is more precise but is limited by its computational cost when tackling industrial configurations.

Recently, the Lattice Boltzmann Method (LBM) appeared as a viable numerical alternative method to perform LES at an affordable cost. The method is based on a collide and stream algorithm, showing great efficiency for high-performance computing, combined with Cartesian grids easily generated. However, the LBM has been little applied to complex turbomachinery flows as the ones found in S-Ducts due to a lack of maturity.

The objective of this Ph.D. is to develop and validate the LBM approach to simulate S-duct configurations of increasing complexity. The development phase concerns the integration and validation of inlet and outlet characteristic boundary conditions suitable for turbomachinery simulations.

These new developments have been applied to simulate an academic S-duct where the ability of the method to recover experimental data is shown. Finally, an S-duct representative of an industrial case is simulated. Lastly, the advantages and limitations of the solver for these test cases are discussed.

Keywords: Lattice-Boltzmann Method, Annular S-Ducts, Computational Fluid Dynamic, turbomachinery, aerodynamic losses, compressor.

Remerciements

Je tiens tout d'abord à remercier les membres du jury : les deux rapporteurs, Stéphane Aubert et Sofiane Khelladi qui ont pris le temps de lire et d'évaluer ce manuscrit. Merci aux examinateurs Jérôme Boudet et Marlène Sanjosé et aux invités d'avoir participé et animé cette soutenance de thèse et d'avoir soulevé des questions pertinentes et constructives.

J'aimerais ensuite remercier mes encadrants : mon directeur de thèse Pierre Sagaut, mon encadrant CERFACS Jean-François Boussge, et mon encadrant à Safran Aircraft Engines Jérôme de Laborderie. Merci Pierre pour tes conseils et ton expertise afin d'enrichir mes articles et ma soutenance. Jean-François, merci pour tes entrées fracassantes dans mon bureau afin d'échanger et faire avancer ce travail de thèse. Enfin un grand merci à toi Jérôme pour ton encadrement régulier et constructif depuis les premiers jours.

Tout ce travail a été grandement facilité par les différentes équipes du CERFACS. La disponibilité et l'écoute du personnel admin a permis de répondre aux difficultés en toute circonstance. L'équipe CSG a été d'une aide précieuse sur tous les problèmes informatiques évitant de nombreuses heures perdues.

Un grand merci à toutes les personnes de l'équipe CFD pour les moments et discussions partagés apportant une aide essentielle à tous moments. Merci aussi pour tous ces étranges débats de la pause du midi qui m'ont permis d'en apprendre autant sur des sujets si variés.

Enfin, je remercie de tout mon coeur ma famille ainsi qu'Anne-Laure de m'avoir supporté, écouté et conseillé lorsque j'en avais besoin.

« *Maybe the knowledge is too great and maybe men are growing too small. Maybe, kneeling down to atoms, they're becoming atom-sized in their souls. Maybe a specialist is only a coward, afraid to look out of his little cage. And think what any specialist misses, the whole world over his fence.* »

John Steinbeck, *East of Eden*

Nomenclature

Miscellaneous variables and constants

$\boldsymbol{\tau}_w$	Wall shear stress	$\mathrm{kg \cdot m^{-1} \cdot s^{-2}}$
$\boldsymbol{q}$	Heat flux	$\mathrm{kg \cdot s^{-3}}$
$\boldsymbol{u} = [u_x, u_y, u_z]^T$	Cartesian velocity	$\mathrm{m \cdot s^{-1}}$
$\boldsymbol{x} = [x, y, z]^T$	Cartesian space variable	m
κ	Thermal conductivity	$\mathrm{W \cdot m^{-1} \cdot K^{-1}}$
λ_i	Wave speed for $1 \leq i \leq 5$	$\mathrm{m \cdot s^{-1}}$
$\mathcal{L}$	Characteristic (microscopic) length scale	m
μ	Dynamic viscosity	$\mathrm{kg \cdot m^{-1} \cdot s^{-1}}$
ν	Kinematic viscosity ($\nu = \mu/\rho$)	$\mathrm{m^2 \cdot s^{-1}}$
ρ	Fluid density	$\mathrm{kg \cdot m^{-3}}$
c	Air sound speed	$\mathrm{m \cdot s^{-1}}$
C_p	Heat capacity at constant pressure ($\gamma r_g/(\gamma - 1)$)	$\mathrm{J \cdot kg^{-1} \cdot K^{-1}}$
C_v	Heat capacity at constant volume ($r_g/(\gamma - 1)$)	$\mathrm{J \cdot kg^{-1} \cdot K^{-1}}$
E	Total energy, ($u^2/2 + e$)	J
e	Internal energy, ($C_v T$)	J
L	Characteristic (macroscopic) length scale	m
P_s, P_t	Static, total pressure	Pa
r_g	Specific gas constant	$\mathrm{J \cdot mol^{-1} \cdot K^{-1}}$
s	Entropy ($C_v \ln T/\rho^{\gamma-1}$)	$\mathrm{J \cdot K^{-1} \cdot kg^{-1}}$
t	Time	s
T_s, T_t	Static, total temperature	K
U	Characteristic speed	$\mathrm{m \cdot s^{-1}}$

Lattice Boltzmann variables

$\boldsymbol{\xi}, \boldsymbol{\xi}_i$	Continuous, discrete microscopic velocity	m·s^{-1}
$\boldsymbol{a}^{f,(n)}_{\alpha_1 \ldots \alpha_n}$	n^{th}-order Hermite moment of f and f^{eq}	kg/m^{3}m$^{\mathrm{n}}$/s$^{\mathrm{n}}$
$\mathcal{H}^{(n)}$	n^{th}-order Hermite polynomial	m$^{\mathrm{n}}$/s$^{\mathrm{n}}$
Ω, Ω_i	Continuous, discrete collision operator	kg·s^2·m^{-6}
ω, ω_i	Continuous, discrete, velocity weight	s^3·m^{-3}
$\Pi^{f,(n)}_{\alpha_1 \ldots \alpha_n}$	n-th order raw moment of f	kg/m^{3}m$^{\mathrm{n}}$/s$^{\mathrm{n}}$
ψ_i	Compressible correction term	kg·s^2·m^{-6}
$\Psi_{\alpha\beta}$	Second order moment of the compressible correction term	kg·s^2·m^{-6}
σ	Hybrid recursive regularized collision weighting parameter	
τ	Collision relaxation time	s
θ	Normalized temperature	
c_s	Lattice speed of sound ($\sqrt{r_g T_0}$)	
c_s^*	Lattice constant ($\sqrt{1/3}$)	
D	Number of spatial dimensions	
f, f_i	Continuous, discrete distribution function	kg·s^3·m^{-6}
f^{eq}, f_i^{eq}	Continuous, discrete equilibrium distribution function	kg·s^3·m^{-6}
f^{neq}, f_i^{neq}	Continuous, discrete off-equilibrium distribution function	kg·s^3·m^{-6}
f_N	Particle distribution function	s^3·m^{-6}
T_0	Reference temperature	K

Dimensionless numbers

γ_g	Heat capacity ratio (C_p/C_v)
Kn	Knudsen number ($\mathcal{L}/L$)
Ma	Mach number (U/c)
Re	Reynolds number (UL/ν)

Acronymes

ADL

Aerodynamic Duct Loading. 39, 176

AMR

Adaptative Mesh Refinement. 120, 121

AR

Area Ratio. 28, 33, 39, 40, 41

BGK

Bathnagar-Gross-Krook. 70, 72

BL

Boundary Layer. 46, 47, 50, 190

CFD

Computational Fluid Dynamic. 19, 20, 51, 54, 55, 84, 112, 202

DDES

Delayed Detached-Eddy Simulation. 54, 55

DNS

Direct Numerical Simulation. 21, 76, 84, 85

DVBE

Discrete Velocity Boltzmann Equation. 66, 69

HLBM

Hybrid Lattice Boltzmann Method. 71, 73

HPC

High Pressure Compressor. 18, 19, 26, 137, 174

HPT

High Pressure Turbine. 18

HRR

Hybrid Recursive Regularized. 72, 75, 137

ICD

Intermediate Compressor Duct. 18, 19, 26, 202

IDW

Inverse Distance Weighting. 78

IGV

Inlet Guide Vane. 48, 53

LBM

Lattice Boltzmann Method. 21, 22, 57, 59, 60, 63, 68, 69, 70, 72, 73, 74, 76, 81, 82, 84, 85, 104, 110, 115, 116, 143, 145, 159, 163, 174, 189, 190, 192, 203

LE

Leading Edge. 129, 130, 142, 195, 196

LES

Large Eddy Simulation. 21, 54, 55, 76, 84, 85, 95, 104, 202

LGA

Lattice Gas Automata. 57

LIKE

Loss In Kinetic Energy. 111, 120, 121, 122, 123, 124, 125, 142, 147, 178

LODI

Locally One-Dimensional Inviscid. 85, 89, 109, 178

LPC

Low Pressure Compressor. 18, 19, 26, 44, 49, 50, 53

LPT

Low Pressure Turbine. 18

LRF

Local Reference Frame. 79

MRR

Mean Radius Ratio. 28, 40

NDL

Non-Dimensional Length. 28, 40, 41

NFF

No Fully Fluid. 76, 77, 78, 181

NS

Navier-Stokes. 22

NSCBC

Navier Stokes Characteristic Boundary Condition. 82, 85, 89, 97, 104, 107, 110

OGV

Outlet Guide Vane. 55

RANS

Reynold Averaged Navier-Stokes. 21, 51, 52, 53, 54, 55, 84, 104, 115, 130, 145, 156, 159, 163, 180, 188, 189, 192, 193, 201, 202

REA

Radial Equilibrium Assumption. 105, 107

TE

Trailing Edge. 184, 195, 196, 198

URANS

Unsteady Reynold Averaged Navier-Stokes. 54, 84

WRLES

Wall Resolved Large Eddy Simulation. 21

Contents

Chapter 1: Introduction

Contents

1.1 Industrial Context

In recent years, the interplay between climate change and the growth of the aviation industry has become an increasingly pressing global concern. As air traffic expands, so do the environmental challenges associated with carbon emissions, contrails, and other pollutants. The aviation sector must reconcile its growth ambitions with the imperative of mitigating its environmental impact. The recent consensus is that aviation is responsible for 4% of the global increase of 1.2°C measured between the beginning of meteorological reports in the mid 19th century and today, despite being responsible for only 2.4% of global annual emissions of CO2 [1]. While air travel provides unparalleled connectivity and economic benefits, it is crucial to acknowledge and address the environmental consequences associated with its growth that is expected to continue (Fig. 1.1).

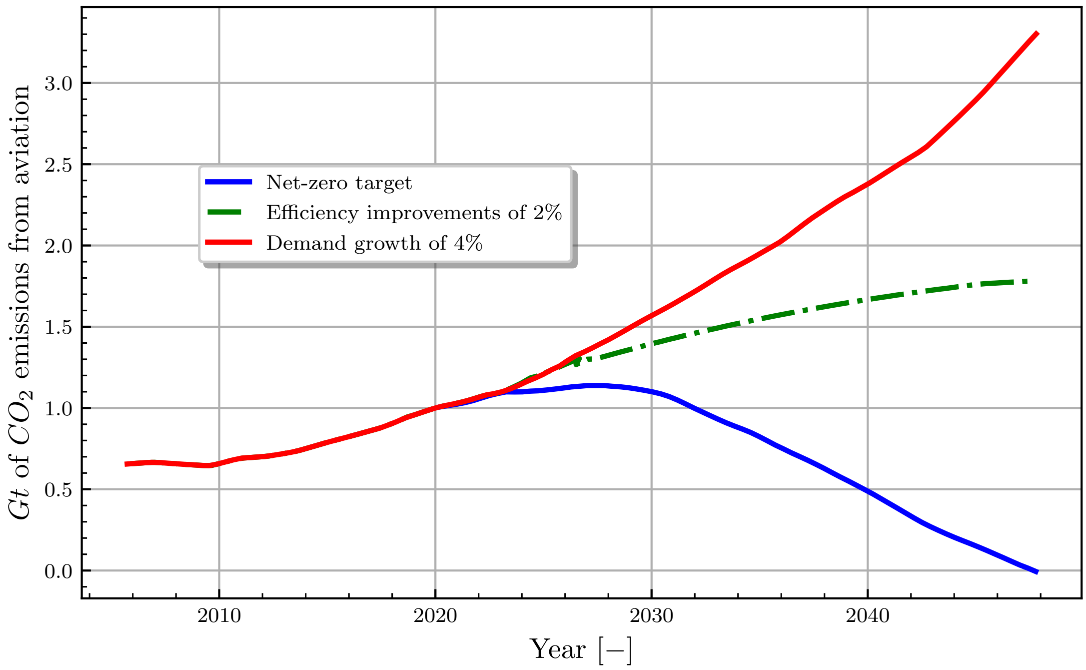

Figure **(1.1)** – Projected CO_2 emissions from aviation [2].

An additional economic constraint is added to this ecological concern when jet fuel represents a significant direct operating cost that could reach 45% of the total cost in the coming years [3]. Recognizing the urgent need for action, the aviation industry has actively sought solutions to mitigate its environmental impact. Efforts have been made to develop and adopt more fuel-efficient aircraft designs, explore alternative fuels, and improve air traffic management systems to reduce congestion and optimize flight routes. The development of lighter, more powerful, and more fuel-efficient engines thus constitutes the main research prospect of turbomachinery designers. To this extent, optimizing every component of an engine to avoid all possible losses seems to be one of the most decisive processes. The result is the continuous improvement of the propulsion efficiency of aircraft engines, with modern airplanes burning an average of 41% less fuel than the ones from 1970 [4].

1.2 Turbofan Jet Engine: a Brief Description

An aircraft engine is, by definition, a turbomachine, meaning a device in which a moving fluid interacts with one or several rows of rotating blades. This interaction allows for energy transfer between the fluid and the rotating shaft. An aircraft engine is more precisely an axial flow turbomachine as the fluid flow is parallel to the axis of rotation. To give a more precise illustration, Fig. 1.2 shows the typical sketch of an aircraft engine and highlights the main components. Recent high bypass-ratio turbofan engines can be decomposed into six major aerodynamic modules.

- The fan is the first stage of compression. Its role is to accelerate the air and divide the flow into two parts: one entering the engine core (primary flux), the other being bypassed (secondary flux). The mass ratio between the bypassed air and the air passing through the core is called the bypass ratio. The secondary flux produces most of the engine's thrust [5, 6, 7]. However, the primary flux is needed to generate the engine's power. To have an order of magnitude, current engines have a bypass ratio ranging from 8 to 12, and around 80% of the thrust is generated from the fan.

- After the fan, the air goes through the Low Pressure Compressor (LPC) and is directed by the Intermediate Compressor Duct (ICD) to the High Pressure Compressor (HPC) that ensure the second and third stages of compression.

- The compressed air leaving the HPC enters the combustion chamber and is mixed with fuel. The mix is then ignited to raise the fluid's energy.

- Next, the fluid energy is extracted in the High Pressure Turbine (HPT), and this energy is used to run the HPC.

- Finally, the Low Pressure Turbine (LPT) drives both the LPC and the fan.

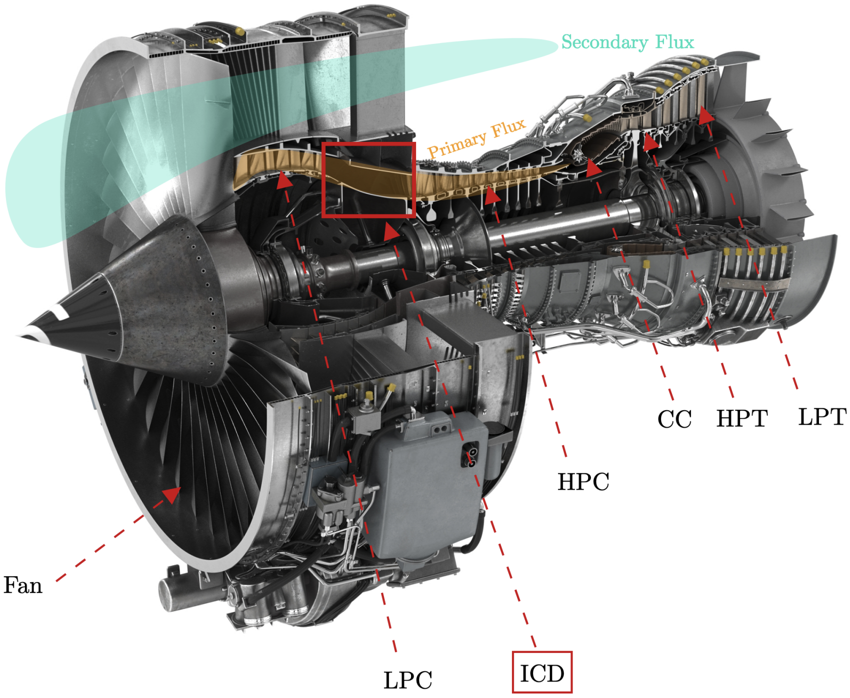

Figure **(1.2)** – Illustration of a CFM56 aero-engine with the ICD highlighted in the red box.

1.3 Inter-Compressor Annular S-Ducts

To improve the engine efficiency, bypass-ratio in modern aircraft engines has continuously increased (see Fig. 1.3) over the last decades, forcing the radial offset between the LPC and HPC to get higher. However, these two parts are connected via an annular S-shaped duct which can be described as an aerodynamic passage used to redirect the fluid from one radial position to another without significantly altering the flow direction. To achieve this, the duct must turn the fluid away from the original direction and back again, giving rise to the specific S-shape. With this increase in bypass ratio, the radius offset is becoming larger and larger, leading to more aggressive S-duct designs with a steeper slope. In this context, the present thesis deals with this specific engine component called an S-duct or a duct.

Over the last decades, the upstream and downstream compressors surrounding the S-Duct have been the primary focus of optimization, using Computational Fluid Dynamic (CFD). This has led to rotating compression components being highly optimized and sophisticated. However, the S-duct itself has not been investigated with the same intensity. The usual design method consists of dividing the engine into several modules and then optimizing them independently. To do so, the effects of the surrounding modules are modeled or simplified. The S-duct was often isolated, and only the stationary components were included. However, this methodology has shown its limits by leading to a potential sub-optimal engine design [8]. To mitigate this issue and the potential expensive redesign work necessary, the design philosophy moves towards the simulation of integrated design that reduces the need to model interactions between components and gives more accurate results [8, 9, 10].

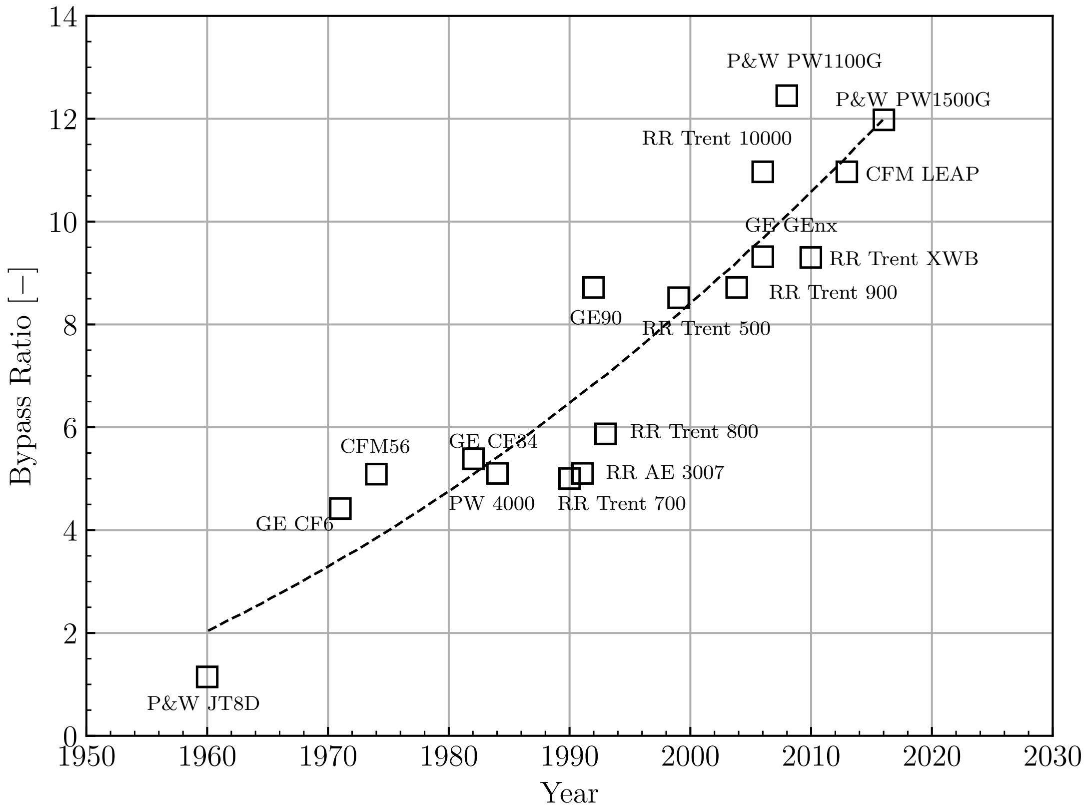

Figure **(1.3)** – Evolution of the bypass-ratio over the years (adapted from [11]).

S-ducts have become of particular interest since they are located between major components, and a length reduction would result in shorter, lighter, and more aerodynamic engines, thus increasing global efficiency. This motivates designers to reduce the duct length as much as possible if the performance is conserved or enhanced. The design of shorter and more aggressive ducts has become an important research topic. Another difficulty is that the duct geometry must be fixed early in the engine design process (as the supply chain of this particular component is especially long), well before the design of the upstream stages, so the exact conditions in which the duct operates are not easily known beforehand.

1.4 The Use of Computational Fluid Dynamics

The S-Duct is thus a component of significant importance to design. However, experimental campaigns are usually expensive, and it shows to be delicate to install the instrumentation. Indeed, the probes may alter the local flow dynamics, especially in a confined environment such as the duct, and may not be well suited for realistic operating conditions. Due to these limitations, the primary tool for designers is CFD, allowing them to simulate a flow field.

1.4.1 Various Approaches of Turbulence Modeling

The flow developing in an S-duct is complex with a high level of turbulence associated with a Reynolds number based on the duct inlet vein height of between 7×10^5 to 10^6 [12]. This means the flow is inherently three-dimensional and composed of a large spectrum of eddy sizes. Considering these aspects, the number of grid points necessary to solve all scales involved using Direct Numerical Simulation (DNS) would be overwhelming and not conceivable to use in the industry. The numerical cost must be reduced by modeling the turbulence using different methods to overcome this issue.

- DNS: This approach solves the Navier-Stokes equations without introducing turbulence modeling. This leads to resolving all the turbulent structures in the flow, making it highly computationally expensive and limiting its application in the industry.

- Reynold Averaged Navier-Stokes (RANS): The principle involves solving the time-averaged Navier-Stokes equations using the Reynolds decomposition [13]. It decomposes an unsteady quantity into a time-averaged part and a fluctuating one. This decomposition introduced a non-linear term called Reynolds stress tensor, which requires additional modeling (turbulence model) to close the RANS equations. RANS methods fully model turbulence and allow for relatively low CPU cost simulations. The RANS methods are widely used in the industry and often provide satisfactory results, mainly for attached and stationary flows. However, if the unsteady characteristics of the flow are relevant to the study or if the flow is highly unsteady or separated, this modeling is not adequate.

- Large Eddy Simulation (LES): The basis of the method relies on Kolmogorov's postulate that turbulent scales are segregated for large Reynolds numbers. The large scales carry the most energy and are specific to the studied case. Then, eddies of various sizes with a universal behavior are encountered. Finally, smaller scales have an essentially dissipating behavior. The principle of the LES is explicitly computing the large scales while the smaller ones are modeled. This results in an approach that is at an intermediate level of fidelity between DNS and RANS. In practice, this means spatial filtering of the Navier-Stokes equations is applied. A closure model is also needed in this approach, the most popular being that of Smagorinsky [14]. This reduces the computational cost compared to a DNS. However, to correctly capture a boundary layer, the number of grid points necessary is proportional to $Re^{1.86}$ [15], making Wall Resolved Large Eddy Simulation (WRLES) not affordable in practice for aeronautical applications. To avoid this issue, boundary layer models have been developed so that a coarser resolution can be used near the walls, reducing CPU and memory costs.

1.4.2 A substitute to the Navier-Stokes Based Solver: The Lattice Boltzmann Method

In this context, the present thesis aims to focus on the ability of the Lattice Boltzmann Method (LBM), to deal with the prediction of pressure losses in the complex unsteady flows that can be found in an annular S-duct. The LBM, based on a representation of the fluid at a mesoscopic level governed by the Boltzmann equation, offers several advantages compared to other standard methods used to solve the Navier-Stokes (NS) equations. Firstly, the efficient and relatively simple "collide-and-stream" allows an attractive return time compared to its NS-based counterparts [16]. Secondly, the LBM is based on Cartesian meshes that, together with a cut-cell approach, allow to handle complex geometries easily and reduce grid generation time. This method has been continuously developed in the aeronautic industry for these two advantages. In an S-duct, the temperature variation is usually negligible. However, the Mach number can reach values up to 0.8, way above the limit of 0.3, so the weakly compressible assumption cannot be considered, and a more complex model that allows the simulation of compressible flows has to be used.

1.5 The ProLB Solver

The solver that will be used in this Ph.D. is the ProLB solver. A consortium of the information technology company CS Group, car manufacturer Renault, aerospace corporation Airbus, aerospace corporation Safran, and research institutions Aix-Marseille Université and Ecole Central de Lyon develops it. Other partnerships allow the participation of ONERA and CERFACS. The code is developed in C++, allowing the resolution of the Lattice Boltzmann equations on a nineteen-velocity lattice running on massively parallel architectures. The traditional weakly compressible, athermal limitation inherent in the method has been overcome recently, making it possible to study compressible and thermal flows.

1.6 Ph.D. Objectives

The main objectives of this Ph.D. are the development and validation of Lattice Boltzmann Method-based Large-Eddy Simulation for accurate turbomachinery simulation of a representative S-duct. These kinds of simulations have already been performed using Navier-Stokes solvers. However, this is a new maturity step for the LBM. Two configurations will be investigated to tackle this challenge. The first one is referred to as CAM1 and represents a simplified S-duct in terms of Mach number and vein geometry. The first compressible LBM simulation of a turbomachinery configuration will be performed on it to define the best practices and study the physics. The second configuration that will be treated, thanks to the best practices defined on the academic S-duct, is called INDUS and is representative of a modern S-duct with a realistic operating point and vein geometry. However, several functionalities are needed to be able to perform these simulations. Indeed, specific boundary conditions and the definition of best practices are necessary and will be developed on increasingly complex test cases. These different developments and studies will pave the way to complex simulations of an S-duct that allow an in-depth analysis of the loss generation mechanism.

1.7 Outline of this Manuscript

The present manuscript is organized as follows:

- Chapter 2 is a literature review on S-ducts. The main physical phenomena driving the S-duct's flow behavior are described. Moreover, the other more classical numerical methods usually used to study an S-duct are evaluated, and their advantages and weaknesses are highlighted.

- Chapter 3 introduces the lattice Boltzmann method. Because of the standard scheme's limitation to weakly compressible and isothermal flows, the solution adopted to extend the range of simulation to compressible and thermal flows will be presented.

- Chapter 4 approaches one of the main developments conducted throughout this thesis and concerns the addition of a boundary condition derived from the Navier-Stokes Characteristic with a formalism allowing to impose total pressure, total temperature, and flow angles. The radial equilibrium assumption at the outlet is validated, and a valve law that allows convergence toward a target mass flow is also presented.

- Chapter 5 treats the development and validation of several additional functionalities and the definition of best practices necessary to perform S-Duct simulations. The academic configuration of interest called AIDA CAM1 is also presented in this chapter to introduce the different needs.

- Chapter 6 presents an in-depth study of the numerical result obtained following the large eddy simulation performed on the academic configuration. The simulation setup and validation against experimental data and other existing computations are presented, followed by the study of the flow features and the loss generation mechanism.

- Chapter 7 examines an industrial configuration of interest for Safran Aircraft Engines at a higher Mach number, using all the best practices and know-how obtained from the academic study on CAM1.

Chapter 2: Literature Review on Inter-Compressor Annular S-ducts

This chapter presents the literature review on inter-compressor annular S-ducts. A general description of this component is first presented before explaining the optimization problem faced by the designers. This component is then geometrically described, and the important notations are defined. Then, physical and design issues are investigated by highlighting the known phenomena and difficulties. The capacity of current methods used in the industry to predict pressure losses and flow phenomena is finally described.

Contents

2.1 Description of S-ducts Diffusers

High expectations already exist on each system component to ensure the increase of performance and sustainability of modern turbofan engines, and the limit of what is possible continues to extend. In today's engines, where even slight improvement in performance due to improved blade design is becoming increasingly complex, the potential gains, that can be achieved from improved duct design, offer much more significant potential returns. Indeed, the Intermediate Compressor Duct (ICD) is a crucial component for the engine, but less work has been performed on it compared to other major components.

2.1.1 General Description

S-ducts diffusers, referred to in the literature as Swan-neck and Goose-neck ducts, are found in modern aircraft engine compressors and turbines as inter-stage components. The role of an inter-compressor annular S-duct is to transmit the flow from a high radius component, the Low Pressure Compressor (LPC), to a lower radius component, the High Pressure Compressor (HPC), while converting kinetic energy to pressure energy. Due to its specific shape, the air passing through is slowed down more rapidly than with a straight duct. This change in geometry allows for shorter designs and, thus, noticeable weight savings. Moreover, as it ensures the connection of the two compression systems, it must incur minimal total pressure losses and deliver nearly uniform flow with a small transverse velocity at the engine compressor entrance to achieve appropriate engine performance. Indeed, distortion at the inlet of the compressor may decrease the performance or, in the worst case scenario, lead to stall and thus surge of the engine, diminishing the stable flow range of the compressor for the different operating conditions of the engine [17, 18]. If the design is too aggressive, that is, if the radial forcing is too steep, it will create stronger adverse pressure gradients, potentially leading to flow separation. This radius evolution along the machine axis gives them their characteristic S-shape. Fig. 2.1 illustrates a scheme of a typical S-duct with the corresponding geometric notations.

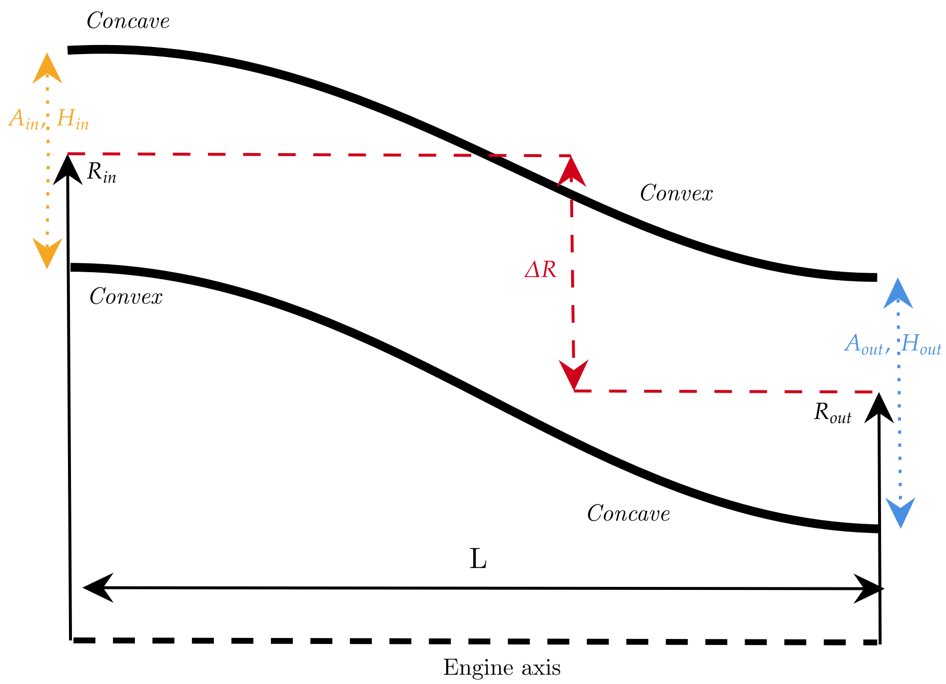

Figure **(2.1)** – Scheme of an S-duct and geometric notations.

2.1.2 Optimization Goal

The aim to continuously increase engine efficiency leads to rising bypass ratios, thus a continuously increasing difference in mean radii between the low and high-pressure compressors. This radius change must be accomplished in the shortest possible length to optimize the compactness and obtain a lightweight engine to reduce the engine's fuel burn.

One constraint is that very early in the engine design process there is a requirement to fix the annulus line. This results in the need to fix the geometry of the compressor inter-spool S-duct. At this point, the designer does not know the blade geometries and is forced into designing the S-duct without accurate knowledge of its inlet flow. This lack of knowledge often leads the designer to select a relatively conservative duct, well away from the limits of the design space.

However, obtaining a more aggressive design is not enough, as it needs to be consistent with limiting flow separation that could adversely affect the downstream compressor performance. Indeed, this kind of troublesome flow feature reduces the efficiency of the S-duct, increases the pressure loss, and creates higher stress levels on the components, finally leading to a shorter operational life expectancy of the engine. Furthermore, what appears to be a relatively simple geometric shape poses some significant aerodynamic challenges because of the complex nature of the flow field that develops in an S-duct.

2.2 Geometrical description

After explaining the role and importance of S-ducts, this section focuses on the geometrical description of the component through the definition of non-dimensional parameters. Then, the influence of these non-dimensional parameters on a basic definition of duct loading is studied. The annular flow path of an S-duct, which has an inlet radius R_{in} and outlet radius R_{out}, can be described by the following geometric parameters:

- the mean radius: $R_m = \frac{(R_{in}+R_{out})}{2}$,
- the annulus height: $h = R_{out} - R_{in}$,
- the annulus area: $A = \pi(H_{out}^2 - H_{in}^2)$.

2.2.1 Fundamental Non-Dimensional Geometrical Parameters

According to Britchford [19], the shape of an S-duct can be described by three non-dimensional parameters, which are the Mean Radius Ratio (MRR), the Area Ratio (AR) and the Non-Dimensional Length (NDL) defined respectively in Eqs. 2.1 to 2.3:

$$MRR = \frac{R_{m,out}}{R_{m,in}} \tag{2.1}$$

$$AR = \frac{A_{out}}{A_{in}} \tag{2.2}$$

$$NDL = \frac{L}{h_{in}} \tag{2.3}$$

Furthermore, to obtain a smooth and continuous flow path, there is a need to align the ends of the duct with the direction of the upstream and downstream passages. The consequence is the induced S-shape, as already mentioned, but also the geometrical curvature of the two bends will be of a similar magnitude but opposite sense.

From these geometrical parameters, Britchford, Manners, McGuirk, et al. [20] described a method established by Rolls-Royce to design the geometry of an S-duct. This method is based on the following physical hypotheses:

- The flow is inviscid and irrotational,
- all streamlines rotate around a common axis.

The duct's shape can be described by any mathematical function relating the radius of the mean line R_m to an axial position x. The inner (hub) and outer (shroud) annulus walls can be specified as individual functions as $R_{hub} = f_i(x)$ and $R_{shroud} = f_o(x)$. The usual design method consists of specifying the mean radius R_m depending on the axial position x/L:

$$R_m = a_1 + a_2 \cos\left(\pi \frac{x}{L}\right) - a_3 \sin^2(\pi \frac{x}{L}) \tag{2.4}$$

The first and second derivatives thus give:

$$R'_m = -a_2 \frac{\pi}{L} \sin\left(\pi \frac{x}{L}\right) - a_3 \frac{\pi}{L} \sin\left(2\pi \frac{x}{L}\right) \tag{2.5}$$

$$R''_m = \frac{1}{R_{curv}} = -a_2 \left(\frac{\pi}{L}\right)^2 \cos\left(\pi \frac{x}{L}\right) - 2a_3 \left(\frac{\pi}{L}\right)^2 \cos\left(2\pi \frac{x}{L}\right) \tag{2.6}$$

The coefficients (a_1, a_2, a_3) are then determined from the end conditions at the duct inlet, $x/L = 0$, and outlet $x/L = 1$. a_1 and a_2 are related to the duct inlet and exit mean radii. The third coefficient is linked to the mean radius of curvature at the inlet and exit and is necessarily zero to have equal curvatures at both ends. If $a_3 \neq 0$, this allows flexibility in how the duct mean radius changes from inlet to outlet as a function of non-dimensional axial position. Fig. 2.2 illustrates the duct geometry obtained while varying a_3.

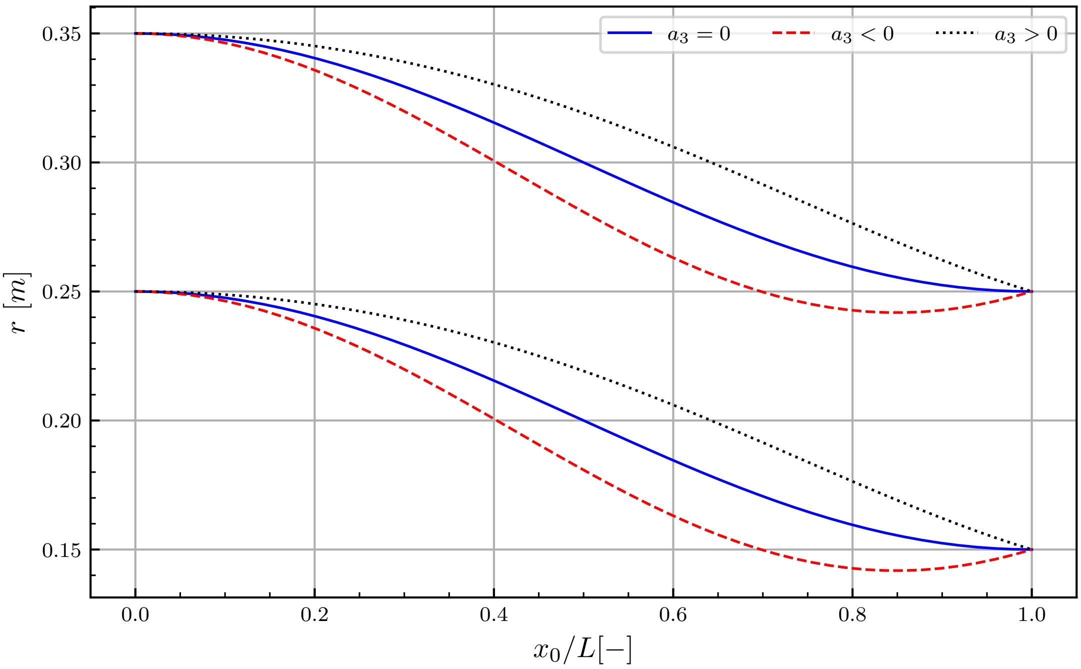

Figure **(2.2)** – Effect of coefficient a_3 on the S-duct geometry.

2.2.2 Difference Between Circular, Annular, Rectangular, Axisymmetric, Non-Axisymmetric Ducts

Considering the degrees of freedom to design an S-duct, several shapes exist, as summarized in Table 2.1. These different types of diffusers are used, depending on the range of applications and conception constraints, but they mainly differ by the shape of their cross-section.

Table **(2.1)** – Presentation of the different kinds of diffuser ducts.

Beginning of Table		
Type of ducts	Uses	Illustration
Annular ducts [21]	These ducts are usually found in modern aero-engines as inter-stage components (compressor or turbine).	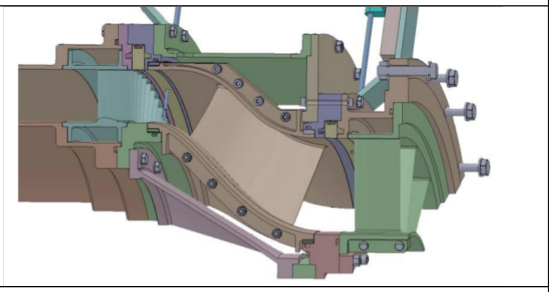
Circular ducts [22]	They are mainly used as air intakes on commercial and military engines for their good performance in terms of weight savings and low noise levels.	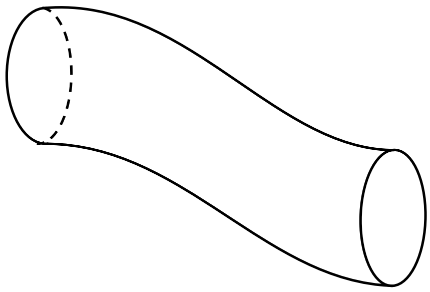
Non-axisymmetric ducts [23]	More aggressive ducts are usually obtained with non-axisymmetric profiling.	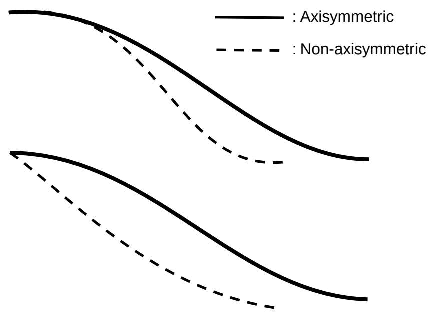
Rectangular ducts [24]	Also used for some aero-engine inlets. The same flow mechanisms are developing in those ducts as in circular ducts.	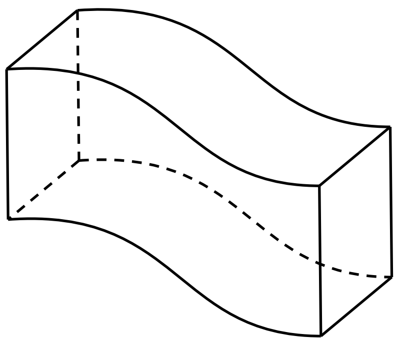

Continuation of Table 2.1		
Type of ducts	Uses	Illustration
Y-shaped or double-offset ducts [25, 26]	Mostly used for single-engine modern combat aircraft.	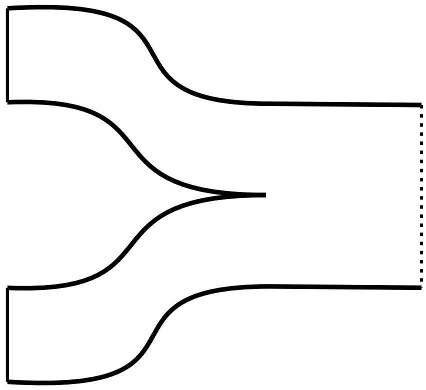
End of Table		

During this Ph.D., the focus was placed on the study of annular inter-compressor S-ducts. Thus, in the following, the literature review will focus on this specific type of duct as it is more relevant in the framework.

2.2.3 Addition of a Strut to an S-duct

The geometry described in the previous section is somehow simplified because of a missing element installed in real aero-engines. Indeed, streamlined struts pass through the annular S-duct as shown in Fig. 2.3. Their role is mainly structural by carrying mechanical loads from the engine's core to the outer structure and for mechanical maintenance. Cables and electronics also go through these struts to access the engine's interior.

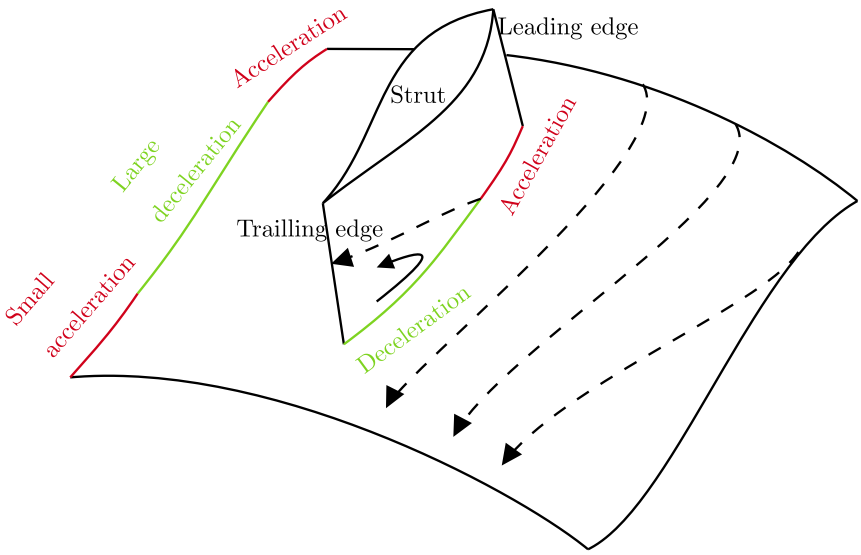

Figure **(2.3)** – Scheme of the flow field developing around a strut (adapted from [27]).

Naturally, these struts can disrupt the flow because of their aerodynamics. They induce a reduction of the S-duct cross-section, creating a convergent-divergent passage, implying first acceleration of the flow and then an additional deceleration. It should also be noted that the struts may not have the same thickness, their number varies depending on the engine considered, and they might not be uniformly distributed in the circumferential direction. For a strutted S-duct, an additional non-dimensional geometrical parameter is added, the thickness to chord ratio, t/c (see Fig. 2.4) as introduced in [12].

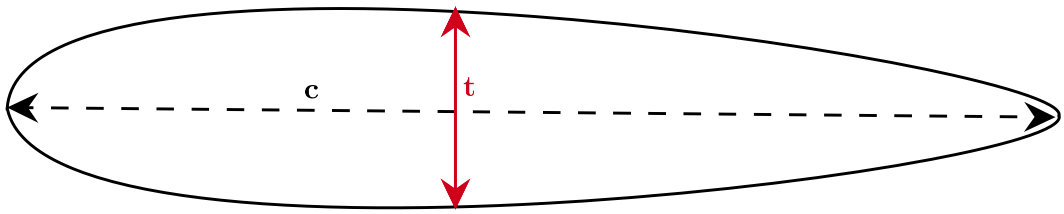

Figure **(2.4)** – Illustration of a strut's thickness to chord ratio (top view).

Finally, in several studies [12, 27, 23], other geometrical parameters close in definition to those defined by Britchford [19] are used. This raises to five the number of non-dimensional geometrical parameters that can describe an S-duct and four if the duct is not strutted. The typical values of these parameters [23] are summed up in Table 2.2 and were represented in Fig. 2.1.

Recent ducts	$\frac{\Delta R}{L} \approx 0.3 - 0.45$	$\frac{A_{out}}{A_{in}} \approx 1.6$	$\frac{L}{h_{in}} \approx 0.1 - 0.3$	$\frac{r_{in}}{L} \approx 1.5 - 1.7$	$\frac{t}{c} \approx 0.14 - 0.3$

Table **(2.2)** – Summary of the geometrical parameters used in the literature.

The non-dimensional radius $\Delta R/L$ reflects the severity of the curvature-induced pressure gradients. The duct area ratio A_{out}/A_{in} reflects the bulk deceleration (or acceleration) of the fluid. The non-dimensional length L/h_{in} will dictate the axial pressure gradient.

2.3 Evaluation of S-ducts Performance

This section is devoted to the introduction of several definitions of loss coefficients. Many formulations have been found during the literature review and are summed up and compared in the following.

2.3.1 Static Pressure Rise Coefficient

Considering that the primary role of an S-duct is to act as a diffuser, performance is usually expressed by measuring the static pressure rise across the passage. To evaluate the performance of axisymmetric or non-axisymmetric duct, it is possible to use the static pressure rise coefficient $Y_{p,s}$ as defined in Eq. 2.7. $\tilde{P}_{s,out}$ refers to the mass-weighted averaged static pressure at the duct outlet, $\tilde{P}_{s,in}$ the mass-weighted averaged static pressure at the duct inlet, where the flow is likely to be more uniform, giving a more reliable reference value. $\tilde{P}_{t,in}$ is the mass-weighted averaged total pressure at the duct inlet. This coefficient represents the energy transformation within the aerodynamic passage [28].

$$Y_{p,s} = \frac{\tilde{P}_{s,out} - \tilde{P}_{s,in}}{\tilde{P}_{t,in} - \tilde{P}_{s,in}} \tag{2.7}$$

2.3.2 Ideal Static Pressure Rise Coefficient

The ideal coefficient of static pressure, $Y_{ps,ideal}$, represents the outlet pressure recovery of an ideal duct where the flow is frictionless and uniform throughout the duct [28]. This coefficient assumes that no total pressure loss occurs within the duct. It represents the maximum possible diffusion if the flow was diffused isentropically. It is computed from the AR parameter according to Eq. 2.8.

$$Y_{ps,ideal} = 1 - \frac{1}{AR^2} \tag{2.8}$$

2.3.3 Diffuser Effectiveness

Several factors, such as wall friction, turbulence generation, and flow separation, imply that the ideal recovery coefficient will never be reached. In this case, its pressure recovery rate is expressed by ϵ (see Eq. 2.9), computed as the ratio between the static and ideal static pressure coefficients.

$$\epsilon = \frac{Y_{ps}}{Y_{ps,ideal}} \tag{2.9}$$

2.3.4 Total Pressure Loss Coefficient

The total pressure loss coefficient, $Y_{p,t}$, is often used to define a notion of loss. It is defined in Eq. 2.10 and illustrates how much total pressure has been lost to overcome the viscous effect as well as the turbulence of the fluid. Here, $\tilde{P}_{t,in}$ is the mass-weighted averaged total pressure at the inlet while $\tilde{P}_{t,out}$ is the mass-weighted averaged total pressure at the outlet.

$$Y_{p,t} = \frac{\tilde{P}_{t,in} - \tilde{P}_{t,out}}{\tilde{P}_{t,in} - \tilde{P}_{s,in}} \tag{2.10}$$

This definition will be used in the following because it shows similarities with most other definitions of losses found during the literature review. The table 2.3 summarizes the different definitions that were also found to evaluate the losses in an S-duct.

Table **(2.3)** – Summary of the loss definitions.

Beginning of Table		
Authors	Definition	Remarks
[29, 23, 30, 10, 31]	$Y_{p,t} = \dfrac{\tilde{P}_{t,in} - \tilde{P}_{t,out}}{\tilde{q}_{in}}$	Where $\tilde{P}_{t,in}$ and $\tilde{P}_{t,out}$ refer to the mass-weighted averaged total pressure at the inlet and the outlet of the S-duct while $\tilde{q}_{in} = (\tilde{P}_t - \tilde{P}_s)_{in}$ refers to the mass-weighted averaged dynamic pressure at the inlet.
Bergstedt [32]	$Y^1_{p,t} = \dfrac{\tilde{P}_{t,in} - \tilde{P}_{t,out}}{\tilde{q}_{out}}$	The dynamic pressure is taken at the duct exit: $\tilde{q}_{out} = (\tilde{P}_t - \tilde{P}_s)_{out}$.
Dueñas, Miller, Hodson, et al. [12], Naylor, Dueñas, Miller, et al. [27]	$Y^2_{p,t} = \dfrac{\tilde{P}_{t,in} - \tilde{P}_{t,out}}{\tilde{q}_{ref}}$	$\tilde{q}_{ref} = (\tilde{P}_t - \tilde{P}_s)_{ref}$ refers to the mass-weighted averaged dynamic pressure at a reference plane, usually well before the duct inlet.
StürzebecherSt, Goinis, Voss, et al. [33]	$C_{\Delta s} = \log\left(\dfrac{P_{t,out,is}/P_{t,in}}{P_{t,out}/P_{t,in,is}}\right)$	Estimate the loss by defining an entropy rise coefficient.
Wallin, Ross, Rusche, et al. [31]	$Y^3_{p,t} = \dfrac{\tilde{P}_{t,in} - \tilde{P}_{t,out}}{\tilde{P}_{t,in}}$	The mass-weighted averaged inlet total pressure is used at the denominator instead of the dynamic pressure in the other definitions.
Wallin, Olsson, Johansson, et al. [21]	$Y^4_{p,t} = \dfrac{\bar{P}_{t,in} - \bar{P}_{t,out}}{\bar{P}_{t,out}}$	In this study, the mass-weighted averaged outlet total pressure is used at the denominator.
Rider, Ingram, and Stowe [34], Asghar, Stowe, Allan, et al. [35], [36, 37, 38]	$\bar{\pi} = \left[\dfrac{\bar{P}_{t,out}}{P_{t,in}}\right]$ $\bar{\gamma} = 1 - \bar{\pi}$	Total pressure ratio $\bar{\pi}$ computed from an area-averaged total pressure ratio between the inlet and outlet. Then, a total pressure loss coefficient, $\bar{\gamma}$, is defined.
End of Table		

2.4 Physical Phenomenon

This section presents the main physical phenomena established in the literature that pilot the S-duct flow field.

2.4.1 Curvature Effects and Resulting Pressure Gradients

This section investigates the pressure variation along the S-duct resulting from the curvature effects. By assuming that the flow is inviscid, moving with velocity U in a circular path of radius R, the radial pressure gradient necessary to maintain the flow in radial equilibrium is given by:

$$\frac{1}{\rho}\frac{\partial p}{\partial r} = \frac{U^2}{R} \tag{2.11}$$

The pressure must increase from the convex to the concave side of each bend. Therefore, the pressure increases from the inner wall (the hub) to the outer wall (the shroud) in the first bend. Since the flow is nominally returned to the axial direction by the second bend, the pressure gradient across this duct part is reversed. Curvature is thus responsible for pressure gradients along the stream-wise and the radial direction influencing the boundary layer development. Fig. 2.5 shows the different directions of the pressure gradients developing in an S-duct.

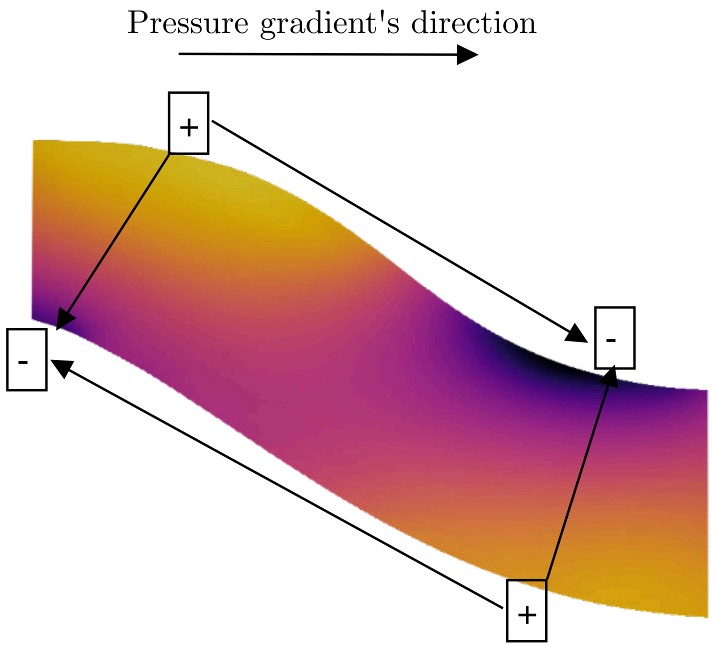

Figure **(2.5)** – Illustration of the pressure gradients in an S-duct.

Fig. 2.6 illustrates the evolution of the pressure distribution in an S-duct by plotting the wall static pressure, C_p, along the inner and outer walls.

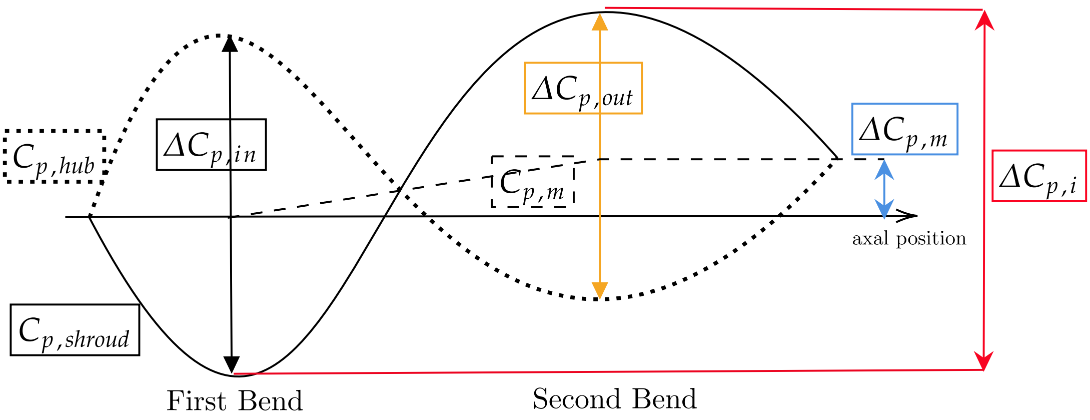

Figure **(2.6)** – Evolution of the pressure distribution in an S-duct.

- $C_{p,hub}$ and $C_{p,shroud}$ represent the evolution of C_p along of the inner and outer wall respectively.
- $\Delta C_{p,in}$ and $\Delta C_{p,out}$ represent the difference of C_p between the inner and outer wall in the first and second bend, respectively.
- $C_{p,m}$ represents the variation of C_p along the duct.
- $\Delta C_{p,m}$ represents the difference of averaged C_p between the inlet and the outlet of the S-duct. It depends on the area ratio ($AR \leq 1$ or $AR \geq 1$).
- $\Delta C_{p,i} = 0.5(\Delta C_{p,in} + \Delta C_{p,out} + \Delta C_{p,m})$ represents the global difference of C_p on the inner wall between the first and second bend of the S-duct.

The last parameter $\Delta C_{p,i}$ is most interesting. From it, it is possible to obtain a non-dimensional number, called the aerodynamic loading, by dividing it by $\frac{L}{h_{in}}$. The aerodynamic loading, as a function of the three non-dimensional geometric parameters, is then given by Eq. 2.12.

$$ADL = \left(\frac{\Delta C_{p,i}}{\frac{L}{h_{in}}}\right)_{total} = 6\left(\frac{\Delta R}{L}\right)\left(\frac{1}{(\frac{L}{h_{in}})^2}\right)(1 + AR^{-2}) + \left(\frac{1 - AR^{-2}}{\frac{L}{h_{in}}}\right) \tag{2.12}$$

A more in-depth study of the evolution of this duct loading will be presented in section 2.4.3.1. For the moment, the focus is placed on the effects of wall curvature on duct physics, as presented in the following.

Bailey, Britchford, Carrotte, et al. [39], in an experimental investigation on a representative inter-compressor annular S-duct, showed that streamwise pressure gradients are present in the duct due to curvature. These gradients can influence the mixing of blade wakes from the upstream compressor stage and the boundary layer development at the inner and outer walls. Moreover, this curvature can also affect the generation and suppression of turbulence. Indeed, turbulence levels are reduced over a convex surface, whereas, near a concave surface, turbulence mixing is increased.

Majumdar, Singh, and Agrawal [40] experimentally studied the flow characteristics in an S-shaped diffusing duct. At the transition between the two bends, a flow reversal was observed. The resulting separation yields to a lower pressure recovery compared to a straight duct. The maximum turbulence intensity was seen just downstream of the inflection plane.

Kumar Gopaliya, Kumar, Kumar, et al. [41] studied the performance evolution of an S-shaped duct when changing the offset between the inlet and outlet, thus increasing the curvature effects. It was concluded that the total pressure recovery coefficient, effectiveness, and non-uniformity decreased as the duct offset increased. This is linked to increased secondary flows as the turning angle is sharper.

To characterize the flows in curved ducts Ng, Luo, Lim, et al. [42] introduced a new parameter denoted Ω. This parameter is computed from the ratio between the radial pressure gradient forces and centrifugal ones. These two forces are dominants in S-duct flows, thus highlighting the need for a non-dimensional parameter to consider those. Finally, it was shown that secondary flows are generated as the fluid at the duct axis has a higher velocity (thus greater centrifugal force) than the fluid near the duct walls.

2.4.2 Introduction of Struts and Induced Modification on the Flow Field

The introduction of struts in an annular S-duct is not transparent as it is situated in the flow path. It is then necessary to consider their presence as their introduction modifies the flow field and can create a strut-hub separation, thus increasing the loss in the duct. Fig. 2.3 illustrates the main physical phenomenon near a strut. A stagnation is created as the flow approaches the strut and accelerates before finally decelerating near the trailing edge. This final deceleration at the trailing edge occurs in the region where the curvature at the outer wall creates a large acceleration. Therefore, considering the conditions at the outer wall, the boundary layer is unlikely to separate. However, the situation is more delicate at the inner wall as the opposite happens. Indeed, at the inner wall near the trailing edge, the deceleration caused by the strut is added to the one established by the adverse pressure gradient, potentially leading to the strut-hub separation raised before. Moreover, struts could engender vortices that, combined with the pressure field, may promote flow separation. If separation occurs, extra losses and distortions that could impact downstream components will be created. For all the reasons presented here, the experimental and numerical studies of strutted ducts have been the subject of extensive research.

Bailey, Britchford, Carrotte, et al. [39] have experimentally studied the effects brought by the introduction of a strut ($t/c = 0.12$). It was shown that the strut induced a blockage effect at the duct inlet, with thicker boundary layers and a small core region of high velocity at the casing. The strut wake is visible downstream, but no separated flow regions were observed. Moreover, it was found that the static pressure distribution around the strut was determined not only by the strut profile but also by the pressure distribution induced by the duct itself. Finally, introducing a single strut had a minimal impact on the performance (a slight increase of 5% of the loss coefficient), but only one strut was considered. Usually, for a modern engine, several struts are used, meaning that each strut will add a similar contribution to the total pressure loss, assuming that each strut is independent of its nearest neighbor.

Norris, Dominy, and Smith [43] experimentally studied a representative inter-turbine annular duct diffusers. It is presented that aerofoil struts have an associated diffusion and an additional blockage effect, potentially leading to flow separation. It is recalled that the actual duct loss with the in situ struts could be larger than the sum of the isolated strut and duct losses. In this study, 26 struts were used with an inlet Reynolds number of 3.9×10^5. They measured that the corner between the strut and the casing mostly contributes to the duct loss. Moreover, the added diffusion of the strut where the boundary layer is unstable increases the size of the separation bubble and, thus, the total pressure loss. In the end, the struts introduction raises the overall duct loss in the axial region by almost 190%, and the static pressure rise coefficient was reduced by 28.5%, diminishing the goal performance of the stage.

Sonoda, Arima, and Oana [44] investigated the effect on the performance of placing radial struts within the duct. The inlet Mach number was 0.386, and six struts were included based on NACA 0021 profiles. It was observed that a typical horseshoe vortex is created at the leading edge of the strut. This resulted in a large total pressure loss near the hub due to the instability of the flow.

Wallin and Eriksson [45] numerically studied an inter-compressor duct equipped with eight struts and compared it to a baseline duct without struts. They found that the wakes created by the struts cause major losses, increasing the loss coefficient from 4% for the baseline to 7.9% when struts are added.

Naylor, Dueñas, Miller, et al. [27] presented a new design methodology for strutted inter-compressor S-ducts at Reynolds number 2.7×10^5. It was shown that the strut ($t/c = 0.271$) causes additional pressure gradients to be imposed on the duct wall close to the strut. This leads to a potential corner separation between the strut and the hub wall as strut and duct diffusion may add their effect. The strut's blockage was found to have a large effect on the duct's pressure field. In their study, pressure loss is more sensitive at the hub than at the shroud.

Milanovic, Whiton, Florea, et al. [46] presented a numerical investigation of an inter-compressor annular duct equipped with one or six struts with thickness-to-chord ratio $t/c = 0.12$. The main finding was that total pressure loss is proportional to the number of struts introduced.

Bu, Tan, Chen, et al. [47] studied the secondary flows on a realistic annular S-duct geometry with struts at Mach number 0.46 and Reynolds number around 10^5. They showed that struts will influence the internal flow, creating vortices and wakes. The goal was to clarify the generation and evolution of the strut-induced vortices. Their geometry consisted of eight struts, whose four are thick ($t/c = 0.17$) and four are thin ($t/c = 0.085$). Due to the struts, Mach number gradients appear near the leading edge and trailing edge, as well as a separation in the strut-hub corner. The struts create vortices near the hub and shroud, leading to high total pressure loss. At the hub, vortices evolve from horseshoe vortices created at the strut leading edge, while the shroud vortices are created at the trailing edge. However, the streamwise pressure gradients influence the vortex characteristics. For instance, an adverse streamwise pressure gradient facilitates the accumulation of low-momentum fluid, promoting the generation of vortices.

Baloni, Kumar, and Channiwala [48] performed a numerical analysis to study the flow phenomenon and pressure loss inside a compressor transition S-duct at Mach number 0.675 and Reynolds number 5.41×10^5. Several cases are studied where four, six, or eight struts are considered. The main finding is that as the strut number increases, so does the loss inside the duct. Moreover, more flow non-uniformities are found within the duct when more struts are added.

Wallin, Ross, Rusche, et al. [31] investigated the loss impact on production like-features in an inter-compressor S-duct at Mach number 0.4 and Reynolds number 3.5×10^5. This study used two types of struts with thickness-to-chord $t/c = 0.13$ or $t/c = 0.17$. It was found that a greater thickness-to-chord ratio induced higher pressure loss.

This section concludes that the presence of struts in the S-duct is mainly detrimental, with the production of additional pressure losses linked to the number and thickness of the struts.

2.4.3 Consequence of Varying Geometrical Parameters: Area Ratio, Length Reduction, Radial Offset, Aspect Ratio

To design new S-ducts with more aggressive geometries, understanding the effect of changing the main geometrical parameters on the flow developing in the duct is of prime interest. To recall, the flow may be sensitive to the AR, the radial offset, also called the angle of turn, and the duct length.

2.4.3.1 Study of Influence of the Non-Dimensional Geometrical Parameters on the Aerodynamic Loading

Having defined a non-dimensional coefficient to characterize the Aerodynamic Duct Loading (ADL) (see section 2.4.1), it is now of prime interest to study the effect of a geometric variation on this parameter. Fig. 2.7 presents the duct loading evolution when one non-dimensional parameter varies while the others are kept constant.

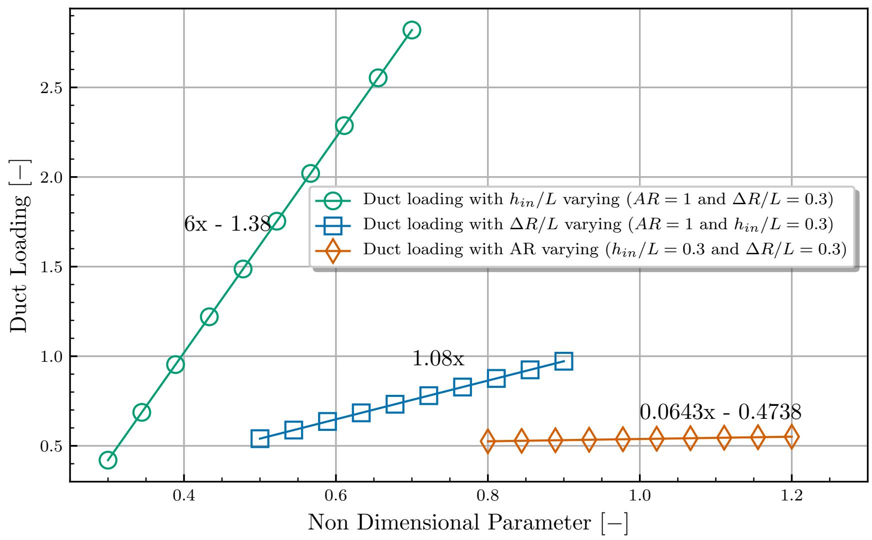

Figure **(2.7)** – Evolution of the duct loading with the variation of one geometrical parameter.

From Fig. 2.7, it can be seen that the variation of non-dimensional height, $\frac{h_{in}}{L}$, influences the aerodynamic loading six times more important than the slope, and almost 100 times more than the AR. It is thus the most sensitive parameter. To better understand how these parameters affect aerodynamic loading, an in-depth study has been conducted at iso-aerodynamic loading.

The AR drives ΔCp_m as illustrated in Fig 2.8. Indeed, if the S-duct is diverging (AR >1), the flow decelerates. Thus, the adverse pressure gradient and the aerodynamic loading are increased.

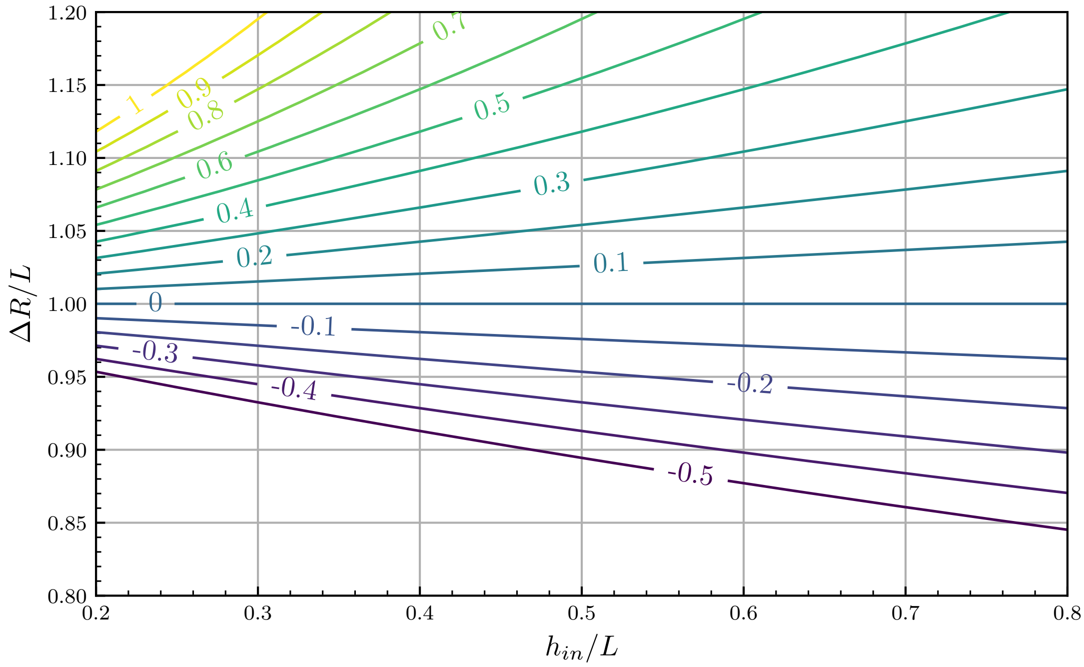

Figure **(2.8)** – Iso-duct loading with AR and h_{in}/L varying.

The NDL and MRR consider the slope and the inlet height over the length of the duct. Fig 2.9 illustrates their influence on duct loading. They pilot the effects related to the curvature of the S-duct through the values of ΔCp_{in} and ΔCp_{out}.

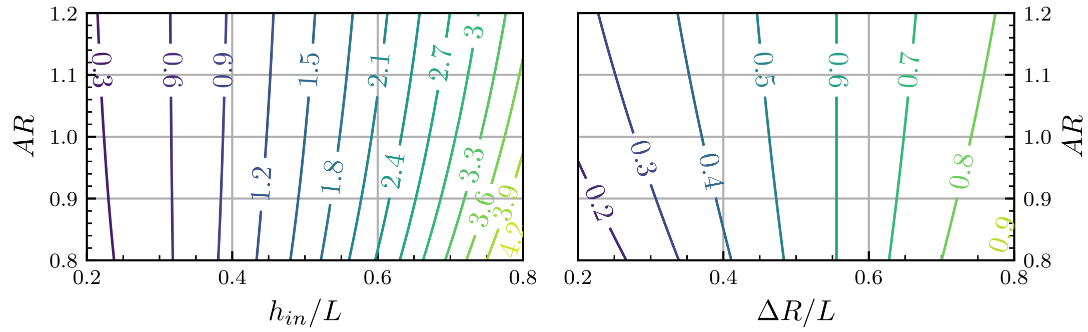

Figure **(2.9)** – Iso-loading with $\Delta R/L = 0.5$ (left) and $h_{in}/L = 0.3$ (right).

These graphics confirm the predominant effect of the NDL, $\frac{h_{in}}{L}$, on the S-duct loading because a small variation of $\frac{h_{in}}{L}$ will induce a shift between two duct loadings while a larger change of $\frac{\Delta R}{L}$ is needed to obtain the same shift. Finally, Fig 2.10 shows the iso-loading level by varying $\frac{\Delta R}{L}$ as a function of $\frac{h_{in}}{L}$ with $AR = 1$ fixed.

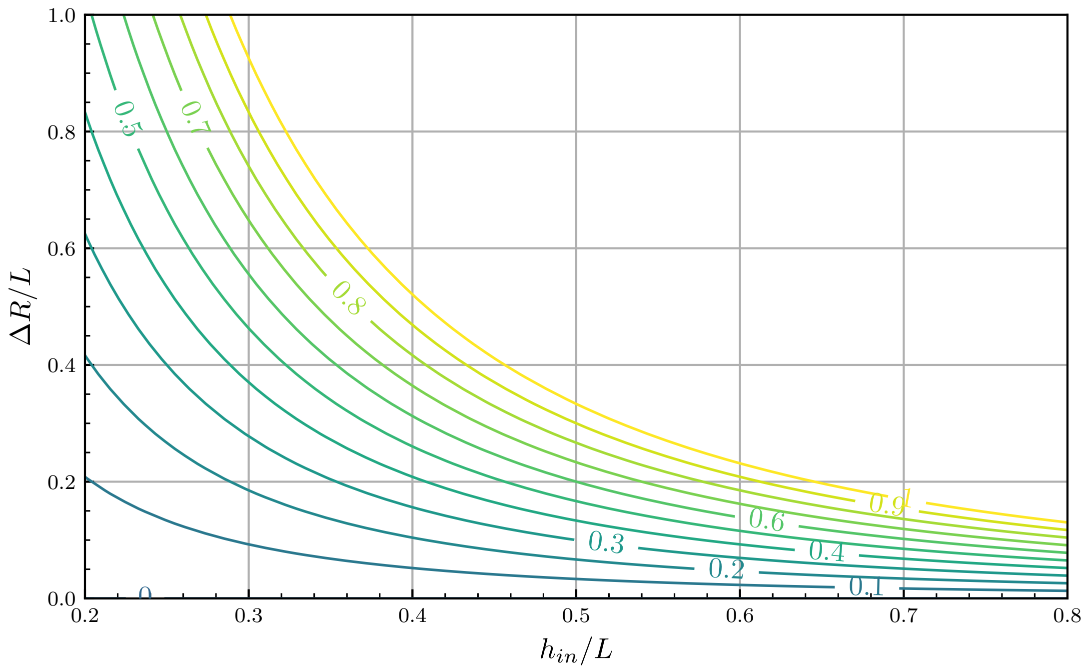

Figure **(2.10)** – Iso-duct loading at fixed AR $= 1$.

It is essential to remember that these results are obtained under strong geometrical and physical hypotheses. Indeed, in real aero-engines, the following hypotheses are usually not verified:

- The S-duct is symmetric.
- There are horizontal tangential walls at the inlet and outlet of the S-duct.

- The flow is non-rotational and inviscid.

Moreover, this definition of duct loading solely depends on geometrical considerations. It would be worthwhile to consider aerodynamic effects such as inlet velocity and distortion to improve the definition. It is thus concluded that it is impossible to estimate the actual performance of an S-duct solely from the value of the duct loading. However, these geometrical parameters can be used to characterize the overall difficulty of an S-duct to transmit the flow with a minimal level of losses. Indeed, it is legitimate to think that S-ducts with unfavorable geometries will be harder to incorporate in the final design to obtain the wanted level of performance.

2.4.3.2 Change in Area Ratio

The effect of changing the area ratio of the duct has been investigated in several studies, and it confirms a low level of influence on the pressure loss developing in the duct. Sinha, Mullick, Halder, et al. [49] experimentally studied an annular diffusing duct with an area ratio varying from 1.25 to 2 at Reynolds number 2×10^5. The main findings are that as the area ratio increases, static pressure recovery also increases and that the total pressure loss coefficient stays almost constant with this change in area ratio with similar inlet conditions.

Sinha, Mullick, Halder, et al. [50] studied a more extensive range of area ratio between 1 and 3.75 on an annular diffusing duct with an angle of turn fixed at 30°. The Reynolds number slightly differs from the previous study, this time fixed at 2.15×10^5. The static pressure recovery rose to an area ratio of 2.85 before steadily diminishing for a greater area ratio between 2.85 and 3.75. However, the total pressure loss coefficient remains constant even with a more considerable change in area ratio, as illustrated in Fig. 2.11.

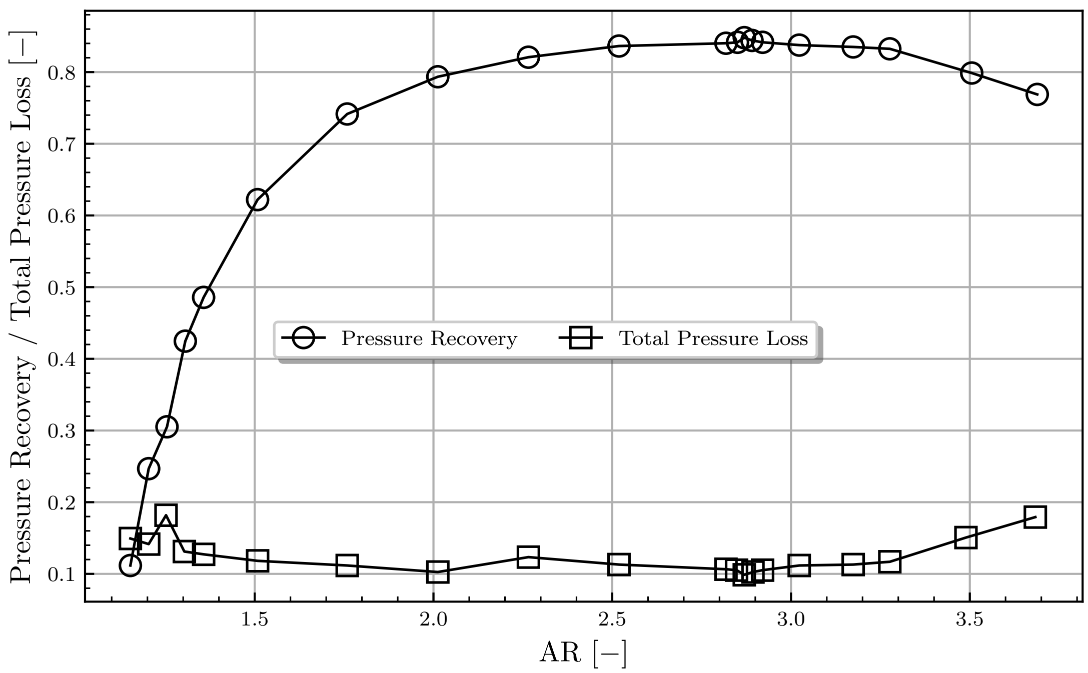

Figure **(2.11)** – Evolution of the mass average pressure recovery and total pressure loss coefficient with the area ratio (adapted from [50]).

Considering these two studies performed on annular S-ducts, as well as other investigations on circular [51] or rectangular Ducts [52], it is concluded that the area ratio is not the main geometrical factor that limits the S-duct performance.

2.4.3.3 Radial Offset (Angle of Turn)

Sinha, Mullick, Halder, et al. [49] investigated both numerically and experimentally an annular S-duct at Reynolds number 2×10^5 for angles of turn between 30 and 75°. They observed that the angle of turn had almost no influence on the total pressure loss coefficient except for the highest value, where a slight increase in loss happens as well as a slight decrease in pressure recovery (see Fig. 2.12).

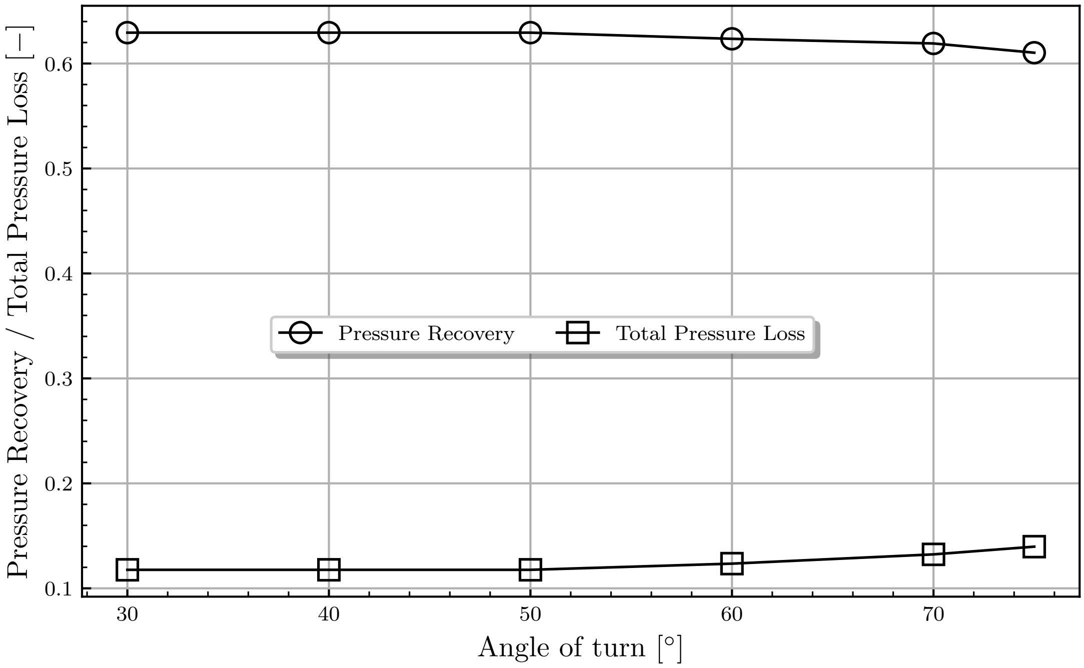

Figure **(2.12)** – Evolution of the total pressure loss and pressure recovery with the angle of turn (adapted from [49]).

This illustrates that the radial offset has the same negligible influence as the area ratio on the loss evolution in the duct.

2.4.3.4 Duct Length Reduction

Lastly, the duct length has received most of the focus as it is the main geometrical parameter to modify to design an aggressive S-duct.

Jinhan Kim, Chang Ho Choi, Jungu Noh, et al. [53] numerically studied the flow in an inter-compressor annular S-shaped duct to find the limit regarding length and radius reduction. The geometry studied is similar to the one of Britchford, Manners, McGuirk, et al. [20], integrating the complete LPC upstream of the duct. The duct length has been reduced progressively until 76% of the initial one. At this point, flow separation started to occur. This is due to the adverse pressure gradient becoming stronger, coupled with a thickening of the boundary layer at the inner wall.

Dueñas, Miller, Hodson, et al. [12] investigated the effect of length reduction at two Reynolds numbers, 1.6×10^5 and 2.6×10^5. To do so, a baseline duct was first studied before designing two ducts of 74% and 64% duct length. The net wall loss was found to be a weak function of the duct length. If the flow remains attached, the shape of the exit loss profile at the inner or outer walls did not vary with the duct length. It was also noted that the net wall loss is higher at the inner wall.

StürzebecherSt, Goinis, Voss, et al. [33] numerically studied an optimization problem to reduce the duct length. A baseline duct was characterized before axial length was reduced. The loss was evaluated using an entropy rise coefficient. It was found that as the length decreased, the losses first stayed constant before rising exponentially. This is because separation areas at the hub grow larger as the pressure gradient strengthens.

Dygutsch, Kasper, and Voss [54] also studied an optimization problem to reduce the length of an inter-compressor S-duct. Several design points were also tested (idle speed, part speed, design speed, over speed). A similar trend as [33] in the loss evolution has been found with first a reduction of losses before a significant rise (see Fig. 2.13. This is linked to a loss increase in the lower 30% of duct height caused by secondary flow structures.

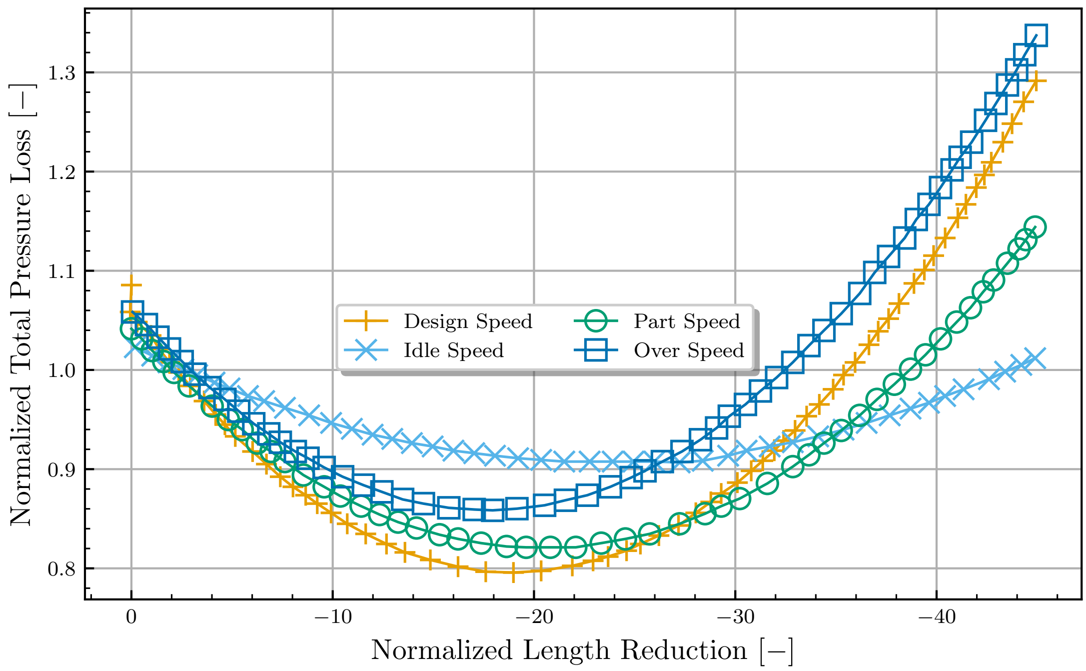

Figure **(2.13)** – Evolution of the total pressure loss with the duct length reduction (adapted from [54]).

These different studies show that duct length reduction is the geometrical parameter that affects the S-duct performance most and should be treated with care. It is also interesting to note that in most studies, a length reduction of about 20% of the initial design corresponding to today's practice could be performed without significantly increasing the loss level, meaning that significant gains can be expected from new designs.

2.4.4 Influence of Changing Inlet Conditions

This section investigates how changing the inlet conditions affects the duct flow characteristics and performance. The inlet conditions are of primary importance as they may promote the secondary flow structures described previously. These secondary flows will modify the outlet velocity and pressure profiles, finally acting on the downstream compressor.

2.4.4.1 Reynolds Number

Dueñas, Miller, Hodson, et al. [12], studied the effect of two Reynolds number, 1.6×10^5 and 2.6×10^5 on the flow developing in an annular S-duct. A small effect on the static pressure coefficient at the inner wall was noticed, and net loss rose by 0.001 with a reduction of the Reynolds number. At the outer wall, little effect on the static pressure coefficient was also found but reducing the Reynolds number raises the wall net loss by 0.005. Indeed, a separation bubble was found downstream of the peak suction location at the lowest Reynolds number. The effect was amplified for S-duct with reduced length by doubling the separation bubble's length for the lowest Reynolds number.

It was finally concluded that the net loss depends on the Reynolds number (see Fig. 2.14), as it influences the occurrence and the separation size, and that it would be important to investigate S-duct performance at representative Reynolds numbers between 7×10^5 and 10^6.

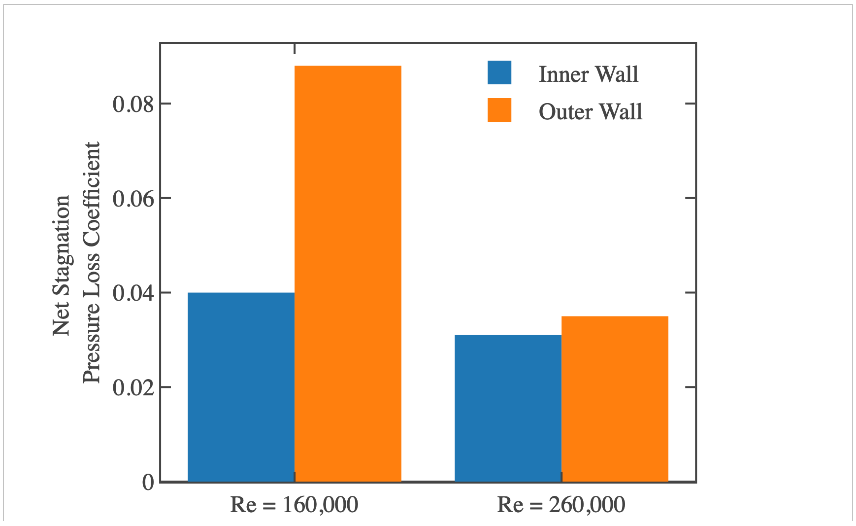

Figure **(2.14)** – Evolution of the total pressure loss with the Reynolds number (adapted from [12]).

2.4.4.2 Inlet Boundary Layer

Sonoda, Arima, and Oana [29] carried out an experimental and numerical investigation to understand the effect of the inlet Boundary Layer (BL) on the flow characteristics within an S-duct. For this study, an inlet Mach number of 0.386 was used, and two BL thicknesses were investigated and referred to as thin and thick BL. The inlet BL on the hub and shroud are of the same order, around 5% of the passage height for the thin case compared to 30% for the thick one. It was observed that the saddle point of the horseshoe vortex at the strut leading edge is moved upstream as the BL thickness increases. Moreover, the radial pressure gradient from the hub to the casing is reduced near the duct outlet as the curvature effect is diminished with the thick BL. Another observation was that a high-loss region was present on either side of the strut wake near the hub with the thick BL. Indeed, with the thick BL, a vortex pair is generated near the hub, and their counter-rotating action is pumping the low total pressure fluid from the hub into the passage, creating a hole of low total pressure.

It is concluded that the aerodynamic behavior of the duct is highly sensitive to the inlet BL thickness, with remarkable changes in the flow pattern, and that the total pressure loss is greatly increased with a thick inlet BL (going from 6.4% to 11.8%) (see Fig. 2.15).

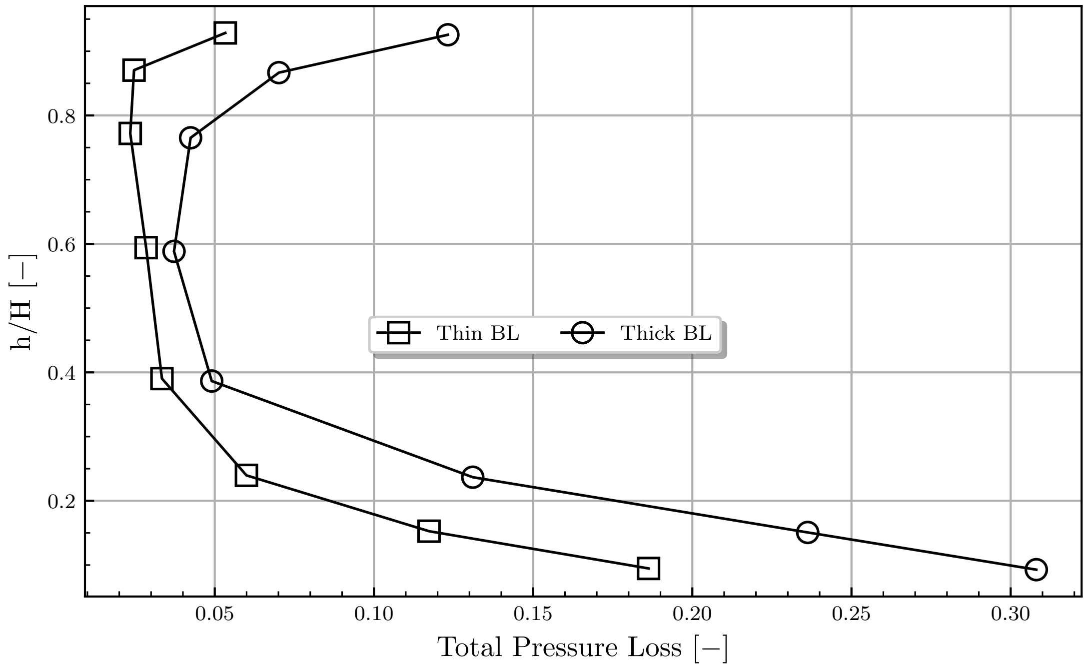

Figure **(2.15)** – Total pressure loss for the thin and thick BL (adapted from [29]).

2.4.4.3 Mach Number

Gao, Deng, Feng, et al. [55] studied the influence of inlet Mach number on the internal flow field of an inter-compressor annular S-duct with eight struts. The Mach number varied between 0.16 and 0.54. Fig. 2.16 illustrates that as the Mach number rises, the total pressure recovery coefficient follows a parabolic decrease. When the Mach number is increased, the global velocity through the duct rises, but the high-speed region grows more rapidly as the flow is accelerated around a convex surface. This combines with the strut loss, exacerbating the loss at the duct exit.

To conclude, the duct's exit flow and total pressure recovery deteriorated with an increase in the inlet Mach number.

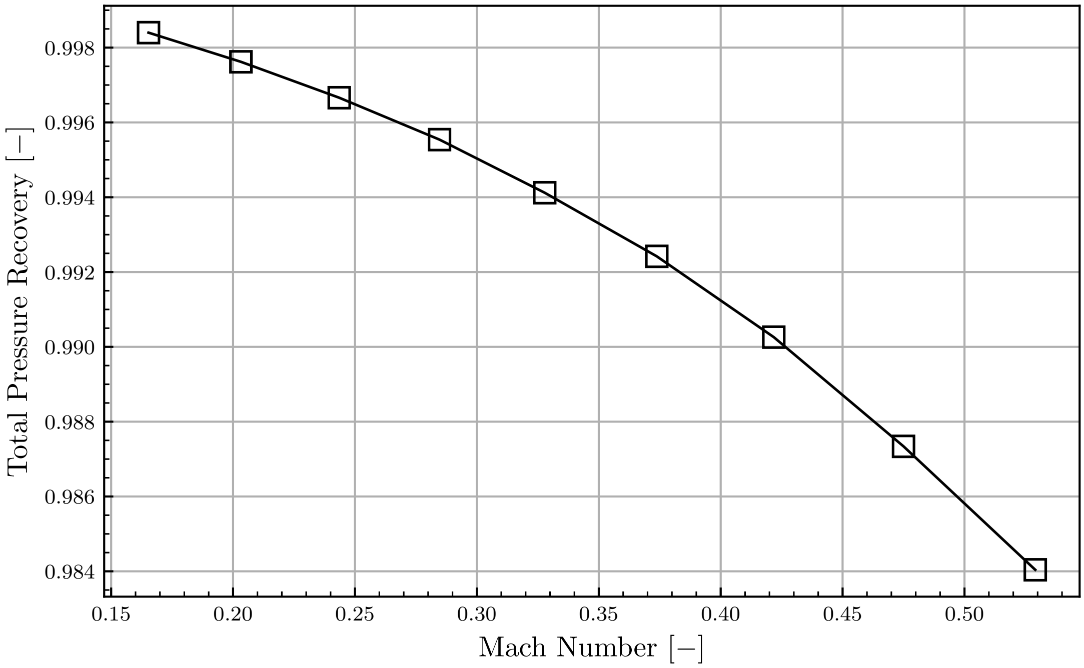

Figure **(2.16)** – Evolution of the total pressure recovery with the inlet Mach number (adapted from [55]).

2.4.4.4 Inlet Swirl

The flow entering the S-duct often has a swirl component because of insufficient straightening from the last Inlet Guide Vane (IGV) or constraints induced by the downstream component. Compressor performance and operability are affected by fluctuations of the flow entering, such as pressure and temperature distortion and flow angle.

It is of prime interest to study the influence of swirl, defined as the circumferential component of the absolute velocity vector, on the flow developing in the S-duct. Some studies have shown that a swirling flow would alter the turbulence structure, promoting flow separation. To understand that, it should be noted that turbulence mixing over the convex curvature is suppressed, whereas, over a concave curvature, it is enhanced. Thus, at the hub where the flow sees a convex followed by concave curvature, it is more prone to separation because of the adverse pressure gradient. To avoid or delay flow separation, keeping the conservation of tangential momentum along the continuously varying radius of the S-duct is necessary. This means that as the radius decreases, swirl velocity should increase. This could help lower the adverse pressure gradient at the hub and reduce the risk of separation. Several authors concluded that injecting a swirl into an S-duct indeed affected the pressure distribution, especially at the inner wall where flow separation was usually stronger. However, because of the high level of turbulence generated by the swirling effect, higher total pressure loss was obtained compared to a case without a swirl or upstream compressor.

Lohmann, Markowski, and Brookman [56] studied the performance of several diffusers over a range of inlet flow swirls. The experiment was conducted at an inlet Mach number of 0.3 and a Reynolds number of 1.3×10^5. Swirl angles of 0, 30, and 48 degrees were applied. It was observed that when a swirl is present at the inlet, an additional radial pressure gradient establishes across the passage. Moreover, an increase in the inlet swirl creates additional distortion at the diffuser exit, decreases pressure recovery, and alters the turbulent structure, potentially leading to premature flow separation.

Bailey and Carrotte [57] carried out an experimental investigation to determine the effect of inlet swirl on the flow development in an inter-compressor S-duct. To do that, the outlet guide vane upstream of the duct was removed, generating swirl angles of around 30° entering the duct. They observed that the most significant changes in the flow field happen at the inner wall, where the relative change in radius is the greatest. Because of the decrease in radius, swirl velocities rise, especially near the hub, affecting the development of the boundary layer. Stagnation pressure loss increases and apparent changes appear in the turbulence field when the inlet flow has a swirl component.

Gao, Deng, Feng, et al. [55] studied the influence of inlet pre-swirl angle on an inter-compressor S-duct equipped with eight struts at Mach number 0.52. The pre-swirl angle varies between 0 to 25° by increment of 5°. The numerical results predict that the total pressure recovery decreases linearly with the pre-swirl angle. This is due to the unequal repartition of the flow impacting the strut, creating a flow separation near the hub (where the fiercest effect is measured) on the opposite side of the strut. Moreover, this causes an increase in pressure distortion intensity.

Walker, Mariah, Tsakmakidou, et al. [58] investigated the effect of inlet swirl on an S-duct situated between the fan and the LPC. The bulk swirl at the inlet was varied between $-10°$ and 14° in steps of 2°. A negative swirl was found to have only a small effect on the exit flow structures. For a positive swirl, minor changes were observed, but a higher level of non-uniformity was obtained. Concerning the total pressure loss, for the negative swirl, it first increases marginally before rising significantly for the positive swirl as a separation region appears.

To conclude, the effect of a swirl on an S-duct is primarily detrimental. Optimum swirl injection can be achieved in some cases to delay hub separation. However, most of the time, even if swirl enhances the velocity flow throughout the duct, this tends to turn the flow towards a turbulent region. This increases the boundary layer thickness and secondary flow effects, resulting in a higher pressure loss (see Fig. 2.17).

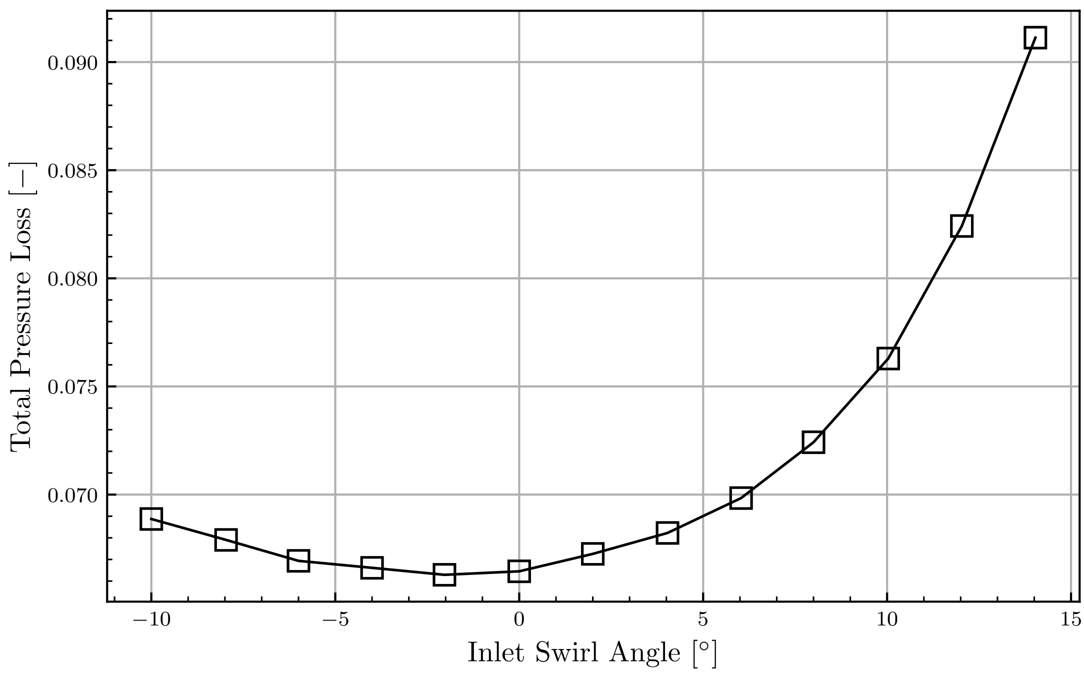

Figure **(2.17)** – Total pressure loss evolution with the inlet swirl angle (adapted from [58]).

2.4.5 Realistic Inlet Conditions from Upstream Components

Integrated design has become popular among the community due to the need to shorten the duct length. However, a clear view of the potential effects of the surrounding components, especially the upstream compressor feeding the S-duct, is required. Indeed, the inflow conditions delivered by the LPC upstream may affect the limits of the duct design, limiting the selection of a more aggressive duct.

Britchford, Manners, McGuirk, et al. [20] studied the effect of the wakes coming from an upstream stage on the flow development in an annular S-duct at Reynolds number 2.8×10^5. They observed that the stator wakes create regions of high loss at the duct inlet and are still visible at the duct exit. However, the blades' presence leads to reduced distortion of the boundary layers by the flow curvature. Indeed, the wake is driven radially inward and reenergizes the boundary layer, helping it to resist the adverse pressure gradient and reducing the flow separation tendency at the inner wall. This observation is corroborated by the study of D. W. Bailey [59] and Britchford, Carrotte, Kim, et al. [60]. However, they noticed that the additional mixing induced by the stator wakes increased the total pressure loss measured.

Later, Karakasis, J Naylor, Miller, et al. [23] investigated this mechanism in detail on an inter-compressor annular S-duct. They illustrated that the wakes cause the main impact of an upstream stage as they generate rows of streamwise counter-rotating vortices. These vortices increased duct loss by 54% in the case of the axisymmetric duct, mainly due to the increase in the mixing loss of the BL at the inner wall, which is pumped into the free stream. This effect is weaker for the non-axisymmetric duct as this geometry avoided the strut-hub separation and limited the rise of pressure loss to 28%.

The research conducted in this area concluded that the main effect of the upstream compressor was due to its wakes entering the duct. Indeed, a reduction of the flow separation was observed as the wakes reenergized the boundary layer situated at the inner wall, reducing the adverse pressure gradient promoting the separation. However, even though this positive effect was recognized, the generation of vortices induced by the wakes increased duct losses. The flow is illustrated in Fig. 2.18. The conclusion holds for axisymmetric or non-axisymmetric ducts, still, non-axisymmetric ducts have better behavior by suppressing part of the wakes.

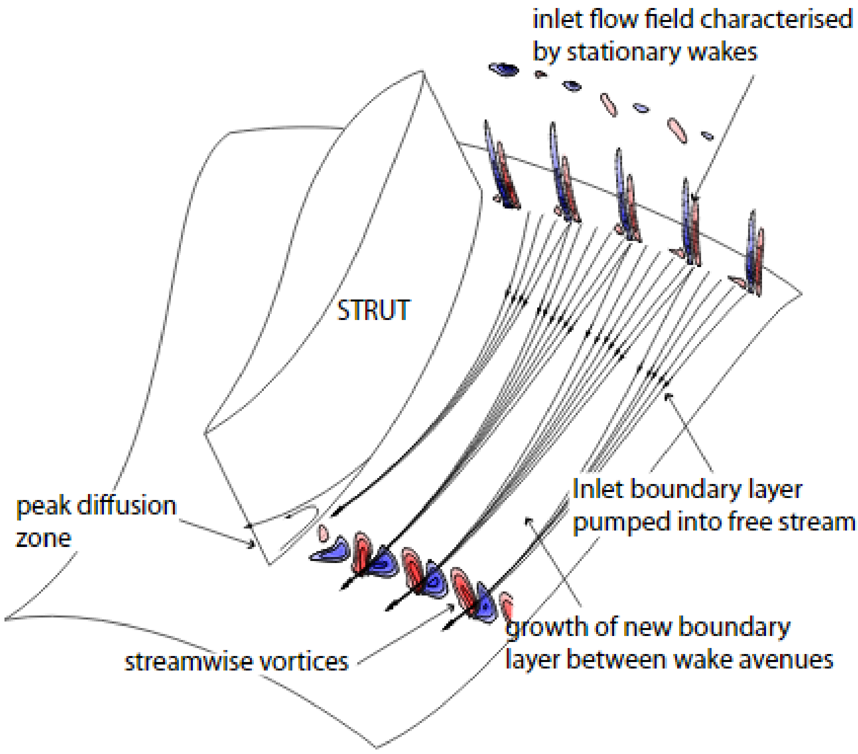

Figure **(2.18)** – Illustration of the wakes entering the S-duct and the resulting phenomenon [23].

2.5 Previous Numerical Simulations of Annular S-Ducts

Considering the complexity of the physical phenomenon occurring in an annular S-duct and the difficulty of obtaining qualitative data experimentally, especially inside the duct, it is desired to simulate the flow behavior using Computational Fluid Dynamic (CFD) codes. However, a wide variety of methods are available to run these simulations. This section is dedicated to the literature review of the numerical investigations done to study the flow behavior in an annular S-duct.

The Reynold Averaged Navier-Stokes (RANS) modeling approach is the most commonly encountered method for S-duct simulation, even with the recent emergence of high-fidelity methods. Indeed, it is widespread in the industry nowadays thanks to an interesting computational time.

2.5.1 Use of Mixing Planes

The mixing planes method is a recurrent technique in turbomachinery simulations (Fig. 2.19). It reduces the computational cost by cutting the domain size necessary to run the simulation. However, according to Jinhan Kim, Chang Ho Choi, Jungu Noh, et al. in [53], using a mixing plane at the duct inlet to study S-ducts seems unacceptable. Indeed, the results showed differences when comparing the solution where the inlet condition is adopted from the mixing plane and when the inlet condition is obtained from the experimental data. Another known consequence of mixing planes in a simulation is the incorrect prediction of the unsteadiness coming from the upstream rotor. The mixing plane weakens the wake flow of the rotor blades, and even though the overall performance is fairly predicted, the detailed flow structures, such as boundary layers, are not. The same conclusion was reached by Kumar, Alone, and Pradeep [61] where the mixing plane method used at the interface of each component seems less accurate in predicting the actual magnitude of the secondary flow structures getting transferred across.

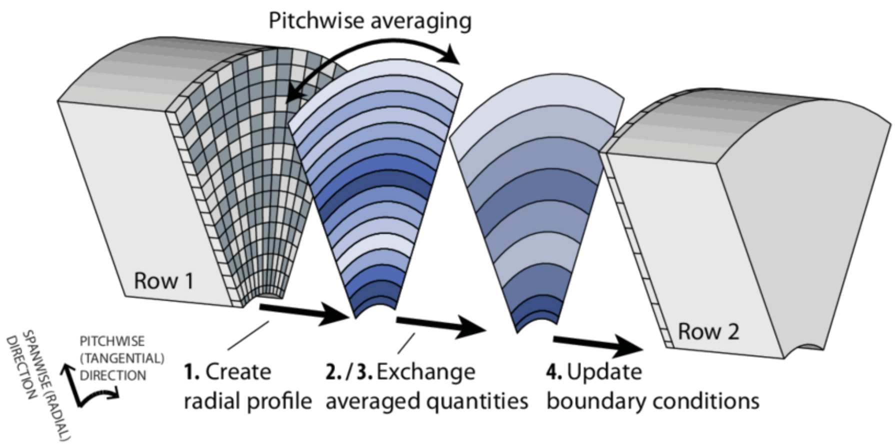

Figure **(2.19)** – Schematic representation of the multistage mixing-plane interface steps [62].

Nonetheless, several other authors in studies [32, 23, 33, 21] have used this method and did not make any comment on its influence on the results.

2.5.2 RANS Simulations

This section presents studies performed on S-ducts using the RANS formalism.

Walker, Wallin, Bergstedt, et al. [63] pursued the study of lifting struts in a compressor transition duct. The RANS equations are solved using a $k - \omega$ SST turbulence model. Boundary layers have been fully resolved, and a transition model was used, but it did not significantly impact the results. The results presented show an overall under-prediction of loss by 10% (see Fig. 2.20)

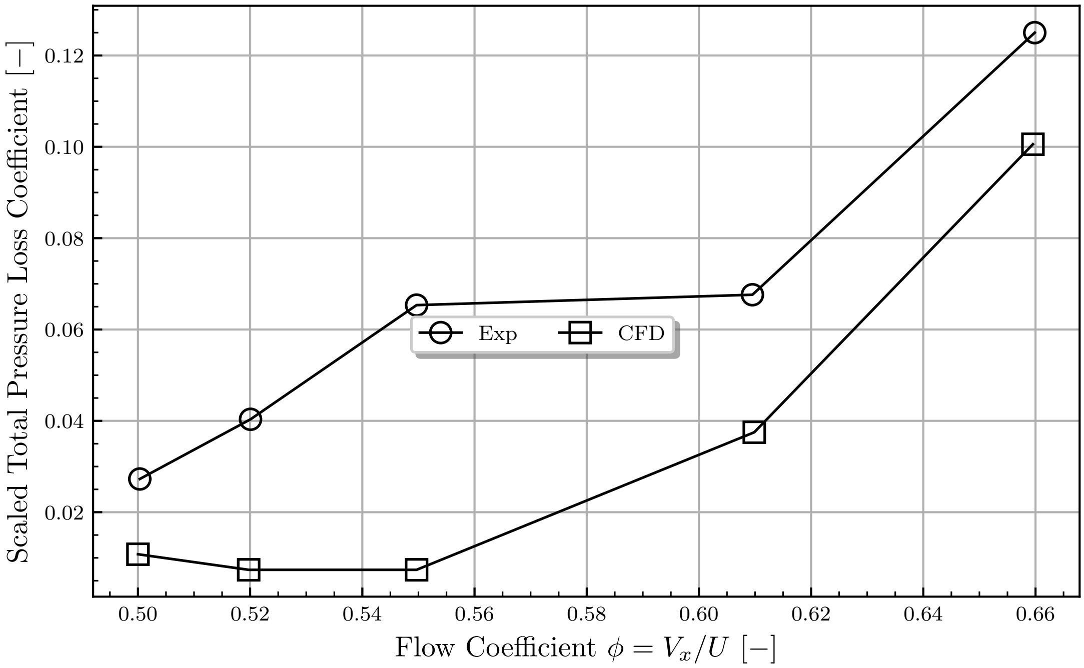

Figure **(2.20)** – Total pressure loss evolution with the flow coefficient (adapted from [63]).

Walker, Mariah, Tsakmakidou, et al. [58] studied the influence of fan root flow on the aerodynamic of a LPC transition S-duct. Solution of the RANS equations was obtained with a Reynolds stress turbulence model. A high-order model was required to capture the effects of curvature. A mixing plane was also used between the rotational and stationary domains, as well as a wall law. The results show good agreement except at $h/H = 90\%$ due to the tip leakage flows, which are challenging to capture for a steady solver. The size and strength of the main features are captured, even though some IGV wakes seem a bit dissipated. The predicted loss development is comparable through the duct, but the level is once again underestimated (see Fig. 2.21).

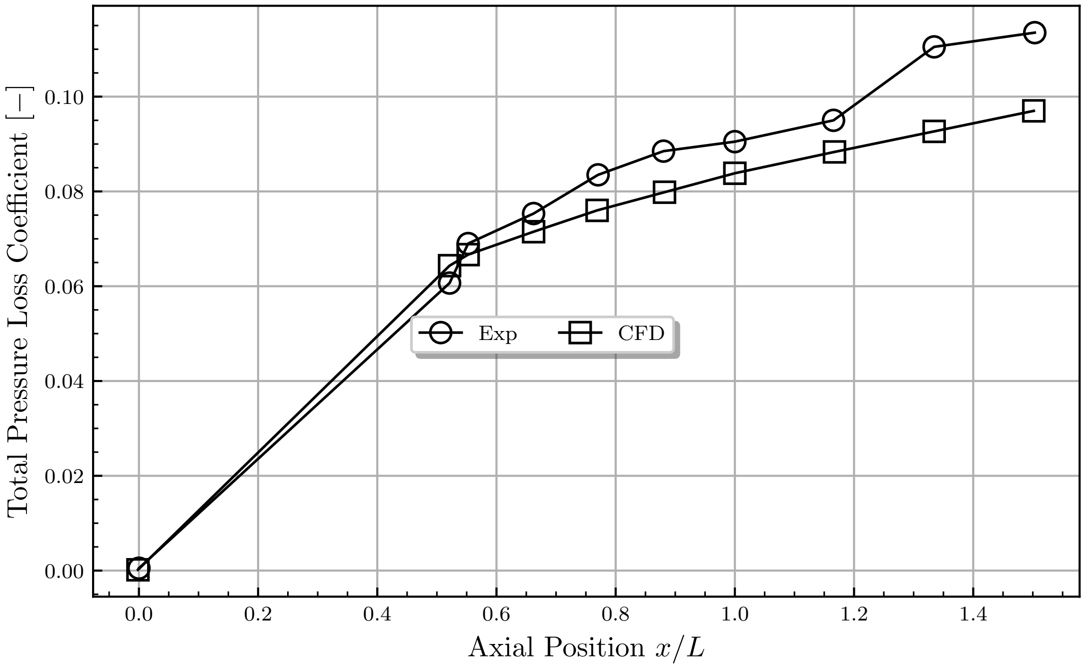

Figure **(2.21)** – Total pressure loss evolution with the axial position (adapted from [58]).

2.5.3 DDES Simulations

Considering the limitations of the RANS simulations presented previously, some authors have studied the accuracy of other numerical methods.

Siggeirsson [64] studied the validation of Delayed Detached-Eddy Simulation (DDES), RANS and Unsteady Reynold Averaged Navier-Stokes (URANS) simulations on an off-design S-duct intermediate compressor. It is explained that moving from the standard RANS based approach to more detailed numerical simulation techniques such as Large Eddy Simulation (LES) is necessary to simulate the complex flow physics and interaction effects. However, a hybrid approach is chosen with the DDES because of the computational cost. The main conclusions are that, overall, the CFD simulations are in good agreement with the experimental data. However, some differences are observed in the radial profiles of total pressure downstream of the duct. Moreover, instabilities were observed in the experiment and were partially captured by the DDES. As for URANS, this behavior is not captured, limiting the information acquired.

Siggeirsson, Andersson, and Burak Olander [65] conducted a numerical and experimental study on the aerodynamics of an intermediate S-duct with bleed. The simulations use a hybrid RANS/LES on a single operating point. It is explained that for most modern industrial CFD analysis, RANS models are used as they give reasonable estimations of averaged quantities at a low computation cost. However, these models must be replaced with more advanced techniques to better capture the unsteady flow structures caused by the interactions between the curvature effects and the adverse pressure gradients. As the cost of a pure LES remains high for turbomachinery applications at high Reynolds numbers, they used a hybrid method combining the advantages of the two models. The simulation results are then compared to the experiment. It was found that the CFD simulations could predict the measured pressure, even though some deviations are observed for the lowest level of bleed. The results can provide improved predictions for the total pressure profile downstream of the duct due to better mixing of the Outlet Guide Vane (OGV) wakes.

2.6 Chapter Summary

This first part of the literature review focuses on the flow developing in an S-duct. It began by highlighting the major role of S-shape diffusing ducts and what is at stake in improving their designs. Then, a basic description of the different kinds of S-ducts likely to be encountered in aeronautic applications and the definition of the main geometrical parameters have been given. The different notions of losses used later have been defined before developing the physical phenomena that occur in an S-duct. It was shown that the loss level was mainly influenced by a change of inlet conditions, especially from the upstream stator wakes, or by a reduction of duct length.

The second part presented numerous studies on inter-compressor S-ducts focused on the numerical simulation of the flow behavior. Most of them used the RANS formulation for the simulations, with a recurrent conclusion that this formalism is not the best suited for the simulation of flow phenomenon occurring inside an S-duct. Indeed, it was shown that the simulation quality is first highly influenced by the choice of the turbulence model. Some models seem not suited for this kind of simulation as they do not perform well when wall curvature is involved [12, 66, 46]. Moreover, several studies have shown that the total pressure loss level, which is a main quantity of interest, seems especially hard to predict accurately and is usually under-estimated [21, 63, 58, 65, 54] by the RANS.

Finally, to the author's knowledge, very few high-fidelity simulations on annular S-ducts have been found during the literature review, except for the different studies employing DDES [65]. The use of LES was found only for some studies on circular S-duct and has never been evaluated on a realistic inter-compressor S-duct.

Chapter 3: The Lattice Boltzmann Method

This chapter presents the lattice Boltzmann method with a traditional derivation from the mesoscopic description of fluids. This derivation links the collide-and-stream algorithm to the weakly compressible isothermal scheme. Then, the hybrid recursive regularized collision operator, which is used in the following of this manuscript, is described, as well as the various numerical ingredients necessary to get a thermal compressible LBM formulation. Finally, the version of the ProLB solver used for all the simulations is presented.

Contents

3.1 Introduction

The Lattice Boltzmann Method (LBM) finds its origin from the Lattice Gas Automata (LGA) or lattice gas models [67] introduced by Hardy, Pomeau, and Pazzis [68] and was developed as an alternative tool for computational fluid dynamics. This relatively new approach has demonstrated its capability to handle complex geometries using Cartesian grids coupled with a cut-cell approach [69, 70, 71, 72]. Moreover, the low dissipation properties demonstrated by the LBM allow small acoustic pressure fluctuations to be captured [73, 74]. These properties have made the LBM a subject of intensive research in aerodynamics [75, 76, 77] and aero-acoustics [78], and have also stimulated its extension to weakly compressible thermal flows [79, 80, 81] and fully compressible flows [82, 83, 84, 85]. Finally, the algorithm of the method is well adapted to High-Performance Computing thanks to easy parallelization [86], allowing for a competitive computational time compared to traditional Navier-Stokes solvers.

3.2 Kinetic Theory of Gases

3.2.1 Mesoscopic Fluid Description

The usual fluid representation is based on a macroscopic level, where for any position within the domain, the density, momentum, and total energy vary continuously in space and time. On the other hand, a microscopic description considers many independent particles with their own characteristics interacting with each other. Finally, the mesoscopic point of view is an intermediate vision where particles are viewed within a statistical framework. In such modeling, the particle distribution function $f_N(\boldsymbol{x}, \boldsymbol{\xi}, t)$ is used to describe a set of particles as:

$$dN = f_N(\boldsymbol{x}, \boldsymbol{\xi}, t) d\boldsymbol{x} d\boldsymbol{\xi} \tag{3.1}$$

where dN is the total number of particles at a position $\boldsymbol{x}$, with a velocity $\boldsymbol{\xi}$ at time t inside the volume $d\boldsymbol{x}$. Assuming that all the gas particles have an identical mass m, the probability density distribution function is given as:

$$f(\boldsymbol{x}, \boldsymbol{\xi}, t) = m f_N(\boldsymbol{x}, \boldsymbol{\xi}, t) \tag{3.2}$$

This distribution function defined in Eq. 3.2 gives access to the macroscopic quantities at the point $\boldsymbol{x}$ from the computation of its moments:

$$\Pi^{f,(0)} = \int_{\mathbb{R}^{\mathcal{D}}} f d\boldsymbol{\xi} = \rho \tag{3.3}$$

$$\Pi^{f,(1)}_{\alpha} = \int_{\mathbb{R}^{\mathcal{D}}} \xi_\alpha f d\boldsymbol{\xi} = \rho u_\alpha \tag{3.4}$$

$$\Pi^{f,(2)}_{\alpha\beta} = \int_{\mathbb{R}^{\mathcal{D}}} \xi_\alpha \xi_\beta f d\boldsymbol{\xi} \tag{3.5}$$

$$\Pi^{f,(3)}_{\alpha\beta\gamma} = \int_{\mathbb{R}^{\mathcal{D}}} \xi_\alpha \xi_\beta \xi_\gamma f d\boldsymbol{\xi} \tag{3.6}$$

$$\Pi^{f,(4)}_{\alpha\beta\gamma\delta} = \int_{\mathbb{R}^{\mathcal{D}}} \xi_\alpha \xi_\beta \xi_\gamma \xi_\delta f d\boldsymbol{\xi} \tag{3.7}$$

The trace of the second-order moment gives:

$$\int_{\mathbb{R}^{\mathcal{D}}} \xi_\alpha \xi_\alpha f d\boldsymbol{\xi} = 2\rho E(\boldsymbol{x}, t) \tag{3.8}$$

The integration is performed over the space of all velocities $\mathbb{R}^D$. The trace of the zeroth, first and second order moments give a link between the distribution function and density ρ, momentum $\rho\boldsymbol{u}$, and double the total energy $2\rho E$.

3.2.2 The Boltzmann Equation

To describe the evolution of the distribution function, Boltzmann [87] established the Boltzmann equation without external force:

$$\frac{\partial f}{\partial t} + \xi_\alpha \frac{\partial f}{\partial x_\alpha} = \Omega(f) \tag{3.9}$$

The left-hand side of Eq. 3.9 represents the transport of the distribution function due to their velocities. The right-hand side is the collision operator, for two monatomic gas particles noted A and B:

$$\Omega(f) = \int_{\mathbb{R}^{\mathcal{D}}} \int_{\mathbb{R}^{\mathcal{D}}} \left[f(\boldsymbol{x}, \boldsymbol{\xi}'_A, t) f(\boldsymbol{x}, \boldsymbol{\xi}'_B, t) - f(\boldsymbol{x}, \boldsymbol{\xi}_A, t) f(\boldsymbol{x}, \boldsymbol{\xi}_B, t) \right]_A |\boldsymbol{\xi}_A - \boldsymbol{\xi}_B| r^2 d\boldsymbol{\xi}_A d\boldsymbol{\xi}_B \tag{3.10}$$

Where $\boldsymbol{\xi}$ and $\boldsymbol{\xi}'$ are the pre and post-collision velocities of the two particles and r^2 the effective cross-section of the collision. However, solving this collision operator in practice is impossible, thus the problem is solved using simplified models.

3.2.3 The Boltzmann-BGK Equation

According to Boltzmann's H-theorem, the system will reach equilibrium after sufficient time. This is expressed using the Maxwell-Boltzmann equilibrium function:

$$f^{eq} = \frac{\rho}{(2\pi r_g T)^{D/2}} \exp\left\{ -\frac{(\boldsymbol{\xi} - \boldsymbol{u})^2}{2 r_g T} \right\} \tag{3.11}$$

Since an equilibrium part is defined, a non-equilibrium component can also be expressed as:

$$f = f^{eq} + f^{neq} \tag{3.12}$$

A simplified collision operator, Ω, was developed [88] under the name BGK (Bhatnagar, Gross an Krook) operator. It models the relaxation of the distribution function towards the equilibrium state with a characteristic time τ:

$$\Omega_{BGK}(f) = -\frac{1}{\tau}(f - f^{eq}) \tag{3.13}$$

It is the simplest collision operator in the field of LBM. The Boltzmann-BGK equation can be rewritten as:

$$\frac{\partial f}{\partial t} + \boldsymbol{\xi}.\nabla f = -\frac{1}{\tau}(f - f^{eq}) \tag{3.14}$$

The moments of the equilibrium distribution function are then adapted as follows:

$$\Pi^{f^{eq},(0)} = \int_{\mathbb{R}^{\mathcal{D}}} f^{eq} d\boldsymbol{\xi} = \rho \tag{3.15}$$

$$\Pi_{\alpha}^{f^{eq},(1)} = \int_{\mathbb{R}^{\mathcal{D}}} \xi_\alpha f^{eq} d\boldsymbol{\xi} = \rho u_\alpha \tag{3.16}$$

$$\Pi_{\alpha\beta}^{f^{eq},(2)} = \int_{\mathbb{R}^{\mathcal{D}}} \xi_\alpha \xi_\beta f^{eq} d\boldsymbol{\xi} = \rho u_\alpha u_\beta + \rho r_g T \delta_{\alpha\beta} \tag{3.17}$$

$$\Pi_{\alpha\beta\gamma}^{f^{eq},(3)} = \int_{\mathbb{R}^{\mathcal{D}}} \xi_\alpha \xi_\beta \xi_\gamma f^{eq} d\boldsymbol{\xi} = \rho u_\alpha u_\beta u_\gamma + \rho r_g T(u_\alpha \delta_{\beta\gamma} + u_\beta \delta_{\alpha\gamma} + u_\gamma \delta_{\alpha\beta}) \tag{3.18}$$

$$\Pi_{\alpha\beta\gamma\delta}^{f^{eq},(4)} = \int_{\mathbb{R}^{\mathcal{D}}} \xi_\alpha \xi_\beta \xi_\gamma \xi_\delta f^{eq} d\boldsymbol{\xi} = \rho u_\alpha u_\beta u_\gamma u_\delta + \rho r_g T(u_\alpha u_\beta \delta_{\gamma\delta} + u_\alpha u_\gamma \delta_{\beta\delta} + u_\alpha u_\delta \delta_{\beta\gamma} + u_\beta u_\gamma \delta_{\alpha\delta} + u_\beta u_\delta \delta_{\alpha\gamma} + u_\gamma u_\delta \delta_{\alpha\beta}) + \rho (r_g T)^2 (\delta_{\alpha\beta}\delta_{\gamma\delta} + \delta_{\alpha\gamma}\delta_{\beta\delta} + \delta_{\beta\gamma}\delta_{\alpha\delta}) \tag{3.19}$$

It can be seen that the zeroth and first-order moments of the equilibrium distribution function are identical to the ones of the distribution function (by construction of f^{eq}3.11). The construction assures the conservation of mass, momentum, and energy of the BGK collision operator. From the definition of the moments of interest (Eqs. 3.4-3.7), we can write:

$$\int_{\mathbb{R}^{\mathcal{D}}} \Omega_{BGK} d\boldsymbol{\xi} = -\frac{1}{\tau} \int_{\mathbb{R}^{\mathcal{D}}} (f - f^{eq}) d\boldsymbol{\xi} = 0 \tag{3.20}$$

$$\int_{\mathbb{R}^{\mathcal{D}}} \boldsymbol{\xi} \Omega_{BGK} d\boldsymbol{\xi} = -\frac{1}{\tau} \int_{\mathbb{R}^{\mathcal{D}}} \boldsymbol{\xi}(f - f^{eq}) d\boldsymbol{\xi} = 0 \tag{3.21}$$

$$\int_{\mathbb{R}^{\mathcal{D}}} \xi_\alpha \xi_\alpha \Omega_{BGK} d\boldsymbol{\xi} = -\frac{1}{\tau} \int_{\mathbb{R}^{\mathcal{D}}} \xi_\alpha \xi_\alpha (f - f^{eq}) d\boldsymbol{\xi} = 0 \tag{3.22}$$

These equations indicate that the zeroth, first, and trace of the second order moments are equivalent for the distribution function f and equilibrium distribution f^{eq}. The density, momentum, and total energy are called collision invariants.

3.2.4 Chapman-Enskog Expansion

To establish the link between mesoscopic theory and macroscopic physics, the traditional method is to derive a Chapmann-Enskog expansion. First, the zeroth order moment of Eq. 3.14 is written as:

$$\int_{\mathbb{R}^{\mathcal{D}}} \frac{\partial f}{\partial t} d\boldsymbol{\xi} + \int_{\mathbb{R}^{\mathcal{D}}} \xi_\alpha \frac{\partial f}{\partial x_\alpha} d\boldsymbol{\xi} = - \int_{\mathbb{R}^{\mathcal{D}}} \frac{1}{\tau}(f - f^{eq}) d\boldsymbol{\xi} \tag{3.23}$$

It is possible to simplify this equation into the continuity equation by using the definitions of the moments (Eqs. 3.4-3.7) and the collision invariance 3.21:

$$\frac{\partial \rho}{\partial t} + \frac{\partial \rho u_\alpha}{\partial x_\alpha} = 0 \tag{3.24}$$

Using the same method for the first-order moment gives the momentum equation:

$$\frac{\partial \rho u_\alpha}{\partial t} + \frac{\partial \Pi_{\alpha\beta}^{f,(2)}}{\partial x_\beta} = 0 \tag{3.25}$$

Finally, for the second order moment, this yields:

$$\frac{\partial \Pi_{\alpha\beta}^{f,(2)}}{\partial t} + \frac{\Pi_{\alpha\beta\gamma}^{f,(3)}}{\partial x_\gamma} = -\frac{1}{\tau} \Pi_{\alpha\beta}^{f^{neq},(2)} \tag{3.26}$$

Looking at Eq. 3.26, it can be seen that the right-hand side is nonzero, meaning that the second order moment $\Pi_{\alpha\beta}^{f,(2)}$ is not a collision invariant. Moreover, the equations are not closed as the momentum equation Eq. 3.25 needs the second order moment $\Pi_{\alpha\beta}^{f,(2)}$ that itself needs the third order moment $\Pi_{\alpha\beta\gamma}^{f,(3)}$.

The definition of the Knudsen needs to be introduced here. The microscopic length scale representing the mean free path of the microscopic particles is denoted $\mathcal{L}$, whereas the macroscopic length scale of the fluid domains is denoted L. The Knudsen number compares the ratio between those two length scales:

$$Kn = \frac{\mathcal{L}}{L} \tag{3.27}$$

If the Knudsen number is such as $Kn \ll 1$, the continuum approximation can be made as the distances between the particles are much smaller than the macroscopic distance of interest. This also means in a LBM context that the distance traveled by individual particles between collisions is very small. By introducing a characteristic time τ that represents the time to bring f to the equilibrium state f^{eq} and comparing that to the characteristic macroscopic time t_0 we get:

$$Kn = \frac{\mathcal{L}}{L} \sim \frac{\tau}{t_0} \ll 1 \tag{3.28}$$

From Eq. 3.28, it can be deduced that the relaxation time τ is much smaller compared to t_0. The distribution function is then defined as an equilibrium part plus a small perturbation:

$$f = \sum_{n=0}^{\infty} Kn^n f^{(n)} = f^{(0)} + Knf^{(1)} + Kn^2 f^{(2)} \tag{3.29}$$

By assuming that the zeroth order moment in Knudsen number of the distribution function is the equilibrium distribution function, we get $f^{(0)} = f^{eq}$. Then the time derivative is expanded as:

$$\frac{\partial}{\partial t} = \sum_{n=0}^{\infty} Kn^n \frac{\partial}{\partial t^{(n)}} = \frac{\partial}{\partial t^{(0)}} + Kn\frac{\partial}{\partial t^{(1)}} + Kn^2\frac{\partial}{\partial t^{(2)}} \tag{3.30}$$

The Boltzmann-BGK equation (Eq. 3.14) is rewritten using these relations up to the first order in Kn:

$$Kn^0 : \frac{\partial f^{(0)}}{\partial t^{(0)}} + \xi_\alpha \frac{\partial f^{(0)}}{\partial x_\alpha} = -\frac{1}{\tau} f^{(1)} \tag{3.31}$$

$$Kn^1 : \frac{\partial f^{(1)}}{\partial t^{(0)}} + \frac{\partial f^{(1)}}{\partial t^{(1)}} + \xi_\alpha \frac{\partial f^{(1)}}{\partial x_\alpha} = -\frac{1}{\tau} f^{(2)} \tag{3.32}$$

Then, using the equilibrium moments, Eqs. 3.16-3.19 and the collision invariants Eqs. 3.20-3.22, the zeroth and first-order moments as well as the trace of the second order moment of the order Kn^0 can be computed:

$$\frac{\partial \rho}{\partial t^{(0)}} + \frac{\partial \rho u_\alpha}{\partial x_\alpha} = -\frac{1}{\tau}\cancel{\Pi_0^{f^{(1)},(0)}} \tag{3.33}$$

$$\frac{\partial \rho u_\alpha}{\partial t^{(0)}} + \frac{\partial(\rho u_\alpha u_\beta + P_s \delta_{\alpha\beta})}{\partial x_\beta} = -\frac{1}{\tau}\cancel{\Pi_\alpha^{f^{(1)},(1)}} \tag{3.34}$$

$$\frac{\partial \rho E}{\partial t^{(0)}} + \frac{\partial(\rho E u_\alpha + P_s u_\alpha)}{\partial x_\alpha} = -\frac{1}{2\tau}\cancel{\Pi_{\alpha\alpha}^{f^{(1)},(2)}} \tag{3.35}$$

The resulting equations correspond to the Euler equations using the ideal gas law. The procedure is then repeated at order Kn^1:

$$\cancel{\frac{\partial \Pi^{f^{(1)},(0)}}{\partial t^{(0)}}} + \frac{\partial \rho}{\partial t^{(1)}} + \cancel{\frac{\partial \Pi_\alpha^{f^{(1)},(1)}}{\partial x_\alpha}} + = -\frac{1}{\tau}\cancel{\Pi^{f^{(2)},(0)}} \tag{3.36}$$

$$\cancel{\frac{\partial \Pi_\alpha^{f^{(1)},(1)}}{\partial t^{(0)}}} + \frac{\partial \rho u_\alpha}{\partial t^{(1)}} + \frac{\partial \Pi_{\alpha\beta}^{f^{(1)},(1)}}{\partial x_\beta} = -\frac{1}{\tau}\cancel{\Pi_\alpha^{f^{(2)},(1)}} \tag{3.37}$$

$$\cancel{\frac{1}{2}\frac{\partial \Pi_{\alpha\alpha}^{f^{(1)},(2)}}{\partial t^{(0)}}} + \frac{\partial \rho E}{\partial t^{(0)}} + \frac{1}{2}\frac{\partial \Pi_{\alpha\alpha\beta}^{f^{(1)},(3)}}{\partial x_\beta} = -\frac{1}{2\tau}\cancel{\Pi_{\alpha\alpha}^{f^{(2)},(2)}} \tag{3.38}$$

These equations are then rewritten to obtain the expression of $\rho, \rho u_\alpha$ and ρE up to Kn^1:

$$\frac{\partial \rho}{\partial t^{(0+1)}} + \frac{\partial \rho u_\alpha}{\partial x_\alpha} = 0 \tag{3.39}$$

$$\frac{\partial \rho u_\alpha}{\partial t^{(0+1)}} + \frac{\partial (\rho u_\alpha u_\beta + P_s \delta_{\alpha\beta})}{\partial x_\beta} = -\frac{\partial \Pi_{\alpha\beta}^{f^{(1)},(2)}}{\partial x_\beta} \tag{3.40}$$

$$\frac{\partial \rho E}{\partial t^{(0+1)}} + \frac{\partial (\rho E u_\alpha + P_s u_\alpha)}{\partial x_\alpha} = -\frac{1}{2}\frac{\partial \Pi_{\alpha\alpha\beta}^{f^{(1)},(3)}}{\partial x_\beta} \tag{3.41}$$

The off equilibrium moments $\Pi_{\alpha\beta}^{f^{(1)},(2)}$ and $\Pi_{\alpha\alpha\beta}^{f^{(1)},(3)}$ are determined by taking the second and third order moments of Eq. 3.32:

$$\frac{\Pi_{\alpha\beta}^{f^{(0)},(2)}}{\partial t^{(0)}} + \frac{\Pi_{\alpha\beta\gamma}^{f^{(0)},(3)}}{\partial x_\gamma} = -\frac{1}{\tau}\Pi_{\alpha\beta}^{f^{(1)},(2)} \tag{3.42}$$

$$\frac{\Pi_{\alpha\alpha\beta}^{f^{(0)},(3)}}{\partial t^{(0)}} + \frac{\Pi_{\alpha\alpha\beta\gamma}^{f^{(0)},(4)}}{\partial x_\gamma} = -\frac{1}{\tau}\Pi_{\alpha\alpha\beta}^{f^{(1)},(3)} \tag{3.43}$$

These relations show that $\Pi_{\alpha\alpha\beta}^{f^{(1)},(3)}$ is needed to compute $\Pi_{\alpha\beta}^{f^{(1)},(2)}$ and that $\Pi_{\alpha\alpha\beta}^{f^{(1)},(3)}$ is dependent on the fourth order moment of the equilibrium $\Pi_{\alpha\beta\gamma\delta}^{f^{(0)},(4)}$. Numerous mathematical manipulations [89] are thus required to obtain the off-equilibrium moments:

$$\Pi_{\alpha\beta}^{f^{(1)},(2)} = -\mathcal{F}_{\alpha\beta} \tag{3.44}$$

$$\Pi_{\alpha\alpha\beta}^{f^{(1)},(3)} = -2u_\alpha \mathcal{F}_{\alpha\beta} + 2q_\beta \tag{3.45}$$

with $\mathcal{F}_{\alpha\beta}$ the viscous stress tensor such as $\mathcal{F}_{\alpha\beta} = \mu\left(\frac{\partial u_\alpha}{\partial x_\beta} + \frac{\partial u_\beta}{\partial x_\alpha} - \delta_{\alpha\beta}\frac{2}{D}\frac{\partial u_\gamma}{\partial x_\gamma}\right)$, and $q_\beta = -\lambda\frac{\partial T}{\partial x_\beta}$. The equivalent macroscopic equations of the Boltzmann-BGK equation are the compressible Navier-Stokes-Fourier equations:

$$\frac{\partial \rho}{\partial t} + \frac{\partial \rho u_\alpha}{\partial x_\alpha} = 0 \tag{3.46}$$

$$\frac{\partial \rho u_\alpha}{\partial t} + \frac{\partial (\rho u_\alpha u_\beta + P_s \delta_{\alpha\beta})}{\partial x_\beta} = \frac{\partial \mathcal{F}_{\alpha\beta}}{\partial x_\beta} \tag{3.47}$$

$$\frac{\partial \rho E}{\partial t} + \frac{\partial (\rho E u_\alpha + P_s u_\alpha)}{\partial x_\alpha} = \frac{\partial (u_\alpha \mathcal{F}_{\alpha\beta})}{\partial x_\beta} - \frac{\partial q_\beta}{\partial x_\beta} \tag{3.48}$$

with the following characteristics:

$$\mu = \tau P_s \tag{3.49}$$
$$\gamma_g = \frac{c_p}{c_v} = \frac{D+2}{D} \tag{3.50}$$
$$Pr = 1 \tag{3.51}$$

The monatomic gas assumption imposes the value of γ_g, and the Pr comes from the single-relaxation time BGK operator [67].

3.2.5 The Discrete Velocity Boltzmann Equation

Moving towards the LBM requires an additional step. Until now, f represents the distribution function for any possible velocities $\boldsymbol{\xi}$ at point x and at time t. The continuous velocity space is thus discretized into a finite number of velocities to reduce the problem:

$$\boldsymbol{\xi} \to \xi_i, \forall i \in [[0, V-1]] \tag{3.52}$$
$$f(\boldsymbol{\xi}, \boldsymbol{x}, t) \to f_i(\boldsymbol{x}, t), \forall i \in [[0, V-1]] \tag{3.53}$$

The goal is to obtain discrete distribution functions f_i corresponding to the i-th velocity ξ_i. The integration of the distribution functions over the velocity space becomes:

$$\int_{\mathbb{R}^{\mathcal{D}}} f d^3\boldsymbol{\xi} \to \sum_{i=0}^{V-1} f_i \tag{3.54}$$
$$\int_{\mathbb{R}^{\mathcal{D}}} \xi_\alpha f d^3\boldsymbol{\xi} \to \sum_{i=0}^{V-1} \xi_{i\alpha} f_i \tag{3.55}$$

To ensure the same physical behavior (compressible Navier-Stokes equations) at the macroscopic level, the discrete moments up to the order four must be identical to the continuous ones and verify their collision invariance properties [90]:

$$\int_{\mathbb{R}^{\mathcal{D}}} f d^3\boldsymbol{\xi} = \int_{\mathbb{R}^{\mathcal{D}}} f^{eq} d^3\boldsymbol{\xi} = \sum_{i=0}^{V-1} f_i = \sum_{i=0}^{V-1} f_i^{eq} = \rho \tag{3.56}$$
$$\int_{\mathbb{R}^{\mathcal{D}}} \xi_\alpha f d^3\boldsymbol{\xi} = \int_{\mathbb{R}^{\mathcal{D}}} \xi_\alpha f^{eq} d^3\boldsymbol{\xi} = \sum_{i=0}^{V-1} \xi_{i\alpha} f_i = \sum_{i=0}^{V-1} \xi_{i\alpha} f_i^{eq} = \rho u_\alpha \tag{3.57}$$

This leads to the constraint that the discrete moments that can be expressed as $\sum_{i=0}^{V-1} P^n f_i$ with P^n a polynomial in $\xi_{i\alpha}$ of order N must follow a quadrature rule. The method applied is to use a Gauss-Hermite quadrature to rewrite the continuous equilibrium distribution function under a polynomial form. This allows us to recover the desired moments since the Gaussian quadrature gives the exact integral of polynomials using discrete sums [91]. This gives the following expression for the continuous equilibrium distribution function using an expansion on Hermite polynomials:

$$f^{eq}(\boldsymbol{\xi}) = \frac{\rho}{(2\pi r_g T)^{D/2}} \exp\left\{-\frac{(\boldsymbol{\xi}-\boldsymbol{u})^2}{2 r_g T}\right\} = \omega(\boldsymbol{\xi}) \sum_{n=0}^{\infty} \frac{1}{n! r_g T_0} \boldsymbol{a}^{f^{eq},(n)}_{\alpha_1 \dots \alpha_n} : \boldsymbol{\mathcal{H}}^{(n)}_{\alpha_1 \dots \alpha_n}(\boldsymbol{\xi}) \quad (3.58)$$

with ω a weight linked to a given velocity $\boldsymbol{\xi}$. $\boldsymbol{\mathcal{H}}$ is a Hermite polynomial of order n, that is expressed up to order four as:

$$\mathcal{H}^{(0)}(\boldsymbol{\xi}) = 1 \quad (3.59)$$

$$\mathcal{H}^{(1)}_{\alpha}(\boldsymbol{\xi}) = \xi_\alpha \quad (3.60)$$

$$\mathcal{H}^{(2)}_{\alpha\beta}(\boldsymbol{\xi}) = \xi_\alpha \xi_\beta - c_s^2 \delta_{\alpha\beta} \quad (3.61)$$

$$\mathcal{H}^{(3)}_{\alpha\beta\gamma}(\boldsymbol{\xi}) = \xi_\alpha \xi_\beta \xi_\gamma - c_s^2(\delta_{\alpha\beta}\xi_\gamma + \delta_{\alpha\gamma}\xi_\beta + \delta_{\beta\gamma}\xi_\alpha) \quad (3.62)$$

$$\mathcal{H}^{(4)}_{\alpha\beta\gamma\delta}(\boldsymbol{\xi}) = \xi_\alpha \xi_\beta \xi_\gamma \xi_\delta - c_s^2(\delta_{\alpha\beta}\xi_\gamma\xi_\delta + \delta_{\alpha\gamma}\xi_\beta\xi_\gamma + \delta_{\alpha\delta}\xi_\beta\xi_\gamma + \delta_{\beta\gamma}\xi_\alpha\xi_\delta + \delta_{\beta\delta}\xi_\alpha\xi_\gamma + \delta_{\gamma\delta}\xi_\alpha\xi_\beta) + c_s^4(\delta_{\alpha\beta}\delta_{\gamma\delta} + \delta_{\alpha\gamma}\delta_{\beta\delta} + \delta_{\alpha\delta}\delta_{\beta\gamma}) \quad (3.63)$$

Here $c_s = \sqrt{r_g T_0}$ is the reference speed of sound with T_0 a reference temperature. The Hermite equilibrium moments, $\boldsymbol{a}^{eq}_n$ are defined as:

$$a^{f^{eq},(0)} = \rho \quad (3.64)$$

$$a^{f^{eq},(1)}_{\alpha} = \rho u_\alpha \quad (3.65)$$

$$a^{f^{eq},(2)}_{\alpha\beta} = \rho u_\alpha u_\beta + (P_s - \rho c_s^2)\delta_{\alpha\beta} \quad (3.66)$$

$$a^{f^{eq},(3)}_{\alpha\beta\gamma} = \rho u_\alpha u_\beta u_\gamma + (P_s - \rho c_s^2)(\delta_{\alpha\beta} u_\gamma) \quad (3.67)$$

$$a^{f^{eq},(4)}_{\alpha\beta\gamma\delta} = \rho u_\alpha u_\beta u_\gamma u_\delta + (P_s - \rho c_s^2)(\delta_{\alpha\beta} u_\gamma u_\delta + \delta_{\alpha\gamma} u_\beta u_\delta + \delta_{\beta\delta} u_\beta u_\gamma + \delta_{\beta\gamma} u_\alpha u_\delta + \delta_{\beta\delta} u_\alpha u_\gamma + \delta_{\gamma\delta} u_\alpha u_\beta)(P_s r_g T - 2P_s c_s^2 + \rho c_s^4)(\delta_{\alpha\beta}\delta_{\gamma\delta} + \delta_{\alpha\gamma}\delta_{\beta\delta} + \delta_{\alpha\delta}\delta_{\beta\gamma}) \quad (3.68)$$

It should be noticed that the Hermite equilibrium moments are similar and sometimes identical to the raw equilibrium moments $\boldsymbol{\Pi}^{f^{eq},(n)}$ from Eqs. 3.4-3.7. The conservation of the raw and Hermite equilibrium moments are equivalent [92, 93]. The truncation at the order N of the Hermite expansion of the equilibrium distribution function gives:

$$f^{eq}(\boldsymbol{\xi}) \approx f^{eq,N}(\boldsymbol{\xi}) = \omega(\boldsymbol{\xi}) \sum_{n=0}^{N} \frac{1}{n! c_s^{2n}} \boldsymbol{a}^{f^{eq},(n)}_{\alpha_1 \dots \alpha_n} : \boldsymbol{\mathcal{H}}^{(n)}_{\alpha_1 \dots \alpha_n}(\boldsymbol{\xi}) \quad (3.69)$$

In the previous section, it has been shown that the fourth-order moment ($N = 4$) is necessary to obtain the fully compressible Navier-Stokes equations. Using this quadrature, it has been shown that this would lead to what is usually called multi-speed lattices that are especially costly to solve and prone to instability [94]. To avoid this problem, using lattices with a lower quadrature order called standard lattices is more common. These lattices correspond to the $D1Q3$, $D2Q9$, $D3Q19$, and $D3Q27$ allowing for $N = 2$. The incorrect evaluation of the third-order equilibrium moment leads to an error in the viscous terms in the momentum equation such that:

$$\Pi_{\alpha\beta}^{f^{neq},(2)} = -\mu\left(\frac{\partial u_\alpha}{\partial x_\beta} + \frac{\partial u_\beta}{\partial x_\alpha}\right) + \mathcal{O}(Ma^3) \tag{3.70}$$

The physical behavior retrieved thus corresponds to the athermal weakly compressible Navier-Stokes equations (due to the $\mathcal{O}(Ma^3)$ term) and because no energy equation is present. This athermal approximation changes the definition of the pressure and the speed of sound. Indeed, since $T = T_0$, the pressure is then given by $P = \rho r_g T_0$ and the speed of sound by $c_s = \sqrt{r_g T} \neq c$. This allows rewriting the pressure as $P = \rho c_s^2$ with c_s being called the Lattice speed of sound differing from the true speed of sound by a factor $\sqrt{\gamma_g}$.

The different standard lattices usually encountered are represented in Figs. 3.1 and 3.2

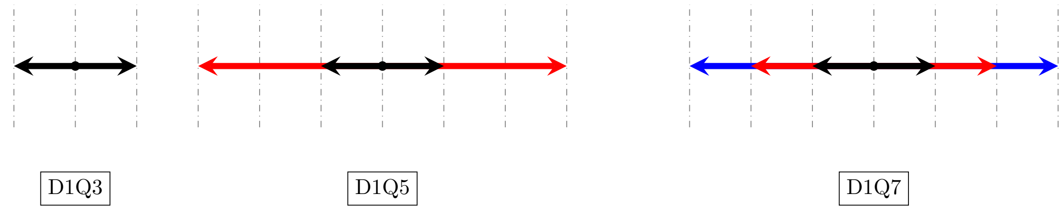

Figure **(3.1)** – Scheme of the D1Q3, D1Q5, D1Q7 lattices.

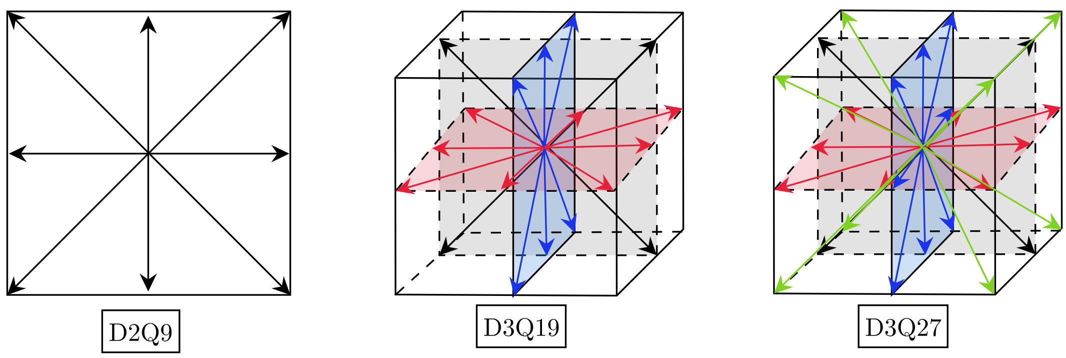

Figure **(3.2)** – Illustration of on-grid Cartesian velocity lattices.

The properties of these lattices are illustrated in Table 3.1.

Lattice	$\boldsymbol{\xi}_i/\sqrt{3}c_s$	ω_i
D3Q19	(0,0,0)	1/3
	$(\pm1,0,0)$, $(0,0,\pm1)$	1/18
	$(\pm1,\pm1,0)$, $(\pm1,0,\pm1)$, $(0,\pm1,\pm1)$	1/36
D3Q27	(0,0,0)	8/27
	$(\pm1,0,0)$, $(0,\pm1,0)$, $(0,0,\pm1)$	2/27
	$(\pm1,\pm1,0)$, $(\pm1,0,\pm1)$, $(0,\pm1,\pm1)$	1/54
	$(\pm1,\pm1,\pm1)$	1/216

Table **(3.1)** – Summary of the weights and discrete velocities for the standard 2D and 3D lattices.

Now that the choice of discrete velocities has been made using standard lattices, the Boltzmann-BGK equation becomes the Discrete Velocity Boltzmann Equation (DVBE) such that:

$$\frac{\partial f_i}{\partial t} + \xi_{i\alpha}\frac{\partial f_i}{\partial x_\alpha} = -\frac{1}{\tau}(f_i - f_i^{eq}), \forall i \in [[0, V-1]] \tag{3.71}$$

with

$$\begin{aligned} f^{eq,2}(\boldsymbol{\xi}) &= \omega_i \sum_{n=0}^{2} \frac{1}{n! c_s^{2n}} \boldsymbol{a}^{f^{eq}}_{\alpha_1\ldots\alpha_n} : \boldsymbol{\mathcal{H}}^{(n)}_{i\alpha_1\ldots\alpha_n}(\boldsymbol{\xi}) \\ &= \omega_i \left[\rho + \frac{\xi_{i\alpha}}{c_s^2}\rho u_\alpha + \frac{\mathcal{H}^{(2)}_{i\alpha\beta}}{2c_s^4}\rho u_\alpha u_\beta\right] \end{aligned} \tag{3.72}$$

3.2.6 Establishment of the Lattice Boltzmann Method, Space, and Time Discretization

This section aims to establish the final formulation of the standard Lattice Boltzmann Method by performing a discretization in space and time of the well-established DVBE that reproduces the weakly compressible athermal Navier-Stokes equations on standard lattices. The DVBE (Eq. 3.71) is integrated along a characteristic line defined as $(x_\alpha + \xi_{i\alpha}s, t+s)$ where s is a time interval:

$$\int_0^{\Delta t} \frac{\partial}{\partial t} f_i(x_\alpha + \xi_{i\alpha}\Delta t, t+\Delta t) ds + \int_0^{\Delta t} \xi_{i\alpha}\frac{\partial}{\partial x_\alpha} f_i(x_\alpha + \xi_{i\alpha}s, t+s) = \int_0^{\Delta t} \Omega_i(x_\alpha + \xi_{i\alpha}s, t+s) \tag{3.73}$$

where $\Omega_i = -\frac{1}{\tau}(f_i - f_i^{eq})$ is the discrete collision operation. Considering that $\xi_{i\alpha}$ is a constant in time and space (fixed by the choice of the discrete velocities 3.1), the left-hand side of the equation can be computed using the method of characteristics. Moreover, the right-hand side terms are computed using a trapezoidal rule:

$$f_i(x_\alpha + \xi_{i\alpha}\Delta t, t+\Delta t) - f_i(x_\alpha, t) = \frac{\Delta t}{2}\left[\Omega_i(x_\alpha + \xi_{i\alpha}\Delta t, t+\Delta t) + \Omega_i(x_\alpha, t)\right] + \mathcal{O}(\Delta t^2) \tag{3.74}$$

A change of variables is introduced to deal with the implicit scheme obtained:

$$\overline{f_i} = f_i - \frac{\Delta t}{2}\Omega_i \tag{3.75}$$

with $\overline{f_i}$ being the offset distribution function. Reintroducing this expression in 3.74 gives:

$$\begin{aligned}
&\overline{f_i}\left(x_\alpha + \xi_{i\alpha}\Delta t, t+\Delta t\right) \cancel{+\frac{\Delta t}{2}\Omega_i\left(x_\alpha + \xi_{i\alpha}\Delta t, t+\Delta t\right)} - \overline{f_i}\left(x_\alpha, t\right) - \frac{\Delta t}{2}\Omega_i\left(x_\alpha, t\right) \\
&= \frac{\Delta t}{2}\left[\cancel{\Omega_i\left(x_\alpha + \xi_{i\alpha}\Delta t, t+\Delta t\right)} + \Omega_i\left(x_\alpha, t\right)\right] + \mathcal{O}\left(\Delta t^2\right),
\end{aligned} \tag{3.76}$$

This expression can be rewritten into an explicit collide-and-stream scheme:

$$\overline{f_i}\left(x_\alpha + \xi_{i\alpha}\Delta t, t+\Delta t\right) = \overline{f_i^{col}}(x_\alpha, t) = \overline{f_i}\left(x_\alpha, t\right) + \Delta t\Omega_i(x_\alpha, t) + \mathcal{O}(\Delta t^2) \tag{3.77}$$

$\overline{f_i^{col}}(x_\alpha, t)$ represents the post-collision offset distribution functions to be streamed. Eq. 3.77 is finally slightly modified to correspond to the norm of the ProLB solver giving:

$$\overline{f_i}\left(x_\alpha, t+\Delta t\right) = \overline{f_i^{col}}(x_\alpha - \xi_{i\alpha}\Delta t, t) = \overline{f_i}\left(x_\alpha - \xi_{i\alpha}, t\right) + \Delta t\Omega_i(x_\alpha - \xi_{i\alpha}\Delta t, t) + \mathcal{O}(\Delta t^2) \tag{3.78}$$

Then the collision operator is rewritten in terms of $\overline{f_i}$:

$$\begin{aligned}
&\Omega_i = -\frac{1}{\tau}\left(f_i - f_i^{eq}\right) = -\frac{1}{\tau}\left(\overline{f_i} + \frac{\Delta t}{2}\Omega_i - f_i^{eq}\right) \\
&\to \left(1 + \frac{\Delta t}{2\tau}\right)\Omega_i = -\frac{1}{\tau}\left(\overline{f_i} - f_i^{eq}\right) \\
&\to \left(\frac{2\tau + \Delta t}{2\tau}\right)\Omega_i = -\frac{1}{\tau}\left(\overline{f_i} - f_i^{eq}\right) \\
&\to \Omega_i = -\frac{1}{\tau + \Delta t/2}\left(\overline{f_i} - f_i^{eq}\right)
\end{aligned} \tag{3.79}$$

To take into account this change in variables, a new offset relaxation time $\overline{\tau} = \tau + \frac{\Delta t}{2}$ is defined. This leads to an explicit BGK collision operator under the expression:

$$\begin{aligned}
\overline{f_i}\left(x_\alpha, t+\Delta t\right) &= \overline{f_i^{col}}(x_\alpha - \xi_{i\alpha}\Delta t, t) \\
&= \overline{f_i}(x_\alpha - \xi_{i\alpha}\Delta t, t) - \frac{\Delta t}{\overline{\tau}}\left[\overline{f_i}(x_\alpha - \xi_{i\alpha}\Delta t, t) + f_i^{eq}(x_\alpha - \xi_{i\alpha}\Delta t, t)\right] + \mathcal{O}(\Delta t^2)
\end{aligned} \tag{3.80}$$

The scheme in Eq. 3.77 can also be rewritten in terms of $\overline{f_i^{neq}}$, the offset non-equilibrium distribution function.

$$
\begin{aligned}
f_i &= f_i^{eq} + f_i^{neq} = \overline{f_i} + \frac{\Delta t}{2}\Omega_i \\
&= \overline{f_i} - \frac{\Delta t}{2\overline{\tau}}(\overline{f_i} - f_i^{eq}) \\
&= \left(1 - \frac{\Delta t}{2\overline{\tau}}\right)\overline{f_i} + \frac{\Delta t}{2\overline{\tau}} f_i^{eq} \\
\rightarrow f_i^{neq} &= \left(1 - \frac{\Delta t}{2\overline{\tau}}\right)\overline{f_i} - \left(1 - \frac{\Delta t}{2\overline{\tau}}\right) f_i^{eq} \\
\rightarrow \overline{f_i^{neq}} &= \overline{f_i} - f_i^{eq} = \frac{2\overline{\tau}}{2\overline{\tau} - \Delta t} f_i^{neq}
\end{aligned}
\tag{3.81}
$$

Finally, the collide-and-stream algorithm can be rewritten as:

$$
\overline{f_i}(x_\alpha, t + \Delta t) = f_i^{eq}(x_\alpha - \xi_{i\alpha}\Delta t, t) + \left(1 - \frac{\Delta t}{\overline{\tau}}\right)\overline{f_i^{neq}}(x_\alpha - \xi_{i\alpha}\Delta t, t) + \mathcal{O}(\Delta t^2) \tag{3.82}
$$

The next step is to write the scheme into non-dimensional units. As the DVBE imposes the characteristic velocity magnitude $c_0 = \sqrt{3r_gT_0}$ for a D3Q19 lattice, this gives the following relation between the space and time steps:

$$
\frac{\Delta x}{\Delta t} = c_0 = \sqrt{3r_gT_0} \rightarrow \Delta t = \frac{\Delta x}{\sqrt{3r_gT_0}} \tag{3.83}
$$

Using this relation, and by specifying values for the gas constant r_g, reference temperature T_0, and reference density ρ_0 as well as the mesh size Δx, all the working variables can be written in lattice units as:

$$
\begin{aligned}
\xi_{i\alpha}^* = \tfrac{\xi_{i\alpha}}{c_0} = \tfrac{\xi_{i\alpha}}{\sqrt{3}c}; c_s^* = \tfrac{c_s\Delta t}{\Delta x} = \tfrac{\sqrt{rT_0}}{\sqrt{3RT_0}} = \tfrac{1}{\sqrt{3}}; \boldsymbol{u}^* = \tfrac{\boldsymbol{u}\Delta t}{\Delta x}; \boldsymbol{x}^* = \tfrac{\boldsymbol{x}}{\Delta x}; \\
t^* = \tfrac{t}{\Delta t}; \overline{\tau}^* = \tfrac{\overline{\tau}}{\Delta t}; \rho^* = \tfrac{\rho}{\rho_0}; \theta = \tfrac{T}{T_0} = 1; p^* = \tfrac{\rho c_s^2}{\rho_0 c_0^2} = \rho c_s^{*2}; \overline{f_i}^* = \tfrac{\overline{f_i}}{\rho_0}\left(\tfrac{\Delta x}{\Delta t}\right)^{\mathcal{D}}
\end{aligned}
\tag{3.84}
$$

The non-dimensional speed of sound noted c_s^* comes from the quadrature abscissa of the DVBE and is called the lattice constant. The collide-and-stream algorithm in non-dimensional form is then:

$$
\overline{f_i}^*(x_\alpha^*, t^* + 1) = \overline{f_i}^*(x_\alpha^* - \xi_{i\alpha}^*, t^*) - \frac{1}{\overline{\tau}^*}\left[\overline{f_i}^*(x_\alpha^* - \xi_{i\alpha}^*, t^*) - f_i^{eq,*}(x_\alpha^* - \xi_{i\alpha}^*, t^*)\right] \tag{3.85}
$$

In the following, the superscript $*$ is kept to specify variables expressed in lattice units. For the temperature, the variable θ will be used to conform with this common choice in the literature.

3.3 Standard Derivation: Limits and Overcoming

To introduce the LBM, the most common way consists in linking the physical behavior recovered by the collide and stream algorithm to the weakly compressible Navier-Stokes equations starting from kinetic theory, followed by the Boltzmann-BGK equation, the Chapman Enskog expansion, the DVBE and finally the LBM. However, this methodology has been questioned recently in the work of Farag [95, 96] because several points remained unanswered using this approach. Indeed, he points out that the truncation of the distribution function f to order Kn^1 (Kn being the Knudsen number) in the Chapman Enskog expansion) is not rigorously justified. Also, since the Chapman-Enskog is based on the Boltzmann-BGK equation, applying this approach to more complex collision operators is impossible. Moreover, it was not proven that the very coarse velocity discretization used in LBM methods is sufficient to keep the mesoscopic behavior of the Boltzmann equation. Finally, the Chapman Enskog expansion differs depending on the references, and they do not produce the same results at Kn^2.

Considering these issues, the work of Farag consisted in considering the LBM as a purely numerical method relying on the Hermite moments and not using a kinetic justification for the LBM scheme. With this vision, the distribution function f_i is only a tool to transport the moments.

The goal is to show that the discretized LB scheme recovers the continuous Navier-Stokes equations. The first step consists in retrieving the DVBE from the collide and stream algorithm:

$$\begin{aligned} \overline{f_i}(x_\alpha, t+\Delta t) &= \overline{f_i^{col}}(x_\alpha - \xi_{i\alpha}\Delta t, t) \\ \rightarrow f_i(x_\alpha, t+\Delta t) &= \overline{f_i^{col}}(x_\alpha - \xi_{i\alpha}\Delta t, t) + \frac{\Delta t}{2}\Omega_i(x_\alpha - \xi_{i\alpha}\Delta t, t) \end{aligned} \tag{3.86}$$

Then by using the generalized raw moments to rewrite this equation:

$$\mathbf{\Pi}^{f_i,(n)}_{\alpha_1\ldots\alpha_n}(x_\alpha, t+\Delta t) = \mathbf{\Pi}^{\overline{f_i^{col},(n)}}_{\alpha_1\ldots\alpha_n}(x_\alpha - \xi_{i\alpha}\Delta t, t) + \frac{\Delta t}{2}\mathbf{\Pi}^{\Omega_i,(n)}_{\alpha_1\ldots\alpha_n}(x_\alpha, t+\Delta t) \tag{3.87}$$

Next, a Taylor expansion and several simplifications are operated but not presented here for concision to obtain the continuous lattice Boltzmann algorithm in space and time:

$$\frac{\partial \mathbf{\Pi}^{f_i,(n)}_{\alpha_1\ldots\alpha_n}}{\partial t} + \frac{\partial \mathbf{\Pi}^{f_i,(n+1)}_{\alpha_1\ldots\alpha_n}}{\partial \boldsymbol{x}} = \mathbf{\Pi}^{\Omega_i,(n)}_{\alpha_1\ldots\alpha_n} + \mathcal{O}(\Delta t^2) \tag{3.88}$$

which is simply the moments of the DVBE:

$$\frac{\partial \rho}{\partial t} + \frac{\partial \rho u_\alpha}{\partial x_\alpha} = 0 \tag{3.89}$$

$$\frac{\partial \rho u_\alpha}{\partial t} + \frac{\partial(\rho u_\alpha u_\beta + \delta_{\alpha\beta})}{\partial x_\beta} = -\frac{\partial \Pi^{f_i^{neq},(2)}_{\alpha\beta}}{\partial x_\beta} \tag{3.90}$$

$$\frac{\Pi^{f_i,(2)}_{\alpha\beta}}{\partial t} + \frac{\partial \Pi^{f_i,(3)}_{\alpha\beta\gamma}}{\partial x_\gamma} = -\frac{1}{\tau}\Pi^{f_i^{neq},(2)}_{\alpha\beta} \tag{3.91}$$

This last equation is different from the one obtained with the Chapman-Enskog expansion recalled here:

$$\frac{\partial \Pi_{\alpha\beta}^{f_i^{(0)},(2)}}{\partial t^{(0)}} + \frac{\partial \Pi_{\alpha\beta\gamma}^{f_i^{(0)},(3)}}{\partial x_\gamma} = -\frac{1}{\tau}\Pi_{\alpha\beta}^{f_i^{(1)},(2)} \tag{3.92}$$

No assumptions on the expansion of Kn or scale separation are needed for this Taylor expansion, leading after numerous manipulations to:

$$\begin{aligned}\Pi_{\alpha\beta}^{f_i^{neq},(2)} &= -\tau\rho c_s^2\left(\frac{\partial u_\alpha}{\partial x_\beta} + \frac{\partial u_\beta}{\partial x_\alpha}\right) + \mathcal{O}(Ma^3) - \tau\left[\frac{\partial \Pi_{\alpha\beta}^{f_i^{neq},(2)}}{\partial t} + \frac{\Pi_{\alpha\beta\gamma}^{f_i^{neq},(3)}}{\partial x_\gamma}\right] \\ &+ \tau\left[u_\alpha \frac{\partial \Pi_{\beta\gamma}^{f_i^{neq},(2)}}{\partial x_\gamma} + u_\beta \frac{\partial \Pi_{\alpha\gamma}^{f_i^{neq},(2)}}{\partial x_\gamma}\right] \\ &\neq -\tau\rho c_s^2\left(\frac{\partial u_\alpha}{\partial x_\beta} + \frac{\partial u_\beta}{\partial x_\alpha}\right) + \mathcal{O}(Ma^3)\end{aligned} \tag{3.93}$$

Considering that the weakly-compressible Navier-Stokes equations can be written as:

$$\Pi_{\alpha\gamma}^{f_i^{neq},(2)} \approx -\tau\rho c_s^2\left(\frac{\partial u_\alpha}{\partial x_\beta} + \frac{\partial u_\beta}{\partial x_\alpha}\right) \tag{3.94}$$

a non-dimensionalization is performed to obtain non-dimensional variables at $\mathcal{O}(1)$:

$$\Pi_{\alpha\gamma}^{f_i^{neq},(2)*} = -\tau\rho c_s^{2*}\left(\frac{\partial u_\alpha^*}{\partial x_\beta^*} + \frac{\partial u_\beta^*}{\partial x_\alpha^*}\right) + \mathcal{O}\left(\frac{\mu Q_0}{\rho_0 c_s^2 L_0 \Pi_0}\right) + \mathcal{O}(\frac{Ma^3}{Re}) + \mathcal{O}(Ma^3) \tag{3.95}$$

here $\mu Q_0/\rho_0 c_s^2 L_0 \Pi_0$ is a scaling term. The superscript $*$ is kept to specify variables expressed in lattice units. The Taylor expansion approach gives a more precise macroscopic explanation of the LBM behavior than the standard Chapman-Enskog expansion. If the terms in $\mathcal{O}(\frac{Ma^3}{Re})$ and $\mathcal{O}(Ma^3)$ are sufficiently small, the LBM with the Bathnagar-Gross-Krook (BGK) collision operator retrieves the weakly-compressible Navier-Stokes equations.

3.4 Overcoming the Weakly-Compressible Limitation

Three main approaches exist to extend the LBM to fully compressible flows: multi-speed, double-distribution function, and hybrid approaches. Only the hybrid approach has been used in this manuscript and will be described. Moreover, several formulations of the hybrid approach have been developed over the years [97, 98, 99]. Still, this section focuses on the latest formulation proposed by Farag, Coratger, Wissocq, et al. [100] used throughout the manuscript.

To be able to treat compressible flows, the LBM needs to overcome the following limitations:

- The temperature is constant, $T = T_0$.
- The speed of sound is thus $c_s = \sqrt{r_g T_0}$ also constant instead of $c_s = \sqrt{\gamma r_g T}$.
- Because of this constant temperature, the equation of state for pressure becomes $P = \rho r_g T_0$ and not $P = \rho r_g T$.
- Finally, the stress tensor obtained is:

$$\Pi_{\alpha\beta}^{f_i^{neq}} \approx -\mu \left(\frac{\partial u_\alpha}{\partial x_\beta} + \frac{\partial u_\beta}{\partial x_\alpha} \right) + \mathcal{O}(Ma^3) \tag{3.96}$$

and not:

$$\Pi_{\alpha\beta}^{f_i^{neq}} \approx -\mu \left(\frac{\partial u_\alpha}{\partial x_\beta} + \frac{\partial u_\beta}{\partial x_\alpha} - \frac{2}{\mathcal{D}} \frac{\partial u_\gamma}{\partial x_\gamma} \delta_{\alpha\beta} \right) \tag{3.97}$$

An additional transport equation is used to solve the first three points, and the equilibrium distribution function is modified to consider a non-constant temperature. Corrections terms are introduced to solve the issue concerning the stress tensor. Finally, a collision operator must be chosen to ensure numerical stability. The choices adopted to treat these different points are presented in the following sections.

3.4.1 Entropy Formulation

The total energy equation on ρE is used in the fully compressible Navier-Stokes Fourier equations. However, this approach is unstable for Hybrid Lattice Boltzmann Method (HLBM) schemes as shown by Renard, Wissocq, Boussuge, et al. [94]. To avoid this issue the compressible HLBM on standard lattices treated in this manuscript uses a transport equation on entropy s. This solution was adopted at the time as it was the most mature one and had already demonstrated its capability to simulate high subsonic flows [96]. It is worth mentioning that recent work [101] allows for a total energy formulation of the HLBM. However, this approach was too recent and lacked the maturity and validation to apply it during this Ph.D.

$$\frac{\partial s}{\partial t} + u_\alpha \frac{\partial s}{\partial x_\alpha} = \frac{1}{\rho T} \left(\frac{\partial u_\alpha}{\partial x_\beta} \mathcal{F}_{\alpha\beta} - \frac{\partial q_\beta}{\partial x_\beta} \right) \tag{3.98}$$

The link between entropy and temperature is given by:

$$s = c_v \ln\left(\frac{T}{\rho^{\gamma-1}} \right) \tag{3.99}$$

$$T = \rho^{\gamma-1} \exp\left(\frac{s}{c_v} \right) \tag{3.100}$$

Eq. 3.98 is discretized using a finite difference / finite volume approach. The convective term on the left-hand side is discretized with a third-order MUSCL-Hancock scheme [102], whereas a second-order central difference scheme is used for the right-hand side terms. This formulation on the primitive entropy has been validated on several subsonic flows [103, 104, 98, 105, 99, 100].

3.4.2 The Hybrid Recursive Regularized Collision Operator

The BGK collision operator has the advantage of being a simple choice for LBM simulation but is limited by stability issues [106]. To counter these issues, several collision operators have been studied in the literature [107, 108]:

- Multi-Relaxation Time (MRT) [106, 109] collision operators that allow a relaxation of the moments with different relaxation times independently instead of relaxing f_i to f_i^{eq}.
- Entropic collision operators [110], where the entropy growth of the particle collisions follows Boltzmann's H-theorem.
- Regularized collision operators [111], that filter out the non-physical modes using regularization of the off-equilibrium distribution function.

During this Ph.D., all the simulations were performed using the hybrid recursive regularized collision operator.

The method is established as follows. First, the rewritten collide and stream algorithm is:

$$\overline{f_i}(x_\alpha, t+\Delta t) = f_i^{eq}(x_\alpha - \xi_{i\alpha}\Delta t, t) + \left(1 - \frac{\Delta t}{\overline{\tau}}\right)\overline{f_i^{neq}}(x_\alpha - \xi_{i\alpha}\Delta t, t) + \mathcal{O}(\Delta t^2) \quad (3.101)$$

where $\overline{f_i^{neq}} = \overline{f_i} - f_i^{eq}$ using the BGK collision operator. The main idea of the regularization is to project $\overline{f_i^{neq}}$ onto the Hermite basis. With a hybrid recursive-regularized method, this gives [112]:

$$a_{\alpha\beta}^{\overline{f_i^{neq}},(2),HRR} = \sigma a_{\alpha\beta}^{\overline{f_i^{neq}},(2),PR} + (1-\sigma) a_{\alpha\beta}^{\overline{f_i^{neq}},(2),FD} \quad (3.102)$$

$$a_{\alpha\beta}^{\overline{f_i^{neq}},(2),FD} = -\rho c_s^2 \overline{\tau}\left(\frac{\partial u_\alpha}{\partial x_\beta} + \frac{\partial u_\beta}{\partial x_\alpha} - \frac{2}{D}\frac{\partial u_\gamma}{\partial x_\gamma}\delta_{\alpha\beta}\right) \quad (3.103)$$

$a_{\alpha\beta}^{\overline{f_i^{neq}},(2),HRR}$ is evaluated using second order centered finite differences. The third order Hermite moment $a_{\alpha\beta\gamma}^{\overline{f_i^{neq}},(3),HRR}$ is computed via recursion leading to the off-equilibrium offset distribution function $\overline{f_i^{neq}}^{HRR}$. The coefficient σ is a weighting parameter varying between zero and one. Adding a part of finite difference to the off-equilibrium distribution function allows a large improvement in stability but creates numerical dissipation. For the following simulations, $\sigma = 0.99$ is used unless specified otherwise.

Finally, the Hybrid Recursive Regularized (HRR) collision operator is slightly modified using a traceless collision operator [105]:

$$a_{\alpha\beta}^{\overline{f_i^{neq}},(2),PR,traceless} = a_{\alpha\beta}^{\overline{f_i^{neq}},(2),PR} - \frac{1}{3} a_{\gamma\gamma}^{\overline{f_i^{neq}},(2),PR}\delta_{\alpha\beta} \quad (3.104)$$

$a_{\alpha\beta}^{\overline{f_i^{neq}},(2),PR,traceless}$ is used to construct $a_{\alpha\beta}^{\overline{f_i^{neq}},(2),HRR}$ and thus $a_{\alpha\beta\gamma}^{\overline{f_i^{neq}},(3),HRR}$ and $\overline{f_i^{neq}}^{,HRR}$. This approach improves the stability of the solver and corrects numerical errors.

3.4.3 Equilibrium Formulation and Corrective Terms

The HLBM approach used throughout this thesis, known as *improved density-based* [113, 100], has been developed as a complement of a previous approach, called *pressure based* proposed by [105] [105].

The equilibrium distribution function is expressed as:

$$
\begin{aligned}
f_i^{eq} = \omega_i [\rho + d_i + \frac{\xi_{i\alpha}}{c_s^2}\rho u_\alpha + \frac{\mathcal{H}^{(2)}_{i\alpha\beta}}{2c_s^4}\rho u_\alpha u_\beta \\
&+ \frac{1}{6c_s^6}\left(3\left(\mathcal{H}^{(3)}_{ixxy} + \mathcal{H}^{(3)}_{iyzz}\right)(\rho u_x u_x u_y + \rho u_y u_z u_z) + \left(\mathcal{H}^{(3)}_{ixxy} - \mathcal{H}^{(3)}_{iyzz}\right)(\rho u_x u_x u_y - \rho u_y u_z u_z)\right. \\
&+ 3\left(\mathcal{H}^{(3)}_{ixzz} + \mathcal{H}^{(3)}_{ixyy}\right)(\rho u_x u_z u_z + \rho u_x u_y u_y) + \left(\mathcal{H}^{(3)}_{ixzz} - \mathcal{H}^{(3)}_{ixyy}\right)(\rho u_x u_z u_z - \rho u_x u_y u_y) \\
&\left. +3\left(\mathcal{H}^{(3)}_{iyyz} + \mathcal{H}^{(3)}_{ixxz}\right)(\rho u_y u_y u_z + \rho u_x u_x u_z) + \left(\mathcal{H}^{(3)}_{iyyz} - \mathcal{H}^{(3)}_{ixxz}\right)(\rho u_y u_y u_z - \rho u_x u_x u_z)\right)\Big], \quad (3.105)
\end{aligned}
$$

with d_i defined as:

$$
d_i = \begin{cases} \frac{w_0 - 1}{w_0}\left(T - T_0\right), & \boldsymbol{c}_i = (0,0,0) \\ T - T_0, & \text{else} \end{cases} \quad (3.106)
$$

Moreover, the correction term is expressed as:

$$
\Psi_{\alpha\beta} = \rho c_s^2 \frac{2}{\mathcal{D}}\frac{\partial u_\gamma}{\partial x_\gamma} + c_s^2\left[u_\alpha \frac{\partial \rho (T - T_0)}{\partial x_\beta} + u_\beta \frac{\partial \rho (T - T_0)}{\partial x_\alpha}\right] + \frac{\rho c_s^2 (T - T_0)}{\partial t}\delta_{\alpha\beta} + \frac{\partial Err_{\alpha\beta\gamma}}{\partial x_\gamma} \quad (3.107)
$$

with $Err_{\alpha\beta\gamma}$:

$$
\frac{\partial Err_{\alpha\beta\gamma}}{\partial x_\gamma} = -\begin{bmatrix} \frac{\partial \rho u_x u_x u_x}{\partial x} & \frac{\partial \rho u_x u_y u_z}{\partial z} & \frac{\partial \rho u_x u_y u_z}{\partial y} \\ \frac{\partial \rho u_x u_y u_z}{\partial z} & \frac{\partial \rho u_y u_y u_y}{\partial y} & \frac{\partial \rho u_x u_y u_z}{\partial x} \\ \frac{\partial \rho u_x u_y u_z}{\partial y} & \frac{\partial \rho u_x u_y u_z}{\partial z} & \frac{\partial \rho u_z u_z u_z}{\partial z} \end{bmatrix} \quad (3.108)
$$

The derivatives involved in the correction term are computed using second-order centered finite differences, while the temporal derivatives are computed using the first-order backward Euler method.

3.4.4 Addition of the Isotropic Equilibrium Scheme

As some isotropy issues involving the $D3Q19$ have been reported in the literature, a recent development proposed by [114] has been implemented. The equilibrium distribution function is modified to obtain an additional fourth-order moment. For the fully compressible LBM, the equilibrium distribution function is split into four parts corresponding to the different moments:

$$
f_i^{eq} = \omega_i \rho (f_i^{eq,(0)} + f_i^{eq,(1)} + f_i^{eq,(2)} + f_i^{eq,(3)}) \quad (3.109)
$$

The first moment contains the thermal information used to couple the LBM solver with the ideal gas law:

The second moment is unchanged from classic LBM approaches and given as:

$$f_i^{eq,(1)} = \frac{\xi_{i\alpha}}{c_s^2} u_\alpha \tag{3.110}$$

The third part is given by Eq. 3.111 and is identical to the classic LBM to the improved density-based model used.

$$f_i^{eq,(2)} = \frac{1}{2c_s^2} \mathcal{H}_{i\alpha\beta}^{(2)} u_\alpha u_\beta \tag{3.111}$$

And finally, the fourth part is:

$$\begin{aligned} f_i^{eq,(3)} = \frac{1}{6c_s^2}[&3(\mathcal{H}_{ixxy}^{(3)} + \mathcal{H}_{iyzz}^{(3)})(u_x u_x u_y + u_y u_z u_z) + (\mathcal{H}_{ixxy}^{(3)} - \mathcal{H}_{iyzz}^{(3)})(u_x u_x u_y - u_y u_z u_z) + \\ &3(\mathcal{H}_{ixzz}^{(3)} + \mathcal{H}_{ixyy}^{(3)})(u_x u_z u_z + u_x u_y u_y) + (\mathcal{H}_{ixzz}^{(3)} - \mathcal{H}_{ixyy}^{(3)})(u_x u_z u_z - u_x u_y u_y) + \\ &3(\mathcal{H}_{iyyz}^{(3)} + \mathcal{H}_{ixxz}^{(3)})(u_y u_y u_z + u_x u_x u_z) + (\mathcal{H}_{iyyz}^{(3)} - \mathcal{H}_{ixxz}^{(3)})(u_y u_y u_z - u_x u_x u_z)] \end{aligned} \tag{3.112}$$

The modification proposed by Bauer, Silva, and Rüde [114] consists in rewriting the third part as:

$$f_i^{eq,2} = \begin{cases} -u_\alpha u_\alpha, & \boldsymbol{\xi}_i = (0,0,0) \\ -3u_\alpha u_\alpha + 6\left(\xi_{i\alpha} u_\alpha\right)^2, & \boldsymbol{\xi}_i \in \{(\pm 1, 0, 0) \\ & (0, \pm 1, 0), (0, 0, \pm 1)\} \\ -\frac{3}{2}\xi_{i\alpha}^2 u_\alpha^2 + \frac{9}{2}\left(\xi_{i\alpha} u_\alpha\right)^2, & \text{else} \end{cases} \tag{3.113}$$

By doing so, the additional fourth order moments $\Pi_{xxyy}^{f_i^{eq},(4)}$, $\Pi_{xxzz}^{f_i^{eq},(4)}$, $\Pi_{yyzz}^{f_i^{eq},(4)}$ are correctly recovered.

3.5 The ProLB Solver

3.5.1 History

ProLB is a LBM solver, allowing parallel computation written in C++ and using the message passing interface (MPI) library. It is owned and developed by a consortium composed of C.S. Systèmes, Airbus, Renault, Aix-Marseille Université, and École Centrale de Lyon. Safran recnetly joined the consortium in 2023. It is in continuous improvement via the contribution of the consortium and other external partners, such as CERFACS and ONERA. The code is written to ease the process of implementing physical models by clearly distinguishing the core of the solver (including parallel communications and pre-processing, such as mesh generation) and the physical modeling. It also features a graphical user interface (GUI) called LBPre, which enables easier pre-treatment of complex geometry. The version of ProLB used during this Ph.D. is version 2.8.0. ProLB was initially developed as an athermal, weakly compressible LBM solver and has been adapted for compressible flows.

3.5.2 Core Model

During this Ph.D., the improved density-based model, with the HRR collision operator, the primitive entropy equation for s discretized with the MUSCL-Hancock scheme when a large stencil is available is used for the thermal compressible version of ProLB. This allows for the fully-compressible thermal Navier-Stokes equations to be resolved. The dynamic viscosity is variable according to temperature and follows Sutherland's law.

3.5.3 Summary of the Algorithm

The algorithm follows a stream and collide procedure that can be summarized as follow for the uniform grid nodes in the core of the fluid domain:

1. Initial time t^*: $\overline{f_i^{col*}}$, $\rho^*(t), \boldsymbol{u}^*(t), \theta(t), s^*(t)$ are known.
2. $s^*(t^*+1)$ is obtained by time integration of the entropy scheme.
3. $\overline{f_i^{col*}}$ is propagated, giving $\overline{f_i^*}(t^*+1) = f_i^*(t^*+1) - \frac{1}{2}\psi_i^*(t^*+1)$
4. $\overline{f_i^*}(t^*+1)$ and $s(t^*+1)$ give access to the macroscopic variables $\rho^*(t^*+1), \boldsymbol{u^*}(t^*+1), \theta(t^*+1)$.
5. Gradients are computed, yielding $\frac{\partial u_\alpha^*}{\partial x_\beta^*}$, $\frac{\partial \theta}{\partial x_\alpha^*}$ and $\boldsymbol{\Psi}_{\alpha\beta}^*$.
6. $f_i^{eq}(t^*+1)$ is computed from $\rho(t^*+1), \boldsymbol{u}(t^*+1), T(t^*+1)$.
7. $f_i^{neq*}(t^*+1)$ is computed $from f_i^{eq*}(t^*+1), \overline{f_i^*}(t^*+1), \frac{\partial u_\alpha^*}{\partial x_\beta^*}, \boldsymbol{\Psi^*}_{\alpha\beta}, a_{\alpha\beta}^{\overline{f_i^{neq}},(2)*}$.
8. The HRR collision is performed to obtain $\overline{f_i^{col*}}$.

   This procedure is repeated at each time step until reaching the time limit.

3.5.4 Meshing

ProLB uses an octree mesh structure where refinement zones, also called resolution domains (RD), can be specified. These RD allow local grid refinement to capture the flow physics adequately. Fig. 3.3 illustrates an octree refinement. In the following, RD1 refers to the zone with the smallest grid size Δx. Consequently, RD2 has a grid size of $2\Delta x$. The solver handles this mesh generation, and the definition of the refinement zones is greatly assisted by the Graphic User Interface LbPre, minimizing the human time spent generating meshes.

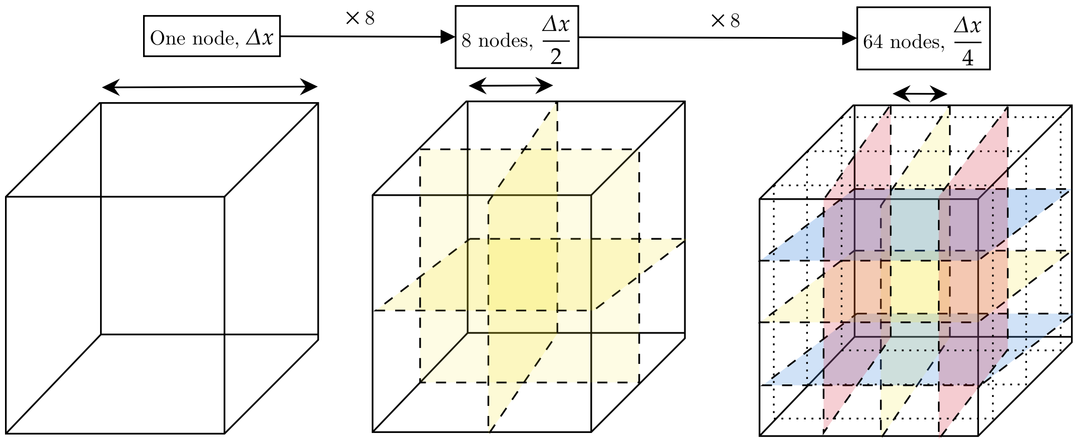

Figure **(3.3)** – Illustration of an octree type mesh refinement on a cube.

3.5.5 Turbulence Modelling

Two options are available in ProLB, Direct Numerical Simulation (DNS) or Large Eddy Simulation (LES). In the first case, no subgrid-scale model is used, whereas for the second, subgrid-scale models such as the Shear-Improved Smagorinsky Model (SISM) [115] or the Vreman model [116] can be chosen. The subgrid-scale viscosity μ_{sgs} is integrated into the collision operator by a modification of the relaxation time:

$$\tau = \frac{\mu + \mu_{sgs}}{\rho c_s^2} \tag{3.114}$$

3.5.6 Boundary Conditions

This section briefly presents the treatment applied at the boundary with the LBM. Considering that Cartesian grids are used, this prevents using body-fitted meshes on complex geometry. A particular treatment at the boundary must be applied, which is called cut-cells [117]. The idea is that the volume crossing the boundary condition is removed from the computational domain. As the method is based on the propagation of distribution functions on a grid, at some boundary nodes called No Fully Fluid (NFF), the distributions coming from outside the domain are missing, as illustrated in Fig. 3.4.

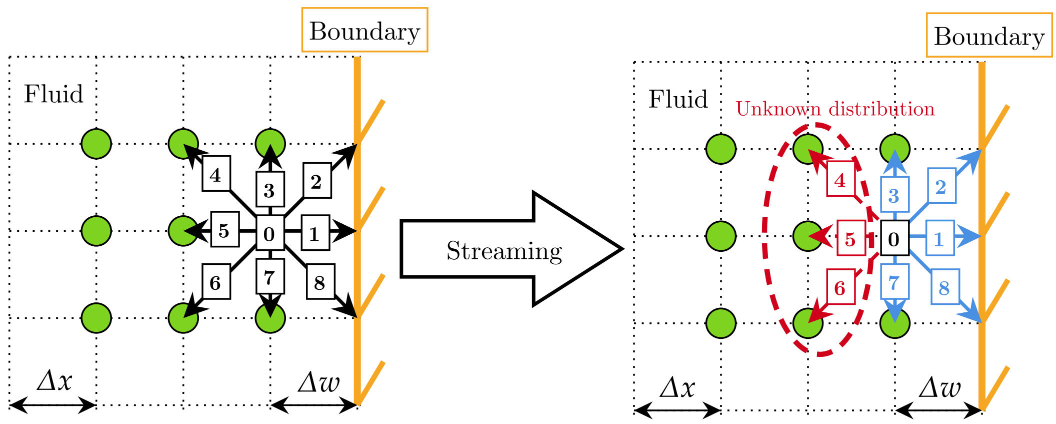

Figure **(3.4)** – Issue at a boundary node illustrated on a D2Q9 lattice. The red dashed arrows represent the unknown populations. Δx is the mesh size and Δw the distance between the boundary node and the boundary.

To solve this issue, the boundaries are treated via a full reconstruction of the distribution functions. This means that for all the i distribution functions, $\overline{f_i} = f_i^{eq} + \overline{f_i^{neq}}$. In this case, f_i^{eq} is known and determined by ρ, $\boldsymbol{u}$, and T so that the boundaries are set from macroscopic quantities. Then, $\overline{f_i^{neq}}$ is rewritten in terms of $a_{\alpha\beta}^{\overline{f_i^{neq}},FD}$ and computed using finite differences. This method can apply any Dirichlet or Neumann conditions on NFF nodes. Here a brief presentation of the full reconstruction with the cut-cell approach performed by the ProLB solver is recalled (see [103] for more details).

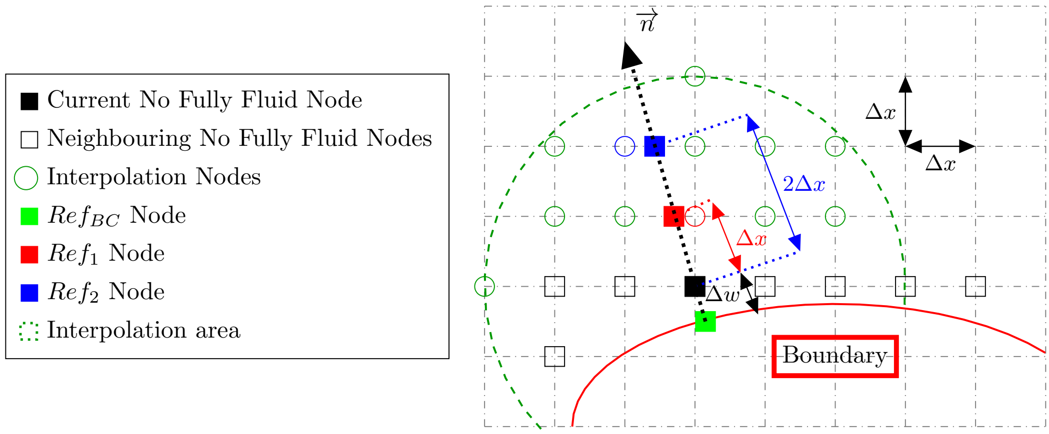

Figure **(3.5)** – Interpolation/extrapolation scheme for the boundary treatment.

Fig. 3.5 presents the boundary treatment and the corresponding notation. The red zone at the bottom represents the boundary (whatever the type). The way to treat the boundary can be summarized as follows:

1. The volume defined as a boundary condition is removed from the domain.

2. The points with a missing population because a lattice link touches the boundary, are flagged as NFF.

3. A normal vector, $\boldsymbol{n}$, facing outward of the boundary is created between the NFF node and the closest point on the boundary (Ref_{BC}).

4. Along the vector $\boldsymbol{n}$, two fictitious points, Ref_1 and Ref_2, are placed respectively at a distance Δx and $2\Delta x$ of the NFF.

5. The entropy scheme, streaming phase, and calculation of the macroscopic variables are performed in the core of the domain (Fully Fluid nodes).

6. Then, using an Inverse Distance Weighting (IDW) [118], the values of ρ, $\boldsymbol{u}$ and T are determined on the Ref_1 and Ref_2 nodes using the neighboring values. Some NFF nodes are used during this interpolation, which could create an issue as their values are still unknown. It was decided that the macroscopic values at the NFF nodes at the previous time step would be used to correct this. This represents a numerical error, however, considering that the IDW method is used, a small weight is attributed to these nodes keeping the error relatively small.

7. Now that values are known for Ref_1 and Ref_2, the value at the current NFF node can be imposed using interpolation or extrapolation. For a Dirichlet condition, a second-order Lagrange interpolation is performed (see Eq. 3.115). For a Neumann condition, the value is first calculated at the Ref_{BC} point via a Taylor expansion of the derivative (see Eq. 3.116) before using a Lagrange interpolation again. Concerning the notations, ϕ_{NFF}, ϕ_{Ref1} and ϕ_{Ref2} denote the generic macroscopic values at nodes Ref_{BC}, Ref_1, and Ref_2, respectively, and Δw is the normal distance to the wall (distance between the NFF node and the Ref_{BC} node).

$$\phi_{NFF} = \frac{2\Delta x^2}{(\Delta w + \Delta x)(\Delta w + 2\Delta x)}\phi_{Ref_{BC}} + \frac{2\Delta w}{\Delta w + \Delta x}\phi_{Ref_1} + \frac{-\Delta w}{\Delta w + 2\Delta x}\phi_{Ref_2} \tag{3.115}$$

$$\phi_{NFF} = \frac{4(\Delta w + \Delta x)\phi_{Ref_1} - (2\Delta w + \Delta x)\phi_{Ref_2}}{2\Delta w + 3\Delta x} \tag{3.116}$$

At the end of this procedure, all macroscopic variables are available in the domain. On the NFF nodes, $\boldsymbol{\Psi}_{\alpha\beta}$ and $\frac{\partial u_\alpha}{\partial x_\beta}$ can be computed using finite differences with a second order stencil if possible. $\overline{f_i^{neq}}$ is also computed, and $\overline{f_i^{col}}$ being known on the NFF nodes, can be propagated to its fully fluid neighbors.
Since no distributions are streamed to the NFF nodes, the collision performed at these nodes is equivalent to one where $\sigma = 0$. Moreover, the finite difference entropy scheme is not performed on these nodes either, and the MUSCL scheme can not be used either, as the surrounding NFF nodes lack the necessary stencil. This restriction locally degrades the quality of the method. Additionally, the interpolation/extrapolation algorithm can create mass leakage. This has been fixed by imposing ρ_{NFF} as the density that would be found if a bounce-back had been performed.

3.5.7 Wall Law

Considering the turbulent flows around complex geometries involved during this Ph.D., the resolution of the boundary layers is a priori not affordable, pushing for the use of a wall law. This ensures that the flow variables at the first off-wall nodes are coherent with the unresolved boundary-layer dynamics. In the solver, the wall law follows the formulation described by Boudet et al. [119] and repeated here. It is derived from the classical log law for a turbulent boundary layer over a flat plate (3.117):

$$U_0^+(y^+) = \frac{1}{\kappa} log(y^+) + B \tag{3.117}$$

where $U_0^+ = U_0/u_w$ and $y^+ = \frac{yu_w}{\nu}$ represent the velocity and the distance to the boundary in wall units, determined using u_w the friction velocity, and ν the kinematic viscosity of the fluid. $\kappa = 0.41$ and $B = 5.2$ are constants [120]. The wall law used in the solver is extended to take into account the curvature of the boundary, the pressure gradient, and the near-wall damping using the respective corrective terms F_c, F_p, and F_d. The full wall law formulation then writes:

$$U^+(y^+) = \left(U_0^+(y^+) + F_c(y^+) + F_p(y^+)\right) F_d(y^+) \tag{3.118}$$

with the curvature correction:

$$F_c(y^+) = \alpha K^+ y^+ \left(U_0^+(y^+) - \frac{1}{\kappa}\right) + \mathcal{O}\left((K^+y^+)^2\right) \tag{3.119}$$

where the curvature is expressed as $K = \frac{1}{R}$ with R the radius of curvature of the surface in the streamwise direction. The coefficient $\alpha = 6$ is used. The pressure-gradient correction is defined as:

$$F_p(y^+) = \frac{1}{\kappa}\left[-2\log\left(\frac{\sqrt{1+\Pi^+y^+}+1}{2} + 2(\sqrt{1+\Pi^+y^+}-1)\right)\right] \tag{3.120}$$

with $\Pi^+ = (u_p/u_w)^3$ and $u_p = (\frac{\nu}{\rho}\frac{\partial P}{\partial x})^{1/3}$. Finally, the near-wall damping is given by:

$$F_d(y^+) = \left(1 - \exp\left\{-\frac{y^+}{C_d}\right\}\right) \tag{3.121}$$

with $C_d = 8$. This generalized wall law is calibrated from the second off-wall fluid nodes in the normal direction and used to predict the velocity at the first off-wall boundary nodes. The density is deduced using a Neumman condition assuming a zero-pressure gradient in the wall-normal direction. It should be noted that no wall-law relation is applied to the temperature that is thus evaluated using a Dirichlet condition. This limitation is illustrated and discussed in Chapter 7.

3.5.8 Rotating Domains

For this Ph.D., the capacity to consider rotating geometries is crucial to include the rotors usually found around the S-duct. The simulation of rotating objects is performed in the solver using the overset Local Reference Frame (LRF) method [121]. The principle is that two different meshes exist simultaneously with associated reference frames (see

Fig. 3.6). The fixed mesh has a Galilean reference frame, while the rotating mesh has a non-Galilean one. In the non-Galilean reference frame, fictitious forces such as the Coriolis and centrifugal forces are computed (see Eq. 3.122) and imposed at each time step.

$$\mathbf{F}(\mathbf{x},t) = -2\rho\mathbf{\Omega} \times \mathbf{u}(\mathbf{x},t) + \rho\mathbf{\Omega} \times (\mathbf{\Omega} \times \mathbf{r}) \tag{3.122}$$

$\mathbf{\Omega} = [\omega_1, \omega_2, \omega_3]$ is the angular velocity vector of the rotating mesh, and $\mathbf{r}$ is the coordinate vector with respect to the rotation center. The computed fictitious forces are then imposed on the lattice through the discrete forcing term following Guo's forcing scheme [122].

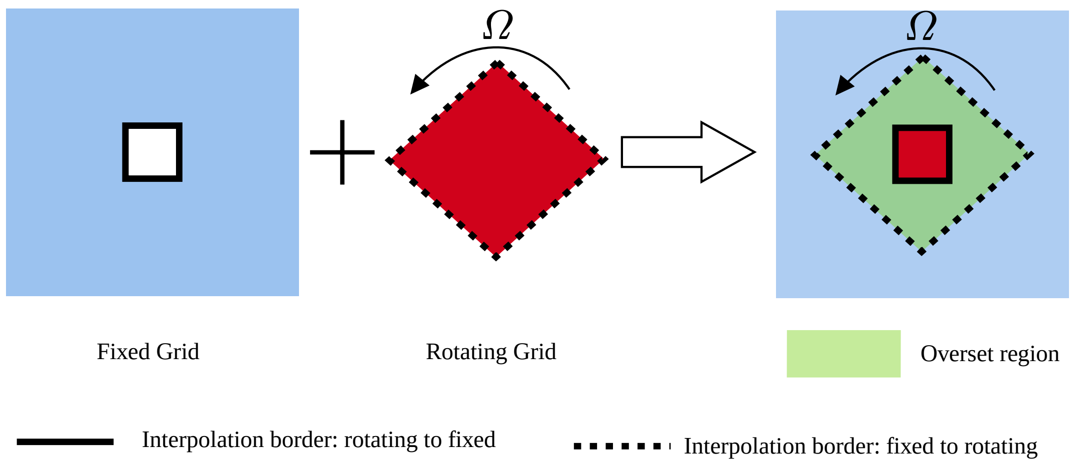

Figure **(3.6)** – Scheme of the overset grids.

Both fixed and rotating grids exit at the same time and exchange their information at the border. The border nodes receive macroscopic values from surrounding nodes in another region via polynomial interpolation [121, 123] (see Fig. 3.7). The receiver border nodes are denoted (X, Y) while the donor nodes are denoted (x, y). The gradient-based quadratic interpolation is applied on ρ, $\mathbf{u}$ and T. At the border, f_i^{eq} and f_i^{neq} are reconstructed from the interpolated macroscopic values before performing collision and streaming.

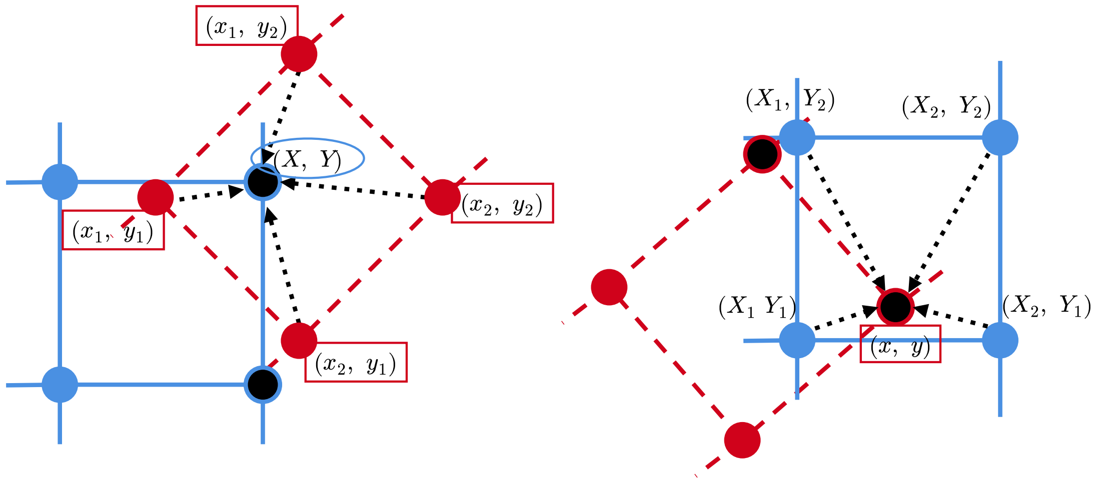

Figure **(3.7)** – Scheme of the interpolation procedure (left: rotating to fixed grid, right: fixed to rotating grid).

3.6 Chapter Summary

In this chapter, the standard derivation of the Lattice Boltzmann method has been presented, as well as its extension to treat compressible and thermal flows. The standard formulation has been written starting from the kinetic theory of gases, followed by a Chapman-Enskog expansion before defining an adequate velocity and space discretization leading to the classic athermal weakly compressible LBM with the collide and stream algorithm.

To extend the formulation to compressible and thermal flows that are to be treated in this Ph.D., the Hybrid Recursive Regularized (HRR) collision model used is presented. A concise introduction to the ProLB solver is then given, displaying the main functionalities of the code.

Chapter 4: Development and Validation of Navier Stokes Characteristic Boundary Conditions

---

This chapter describes the major functionality developments implemented into the ProLB solver within the context of this Ph.D. These functionalities were required to perform the first high-fidelity turbomachinery simulations in a compressible Lattice Boltzmann Method (LBM) framework addressed in this thesis. They concern the implementation of a specific inlet characteristic boundary condition, coupled with synthetic turbulence injection. Moreover, the ability of the outlet condition to recover the radial equilibrium assumption is validated as well as the possibility of using a valve law condition to ensure fast convergence toward a target mass flow rate. This chapter mainly follows the published article:

Gianoli, T., Boussuge, J. F., Sagaut, P., de Laborderie, J. (2022). Development and validation of Navier-Stokes Characteristic Boundary Conditions applied to turbomachinery simulations using the Lattice Boltzmann Method. 1–32. https://doi.org/10.1002/fld.5160

Some notations have been modified to stay consistent with the rest of the manuscript. The LBM presentation and implementation details have been removed, as they are redundant with Chapter 3, except the section detailing the boundary implementation as they are relevant to this chapter. The article has the following abstract:

A procedure to implement and validate non-reflecting boundary conditions applied for turbomachinery simulations, using Navier Stokes Characteristic Boundary Condition (NSCBC) in a compressible Lattice Boltzmann solver, is presented. The implementation of an inlet condition imposing total pressure, total temperature, and flow angles, as well as an outlet condition imposing a static pressure profile that allows the simulation to reach a simplified radial equilibrium, is described within the context of a Lattice Boltzmann approach. The treatment at the boundaries relies on the characteristic methodology to derive non-reflecting conditions in terms of acoustics and is also compatible with turbulence injection at the inlet. These properties are evaluated on test cases of increasing complexity, ranging from a simple 2D periodic domain to an S-duct stage with turbulence injection.

An additional section has been added that presents the valve law strategy employed to ensure the convergence of the simulations towards the target mass flow, which is of primary importance for turbomachinery simulations.

Contents

4.1 Motivations

Studying unsteady turbulent phenomena is required to design innovative engines for modern aircraft. However, turbulence prediction is a major issue, especially considering the complexity of the geometry involved. Thus, simulating the flow developing in modern aircraft engines remains challenging. Reynold Averaged Navier-Stokes (RANS) approaches, which model all the turbulent motions within the flow, remain the most widespread family of methods for turbomachinery simulations. However, these approaches often produce inaccurate results, and with the continuous increase in computing power, Large Eddy Simulation (LES), which resolves large-scale turbulent motions, has become an increasingly appealing choice. However, the high computational cost of LES has limited its adoption in industrial Computational Fluid Dynamic (CFD).

Considering these challenges, the Lattice Boltzmann approach [124, 67, 125] has emerged in the fluid dynamics community as a viable method to solve the Navier-Stokes equations. The LBM has demonstrated its capability to handle complex geometries using Cartesian grids, thanks to immersed boundary conditions [69, 70, 71, 72]. Moreover, the low dissipation properties demonstrated by the LBM allow it to capture the small acoustic pressure fluctuations [73, 74]. All these properties have attracted intensive research in aerodynamics [75, 76, 77], aero-acoustics [78], extension to weakly compressible thermal flows [79, 80, 81], compressible flows [82, 83, 84, 85, 93] and turbulent applications [126, 127, 128]. Finally, the algorithm of the method is well adapted to High-Performance Computing thanks to an easy parallelization [86].

However, specifying inlet and outlet boundary conditions for compressible flow simulations remains a major issue, especially when wave reflections must be controlled [129, 130, 131]. For Navier-Stokes methods, a successful approach is the use of non-reflective boundary conditions based on a treatment of the characteristic waves of the local flow. The extension to the LBM framework is not straightforward considering that the LBM describes the population of particles at the mesoscopic level, whereas the Navier-Stokes description applies at the macroscopic level.

Indeed, in practice, imposing an outlet boundary that is realistic and non-disturbing is a significant issue in most cases. For an outlet condition to be considered ideal, it should have a weak influence on the upstream flow, remain stable, and minimize the reflection and dissipation of acoustic waves. These requirements become especially important when using LES or Direct Numerical Simulation (DNS), which belong to the category of high-fidelity simulations. The principle of such methods is to resolve all or a part of the turbulence scales in highly turbulent and unsteady flows. Thus, the boundary should not create spurious reflections or acoustic waves inside the domain that would deteriorate the solution. In the particular case of turbomachinery flows, strong inhomogeneities are found at the stage exit in the form of wake effects, unsteady flow bubbles, or pressure gradients. Moreover, blades and rotating parts create a flow deviation in the form of a swirling motion of the mean flow. This swirling motion generates a positive radial pressure gradient that is in equilibrium with the square of the tangential velocity. This so-called radial equilibrium has to be thus satisfied by the static pressure profile imposed at the outlet condition. For Unsteady Reynold Averaged Navier-Stokes (URANS) simulations, it is usual for turbomachinery simulations to impose a static pressure profile that satisfies a simplified radial equilibrium. However, this methodology leads to a boundary that is not appropriate for proper LES and DNS as it is fully reflecting. It will be demonstrated that the NSCBC methodology applied at the outlet remains fully compatible with the need to verify the radial equilibrium while also being non-reflective [132].

For the particular case of inlet boundary conditions in the turbomachinery field, the imposed values are usually expressed in terms of total pressure $P_t = P_s \left(1 + \frac{\gamma-1}{2} Ma^2\right)^{\frac{\gamma}{\gamma-1}}$ and total temperature $T_t = T_s \left(1 + \frac{\gamma-1}{2} Ma^2\right)$ [133] where P_s represents the static pressure, T_s the static temperature. Furthermore, the flow direction, determined by the angles ϕ and α must also be specified (see Fig. 4.2). Indeed, these quantities are commonly measured at different sections in an experimental facility using Pitot tubes and thermocouples. Once the total quantities are adequately imposed at the inlet, it must also be able to handle synthetic turbulence injection. Indeed, turbulence may have a significant effect on the flow developing in a turbomachine [134, 135, 136, 137, 138, 139].

Finally, recent progress has been made in adapting characteristic boundary conditions to the LBM formalism. Their use has been extended to high Reynolds number flows using a regularized approach [92]. Moreover, an open boundary condition has been developed [117] using the Locally One-Dimensional Inviscid (LODI) formalism coupled with a hybrid recursive regularized lattice Boltzmann method suited for compressible flow.

This chapter aims to detail and validate an NSCBC methodology in a compressible LBM framework that applies to turbomachinery flows. This consists of the imposition of total pressure, total temperature, and flow direction at the inlet, with the possibility of adding synthetic turbulence injection and a pressure profile satisfying a simplified radial equilibrium at the outlet. The chapter is structured as follows: section 4.2 describes the NSCBC formulation for this particular inlet condition while section 4.4 and 4.5 assess the NSCBC methodology for the inlet and outlet respectively on several academical test-cases.

4.2 Theory of the Navier-Stokes Characteristic Boundary Conditions

Starting from the Navier-Stokes equations, written using Einstein notation, for a compressible viscous flow, one has :

$$\frac{\partial \rho}{\partial t} + \frac{\partial \rho u_i}{\partial x_i} = 0 \tag{4.1}$$

$$\frac{\partial \rho u_i}{\partial t} + \frac{\partial \rho u_i u_j}{\partial x_j} + \frac{\partial P_s}{\partial x_i} = \frac{\partial \tau_{ij}}{\partial x_j} \tag{4.2}$$

$$\frac{\partial \rho E}{\partial t} + \frac{\partial (\rho E + P_s) u_i}{\partial x_i} = \frac{\partial u_i \tau_{ij}}{\partial x_i} - \frac{\partial q_i}{\partial x_i} \tag{4.3}$$

with ρ the local fluid density, u_i the velocity components, P_s the static pressure, T_s the static temperature, E the total energy (Eq. 4.4), and τ_{ij} the viscous stress tensor defined in Eq. 4.5.

$$\rho E = \frac{1}{2}\rho u_k u_k + \frac{P_s}{\gamma - 1} \tag{4.4}$$

$$\tau_{ij} = \mu(\frac{\partial u_i}{\partial x_j} + \frac{\partial u_j}{\partial x_i} - \frac{2}{3}\delta_{ij}\frac{\partial u_k}{\partial x_k}) \tag{4.5}$$

δ_{ij} is the Kronecker symbol and μ the dynamic viscosity. q_i is the heat flux along the x_i direction and is defined as $q_i = -\lambda\frac{\partial T_s}{\partial x_i}$, where λ is the thermal conductivity. The system is finally closed using the ideal gas law:

$$P_s = \rho r_g T_s \tag{4.6}$$

where r_g is the specific constant of the mixture $r_g = \frac{R}{W}$, with W the mean molecular weight of the mixture and $R = 8.3143\ J/mol.K$ is the universal gas constant.

Using characteristic analysis [140, 129, 141], it is possible to transform the vector of conservatives variables $\boldsymbol{U} = (\rho, \rho u, \rho v, \rho w, \rho E)^T$ or the vector of primitive variables expressed in the reference frame $\vec{n}, \vec{t_1}, \vec{t_2}$ written $\boldsymbol{V} = (\rho, P_s, u_n, u_{t_1}, u_{t_2})^T$ into characteristic variables. To do so, the Navier-Stokes equations are written in matrix form:

$$\frac{\partial \boldsymbol{U}}{\partial t} + \boldsymbol{A_U}\frac{\partial \boldsymbol{U}}{\partial \boldsymbol{x}} + \boldsymbol{B_U}\frac{\partial \boldsymbol{U}}{\partial \boldsymbol{y}} + \boldsymbol{C_U}\frac{\partial \boldsymbol{U}}{\partial \boldsymbol{z}} + \boldsymbol{S} = \boldsymbol{0} \tag{4.7}$$

where $\boldsymbol{A_U}$, $\boldsymbol{B_U}$, $\boldsymbol{C_U}$ are the Jacobian matrices of the respective fluxes in the x, y, z directions, and $\boldsymbol{S}$ is the diffusion term. In the same way, $\boldsymbol{V}$ verifies:

$$\frac{\partial \boldsymbol{V}}{\partial t} + \boldsymbol{N}\frac{\partial \boldsymbol{V}}{\partial \boldsymbol{n}} + \boldsymbol{T_1}\frac{\partial \boldsymbol{V}}{\partial \boldsymbol{t_1}} + \boldsymbol{T_2}\frac{\partial \boldsymbol{V}}{\partial \boldsymbol{t_2}} + \boldsymbol{S} = \boldsymbol{0} \tag{4.8}$$

where $\boldsymbol{N}$ is the normal Jacobian, $\boldsymbol{T_1}$, $\boldsymbol{T_2}$ are the two tangential Jacobian along $\vec{t_1}$ and $\vec{t_2}$.

The fully developed primitive equations read:

$$\frac{\partial \rho}{\partial t} + u_n\frac{\partial \rho}{\partial n} + u_{t_1}\frac{\partial \rho}{\partial t_1} + u_{t_2}\frac{\partial \rho}{\partial t_2} + \rho\left(\frac{\partial u_n}{\partial n} + \frac{\partial u_{t_1}}{\partial t_1} + \frac{\partial u_{t_2}}{\partial t_2}\right) = 0 \tag{4.9}$$

$$\frac{\partial P_s}{\partial t} + u_n\frac{\partial P_s}{\partial n} + u_{t_1}\frac{\partial P_s}{\partial t_1} + u_{t_2}\frac{\partial P_s}{\partial t_2} + \gamma P_s\left(\frac{\partial u_n}{\partial n} + \frac{\partial u_{t_1}}{\partial t_1} + \frac{\partial u_{t_2}}{\partial t_2}\right) = 0 \tag{4.10}$$

$$\frac{\partial u_n}{\partial t} + u_n\frac{\partial u_n}{\partial n} + u_{t_1}\frac{\partial u_n}{\partial t_1} + u_{t_2}\frac{\partial u_n}{\partial t_2} + \frac{1}{\rho}\frac{\partial P_s}{\partial n} = 0 \tag{4.11}$$

$$\frac{\partial u_{t_1}}{\partial t} + u_n\frac{\partial u_{t_1}}{\partial n} + u_{t_1}\frac{\partial u_{t_1}}{\partial t_1} + u_{t_2}\frac{\partial u_{t_1}}{\partial t_2} + \frac{1}{\rho}\frac{\partial P_s}{\partial t_1} = 0 \tag{4.12}$$

$$\frac{\partial u_{t_2}}{\partial t} + u_n\frac{\partial u_{t_2}}{\partial n} + u_{t_1}\frac{\partial u_{t_2}}{\partial t_1} + u_{t_2}\frac{\partial u_{t_2}}{\partial t_2} + \frac{1}{\rho}\frac{\partial P_s}{\partial t_2} = 0 \tag{4.13}$$

Considering that the normal at the surface for the boundary is $\vec{n}$, the equations are written as:

$$\frac{\partial \boldsymbol{V}}{\partial t} + \boldsymbol{N}\frac{\partial \boldsymbol{V}}{\partial \boldsymbol{n}} + \boldsymbol{C} = \boldsymbol{0} \tag{4.14}$$

With $\boldsymbol{N}$ expressed in Eq. 4.15 and $\boldsymbol{C}$ is the vector containing all remaining terms which do not involve elements in the normal direction (terms of $\partial \boldsymbol{V}/\partial n$).

$$\boldsymbol{N} = \begin{pmatrix} u_n & 0 & \rho & 0 & 0 \\ 0 & u_n & \gamma P_s & 0 & 0 \\ 0 & 1/\rho & u_n & 0 & 0 \\ 0 & 0 & 0 & u_n & 0 \\ 0 & 0 & 0 & 0 & u_n \end{pmatrix} \tag{4.15}$$

Considering that the speed of sound is $c^2 = \frac{\gamma P_s}{\rho}$, computing the eigenvalues λ_i of $\boldsymbol{N}$ yields the diagonal matrix D with the corresponding eigenvalues: $\lambda_1 = u_n - c$, $\lambda_2 = \lambda_3 = \lambda_4 = u_n$ and $\lambda_5 = u_n + c$.

$$\boldsymbol{D} = \begin{pmatrix} u_n - c & 0 & 0 & 0 & 0 \\ 0 & u_n & 0 & 0 & 0 \\ 0 & 0 & u_n & 0 & 0 \\ 0 & 0 & 0 & u_n & 0 \\ 0 & 0 & 0 & 0 & u_n + c \end{pmatrix} \tag{4.16}$$

The corresponding eigenvectors are:

$$\boldsymbol{l_1^T} = (0, 1, -\rho c, 0, 0) \tag{4.17}$$

$$\boldsymbol{l_2^T} = (c^2, -1, 0, 0, 0) \tag{4.18}$$

$$\boldsymbol{l_3^T} = (0, 0, 0, 1, 0) \tag{4.19}$$

$$\boldsymbol{l_4^T} = (0, 0, 0, 0, 1) \tag{4.20}$$

$$\boldsymbol{l_5^T} = (0, 1, \rho c, 0, 0) \tag{4.21}$$

By inverting these definitions it is possible to write the normal derivative terms $(\partial \boldsymbol{V}/\partial n)$:

$$\frac{\partial \rho}{\partial n} = \frac{1}{c^2}\left(\frac{\mathcal{L}_s}{u_n} + \frac{1}{2}[\frac{\mathcal{L}_+}{u_n + c} + \frac{\mathcal{L}_-}{u_n - c}]\right) \tag{4.22}$$

$$\frac{\partial P_s}{\partial n} = \frac{1}{2}\left(\frac{\mathcal{L}_+}{u_n + c} + \frac{\mathcal{L}_-}{u_n - c}\right) \tag{4.23}$$

$$\frac{\partial u_n}{\partial n} = \frac{1}{2\rho c}\left(\frac{\mathcal{L}_+}{u_n+c} - \frac{\mathcal{L}_-}{u_n-c}\right) \tag{4.24}$$

$$\frac{\partial u_{t_1}}{\partial n} = \frac{\mathcal{L}_{t_1}}{u_n} \tag{4.25}$$

$$\frac{\partial u_{t_2}}{\partial n} = \frac{\mathcal{L}_{t_2}}{u_n} \tag{4.26}$$

Then we substitute these expressions of $\partial \boldsymbol{V}/\partial n$ into the terms of $\boldsymbol{N}\partial \boldsymbol{V}/\partial n$ (Eq. 4.9-4.13) leading to the following primitive equations :

$$\frac{\partial \rho}{\partial t} + \frac{1}{c^2}\left(\mathcal{L}_s + \frac{1}{2}[\mathcal{L}_+ + \mathcal{L}_-]\right) + u_{t_1}\frac{\partial \rho}{\partial t_1} + u_{t_2}\frac{\partial \rho}{\partial t_2} + \rho\left(\frac{\partial u_{t_1}}{\partial t_1} + \frac{\partial u_{t_2}}{\partial t_2}\right) = 0 \tag{4.27}$$

$$\frac{\partial P_s}{\partial t} + \frac{1}{2}(\mathcal{L}_+ + \mathcal{L}_-) + u_{t_1}\frac{\partial P_s}{\partial t_1} + u_{t_2}\frac{\partial P_s}{\partial t_2} + \gamma P_s\left(\frac{\partial u_{t_1}}{\partial t_1} + \frac{\partial u_{t_2}}{\partial t_2}\right) = 0 \tag{4.28}$$

$$\frac{\partial u_n}{\partial t} + \frac{1}{2\rho c}(\mathcal{L}_+ - \mathcal{L}_-) + u_{t_1}\frac{\partial u_n}{\partial t_1} + u_{t_2}\frac{\partial u_n}{\partial t_2} - g_n = 0 \tag{4.29}$$

$$\frac{\partial u_{t_1}}{\partial t} + \mathcal{L}_{t_1} + u_{t_1}\frac{\partial u_{t_1}}{\partial t_1} + u_{t_2}\frac{\partial u_{t_1}}{\partial t_2} + \frac{1}{\rho}\frac{\partial P_s}{\partial t_1} - g_{t_1} = 0 \tag{4.30}$$

$$\frac{\partial u_{t_2}}{\partial t} + \mathcal{L}_{t_2} + u_{t_1}\frac{\partial u_{t_2}}{\partial t_1} + u_{t_2}\frac{\partial u_{t_2}}{\partial t_2} + \frac{1}{\rho}\frac{\partial P_s}{\partial t_2} - g_{t_2} = 0 \tag{4.31}$$

The wave amplitude associated with each characteristic velocity λ_i is noted $\mathcal{L}_i = \lambda_i \frac{\partial \boldsymbol{W}}{\partial n}$, with i the index of the corresponding wave and $\boldsymbol{W}$ is the vector of characteristic variables. The characteristic analysis applied to the Navier-Stokes equations finally leads to the following expression for the characteristic waves $\mathcal{L}_i$ associated with the characteristic velocities, written in the local reference frame:

$$\begin{pmatrix} \mathcal{L}_+ \\ \mathcal{L}_- \\ \mathcal{L}_{t_1} \\ \mathcal{L}_{t_2} \\ \mathcal{L}_S \end{pmatrix} = \begin{pmatrix} (u_n+c)(\frac{\partial u_n}{\partial n} + \frac{1}{\rho c}\frac{\partial P_s}{\partial n}) \\ (u_n-c)(-\frac{\partial u_n}{\partial n} + \frac{1}{\rho c}\frac{\partial P_s}{\partial n}) \\ u_n\frac{\partial u_{t_1}}{\partial n} \\ u_n\frac{\partial u_{t_2}}{\partial n} \\ u_n(\frac{\partial \rho}{\partial n} - \frac{1}{c^2}\frac{\partial P_s}{\partial n}) \end{pmatrix} \tag{4.32}$$

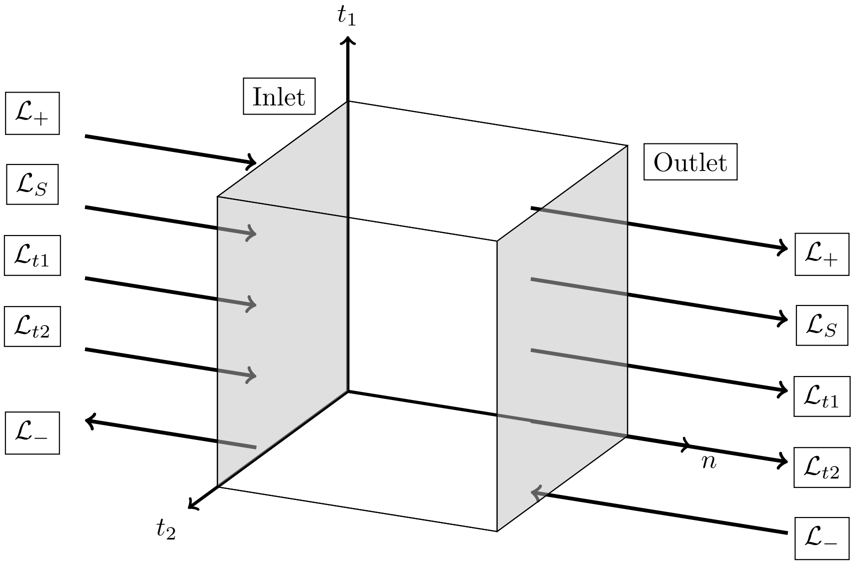

Figure **(4.1)** – Representation of the $\mathcal{L}_i$ waves leaving or entering the computational domain.

As illustrated in Fig. 4.1, for an inlet, $\mathcal{L}_+$ and $\mathcal{L}_-$ are respectively the inward and outward acoustic waves, whereas $\mathcal{L}_{t_1}$ and $\mathcal{L}_{t_2}$ are transverse shear waves, and $\mathcal{L}_s$ is the entropic wave.

The NSCBC strategy used in this paper is based on locally one-dimensional inviscid (LODI) flow on the boundary to specify the amplitude of in-going waves. Under the LODI assumption, the characteristic system for the Navier-Stokes equations becomes:

$$\frac{\partial \rho}{\partial t} + \left(\mathcal{L}_S + \frac{\rho}{2c}(\mathcal{L}_+ + \mathcal{L}_-)\right) = 0 \tag{4.33}$$

$$\frac{\partial P_s}{\partial t} + \frac{\rho c}{2}\left(\mathcal{L}_+ + \mathcal{L}_-\right) = 0 \tag{4.34}$$

$$\frac{\partial T_s}{\partial t} + \frac{(\gamma-1)T_s}{2c}\left(\mathcal{L}_+ + \mathcal{L}_-\right) = 0 \tag{4.35}$$

$$\frac{\partial s}{\partial t} - \frac{c^2\mathcal{L}_s}{(\gamma-1)\rho T} = 0 \tag{4.36}$$

$$\frac{\partial u_n}{\partial t} + \frac{1}{2}(\mathcal{L}_+ - \mathcal{L}_-) = 0 \tag{4.37}$$

$$\frac{\partial u_{t_1}}{\partial t} + \mathcal{L}_{t_1} = 0 \tag{4.38}$$

$$\frac{\partial u_{t_2}}{\partial t} + \mathcal{L}_{t_2} = 0 \tag{4.39}$$

It is necessary to specify the ingoing wave amplitudes to advance the solution in time at the boundary. It should also be noted that only one of the two equations Eqs. 4.34 or 4.35 is needed thanks to the ideal gas law.

Some algebra is required to rewrite the LODI expressions using the P_t and T_t variables. This approach has been first presented by Odier et al. [133] and will be recalled here. First, they need to be expressed as functions of the local Mach number written Ma. Thus, to compute the time derivative of P_t and T_t, the time derivative of the Mach number is involved. However, it is possible to write the Mach number as a function of the kinetic energy e_c, the adiabatic coefficient γ, the specific gas constant r, and the static temperature T_s according to Eq. 4.40:

$$Ma^2 = \frac{u_n^2 + u_{t_1}^2 + u_{t_2}^2}{\gamma r_g T_s} = \frac{2e_c}{\gamma r_g T_s} \tag{4.40}$$

However, the kinetic energy e_c is defined as:

$$e_c = \frac{u_n^2 + u_{t_1}^2 + u_{t_2}^2}{2} \tag{4.41}$$

The kinetic energy temporal derivative is thus:

$$\frac{\partial e_c}{\partial t} = u_n \frac{\partial u_n}{\partial t} + u_{t_1} \frac{\partial u_{t_1}}{\partial t} + u_{t_2} \frac{\partial u_{t_2}}{\partial t} \tag{4.42}$$

Using Eqs. 4.37, 4.38 and 4.39, the temporal derivative of the kinetic energy can be written as:

$$\frac{\partial e_c}{\partial t} = -\frac{u_n}{2}(\mathcal{L}_+ - \mathcal{L}_-) - u_{t_1}\mathcal{L}_{t_1} - u_{t_2}\mathcal{L}_{t_2} \tag{4.43}$$

The temporal derivative of the Mach number is expressed using Eq. 4.43:

$$\frac{\partial Ma^2}{\partial t} = \frac{2}{c^2}\left(\mathcal{L}_+ \left(\frac{(\gamma-1)e_c}{2c} - \frac{u_n}{2}\right) + \mathcal{L}_- \left(\frac{(\gamma-1)e_c}{2c} + \frac{u_n}{2}\right) - u_{t_1}\mathcal{L}_{t_1} - u_{t_2}\mathcal{L}_{t_2} - \frac{e_c}{\rho}\mathcal{L}_s\right) \tag{4.44}$$

Moreover, using the definition of total pressure:

$$P_t = P_s \left(1 + \frac{(\gamma-1)}{2} Ma^2\right)^{\frac{\gamma}{(\gamma-1)}} \tag{4.45}$$

The temporal derivative of total pressure is:

$$\frac{\partial P_t}{\partial t} = \frac{\partial P_s}{\partial t}\left(1 + \frac{(\gamma-1)}{2}Ma^2\right)^{\frac{\gamma}{(\gamma-1)}} + \frac{P_s\gamma}{2}.\frac{\partial Ma^2}{\partial t}\left(1 + \frac{(\gamma-1)}{2}Ma^2\right)^{\frac{\gamma}{(\gamma-1)}-1} \tag{4.46}$$

Using Eq. 4.44 in Eq. 4.46, the total pressure temporal derivative becomes:

$$\begin{aligned}\frac{\partial P_t}{\partial t} =&\mathcal{L}_+ \left(-\frac{\rho c P_t}{2P_s} + \frac{P_t}{r_g T_t}\left(\frac{(\gamma-1)e_c}{2c} - \frac{u_n}{2}\right)\right) + \mathcal{L}_- \left(-\frac{\rho c P_t}{2P_s} + \frac{P_t}{r_g T_t}\left(\frac{(\gamma-1)e_c}{2c} + \frac{u_n}{2}\right)\right)\\ &- \frac{P_t}{r_g T_t}\left(u_{t_1}\mathcal{L}_{t_1} + u_{t_2}\mathcal{L}_{t_2} + \frac{e_c}{\rho}\mathcal{L}_s\right)\end{aligned} \tag{4.47}$$

With the same method, starting from the definition of the total temperature:

$$T_t = T_s\left(1 + \frac{(\gamma-1)}{2}Ma^2\right) \tag{4.48}$$

The temporal derivative of the total temperature is:

$$\frac{\partial T_t}{\partial t} = \frac{\partial T_s}{\partial t}\frac{T_t}{T_s} + T_s\frac{(\gamma-1)}{2}\frac{\partial Ma^2}{\partial t} \tag{4.49}$$

Then using Eqs.4.35 and 4.44:

$$\begin{aligned}\frac{\partial T_t}{\partial t} =&\mathcal{L}_+ \left(-\frac{(\gamma-1)T_t}{2c} + \frac{1}{C_p}\left(\frac{(\gamma-1)e_c}{2c} - \frac{u_n}{2}\right)\right) + \mathcal{L}_- \left(-\frac{(\gamma-1)T_t}{2c} + \frac{1}{C_p}\left(\frac{(\gamma-1)e_c}{2c} + \frac{u_n}{2}\right)\right)\\ &- \frac{1}{C_p}\left(u_{t_1}\mathcal{L}_{t_1} + u_{t_2}\mathcal{L}_{t_2} + \frac{e_c}{\rho}\mathcal{L}_s\right)\end{aligned} \tag{4.50}$$

With C_p being the specific heat ratio:

$$C_p = \frac{\gamma r_g}{\gamma - 1} \tag{4.51}$$

The flow direction is fixed by choosing a flow angle ϕ and α (see Fig. 4.2). Then, $\sin(\phi)$ and $\sin(\alpha)$ can be linked to the local flow velocity vector with:

$$\sin(\phi) = \frac{u_{t_1}}{\left\|\vec{U}\right\|} \tag{4.52}$$

$$sin(\alpha) = \frac{u_{t_2}}{\left\|\vec{U}\right\|} \tag{4.53}$$

$$\text{with} \qquad \left\|\vec{U}\right\| = \sqrt{u_n^2 + u_{t_1}^2 + u_{t_2}^2} \tag{4.54}$$

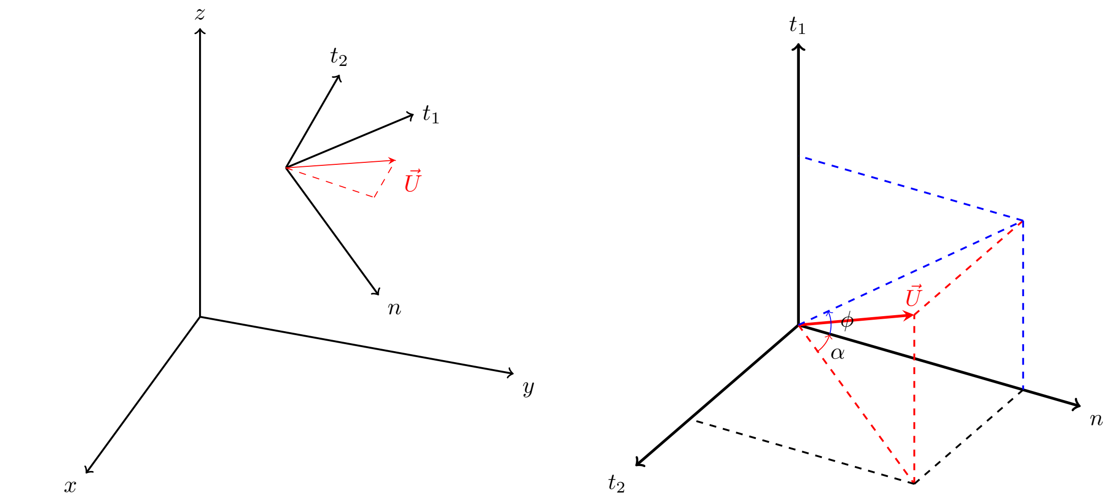

(a) Rotation from Cartesian basis to normal patch.

(b) Flow direction angles ϕ, α associated to the velocity vector $\overrightarrow{U}$.

Figure **(4.2)**

The last step consists in determining the wave expressions of $\mathcal{L}_+$ and $\mathcal{L}_s$ by solving the system constituted by Eqs. 4.47 and 4.50:

$$\mathcal{L}_+ \left(-\frac{\rho c P_t}{2P_s} + \frac{P_t}{r_g T_t} \left(\frac{(\gamma-1)e_c}{2c} - \frac{u_n}{2} \right) \right) - \frac{e_c P_t}{\rho r_g T_t} \mathcal{L}_s = \frac{\partial P_t}{\partial t} - \mathcal{L}_- \left(-\frac{\rho c P_t}{2P_s} + \frac{P_t}{r_g T_t} \left(\frac{(\gamma-1)e_c}{2c} + \frac{u_n}{2} \right) \right) + \frac{P_t}{r_g T_t} \left(u_{t_1} \mathcal{L}_{t_1} + u_{t_2} \mathcal{L}_{t_2} \right) \tag{4.55}$$

$$\mathcal{L}_+ \left(-\frac{(\gamma-1)T_t}{2c} + \frac{1}{C_p} \left(\frac{(\gamma-1)e_c}{2c} - \frac{u_n}{2} \right) \right) - \frac{e_c}{\rho C_p} \mathcal{L}_s = \frac{\partial T_t}{\partial t} - \mathcal{L}_- \left(-\frac{(\gamma-1)T_t}{2c} + \frac{1}{C_p} \left(\frac{(\gamma-1)e_c}{2c} + \frac{u_n}{2} \right) \right) + \frac{1}{C_p} \left(u_{t_1} \mathcal{L}_{t_1} + u_{t_2} \mathcal{L}_{t_2} \right) \tag{4.56}$$

$$\begin{cases} \mathcal{L}_+ F_4 - \mathcal{L}_s.F_1 = \dfrac{\partial P_t}{\partial t} + \dfrac{P_t}{r_g T_t}.F_3 - \mathcal{L}_-.F_6 & (4.57) \\ \mathcal{L}_+ F_5 - \mathcal{L}_s.F_2 = \dfrac{\partial T_t}{\partial t} + \dfrac{1}{C_p}.F_3 - \mathcal{L}_-.F_7 & (4.58) \end{cases}$$

Combining Eq. 4.57 $\times F_2$ and adding Eq. 4.58 $\times F_1$ gives:

$$\mathcal{L}_+ \left(F_4 F_2 + F_5 F_1 \right) = F_2 \frac{\partial P_t}{\partial t} + F_1 \frac{\partial T_t}{\partial t} + \frac{P_t}{r_g T_t} F_3 F_2 + \frac{F_3 F_1}{C_p} - \mathcal{L}_- (F_6 F_2 + F_1 F_7) \tag{4.59}$$

Finally, $\mathcal{L}_+$ can be extracted from Eq. 4.59 and gives Eq. 4.63. Once $\mathcal{L}_+$ has been expressed, the unknown $\mathcal{L}_S$ wave is deduced from Eq. 4.58 giving Eq. 4.64.

Solving this system gives the following expressions for the wave amplitudes:

$$\mathcal{L}_- = (u_n - c)\left(-\frac{\partial u_n}{\partial n} + \frac{1}{\rho c}\frac{\partial P_s}{\partial n}\right) \tag{4.60}$$

$$\mathcal{L}_{t_1} = -\frac{\partial u_{t_1}}{\partial t} \tag{4.61}$$

$$\mathcal{L}_{t_2} = -\frac{\partial u_{t_2}}{\partial t} \tag{4.62}$$

$$\mathcal{L}_+ = \frac{F_1\frac{\partial T_t}{\partial t} + F_2\frac{\partial P_t}{\partial t} + F_1 F_3 \frac{P_t}{rT_t} - (F_2F_6 + F_1F_7)\mathcal{L}_-}{F_4F_2 + F_5F_1} \tag{4.63}$$

$$\mathcal{L}_S = \frac{\frac{\partial T_t}{\partial t} + F_3\frac{1}{C_p} - F_5\mathcal{L}_+ - F_7\mathcal{L}_-}{F_2} \tag{4.64}$$

With the following useful relations:

$$e_c = \frac{u_n^2 + u_{t_1}^2 + u_{t_2}^2}{2} \tag{4.65}$$

$$F1 = \frac{e_c P_t}{\rho r_g T_t} \tag{4.66}$$

$$F2 = \frac{T_t}{\rho} - \frac{e_c}{\rho C_p} \tag{4.67}$$

$$F3 = \mathcal{L}_{t_1} u_{t_1} + \mathcal{L}_{t_2} u_{t_2} \tag{4.68}$$

$$F4 = -\frac{\rho c P_t}{2P_s} + \frac{P_t}{r_g T_t}\left(\frac{(\gamma-1)e_c}{2c} - \frac{u_n}{2}\right) \tag{4.69}$$

$$F5 = -\frac{(\gamma-1)T_t}{2c} + \frac{1}{C_p}\left(\frac{(\gamma-1)e_c}{2c} - \frac{u_n}{2}\right) \tag{4.70}$$

$$F6 = -\frac{\rho c P_t}{2P_s} + \frac{P_t}{r_g T_t}\left(\frac{(\gamma-1)e_c}{2c} + \frac{u_n}{2}\right) \tag{4.71}$$

$$F7 = -\frac{(\gamma-1)T_t}{2c} + \frac{1}{C_p}\left(\frac{(\gamma-1)e_c}{2c} + \frac{u_n}{2}\right) \tag{4.72}$$

$\mathcal{L}_+$ is dependent of $\mathcal{L}_-$ which implies reflection for acoustics. To ensure non-reflectivity $\mathcal{L}_-$ is set to 0 which simplifies Eqs. 4.63 and 4.64. The wave amplitudes are finally written:

$$\mathcal{L}_{-} = (u_n - c)\left(-\frac{\partial u_n}{\partial n} + \frac{1}{\rho c}\frac{\partial P_s}{\partial n}\right) \tag{4.73}$$

$$\mathcal{L}_{t_1} = -\frac{\partial u_{t_1}}{\partial t} \tag{4.74}$$

$$\mathcal{L}_{t_2} = -\frac{\partial u_{t_2}}{\partial t} \tag{4.75}$$

$$\mathcal{L}_{+} = \frac{F_1\frac{\partial T_t}{\partial t} + F_2\frac{\partial P_t}{\partial t} + F_1F_3\frac{P_t}{rT_t}}{F_4F_2 + F_5F_1} \tag{4.76}$$

$$\mathcal{L}_{S} = \frac{\frac{\partial T_t}{\partial t} + F_3\frac{1}{C_p} - F_5\mathcal{L}_{+}}{F_2} \tag{4.77}$$

To avoid a drift between the computed and the target value, a linear relaxation method [142] is used as detailed below to compute the derivative:

$$\frac{\partial X}{\partial t}dt = -\sigma_{cbc}(X_{predicted} - X_{target}) \tag{4.78}$$

Where σ_{cbc} is a user-chosen relaxation coefficient (same for every variable), $X_{predicted}$ is the value predicted by the numerical scheme, and X_{target} is the value imposed at the boundary. These evaluations are used in Eqs. 4.61-4.64 with X being $\sin(\phi)$, $\sin(\alpha)$, P_t, T_t. The condition is partially reflective if σ_{cbc} differs from 0. The consequences of such a relaxation method [143] will be studied later in the paper.

4.3 Translation into LBM Boundary Condition

The wave amplitudes are computed using Eq. 4.73 to 4.77. Once all the waves are known, an Euler first-order time approximation is applied to recover the macroscopic values of ρ, P_s, and $\boldsymbol{u}$ using Eqs. 4.33, 4.34, 4.37, 4.38, and 4.39.

As illustrated in Chapter 3, a problem appears at the boundary after the streaming step [144, 145]. Indeed, on a boundary node, some populations are unknown before the collision since they are coming from outside the computational domain as illustrated in Fig. 3.4.

A finite difference-based reconstruction is applied along with the hybrid regularization procedure [111, 103, 92, 117, 146, 147, 148] to compute the distribution functions at the boundary. The methodology is the following:

- The macroscopic values of ρ, u, P on the boundary nodes are prescribed based on an interpolation/extrapolation scheme through a cut-cell approach [117].
- The entropy s and the temperature T_s can then be estimated thanks to the thermodynamic closure and equation of state.
- Then, using the velocity gradients, the shear stress tensor and correction term ψ are computed at the boundary node with a first-order biased finite-difference scheme.

- Then the distribution functions are computed [117] such as $f_i = f_i^{eq} + f_i^{neq}$. The off-equilibrium distribution function f_i^{neq} is recursively reconstructed from the macroscopic variables and their gradients.

Thus f_i^{eq}, f_i^{neq}, ψ are fully defined at the boundary node, and the recursive collision operation followed by the streaming step towards neighboring nodes in the fluid domain can be performed.

4.4 Validation of the NSCBC Inlet

4.4.1 Convergence Towards the Mean Values

This first simplified 2D test case aims to validate the implementation of the inlet boundary condition. This test case is built similarly to a previous study performed with the compressible LES solver AVBP [133] to be able to compare the results. It is built as a square of dimension $[L_x \times L_y] = [100 \times 100]$mm discretized with $[n_x \times n_y] = [128 \times 128]$ cells (see Fig. 4.3). The minimal mesh size chosen imposes a time step $\Delta t = 1.33 \times 10^{-6}s$. The inlet condition is set to inject air with a total pressure $P_t = 9.8803 \cdot 10^4$ Pa, a total temperature $T_t = 281$ K and a normal flow direction ($\alpha = \phi = 0°$). The kinematic viscosity is set to $1.397 \times 10^{-5} m^2.s^{-1}$ corresponding to air at this temperature. The outlet condition is imposed as an outflow boundary with a static pressure $P_s = 7.1 \cdot 10^4$ Pa. On the other boundaries, periodic conditions are applied. Considering the chosen physical values and the periodicity, the Mach number must reach the expected value of (with $\gamma = 1.4$):

$$Ma = \sqrt{\frac{2}{\gamma - 1}\left[\left(\frac{P_t}{P_s}\right)^{\frac{\gamma-1}{\gamma}} - 1\right]} = 0.7036 \tag{4.79}$$

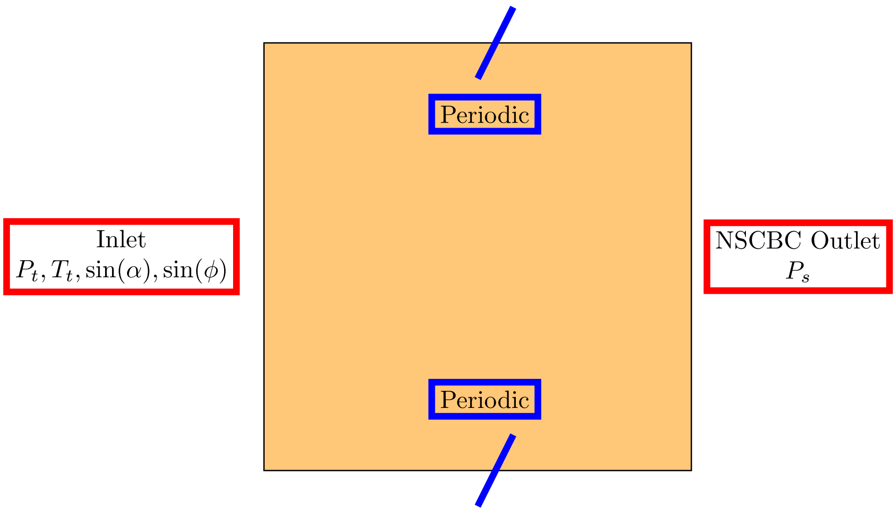

Figure **(4.3)** – Scheme of the 2D square box test case.

The initial solution corresponds to a static pressure field and a static temperature field such that $P_s = P_t$ and $T_s = T_t$. As the fluid is considered a perfect gas, the density ρ is set such as $\rho = \frac{P_t}{r_g T_t}$. The initial velocity is set to $u_x = 10\,\mathrm{m\cdot s^{-1}}$. The initialization is deliberately chosen far from the converged solution to validate the capability to reach the target. All relaxation coefficients are equal in the following. To study the temporal evolution of P_t and T_t, a probe is located at the inlet boundary, and the results are presented in Fig. 4.4.

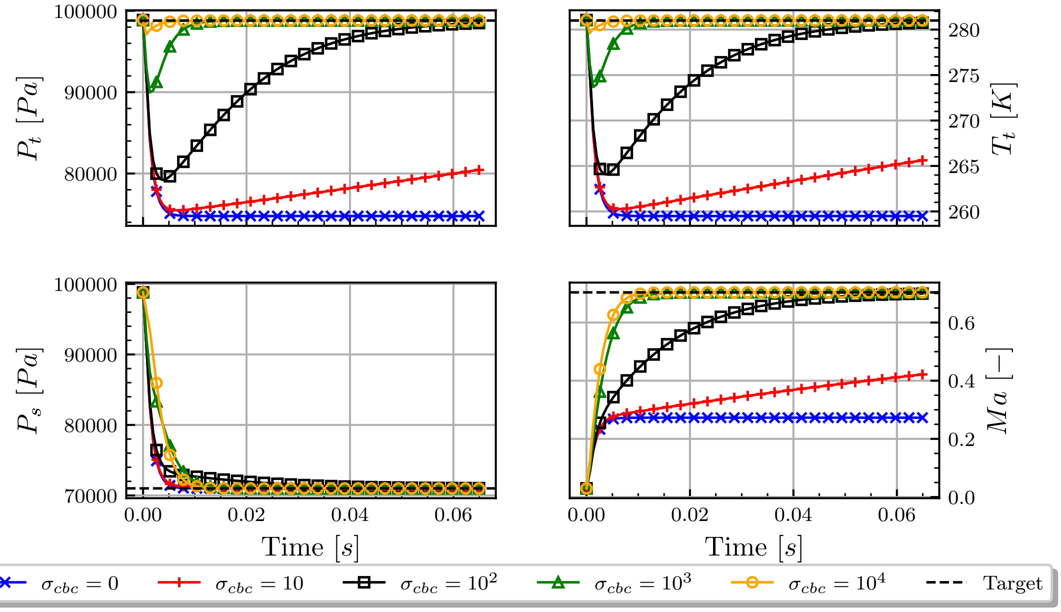

Figure **(4.4)** – Convergence of the macroscopic values towards the imposed value with the $P_t - T_t$ inlet.

The results show that the total quantities converge towards the imposed value for $\sigma_{cbc} \geq 100$. If the relaxation parameter chosen is too low, the simulation cannot recover the desired solution. Moreover, the higher the relaxation parameter, the faster the convergence. Because of the periodic configuration, no loss occurs, and the flow can be considered isentropic. This implies that the static pressure in the domain must be equal to the prescribed outlet static pressure.

4.4.2 Flow Direction Validation

In the second test case, a flow direction is added by introducing an angle $\phi = 15°$ to the flow established in the previous test case. It is then possible to follow the convergence of the flow angle to the desired value depending on the value of the relaxation coefficient as illustrated in Fig. 4.5.

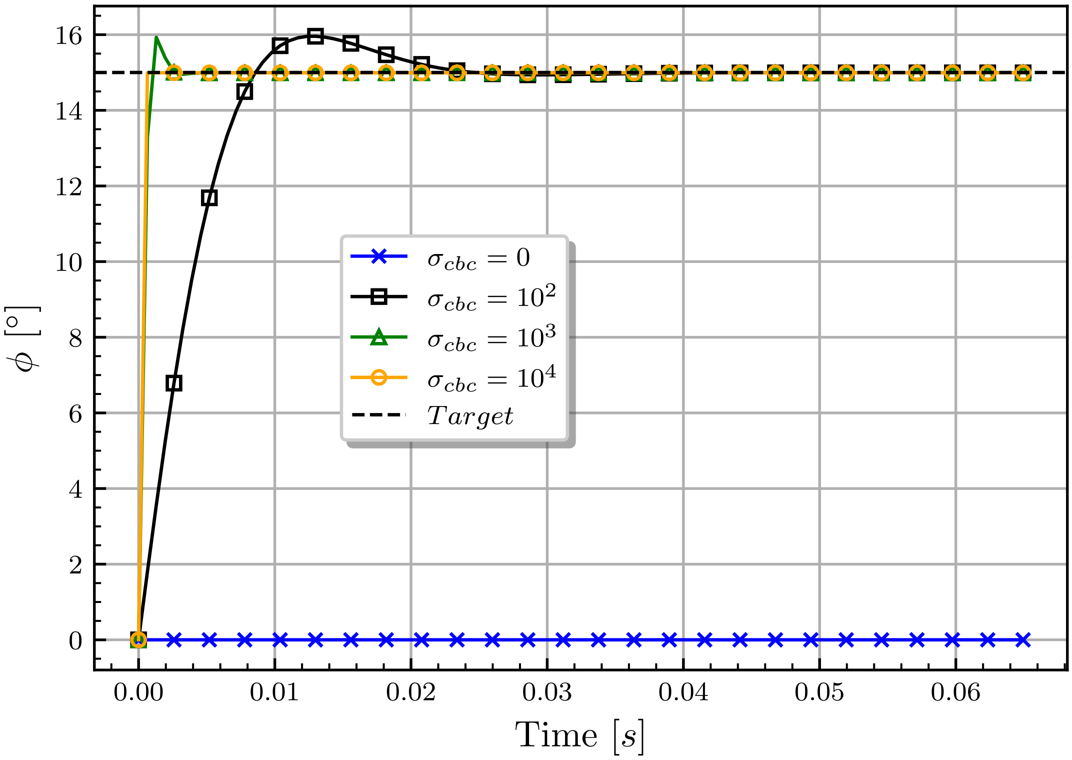

Figure **(4.5)** – Convergence of the flow direction.

Once again, it can be seen that a minimum value of the relaxation coefficient is needed to reach the target value and that a higher value of σ_{cbc} allows a faster convergence.

4.4.3 Imposition of Several Mach Numbers

This section validates the approach for a given range of inlet Mach numbers typically encountered in turbomachinery simulations. The same 2D geometry is used, and the inlet total pressure is adjusted to reach the target Mach number. For all Mach numbers, the relaxation coefficient used for the computation was $\sigma_{cbc} = 10^4$. Fig. 4.6 shows that it is possible to go through all the desired Mach values inferior to 1. If the setup results in a supersonic case, the Mach number converges and stays at 1. Indeed, for the supersonic case, the five waves enter the domain, and the NSCBC approach specifying one outgoing and four incoming waves is no longer valid.

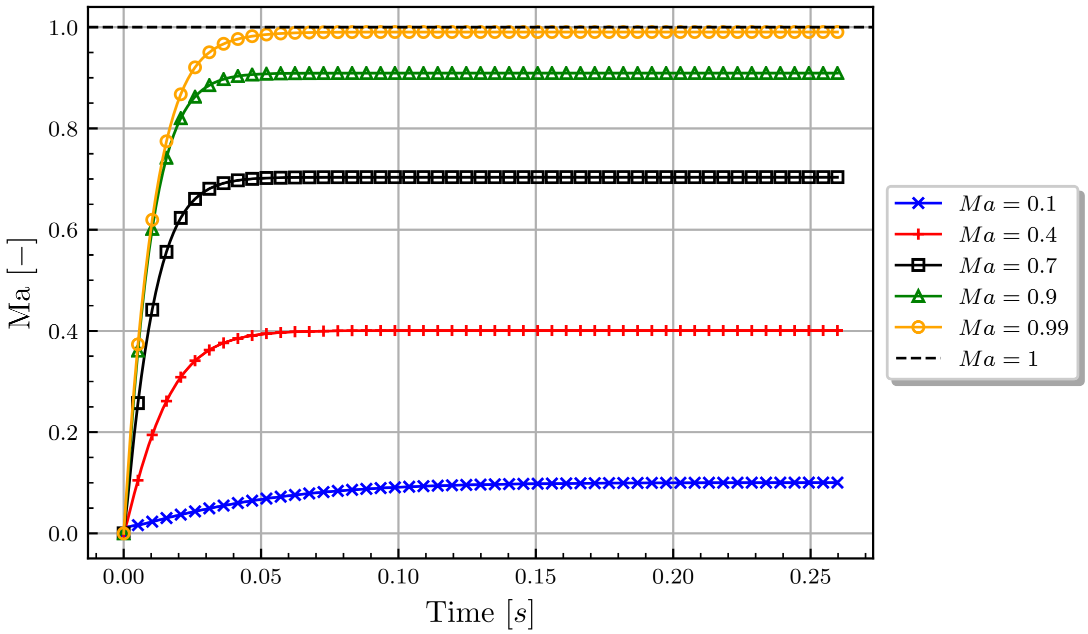

Figure **(4.6)** – Convergence towards all the specified Mach numbers.

4.4.4 Evaluation of the Acoustic Properties

This section evaluates the acoustic reflectivity of the proposed inlet boundary for several values of the relaxation coefficient σ_{cbc}. The setup is: a left-going acoustic wave with a Gaussian shape is superimposed to the flow established in the 2D-square box test case. The perturbation is initially centered at $x_0 = \frac{x}{L_x} = 0.75$ and the perturbation is defined as:

$$p' = -\rho c A \exp^{-\frac{(x-x_0)^2}{\Gamma^2}} \tag{4.80}$$

with the perturbation amplitude $A = 0.001$ and $\Gamma = 0.01$.

Fig. 4.8 illustrates pressure and velocity fluctuation evolution as the acoustic wave crosses the inlet boundary for several values of σ_{cbc}.

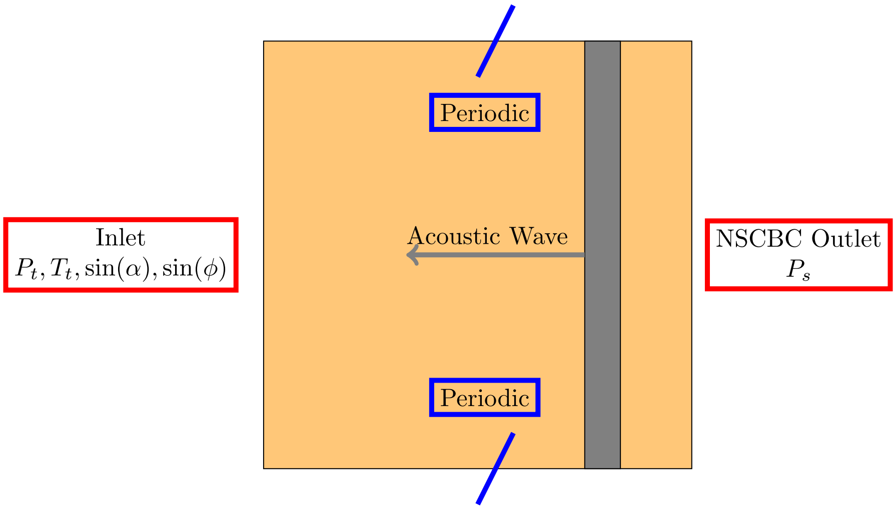

Figure **(4.7)** – Scheme of the 2D-square box with the added acoustic wave.

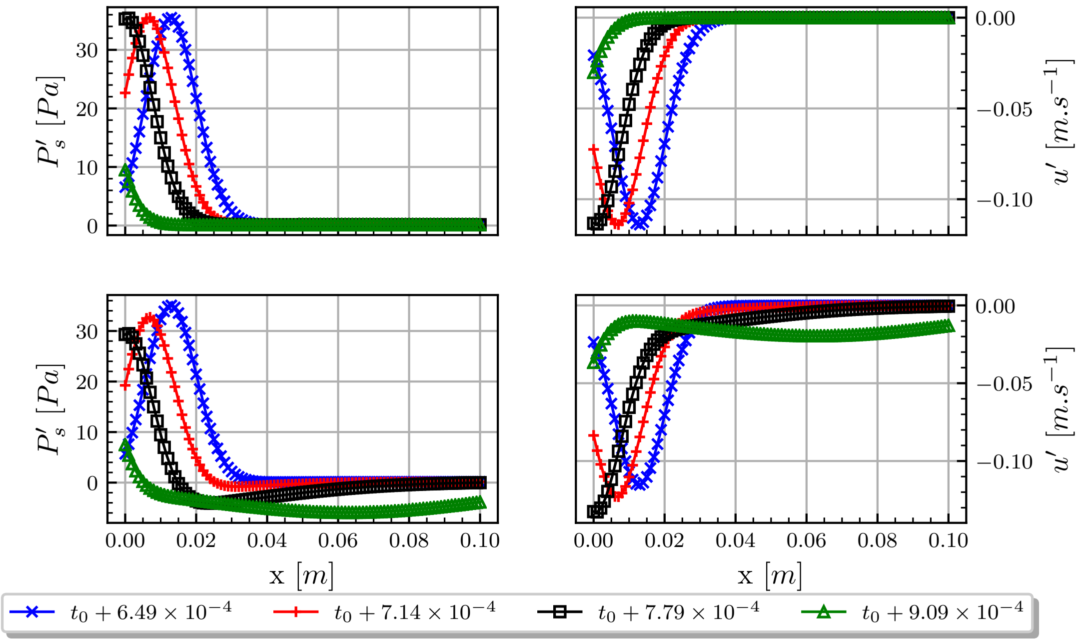

Figure **(4.8)** – Pressure and velocity fluctuations at the inlet for $\sigma_{cbc} = 0$ (top) and $\sigma_{cbc} = 10^5$ (bottom).

For a higher value of the relaxation coefficient, the intensity of the fluctuations on the velocity and pressure increases.

The reflection coefficient R is then evaluated from the pressure, velocity, and density signals recorded at the inlet probe and decomposed into mean and fluctuating components such as:

$$p(t) = \tilde{p} + p'(t) \tag{4.81}$$

$$u(t) = \tilde{u} + u'(t) \tag{4.82}$$

$$\rho(t) = \tilde{\rho} + \rho'(t) \tag{4.83}$$

From these definitions, the inward and backward acoustic waves w_+ and w_- are computed using:

$$\begin{cases} w_+ = p' + \rho c u' & (4.84) \\ w_- = p' - \rho c u' & (4.85) \end{cases}$$

Fig. 4.9 shows the reflection coefficient R and the reconstructed waves w_+ at the inlet for several σ_{cbc}.

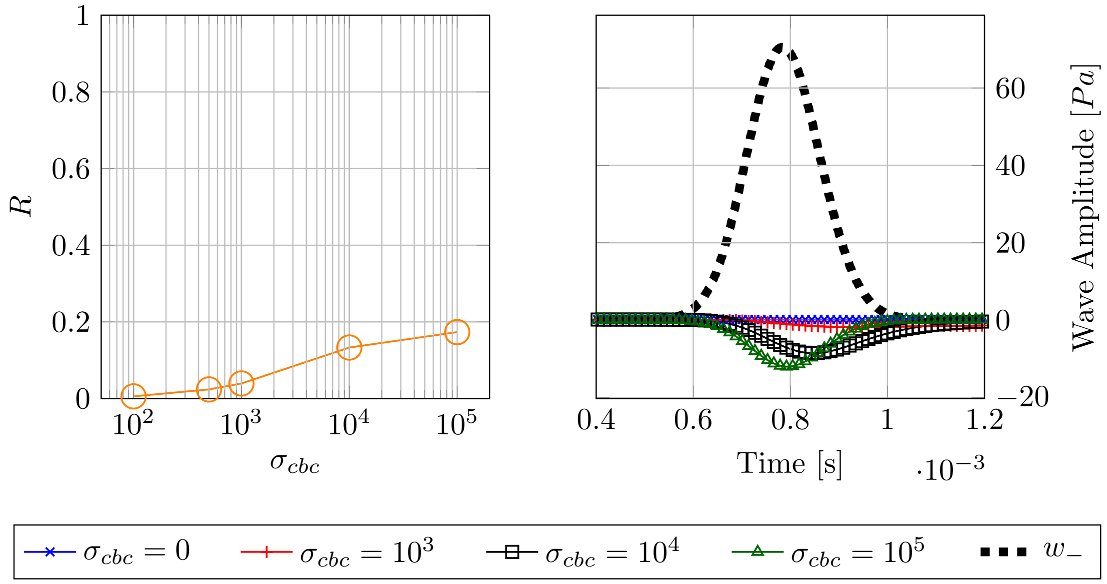

Figure **(4.9)** – Plot of the reflection coefficient and acoustic waves.

It illustrates that the relaxation coefficient is linked to the intensity of the reflection. Moreover, concerning the wave amplitude evolution, w_- should be present as it represents the Gaussian left-going acoustic wave, but any value of w_+ is a sign of reflection, whose amplitude rises proportionally to σ_{cbc}.

Considering that fast convergence of the imposed values at the inlet was observed with $10^3 \leq \sigma_{cbc} \leq 10^4$ on the previous test cases, it is concluded that this order of magnitude is to be favored to achieve the best compromise between inlet imposition and limited reflection.

4.4.5 Synthetic Turbulence Injection

Several turbulence injection methods exist in the literature [149]. In the scope of this Ph.D., the random Fourier sum was the one retained to produce the velocity fluctuations at the inlet. This approach offers a good compromise between accuracy, computational cost, and versatility which motivated its adoption compared to other methods [89]. The principle of the method is to generate an imaginary box of homogeneous isotropic turbulence approximated as the sum of a series of sinusoidal modes. The fluctuations are then convected into the domain via Taylor's frozen turbulence hypothesis [150]. The turbulent fluctuations $\boldsymbol{u'}$ are defined as a sum of N modes [149]:

$$\boldsymbol{u'}(\boldsymbol{x},t) = 2\sum_{n=1}^{N} u_n^{amp} \cos\left[\boldsymbol{\kappa}_n.(\boldsymbol{x} - t\boldsymbol{u}_c) + \phi_n + \omega_n t\right]\boldsymbol{\sigma}_n \tag{4.86}$$

u_n^{amp} is the amplitude, $\boldsymbol{\kappa}_n$ is the wavevector, ϕ_n is the phase, ω_n is the angular frequency, and $\boldsymbol{\sigma}_n$ is the direction of the mode. Finally, $\boldsymbol{u}_c$ is the convection velocity of the turbulent fluctuations. The number N of wavenumbers is specified by the user, who also imposes a large length-scale L_{max} and a small length-scale L_{min}. The amplitude of each mode u_n^{amp} determines the kinetic energy of each mode. It is based on the turbulent kinetic energy spectrum, E_n, the energy of each mode such that:

$$k = \sum_{n=1}^{N}(u_n^{amp})^2, \text{ and therefore, } u_n^{amp} = \sqrt{E_n \Delta k_{mag,n}} \tag{4.87}$$

An appropriate energy spectrum is provided by E_n, with either the von Karman-Pao spectrum (see Eq. 4.89), or the Passot-Pouquet spectrum (see Eq. 4.88).

$$E_n = \frac{32}{3}\frac{k}{\kappa_e}\sqrt{\frac{2}{\pi}}\left(\frac{\kappa_n}{\kappa_e}\right)^4 \exp\left\{-2\left(\frac{\kappa_n}{\kappa_E}\right)^2\right\} \tag{4.88}$$

$\kappa_e = 2\pi/L_e$ is the wavenumber representing the peak in the spectrum, associated with the size of the largest structures L_e, which is specified by the user.

$$E_n = \frac{3}{2}A_{VKP}\frac{k}{\kappa_e}\frac{(\kappa_n/\kappa_e)^4}{[1+(\kappa_n/\kappa_e)^2]^{17/6}} \exp\left\{-2\left(\frac{\kappa_n}{\kappa_{Kol}}\right)^2\right\} \tag{4.89}$$

$A_{VKP} = 1.45276$ and κ_{Kol} is the wave number representing the Kolmogorov length scales. The Passot-Pouquet approach has a clear spectral peak whereas the von Karman-Pao approach has a smooth decline, with the largest structures having the greatest amount of energy [89]. To use the turbulence injection, the user must provide the spectrum type, N, k, L_{max}, L_e, L_{min}, and $\boldsymbol{u}_c$. With these parameters, Eq. 4.86 is fully defined and can be evaluated at each boundary node and at each time step and then added to the mean velocity profile.

The three unsteady velocity components (u'_n, u'_{t1}, u'_{t2}) at the inlet are specified using the previously described synthetic turbulence method. Following the Characteristic Boundary Condition proposed by Guézennec and Poinsot [141], these fluctuations are added to the inlet acoustic wave $\mathcal{L}_+$ and the two transverse shear waves $\mathcal{L}_{t1}, \mathcal{L}_{t2}$ derived in section 4.2 such that:

$$\mathcal{L}_{+,turb} = \mathcal{L}_+ + \frac{\partial u'_n}{\partial t} \tag{4.90}$$

$$\mathcal{L}_{t_1,turb} = \mathcal{L}_{t_1} + \frac{\partial u'_{t_1}}{\partial t} \tag{4.91}$$

$$\mathcal{L}_{t_2,turb} = \mathcal{L}_{t_2} + \frac{\partial u'_{t_2}}{\partial t} \tag{4.92}$$

A turbulent convected flow in a rectangular box is the proposed test case to validate the turbulence injection. The computational domain is a rectangular box of dimensions $[L_x \times L_y \times L_z] = [4 \times 1 \times 1\text{mm}]$, discretized with $[n_x \times n_y \times n_z] = [392 \times 98 \times 98]$ cells (see Fig. 4.10). The minimal mesh size of this test case imposes a time step $\Delta t = 1.7 \times 10^{-8} s$. Total pressure and temperature P_t and T_t are imposed at the inlet, using a relaxation coefficient $\sigma_{cbc} = 10^4$, while static pressure P_s is imposed at the outlet so that the expected mean velocity is $100\,\text{m} \cdot \text{s}^{-1}$. All other boundaries are periodic conditions. The targeted turbulent kinetic energy is $TKE = 37.5\,\text{m} \cdot \text{s}^{-2}$. Since the turbulent kinetic energy is given by $TKE = \frac{u'^2}{2}$, this leads to an inlet velocity fluctuation fixed as $u' = 5\,\text{m} \cdot \text{s}^{-1}$. We used $N = 1000$ modes, $L_{max} = 1\,\text{mm}$, $L_{min} = 60\,\mu\text{m}$ and $L_e = 140\,\mu\text{m}$ with the Passot Pouquet spectrum to build the inlet velocity fluctuation field. Fig. 4.10 shows the injection of vortical structures near the inlet. The simulation is run for 55 convective times based on $L_x / < u_x >$ and statistics are taken over 50 convective times.

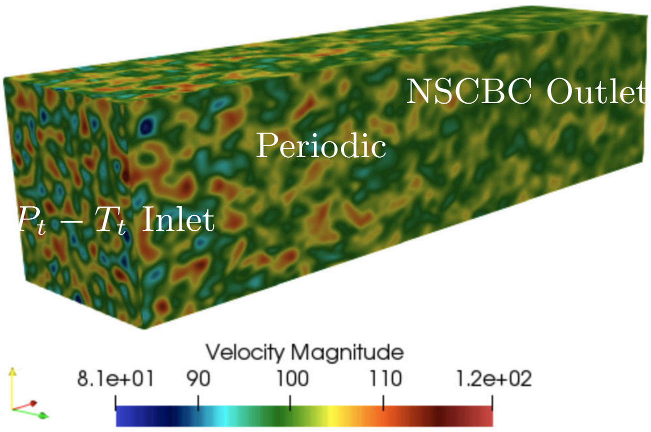

Figure **(4.10)** – Illustration of the computational domain for the three-dimensional turbulent channel.

Fig. 4.11 shows the turbulent kinetic energy decrease as expected within the domain [133]. At the inlet, a value of $TKE = 37.5\,\text{m} \cdot \text{s}^{-2}$ is reached as specified. The RMS fluctuations illustrate that the simulation recovers isotropy of $\sqrt{< u'_x u'_x >} = \sqrt{< u'_y u'_y >} = \sqrt{< u'_z u'_z >} = 5\,\text{m} \cdot \text{s}^{-1}$.

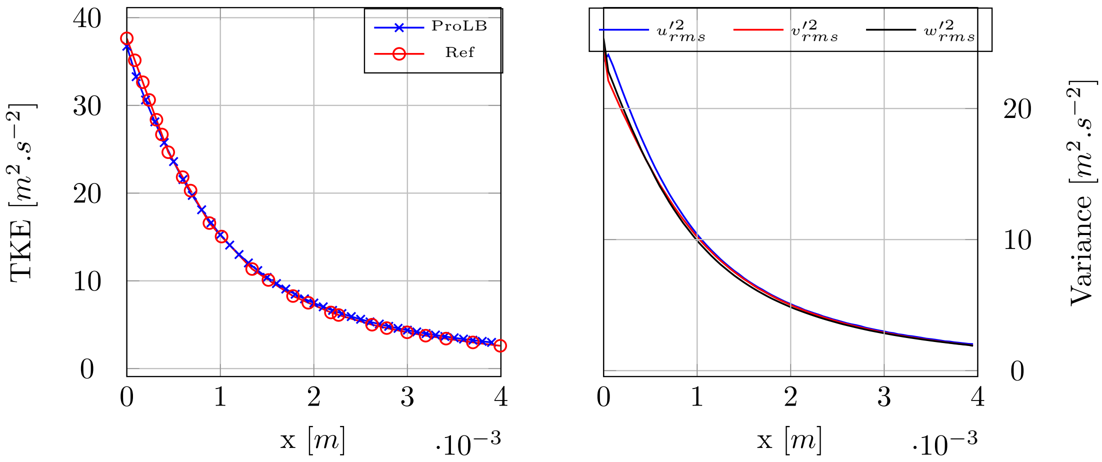

Figure **(4.11)** – Plot of the turbulent kinetic energy and the RMS evolution along the domain.

4.4.6 Enforcing a Radial Profile for Turbomachinery Simulation

Typically, radial profiles of quantities such as total pressure, total temperature, and flow angles are imposed at the inlet of a turbomachinery simulation domain. It is thus necessary to ensure the capability of the boundary condition to impose this kind of data. To do so, radial profiles of each macroscopic value are defined under the form of $Y = f(x, y, z)$ or $Y = f(x, r, \theta)$ with Y being P_t, T_t, ϕ, α and f a polynomial function, dependent on the Cartesian or cylindrical coordinates.

For the radial profile, the expression of f is chosen such that:

- $P_t = (-40 * (y - y_0)^2 + 1.1) * P_{t,mean}$
- $T_t = (-10 * (y - y_0)^2 + 1) * T_{t,mean}$

These expressions are imposed on the inlet boundary of the 2D-square box test case defined in the first section using a relaxation coefficient $\sigma_{cbc} = 10^4$. The numerical and physical parameters are unchanged from the first 2D square box test case. Fig. 4.12 illustrates that the inlet boundary condition correctly produces total pressure and Mach number fields that correspond to the imposed radial profile and outlet static pressure of $P_s = 7.1 \cdot 10^4$ Pa.

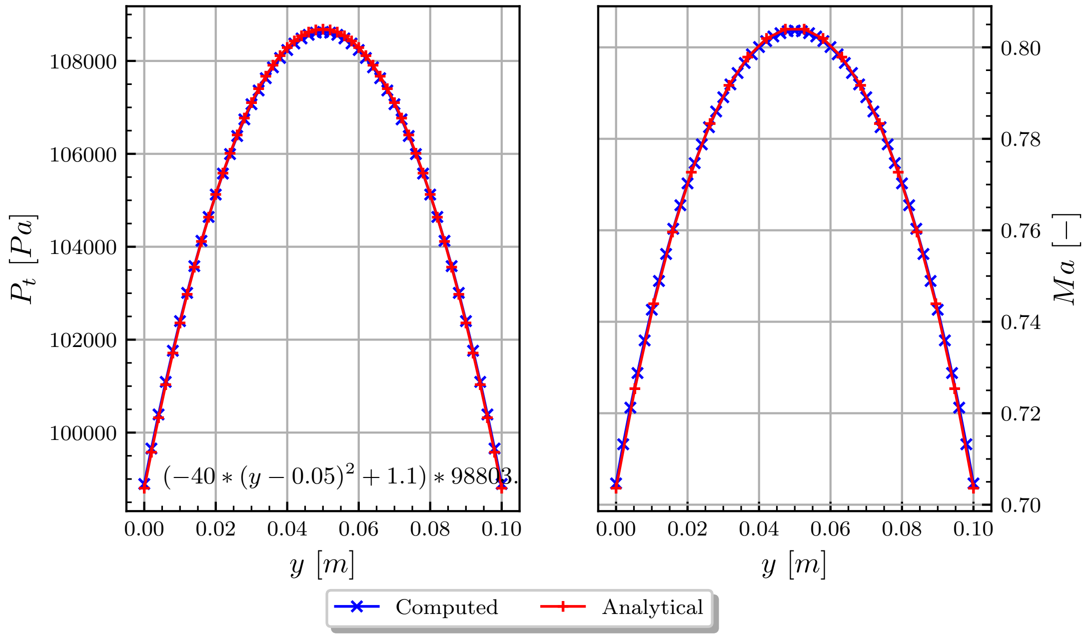

Figure **(4.12)** – Illustration of the imposition of an inlet radial profile.

4.5 Study of the Radial Equilibrium at the Outlet

The usual method used in RANS simulations is to impose an outlet pressure profile consistent with the radial equilibrium. This approach leads to a fully reflecting outlet for acoustic waves. It is not an issue for RANS simulations, which do not capture the acoustics. However, it becomes an issue for LES. To overcome this problem, NSCBC are commonly used. For an outlet, they allow the user to control the influence of the incoming information by manipulating wave amplitudes. The study investigates how NSCBC conditions perform for flows with strong rotation. It is illustrated that the NSCBC formalism can let the physical radial pressure gradient establish naturally so that this formalism can be used at the outlet of turbomachinery simulations without additional treatment. This methodology has already been successfully applied within a standard LES solver AVBP [132]. This study aims to evaluate if it is reproducible in the LBM approach.

4.5.1 Simplified Radial Equilibrium

The radial equilibrium equations were first derived in the 1940s-1950s [151]. It was shown that the whirling motion of a fluid inside a turbomachine creates a centrifugal force that has to be balanced by a centripetal one, thus creating a positive radial pressure gradient. This simplified radial equilibrium is obtained by considering a flow with the following properties:

- No viscous effects,
- negligible heat conduction
- a steady-state ($\frac{\partial}{\partial t} = 0$)
- no gravity or volumic forces

- axisymmetric flow ($\frac{\partial}{\partial\theta} = 0$)
- no radial velocity ($u_r = 0$)

Under these hypotheses, the flow is governed by the Euler equations for a compressible flow with the equation of state for an ideal gas. In cylindrical coordinates (r, θ, x), the momentum equation in the radial direction is

$$\frac{\partial u_r}{\partial t} + u_r \frac{\partial u_r}{\partial r} + \frac{u_\theta}{r}\frac{\partial u_r}{\partial \theta} - \frac{u_\theta^2}{r} + u_x \frac{\partial u_r}{\partial x} = -\frac{1}{\rho}\frac{\partial P}{\partial r} \tag{4.93}$$

Applying the precedent assumptions to Eq. 4.93 leads to the simplified radial equilibrium equation:

$$\frac{1}{\rho}\frac{\partial P}{\partial r} = \frac{u_\theta^2}{r} \tag{4.94}$$

where P is the static pressure, u_θ is the azimuthal velocity component and ρ is the density.

4.5.2 Annulus Test Case

The test cases described below are presented in detail in Koupper et al. [132]. The ability of characteristic boundary conditions to recover the Radial Equilibrium Assumption (REA) pressure profile is assessed in a rotating flow in a simple annulus (Fig. 4.13). The annulus has the following dimensions:

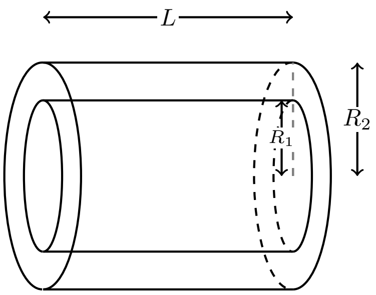

Figure **(4.13)** – Geometry of the annulus test case.

- $R_1 = 0.2\,\mathrm{m}$
- $R_2 = 0.28\,\mathrm{m}$
- $L = 0.32\,\mathrm{m}$
- Aspect ratio : $\frac{L}{R_2 - R_1} = 4$

This geometry is chosen because it produces an analytical solution, which can thus be used to validate the simulation.

Analytical Solution The geometry and flow properties are set to fulfill all hypotheses for the simplified radial equilibrium.

Two configurations are considered, namely the free vortex flow (FVF) (Eq. 4.95) and the solid body rotation (SBR) (Eq. 4.96). The radial pressure profile is obtained by integrating Eq. 4.94 using the perfect gas relation to link density to pressure:

$$u_\theta = \frac{k}{r} \qquad\qquad P(r) = \alpha_1 \exp\left\{ \left(-\frac{k^2}{2r_{gas}T_s r^2} \right) \right\} \tag{4.95}$$

Or

$$u_\theta = C \qquad\qquad P(r) = \alpha_2 r^{\left(\frac{C^2}{r_{gas}*T_s}\right)} \tag{4.96}$$

α_1 and α_2 are integration constants that can be determined using the mean pressure on the outlet plane, $\bar{P}_s$.

$$\bar{P}_s = \frac{1}{A_{annulus}} \int\int P(r) r dr d\theta \tag{4.97}$$

Solving Eq. 4.97 for the two cases gives:

$$\alpha_1 = \frac{\bar{P}_s(R_2^2 - R_1^2)}{\{[(\frac{k^2}{2r_{gas}T})Ei[\frac{-k^2}{2r_{gas}Tr^2}] + r^2 \exp\left\{[\frac{-k^2}{2r_{gas}Tr^2}]\right\}]\}_{R_1}^{R_2}} \tag{4.98}$$

$$\begin{aligned}
\frac{1}{A_{annulus}} \int\int P(r) r dr d\theta &= \frac{2\pi\alpha_2}{\pi(R_2^2 - R_1^2)} \int_{R_1}^{R_2} r^{\left(\frac{C^2}{r_{gas}T_s}\right)} \times r dr \\
&= \frac{2\alpha_2}{(R_2^2 - R_1^2)} \int_{R_1}^{R_2} r^{\left(\frac{C^2}{r_{gas}T_s}+1\right)} dr \\
&= \frac{2\alpha_2}{(R_2^2 - R_1^2)} \frac{[r^{\left(\frac{C^2}{r_{gas}T_s}+2\right)}]_{R_1}^{R_2}}{\frac{C^2}{r_{gas}T_s}+2} \\
&= \bar{P}_s
\end{aligned}$$

It is then possible to isolate α_2:

$$\alpha_2 = \frac{\bar{P}_s(R_2^2 - R_1^2)(\frac{C^2}{r_{gas}T_s} + 2)}{2[r^{\left(\frac{C^2}{r_{gas}T_s}+2\right)}]_{R_1}^{R_2}} \tag{4.99}$$

With the usual notation $[\phi(r)]_a^b = \phi(b) - \phi(a)$, $Ei(x)$ is the exponential integral function defined as $Ei(x) = \int_{-\infty}^{x} \frac{e^t}{t} dt$.

The target pressure is $\bar{P}_s = 1 \cdot 10^5$ Pa. The shape of the pressure profile, governed by radius-dependent terms, is controlled by gas properties and by swirl profile $u_\theta(r)$.

Numerical Resolution The swirling flow is simulated for six values of the outlet reflection coefficient $K_{cbc} = \frac{\sigma_{cbc}(1-Ma^2)c}{R_2-R_1}$, ranging from 1 to 1000, to assess the influence of the level of reflectivity on the radial equilibrium pressure profile. The coefficient

K_{cbc} is determined from the Mach number, the characteristic length of the outlet, and σ_{cbc} imposed by the user. The annulus geometry is discretized with 50 points in the radial direction and 200 in the longitudinal direction. This is equivalent to a mesh size $\Delta x = 1.6 \times 10^{-3} m$ and a time step $\Delta t = 2.66 \times 10^{-6} s$. The Euler equations' physical behavior is retrieved by setting the viscosity to zero to be coherent with the simplified radial equilibrium's inviscid assumption. The summary of the test cases can be found in Table 4.1.

σ_{cbc} (FVF)	2.52×10^{-4}	1.26×10^{-3}	6.30×10^{-3}	1.26×10^{-2}	1.26×10^{-1}
σ_{cbc} (SBM)	2.43×10^{-4}	1.21×10^{-3}	6.06×10^{-3}	1.21×10^{-2}	1.21×10^{-1}
$K_{cbc} = \frac{\sigma_{cbc}(1-Ma^2)c}{R_2-R_1}$	1	5	25	50	500
Flow through times FVF	0.76	0.76	0.64	0.42	0.42
Flow through times SBR	4.11	4.11	2.25	1.8	0.91

Table **(4.1)** – Summary of the parameters used during the simulations.

The inlet boundary condition imposes the adequate swirl profile $u_\theta(r)$ by imposing the corresponding total pressure and azimuthal angle. The axial velocity is set to $u_x = 5\,\mathrm{m{\cdot}s^{-1}}$ for the FVF case or $u_x = 30\,\mathrm{m{\cdot}s^{-1}}$ for the SBR one. The corresponding flow through times is noted τ and defined as $\tau = \frac{L}{u_x}$. The maximum Mach number during the computation is 0.29 for the FVF case and 0.17 for the SBR. The initial velocity field in the annulus is identical to the inlet boundary condition velocity profiles u_x, u_θ. At the outlet, the NSCBC 3D boundary condition is used with an imposed pressure $\bar{P}_s$. The inner and outer walls use slip conditions to avoid any near-wall effect on the velocity profile and, thus, pressure distribution. The initial pressure field is uniform such that $P(r, \theta, x) = \bar{P}_s$ and is thus not consistent with the REA to ensure that the NSCBCs can drive the pressure toward the REA.

To avoid using a rotational domain, the azimuthal velocity u_θ is specified in the Cartesian coordinates at the inlet according to:

$$u_y = -u_\theta \sin(\theta) \qquad\qquad u_z = u_\theta \cos(\theta) \tag{4.100}$$

The required time to establish the pressure field is imposed by the domain size, flow properties, and relaxation parameter σ_{cbc}. Convergence is reached when the local pressure is $\pm 0.1\%$ of $P(t \to \infty)$. Increasing the relaxation parameter σ_{cbc} reduces the convergence time. The pressure profile is only radius-dependent (one-dimensional flow), so it can be plotted at the domain exit. The simulations converge toward the theoretical profile as the relaxation coefficient at the outlet is increased. The relaxation coefficient σ_{cbc} mainly drives the mean pressure toward the target. For $\sigma_{cbc} \to \infty$, the mean pressure would converge to the imposed value, and thus the pressure profile would exactly match the theoretical one. However, in this case, the boundary would become fully reflecting. The pressure profile is plotted at the domain exit in Fig. 4.14. It can be seen that a radial equilibrium pressure profile is established at the end of the simulation and that the profiles converge toward the analytical profile as the relaxation parameter at the outlet increases.

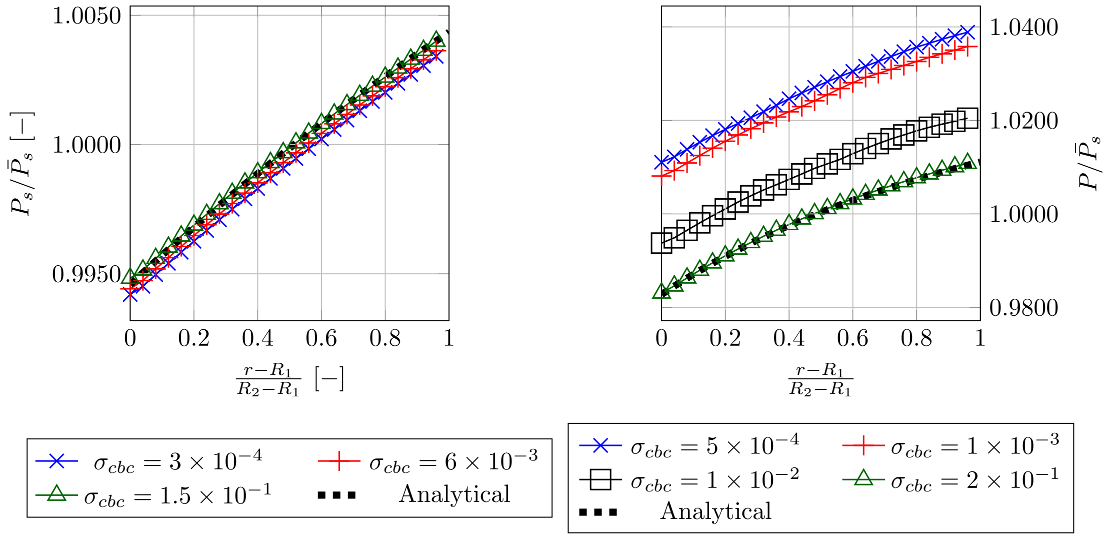

Figure **(4.14)** – Results for the Solid Body Rotation (left) and Free Vortex Flow (right).

The role of the relaxation coefficient is, as explained before, to drive the static pressure toward the target. The offset reduction between the mean pressure and the target when increasing σ_{cbc} is illustrated in Fig. 4.15. It can be seen that the error is inversely proportional to σ_{cbc}.

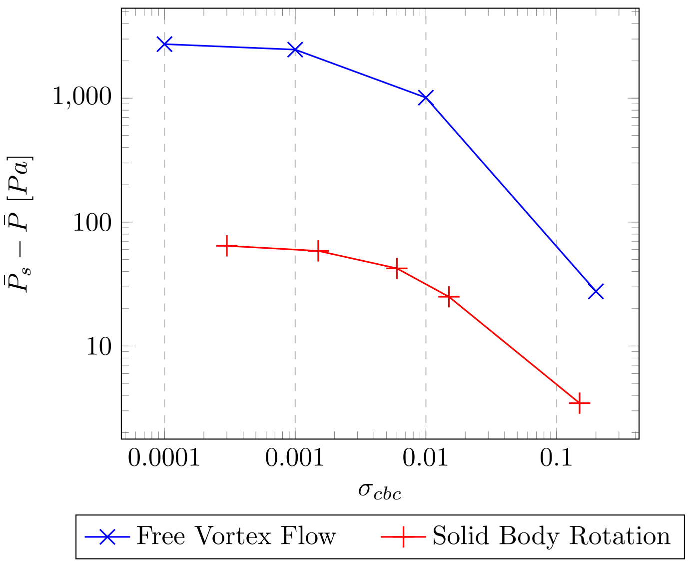

Figure **(4.15)** – Illustration of the convergence towards the target pressure with increasing relaxation parameter σ_{cbc}.

4.6 Valve Law Strategy to Reach the Mass-Flow Rate

This section details the approach adopted to implement a valve law on the outlet boundary condition. The idea is that, in practice, as the total pressure and total temperature are imposed at the inlet, the mass flow obtained in the turbomachine is prescribed by adjusting the outlet static pressure. The issue is that this static pressure is unknown a priori and will depend on the pressure losses generated in the system or the work exchange with the flow. The user must manually find a correct value until the target mass flow is reached. When several operating points are to be simulated, this approach is not practical and too costly. To solve this problem, the valve law formulation adopted is derived from Duchaine and Gicquel [152]. The mass-flow rate is evaluated on a specified period noted N_{update}. Then the outlet static pressure applied at the boundary is corrected using the averaged static pressure outlet, $\bar{P}_s$, averaged mass-flow rate, $\bar{Q}$, and the target mass-flow Q_{target}. The term κ is a relaxation parameter expressed in $\mathrm{m}^{-1} \cdot \mathrm{s}^{-1}$.

$$P_{s,update} = \bar{P}_s + \kappa(\bar{Q} - Q_{target}) \tag{4.101}$$

This approach is evaluated on a test case that consists of a simple S-duct geometry. At the inlet, uniform total pressure and total temperature are imposed with no flow angles. The static pressure is set to $10^5 Pa$ at the outlet by default. A first simulation in these conditions is run, corresponding to the *Without Valve Law* results presented in Fig. 4.16. It illustrates that without valve law, the desired mass flow is not reached, and this would require new computations where the user manually adapts the static outlet pressure. This is inefficient if numerous computations are launched where physical or numerical parameters are modified, leading to potentially significant changes in the pressure losses occurring in the machine.

A second simulation is performed where the valve law is activated. The dynamic pressure adaptation is activated after one rotation so that the transient part of the simulation is passed and the mass flow is converged. The update period is chosen according to Eq. 4.102. The first term represents the time for the information to go from the inlet to the outlet with the average velocity of the flow $\overline{u}$. The second one is the time necessary for the waves coming from the outlet to reach the inlet and ensure that both LODI conditions are adapted.

$$N_{update} = \frac{x_{outlet} - x_{inlet}}{\overline{u}} + \frac{x_{outlet} - x_{inlet}}{(c - \overline{u})} \tag{4.102}$$

The relax coefficient κ is fixed to $250\,\mathrm{m}^{-1} \cdot \mathrm{s}^{-1}$. It is determined so that the global term $\kappa(\bar{Q} - Q_{target})$ is around 50 to $150 Pa$. When the valve law is applied, the target mass flow is reached, even though some oscillations can happen during the convergence due to the adapting pressure. This validates the methodology and will be applied in future turbomachinery simulations unless specified otherwise.

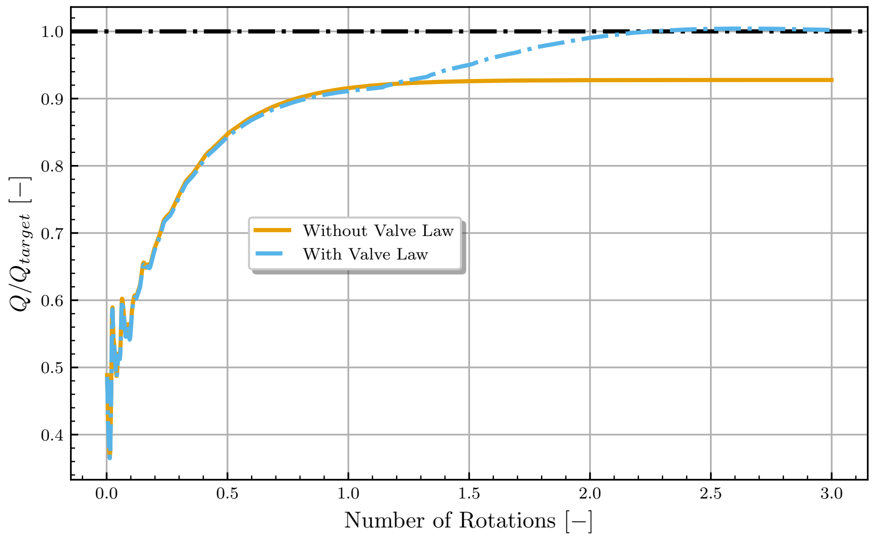

Figure **(4.16)** – Mass-flow rate time evolution, with and without valve law.

4.7 Chapter Summary

The primary results taken from this chapter are the following:

1. Suitable boundary conditions using the NSCBC formulation have been developed in a compressible LBM framework to tackle the simulation of complex turbomachinery flows.

2. The inlet condition has been validated on several academic test cases where several conclusions can be drawn concerning the choice of the relaxation parameter. The first test case shows that the recommended range for the relaxation parameter is between 10^3 and 10^4. These values allow to correctly converge towards the target in a reasonable physical time while keeping a low reflectivity. Choosing a value higher than 10^4 may also lead, in some cases, to stability issues. Moreover, it has been illustrated that uniform values or radial profiles of P_t, T_t, α, and ϕ, with or without turbulence injection, can be imposed at the inlet leading to an adequate inlet condition for turbomachinery simulations.

3. The NSCBC formalism applied on an outlet condition is compatible with strongly rotating flows usually found in turbomachinery. A relaxation coefficient around 0.2 leads to a pressure profile at the outlet close to the one predicted by the theory.

4. A valve law strategy has been implemented and validated to allow a fast convergence towards the target mass flow, another primary requirement for proper turbomachinery simulations.

   This concludes the first part of this Ph.D. which consisted of developing the necessary boundary conditions to perform S-ducts simulations.

Chapter 5: Simplified Studies of the Academic Configuration AIDA CAM1

This chapter presents different studies based on the academic configuration of interest AIDA CAM1. The goal here is to establish the capacity of the ProLB software to simulate the desired configuration and to define best practices useful to conduct S-duct simulations. To do so, several functionalities are studied and validated independently to pave the way for the physical study of the academic configuration.

Contents

5.1 The AIDA Project

Firstly, the AIDA project (Aggressive Intermediate Duct Aerodynamics for competitive & environmentally friendly jet engines) from which the academic case is taken is described. This project aimed to strengthen the competitiveness of European aircraft engine manufacturers and decrease environmental impact through the achievement of the following technical objectives:

- Improved understanding of flow physics in aggressive intermediate ducts.
- System integration.
- Knowledge of how aggressive ducts interact with neighboring components.
- Development and tests of a new class of very aggressive intermediate ducts.
- Assessment of new advanced vane-duct integration concepts.
- Establishment of validated analytical methods and Computational Fluid Dynamic (CFD) best practice.
- Tests and modeling of novel passive separation control devices for super-aggressive ducts.
- Development of new numerical optimization techniques for intermediate ducts.
- Establishment of design rules and a validation database for aggressive ducts.

The objectives of this project were ambitious, with a target of 20% shorter ducts or 20% increase in duct radial offset or 20% increase in duct diffusion rate together with 50% reduction in duct design lead time. These changes would enable a $1 - 2\%$ reduction in engine weight and length and a $0.5 - 1.5\%$ increase in compressor and turbine efficiency. These modifications would translate into improvements in aircraft systems, leading to a 2% reduction in fuel burn and $C0_2$ emissions. On the financial side, this represents a 5% reduction in engine development costs and a 10% cut of engine time-to-market [23].

5.1.1 Description of the Configuration

Several S-ducts were computed and tested during the AIDA project. After a review of all the configurations and in accordance with the aerodynamic experts of Safran Aircraft Engines, the CAM1 configuration tested at Cambridge University appeared to be the most relevant case due to its representative aerodynamic loading and the numerous experimental measurements available. The experimental machine is illustrated in Fig. 5.1, and a scheme of the machine is drawn in Fig. 5.4 with a highlight of the control planes where aerodynamic values were measured. The main characteristics of the CAM1 geometry regarding non-dimensional parameters and operating conditions are presented in table 5.1. Using the definition in Eq. 2.12, the duct loading value of CAM1 is computed and represented in Fig. 5.2 and shows a high value compared to other current engines, making it an a priori good candidate to conduct the study. The design point corresponds to a Reynolds number of 1.55×10^5 based on the vein height and inlet velocity.

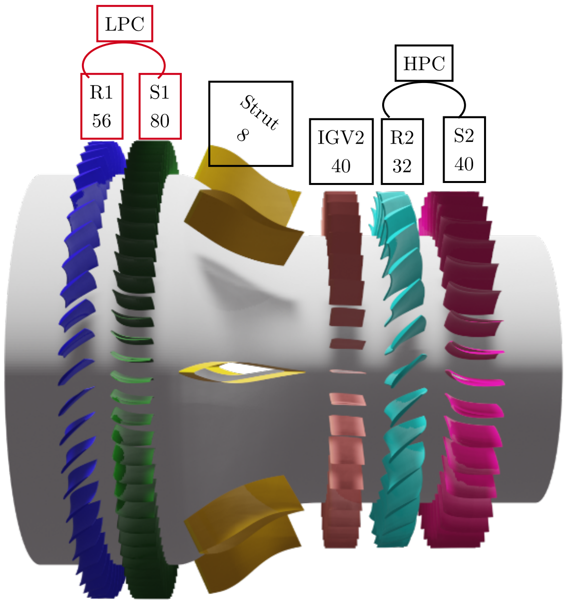

Figure **(5.1)** – CAM1 experimental installation.

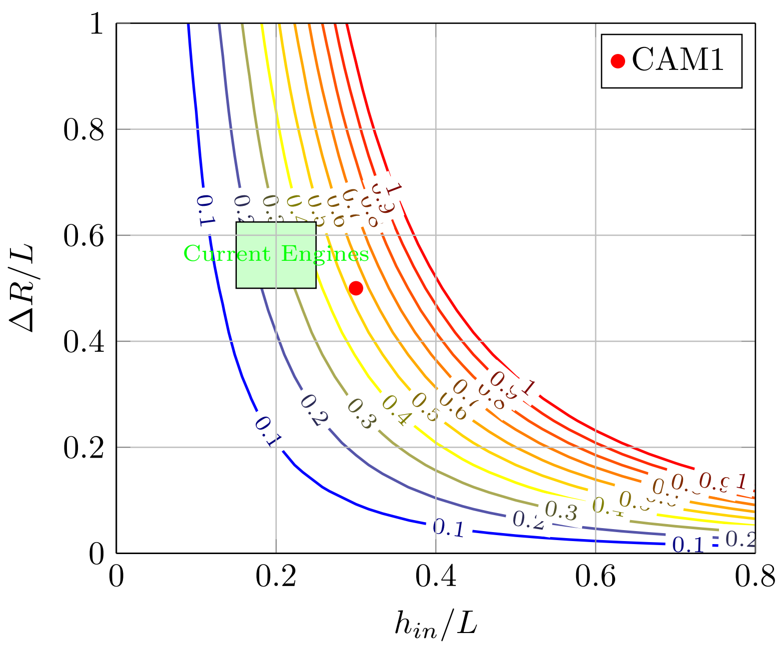

Figure **(5.2)** – CAM1 aerodynamic duct loading.

R1 (rpm)	R2 (rpm)	$\frac{A_{out}}{A_{in}}$	$\frac{h_{in}}{L}$	$\frac{\Delta R}{L}$	$\frac{t}{c}$
2850	3800	1	0.3	0.5	0.2

Table **(5.1)** – Characteristics of the CAM1 geometry and operating conditions.

An exhaustive experimental database is available for this configuration. The measured physical quantities at each control plane are listed below, and the velocity triangle is illustrated in Fig. 5.3:

- P_t/P_{ref}
- P_s/P_{ref}
- Absolute angle, α
- Relative angle, β
- Radial flow angle, ϕ
- Meridional velocity, V_m
- Axial velocity, V_x
- Absolute circumferential velocity, V_θ

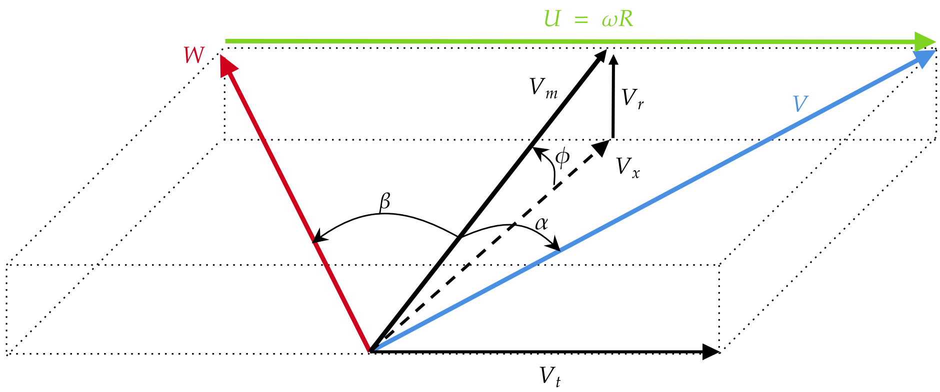

Figure **(5.3)** – Illustration of the measured quantities.

These data were acquired at different control planes between the rows illustrated in Fig. 5.4. It should be noted that no data is available inside the duct because of the intrusiveness of the measurement systems.

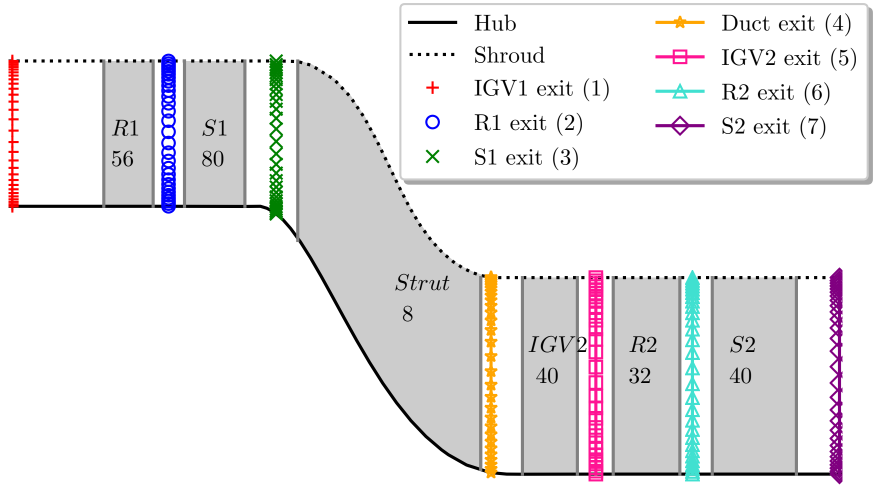

Figure **(5.4)** – Scheme of the full CAM1 configuration.

The experimental data were measured at these different planes using a 5-hole pressure probe on a grid of 72 angulars and 30 radial positions across a 30° sector. These measurements give access to a time-averaged contour map of several macroscopic quantities. Because of the time averaging, the measurements can not show the rotor wakes passing at the interface.

5.1.2 Previous RANS Studies

Reynold Averaged Navier-Stokes (RANS) computations were performed at Safran Aircraft Engines on this configuration and will be used for comparison. The elsA (ONERA) software [153, 154] was used with the RANS model on a structured mesh with an appropriate mesh resolution close to the walls ($y^+ = 1$). For the boundary conditions, radial profiles of total pressure, temperature, and flow angles have been imposed at the inlet. At the outlet, a radial equilibrium was set. The computations were run on a periodic sector representing $1/8^{th}$ of the geometry. No mixing planes were used except when the R1 or R2 rotors were included in the simulation.

5.2 A Priori Difficulties to Simulate the CAM1 Configuration

From the previous sections introducing the CAM1 case, several difficulties can be highlighted concerning the setup and simulation and are enumerated here:

1. As for any turbomachinery simulation, the computation of the mass flow is required with a high level of accuracy. This problem is not trivial when treating annulus geometries with Cartesian grids. There is a need to evaluate the precision reached by the solver as it is used in the valve law and characterizes the operating point.
2. Overall, the configuration is quite complex, with several rows, a large number of blades, and only a few similar simulations [155] have been performed with the Lattice Boltzmann Method (LBM) to draw guidelines on the meshing strategy.

3. Turbulence is of significant importance in turbomachinery applications, and there is a need to specify an appropriate turbulence injection to recover the proper flow behavior.

4. It has been observed in the literature that the LBM shows isotropy issues using the $D3Q19$ lattice. It is desired to know the level of isotropy and if the effect can be damped.

5. Finally, rotors need to be included in the setup. This raises questions about the accuracy of the results when a rotating interface is included and if the rotor tip gap can be considered in the simulations.

To address these different issues, several test cases are built in the following. The goal is to validate the functionalities step-by-step and draw guidelines and best practices that will be applied to the 360° computations for physical analysis.

5.3 Computation and Imposition of the Mass Flow

This section presents the potential issues when computing the mass flow using a Cartesian grid. Mass flow is essential for turbomachinery applications as it characterizes the machine's operating point. Moreover, the accuracy expected is very challenging, under 1%. Thus it is interesting to investigate if the solver can retrieve the correct level of precision on the mass flow. First, the issue of computing the mass flow on a Cartesian grid where a circular geometry is involved is illustrated in Fig. 5.5. Because of the Cartesian grid and the cut-cell approach, a stair-case approximation is obtained near the solid wall surface, and the geometry is not body-fitted. This leads to an error on the fluid surface considered in the simulation.

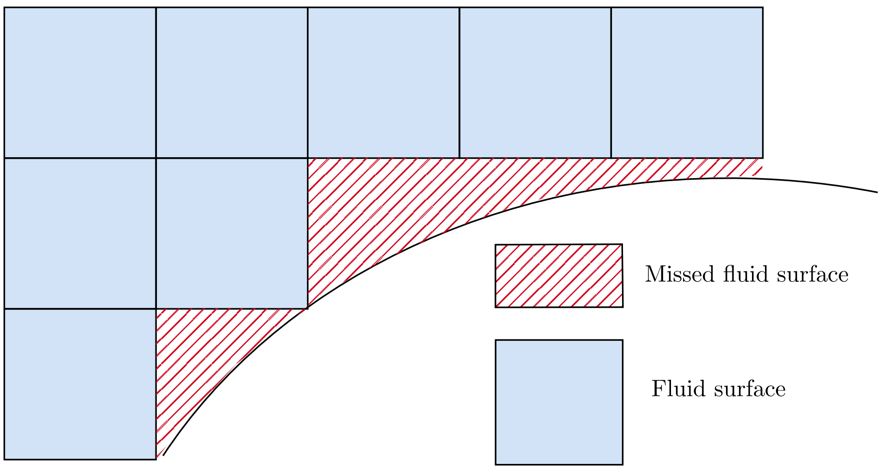

Figure **(5.5)** – Standard mass flow evaluation on a Cartesian grid.

The formulation of the problem is the following. Considering that the valve law described previously (see Chapter 4) will be activated for all the simulations, the mass flow has to be evaluated during the computation using the solver functionality. It is thus necessary to evaluate the level of accuracy reached using the direct solver computation.

5.3.1 Mass Flow Integration of the Solver

Only the values at the LBM points are known in the code, and no mesh is defined between the points and the wall surface. Two possible integration methods are then possible: cell center or cell vertices. When using the solver functionality, a cell center approach is applied. The second method would correspond to post-treatment uses of the Antares or Paraview software. Fig. 5.6 illustrates the two methodologies leading to different mass flow results. The problem is expected to be naturally reduced when refining close to the wall. Moreover, considering that the walls have no-slip conditions for the involved computations, the boundary points' velocity is relatively low, and their weight in the mass flow computation should be limited.

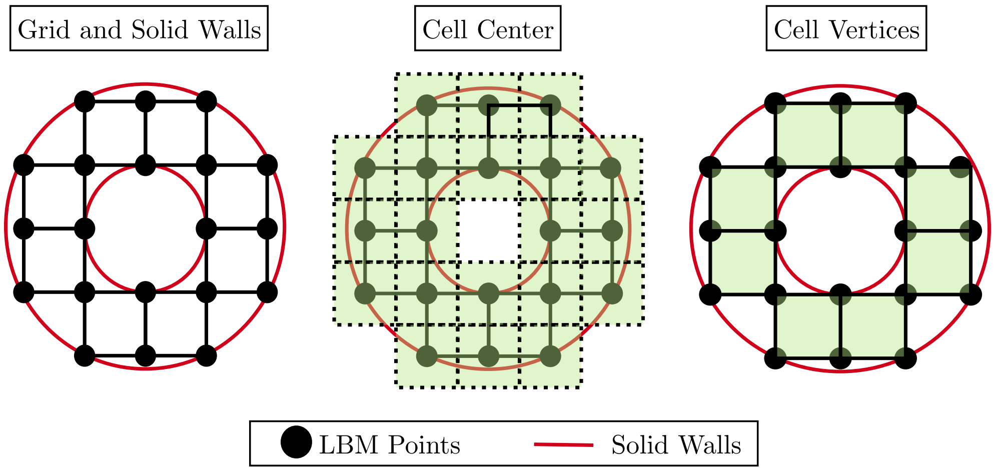

Figure **(5.6)** – Standard mass flow evaluation on a Cartesian grid for an annular geometry.

In version 2.8.0 of ProLB, the integration is performed on a volume (V) that will be multiplied by a known surface (A) of the geometry specified by the user. The volume (V) is time-averaged to obtain an average value of $(\rho u)_{ax}$.

$$\dot{m} = A\frac{1}{V}\int_V (\rho u)_{ax} dV \tag{5.1}$$

Special care of the user is necessary to decide the averaging volume. Indeed, when mesh refinements near walls are used, a mesh similar to the one illustrated in Fig. 5.7 can be obtained:

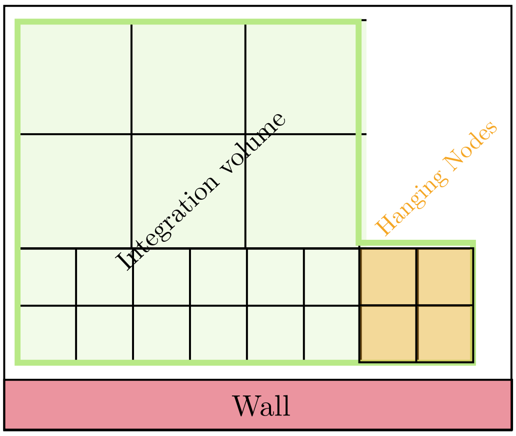

Figure **(5.7)** – Issues when computing the mass flow with mesh refinements.

In this case, "hanging" fine nodes are at the volume limit. These nodes will give additional weight to the points closer to the wall, leading to underestimating the mean momentum. To avoid this problem, a longer integration volume can be chosen in the axial direction or using a uniform integration volume.

5.3.2 Exact Mass Flow Computation in Post-Processing

An additional approach has been studied to compare the mass flow obtained during the computation using the embedded functionality to the target value. As the mass flow uncertainties come from a lack of precision concerning the geometry, the idea here is to reconstruct the missing values close to the walls. To do so, the density, as well as the velocity, are saved on the inner and outer walls (hub and shroud) as well as on the cut plane. Then, a post-processing script will create a Delaunay triangulation between the hub, shroud, and cut plane. This results in a unique mesh that fits the geometry (see Fig. 5.8). For the new elements created by the triangulation, values are assigned by interpolating the ones taken from the hub and shroud surface.

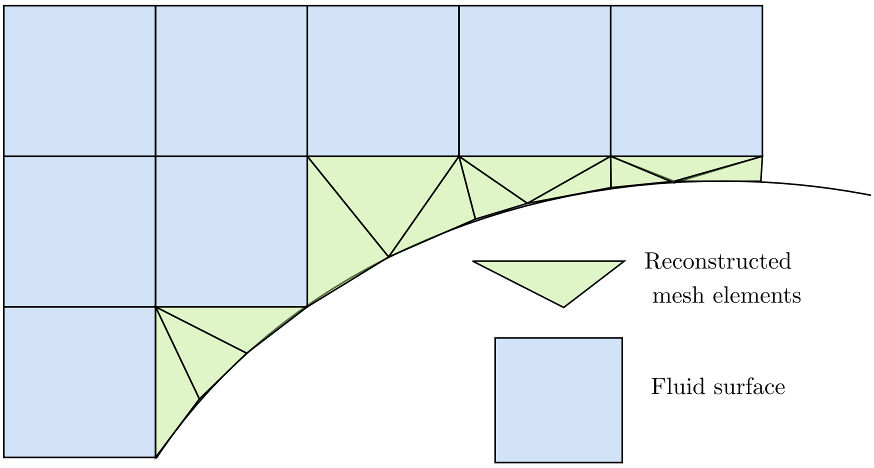

Figure **(5.8)** – Reconstruction of the values close to the walls.

5.3.3 Case Set Up

To evaluate the mass flow computation, a test case consisting of simple annulus geometry is set with a length $L = 0.3\,\mathrm{m}$, an internal radius $r_{in} = 0.19\,\mathrm{m}$ and an outer radius $r_{out} = 0.254\,\mathrm{m}$. Air at $291\,\mathrm{K}$ is injected with an uniform inlet velocity of $50\,\mathrm{m} \cdot \mathrm{s}^{-1}$ and a corresponding density of $1.2\,\mathrm{kg} \cdot \mathrm{m}^{-3}$ for a target mass flow $Q_{target} = 5.346\,\mathrm{kg} \cdot \mathrm{s}^{-1}$. Several mesh sizes Δx are tested in the following. The mass flow reached is compared to the target. The physical parameters are chosen to be close to the ones encountered in the CAM1 configuration. Moreover, the case also represents characteristic vein height and mesh size at the wall so that the conclusions drawn regarding mass flow precision can be easily reported.

5.3.4 Mass Flow Computation Accuracy

Computations are run with the issue of the hanging nodes not corrected (HN) and then without hanging nodes (no HN) by applying a uniform refinement in the slab where the mass flow is evaluated. The results are presented in Tab. 5.2 in terms of mass flow reached at convergence and deviation compared to the target $Q_{target} = 5.346\,\mathrm{kg} \cdot \mathrm{s}^{-1}$:

Mesh (mm)	2	1	0.5	0.25
Mass Flow (HN) $(\mathrm{kg} \cdot \mathrm{s}^{-1})$	5.113	5.236	5.297	5.337
Mass Flow (no HN) $(\mathrm{kg} \cdot \mathrm{s}^{-1})$	5.210	5.319	5.331	5.338
Mass Flow (Post-Proc) $(\mathrm{kg} \cdot \mathrm{s}^{-1})$	5.301	5.320	5.332	5.339
Deviation HN to target (%)	−4.35	−2.05	−0.84	−0.17
Deviation no HN to target (%)	−2.54	−0.505	−0.28	−0.15
Deviation Post-Proc to target (%)	−0.91	−0.48	−0.26	−0.13

Table **(5.2)** – Evolution of the mass flow prediction with varying wall resolutions and integration methods.

The mass flow prediction generally remains slightly underestimated using the solver functionality or the mass flow reconstruction methodology. The error is progressively reduced as the mesh is refined near the wall as expected, and the difference between the solver prediction and the post-processing one becomes negligible for $\Delta x \leq 1\,\text{mm}$. Moreover, the error created by the additional weight of the hanging nodes also diminishes with the mesh size but remains non-negligible until the finest mesh size is used.

5.3.5 Mass Flow Conservation

To ensure that no mass leakage or creation happens in the simulations, the mass flow is evaluated on the same annulus geometry at three different axial positions $x_0 = 0.01\,\text{m}$, $x_1 = 0.15\,\text{m}$ and $x_2 = 0.25\,\text{m}$. The computation is run with a mesh size of 0.5 mm and a uniform refinement in the control volumes to ensure no hanging nodes are present. Table 5.3 shows the mass flow computed at the last time step for the different control planes. It shows that a close value of mass flow is retrieved at the different axial positions with a deviation smaller than the accuracy of the mass flow integration. This confirms that no mass leakage or creation is occurring during the simulations.

Axial Position (m)	0.01	0.15	0.25
Mass Flow $\left(\text{kg} \cdot \text{s}^{-1}\right)$	5.334198	5.332526	5.331391
Deviation between planes (%)	Ref	-0.03	-0.05

Table **(5.3)** – Mass flow at the different axial positions taken at the last time step.

From this study, it is concluded that to compute the mass flow with the desired systematic accuracy of under 1%, a mesh size under 0.5 mm is required at the wall combined with a control volume that does not show hanging nodes. This mesh size corresponds to a y^+ of less than 100. These guidelines will be used in the following applications when mass flow convergence is required and when the valve law is activated.

5.4 Grid Generation

This section describes the process of obtaining a good-quality mesh for the computations. To do so, an Adaptative Mesh Refinement (AMR) methodology based on the LIKE criterion [156] and the y^+ number is used and detailed in the following. The idea is to develop a methodology that allows generating a mesh that captures the correct physical phenomena to obtain an accurate loss level while keeping the number of elements as low as possible to have a competitive computational time.

This approach is particularly suitable when the physics studied is complex and interest zones can not be guessed precisely in advance. When talking about refinement strategies, the procedure can be either dynamic, meaning that it is done during the computation based on an instantaneous quantity of interest $q(t)$, or static, when an averaged value of interest $\tilde{q}$ is extracted and an other mesh is built a posteriori. The latter approach has been chosen as it is easier to implement, and the mesh obtained is independent of the initial solution.

5.4.1 Details on the LIKE Criterion

The global strategy of the AMR is structured as:

- A first computation with a coarse mesh of cell size Δx_0 is performed. Instantaneous macroscopic fields of density and velocity are saved at the end of the computation to be used as the initialization for the following computation. The chosen criterion is computed from the averaged macroscopic quantities in the fluid simulation domain.
- From this criterion, a surface is extracted and imported into the solver, where a refinement zone can be applied.
- Then, a refined simulation with $\Delta x \leq \Delta x_0$ applied on this specific zone is performed.

This strategy offers several advantages, such as:

- Overcome the definition of refinement zones based on simple geometrical shapes (cylinders or boxes).
- Use simultaneously several refinement criteria.
- Optimize the number of cells and improve computation time.

The different steps of this procedure are then repeated until the criterion highlights no more refinement zones. The main question remains how to choose the quantity of interest for this criterion? The choice here was to base the criterion on a physical quantity linked to the kinetic energy dissipation called Ψ. It is linked to the pressure loss expected in the system. For a compressible flow, it is written according to Eq. 5.2:

$$\Psi = \nu_t \left[\frac{4}{3} + \epsilon_{\alpha\beta}\left(\frac{\partial u_{\alpha\beta}}{\partial x_\alpha} + \frac{\partial u_\beta}{\partial x_\alpha}\frac{\partial u_\alpha}{\partial x_\beta} - \frac{2}{3}\frac{\partial u_\alpha}{\partial x_\alpha}\frac{\partial u_\beta}{\partial x_\beta}\right)\right] \tag{5.2}$$

where $\epsilon_{\alpha\beta}$ is the Levi-Civita symbol in two dimensions and $\nu_t = \nu + \nu_{sgs}$ is the total viscosity composed of the fluid viscosity ν and the viscosity induced by the sub-grid modeling ν_{sgs}. From this definition, a non-dimensional, temporally averaged value is computed and corresponds to the LIKE criterion, noted $\bar{\Psi}$ (Eq. 5.3). This approach has been applied previously and has shown its advantages [157].

$$\bar{\Psi} = \left(\frac{\bar{\Psi} - \bar{\Psi}_{min}}{\bar{\Psi}_{max} - \bar{\Psi}_{min}}\right)^p \tag{5.3}$$

where p regulates the variation of $\bar{\Psi}$ into the interval $[0, 1]$. In the following, $p = 0.1$ and it has been observed that a variation of p between 0.05 and 0.25 didn't change significantly the results.

At the same time that the LIKE criterion is used in the wakes, the wall surfaces are refined using a y^+ criterion that ensures that a uniform value of around 70 is obtained on the walls. The non-dimensional distance to the wall is defined as:

$$y^+ = \sqrt{\frac{\tau_w}{\rho}}\frac{y}{\nu_t} \tag{5.4}$$

5.4.2 Application of the AMR Methodology on an Isolated Blade

5.4.2.1 Use of the LIKE Criterion

The criterion is used primarily in the wake zones of the different blades to correctly capture the wakes generated while the y^+ criterion is applied on the walls. It would be too costly to demonstrate this methodology on a 360° geometry, so a simplified test case where only one blade is included is set up instead. The blade chosen from the S1 stage is critical for the CAM1 configuration. Indeed, the S1 blades have the strongest curvature compared to the other blades and, as it was shown in the literature review [23], the wakes of this row placed upstream of the duct have to be correctly predicted to obtain an accurate flow description and loss level in the duct. The simplified test case is conceived as a linear cascade with only one S1 blade as sectorial periodic conditions are not available (see Fig. 5.9).

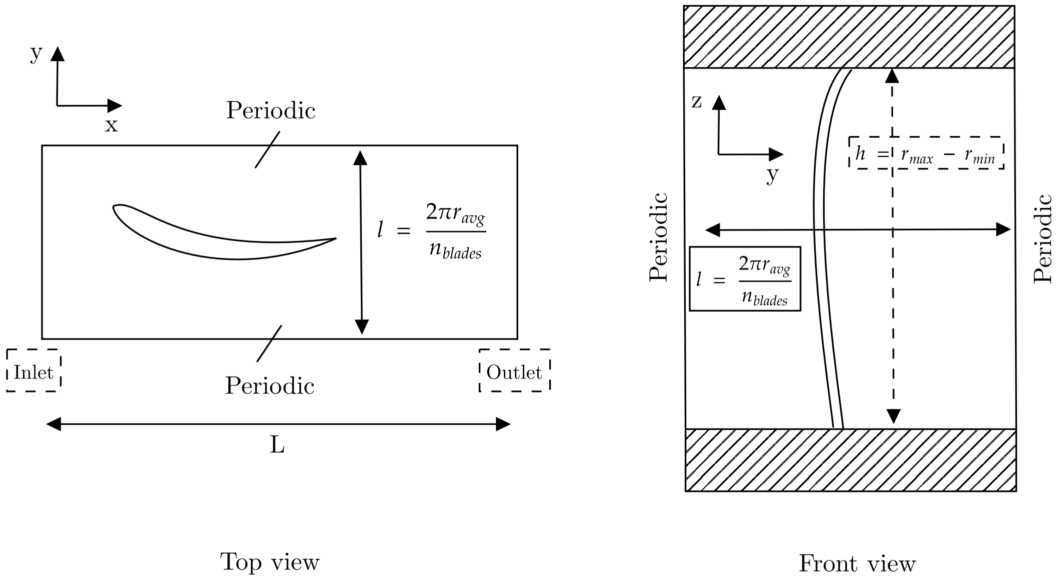

Figure **(5.9)** – Scheme of the linear cascade for the S1 blade.

The inlet corresponds to the R1 exit plane (2), while the outlet is placed one chord away from the S1 exit (3) plane to avoid any interactions. At the inlet, radial profiles taken from the experimental data are imposed in terms of total pressure, total temperature, and flow angles. Static pressure is imposed at the outlet to obtain the correct mass flow. The top and bottom walls are considered adiabatic, while the boundaries in the azimuthal direction are periodic.

With this setup, several computations are run and are referred to as cases (A) to (D). The mesh is uniform with the corresponding mesh size being 0.752 mm, 0.376 mm, 0.188 mm, 0.094 mm. The simulations are run for a physical time corresponding to the equivalent of two rotations of the R1 rotor that would be placed upstream. The statistics are taken during the last rotation. Fig. 5.10 illustrates the mass flow convergence for the different cases and shows that all cases converge towards the target mass flow, thus allowing a fair comparison at the desired operating point. The relative difference to the target is summed up in Table 5.4:

Case	A	B	C	D
Mesh size [mm]	0.752	0.376	0.188	0.094
$(Q - Q_{target})/Q_{target}(\%)$	-1%	$+0.65\%$	-0.39%	$+0.12\%$

Table **(5.4)** – Mass flow error compared to the target.

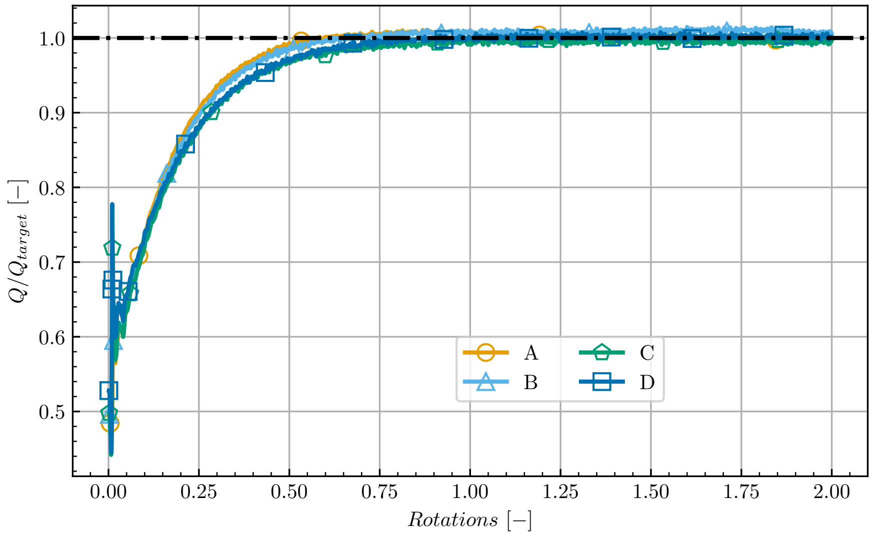

Figure **(5.10)** – Mass flow convergence of cases A to D.

The results are then illustrated in terms of a contour of LIKE criterion at the stator exit in Fig. 5.11. It shows that the LIKE criterion is diminishing as the mesh is refined progressively in the wake region of the stator blade. Moreover, the high value of LIKE criterion in the hub and shroud boundary layers is also significantly reduced.

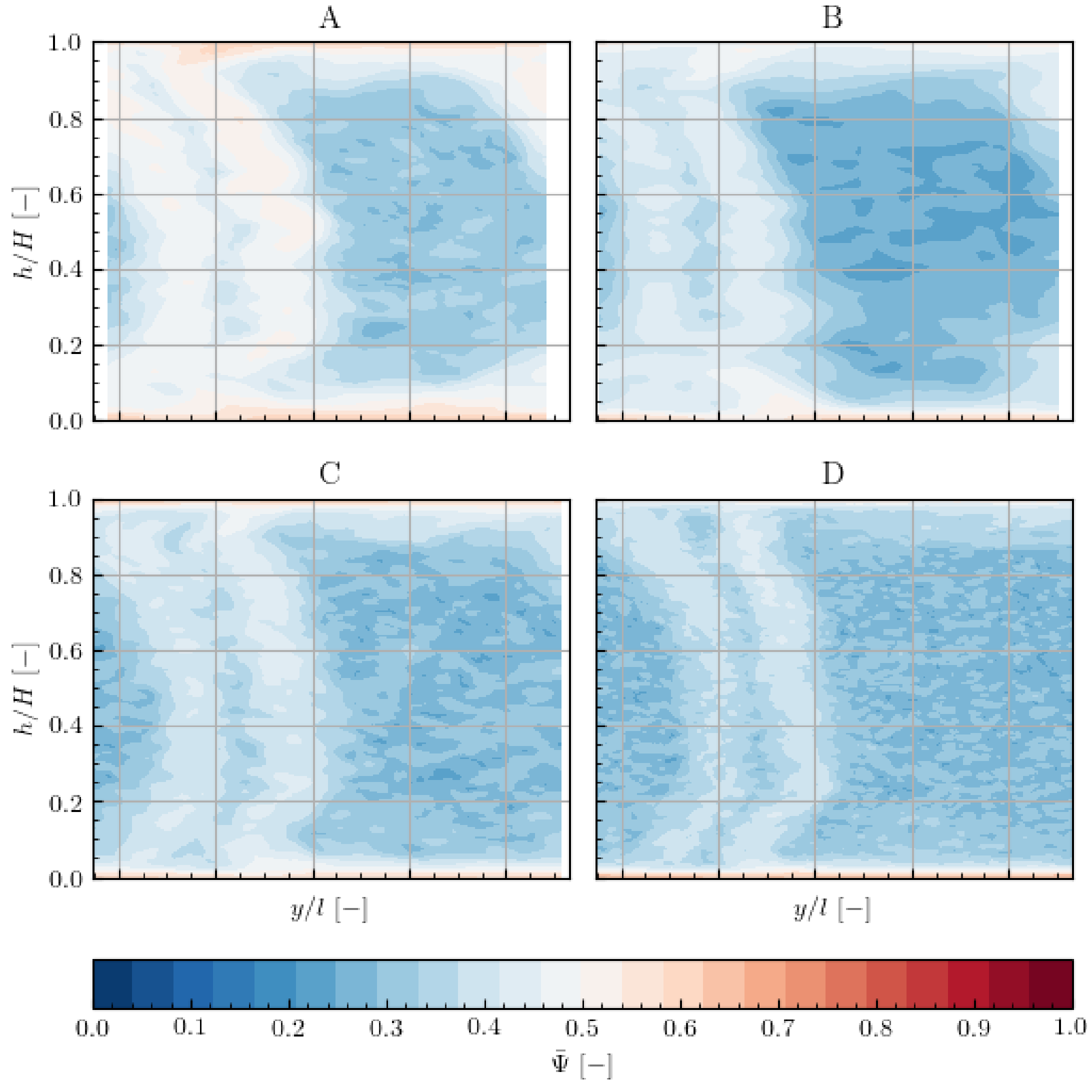

Figure **(5.11)** – Evolution of the LIKE criterion at the stator exit for cases A to D.

A threshold is applied on the LIKE volume output to extract the appropriate refinement zone to keep areas where the criterion is above 0.7 [156]. This gives access to the general shape of the wake to extract to create a refinement zone specific to the S1 blade, as illustrated in Fig. 5.12.

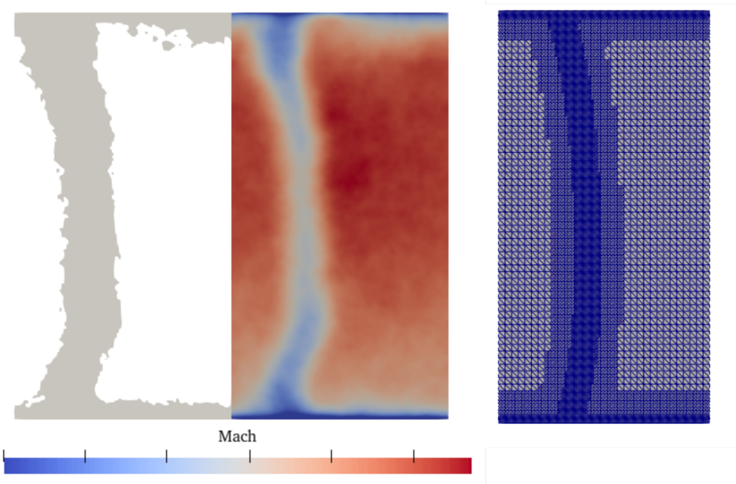

Figure **(5.12)** – Illustration of the mesh refinement in the S1 wake region: LIKE surface extracted on the left and S1 wake in the middle and corresponding mesh on the right.

From this study, it is concluded that a mesh size of 0.376 mm is recommended in the wake region to reach a sufficiently low level of LIKE criterion in the wake. Indeed, case B shows a maximal value of the criterion under 0.7 found in the literature [156]. Moreover, extracting the wake shape using a threshold filter is easy and allows for a precise definition of the refinement region. Finally, the mesh resolution chosen allows discretizing the wake with at least 20 points in the azimuthal direction across the wake.

5.4.2.2 Use of the y^+ Criterion

In the previous section, the focus was placed on obtaining a mesh resolution in the fluid domain adapted to capture the wake produced by the stator blade in terms of LIKE criterion value. This section illustrates the work performed to choose the mesh resolution on the blade to obtain the best quality wake. Indeed, it has been observed during the first simulations that the flow developing around the blade is very sensitive to the meshing strategy. In some cases, this would lead to flow separation happening too early on the blade suction side, creating especially large wakes and thus largely overestimated losses.

The same cases (A) to (D) are used here, and their respective y^+ values obtained are illustrated in Figs. 5.13-5.14. It shows that the y^+ decreases with the mesh size as expected and that the values on the suction side are larger than on the pressure side due to the difference in velocity around the blade.

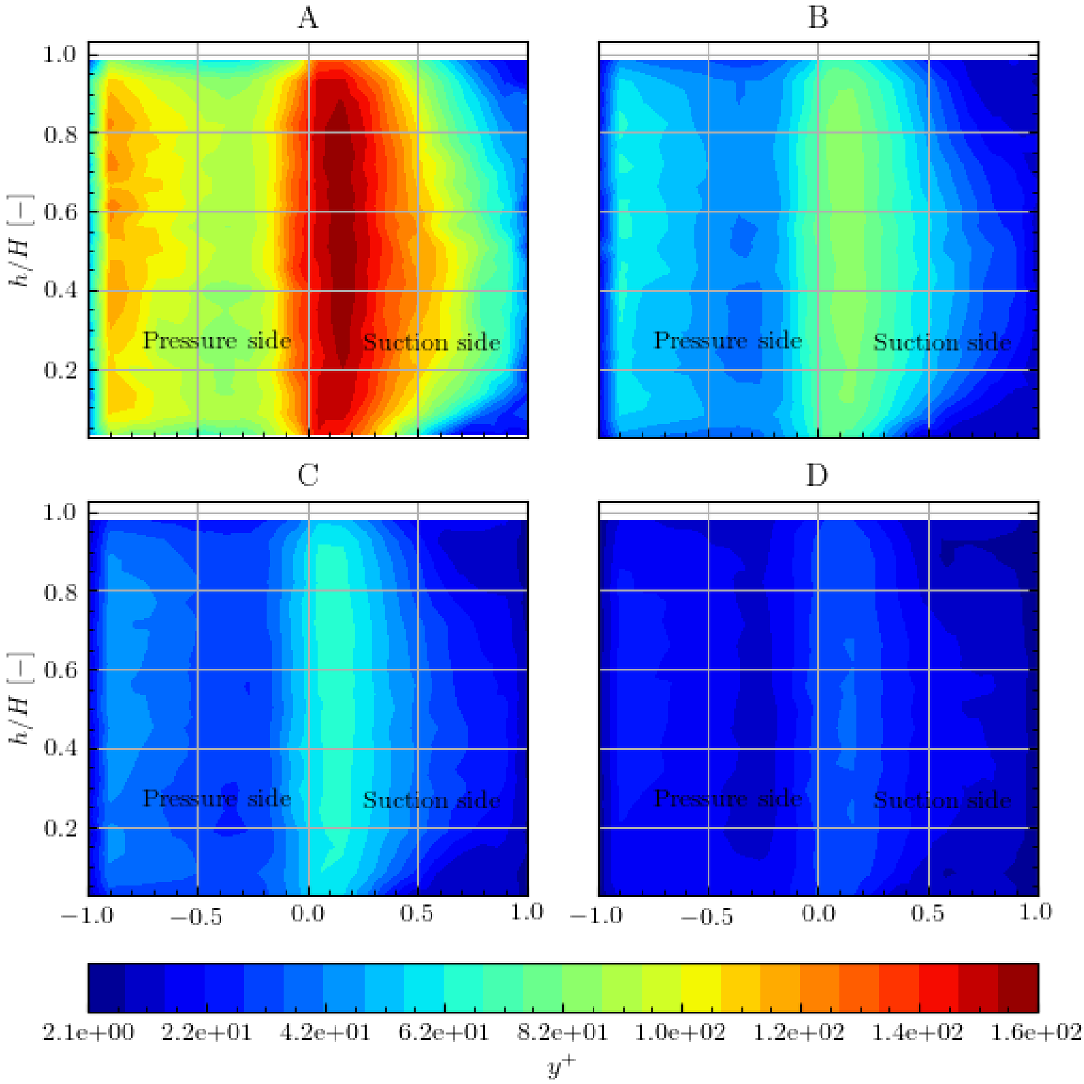

Figure **(5.13)** – y^+ contour map on the S1 blade wall.

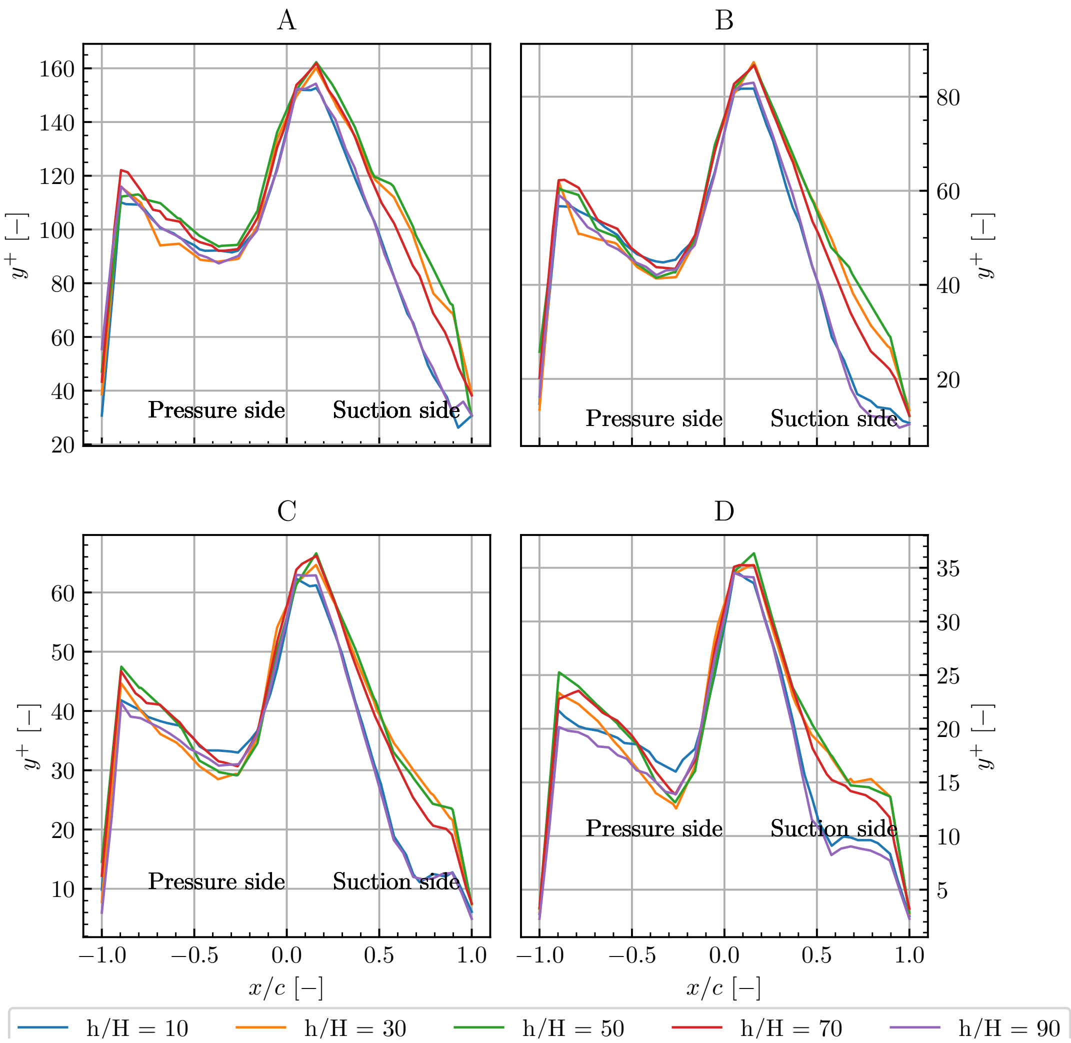

Figure **(5.14)** – y^+ value along the S1 blade at different h/H.

Fig. 5.15 shows the contour map of the Mach number around the blade taken at mid-height. The wake becomes finer as the mesh is refined, and the separation is limited on the suction side.

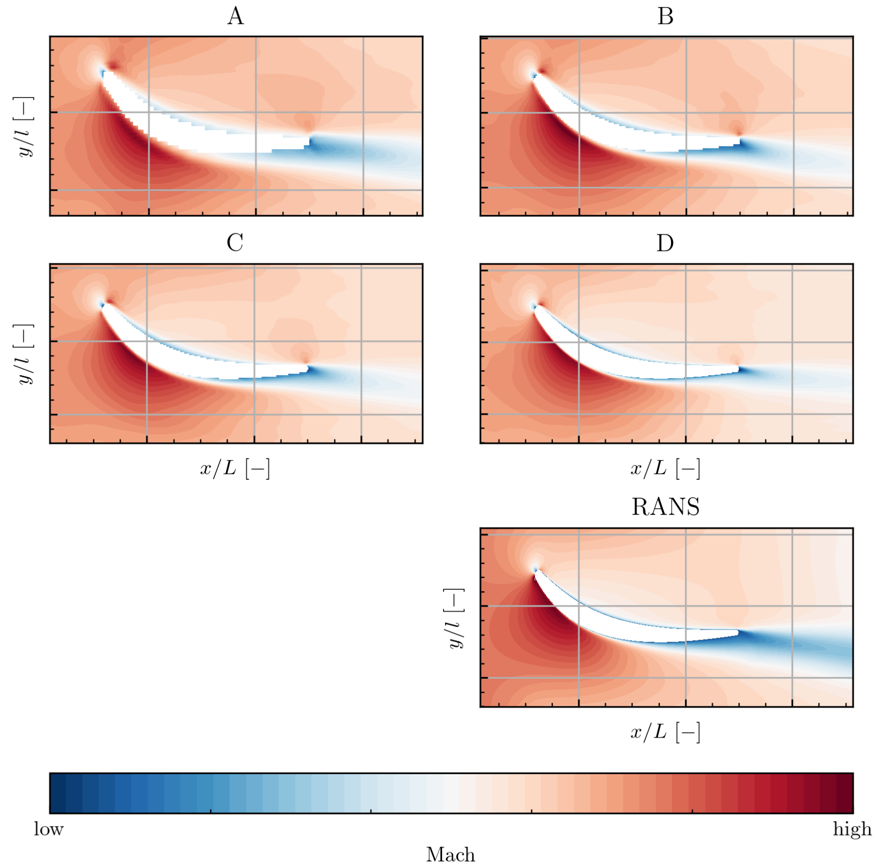

Figure **(5.15)** – Evolution of the Mach number around the blade at $h/H = 50\%$ for cases A to D.

Results are also illustrated in terms of the static pressure coefficient on the blade for the different cases in Fig. 5.16. It shows that case D recovers the general trend and level found by the RANS except at the leading edge, where the resolution is still limited due to the Cartesian mesh.

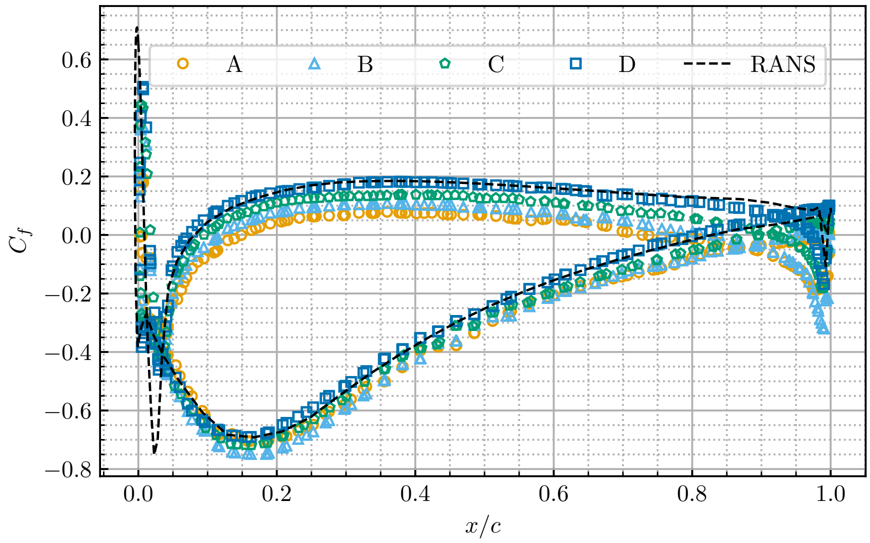

Figure **(5.16)** – Evolution of the static pressure coefficient at $h/H = 50\%$ for cases A to D.

From this section, it is shown that the best results are obtained with the finest mesh resolution used on the wall, $\Delta x = 0.094\,\text{mm}$.

5.5 Turbulence Injection in LES Simulations

This section presents the sensibility study of the different parameters that need to be set for the turbulence injection, namely:

- The characteristic integral length scale.
- The spectrum of turbulence.
- The turbulence intensity prescribed.
- The characteristic mesh size at the inlet.

These parameters can have significant effects on the flow development in the configuration. In this section, several turbulence injection set-ups have been tested, and their influence evaluated. A sensibility study on the integral length, scale, turbulence intensity, and choice of the turbulence spectrum is conducted in the following.

For the test cases in the following, the mesh size at the walls is imposed at $\Delta x = 0.094\,\text{mm}$, and a mesh size in the fluid domain doubled.

5.5.1 Level of Turbulence Intensity

Four turbulence intensities are defined (see 5.5). The experiment measured a level of 5% at the machine's inlet. This, however, does not indicate the exact level that reaches the S1 blade Leading Edge (LE). Nonetheless, considering that the S1 stator is situated after a first rotor row that will create additional turbulence, the level of 5% is the order of magnitude that will be kept in the following as the target level to reach on the blade LE. This is coherent with other simulations [23] and the turbulence level specified in the RANS simulations.

Case	A	B	C	D
Turbulence intensity	0%	2.5%	5%	10%
TKE $[\mathrm{m} \cdot \mathrm{s}^{-2}]$	0	2.34	9.375	37.5

Table **(5.5)** – Level of turbulence intensity for the different test cases.

Mach number contours are presented in Fig. 5.17. It can be seen that when no turbulence is injected, a significant separation is happening on the blade suction side, leading to a significant rise in losses. However, as the turbulence is increased, the size of the separation is reduced until reaching a state of attached flow for case (D). This corresponds to a larger turbulence intensity imposed at the inlet than the 5% given by the experiment. This is due to the decrease of turbulence intensity as observed for the turbulent channel (see Chapter 4). Indeed, as illustrated in Fig 5.18, a smaller turbulence intensity than the one imposed at the inlet reaches the blade's leading edge. To effectively have a level of 5% reaching the blade, a level of 10% must be specified at the inlet. This recommendation will be kept in the following when turbulence is injected.

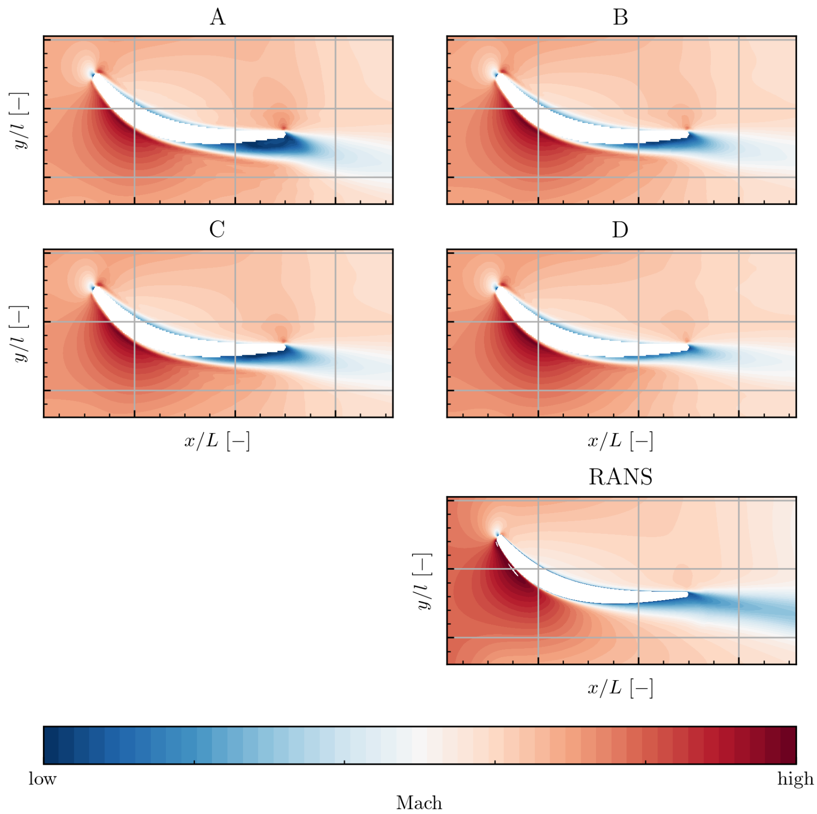

Figure **(5.17)** – Evolution of the Mach number around the blade at $h/H = 50\%$ for several level of turbulence injection.

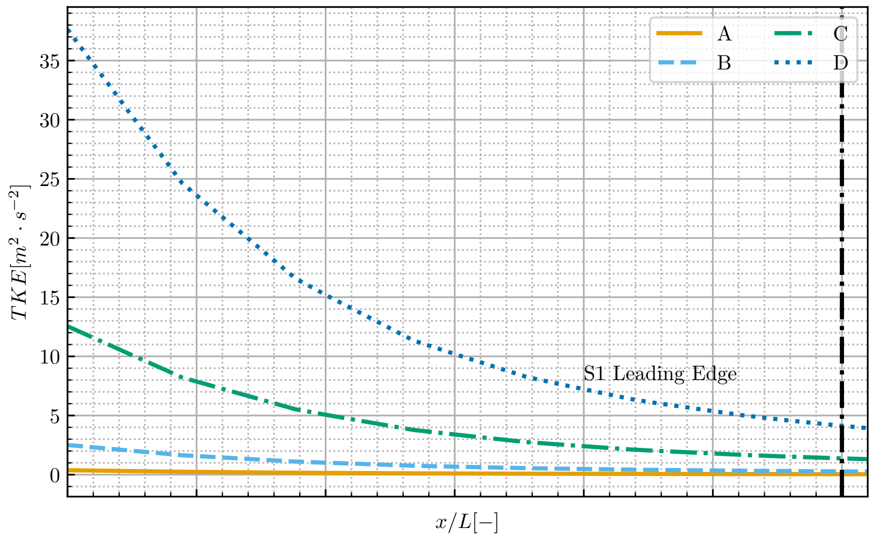

Figure **(5.18)** – Plots of integrated TKE level between the inlet and the blade leading edge for cases (A) to (D).

A turbulence intensity of 10% must be specified at the inlet to reach the target level of 5% at the blade leading edge.

5.5.2 Influence of Integral Length Scale

To study the influence of the integral length scale, λ, four cases are set up using 10% of turbulence intensity. It is recalled that h represents the vein height (Fig. 5.9) and that the mesh size used is 0.094 mm near the wall (RD1) and (RD2) is specified in the fluid region leading to 264 cells in the inlet height h.

Case	A	B	C	D
λ	$h/50$	$h/10$	$h/5$	$h/2$

Table **(5.6)** – Variation of integral length scale for cases A to D.

The results are illustrated in Fig. 5.19. It shows that if the integral length scale is too small, as for case (A), a significant separation occurs. Indeed, not enough turbulent kinetic energy can reach the blade's leading edge in this case to reenergize the boundary layer. For cases B and C, the results are satisfactory. It is interesting to note that case (D) results show a degradation of the obtained flow with a separation starting to occur sooner. This means an integral length scale set too large is not representative enough of the inlet flow that impacts the blade.

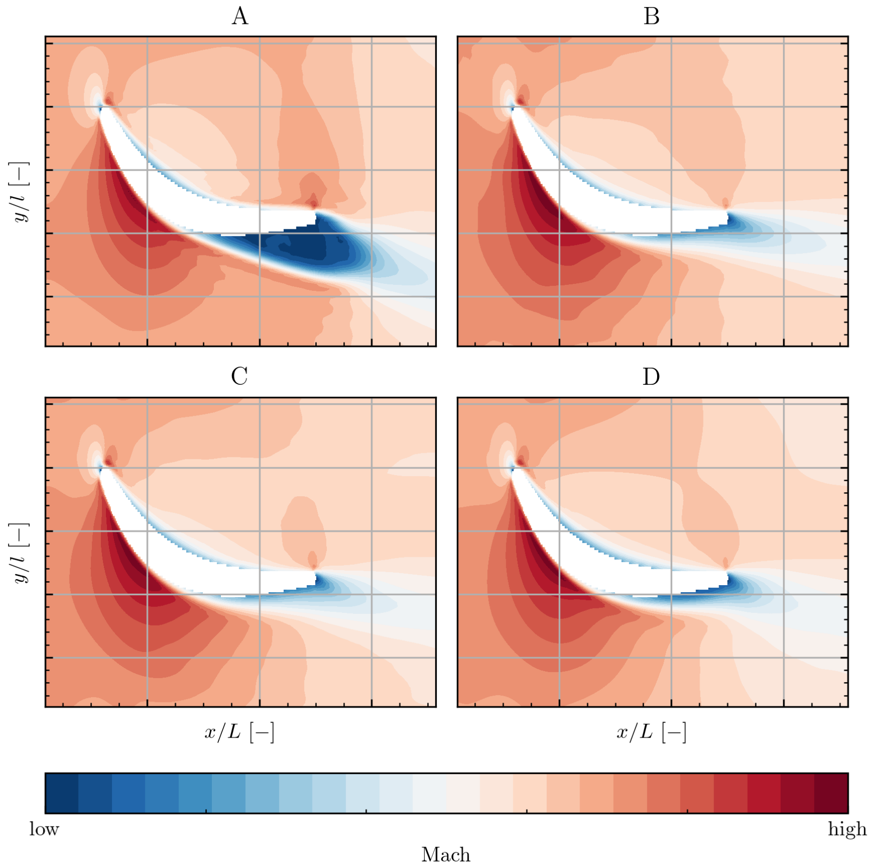

Figure **(5.19)** – Evolution of the Mach number around the blade at $h/H = 50\%$ for several integral length scale.

An integral length scale of $h/5$ or $h/10$ is recommended for the turbulence injection.

5.5.3 Choice of Turbulence Spectrum

The turbulence spectrum can be chosen between the Passot-Pouquet [158] and the Von-Karman [159]. Both turbulence spectra have been tested with a turbulence intensity of 10%, an integral length scale of $h/5$, and a mesh size of 0.094 mm. Fig. 5.20 shows that with the Passot-Pouquet spectrum, the static pressure coefficient is closer to the RANS results at the suction side at an axial position of 0.05 and 0.3. No differences can be noted on the rest of the blade surface as both turbulence spectra give similar results. Other studies [89] have investigated these two spectra extensively. It was shown that they both reproduce the desired turbulent behavior expected. However, the Passot-Pouquet spectrum generated more noise at the inlet than the Von-Karman. For this reason, the Von-Karman spectrum will be kept for the following.

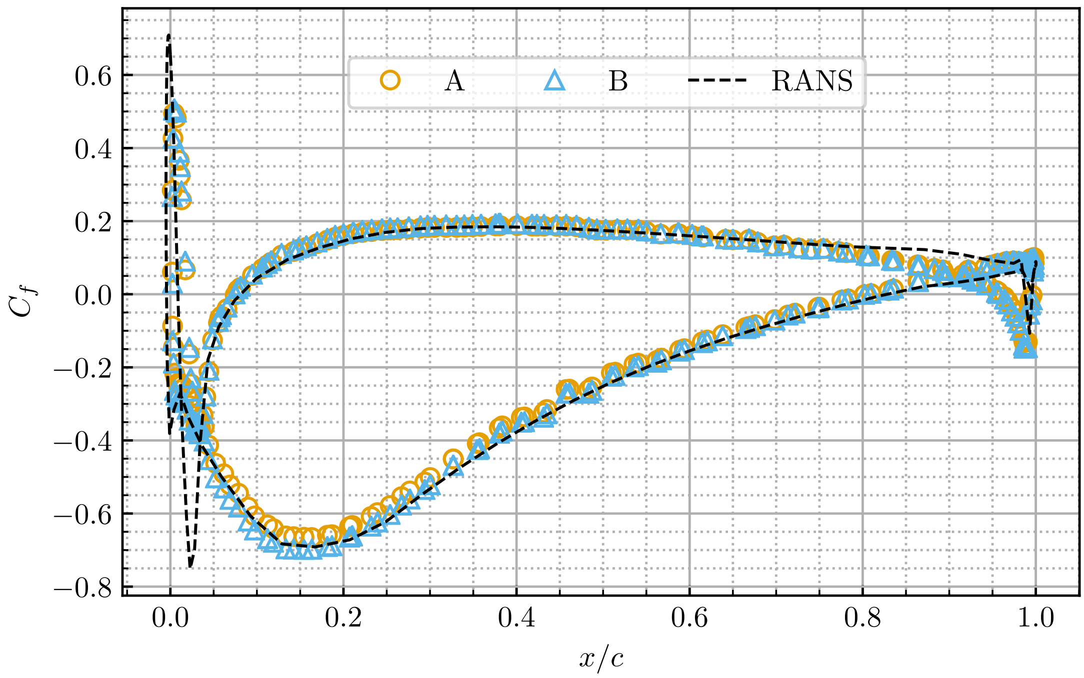

Figure **(5.20)** – Evolution of the static pressure coefficient around the blade for the Passot-Pouquet (A) or Von-Karman (B) turbulence spectrum.

This study established mesh requirements in the wakes and on the walls to capture the correct level of losses and obtain qualitatively correct flow around the S1 blade. As the flow conditions are pretty similar on the other blades of the machine (no significant acceleration or compression and similar incidence angles), the mesh requirement established for this specific blade can be generalized to the other ones. However, the mesh size recommended at the end of this study was found to lead to meshes too large, with over one billion elements causing memory issues by limitation of the ProLB solver. This imposed a degradation of the mesh resolution to $\Delta x = 0.188\,\mathrm{mm}$ in the next simulations of Chapter 6.

5.6 Validation of Isotropic Behavior

This section aims to validate that the results obtained using the ProLB solver verify the isotropic properties expected. Indeed, isotropy problems have been observed previously, mainly on jet flows [89]. To improve the isotropy of the $D3Q19$ lattice, Bauer, Silva, and Rüde [114] proposed a modification of the equilibrium distribution function to reach additional fourth-order moments. This equilibrium has been implemented [160] and tested on a jet flow configuration showing improved results.

To investigate this issue on a more representative flow configuration of CAM1, a simple test case is set up using the 360° strutted S-duct geometry. The eight struts are advantageously located every 45° making it an excellent candidate to check the resulting wake behind the struts between two different sectors, one in the cardinal direction, and the other shifted by 45° (see Fig. 5.21). A uniform axial velocity inlet at $50\,\mathrm{m \cdot s^{-1}}$ is set while static pressure is imposed at the outlet. Two cases are considered, one where the isotropic equilibrium is deactivated (No Iso Eq) and one where it is activated (Iso Eq). The results are compared by looking at the Mach number profiles plotted at different heights in the vein along the azimuthal direction in Fig. 5.22 and Mach number contour at the duct exit 5.24.

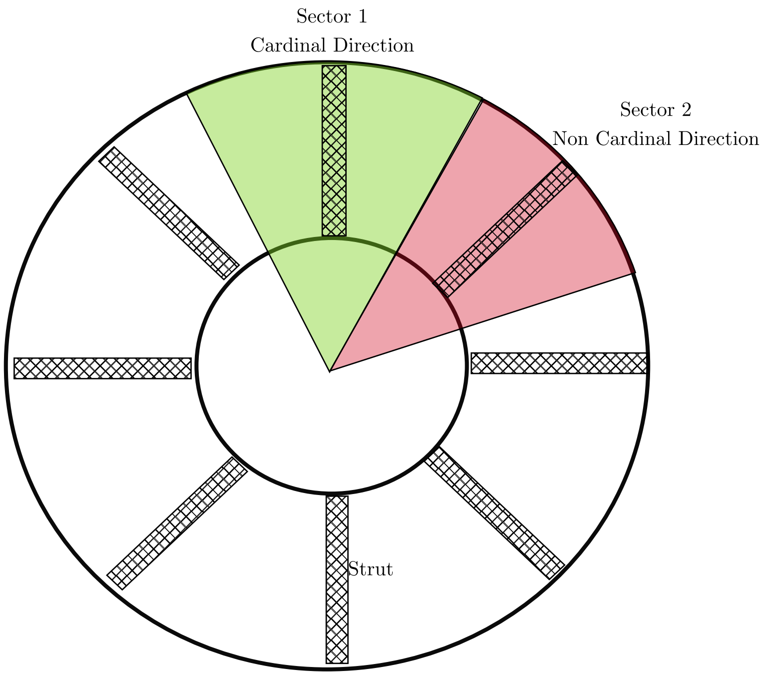

Figure **(5.21)** – Scheme of the extracted sectors from the 360° computation for the isotropy validation.

The azimuthal profiles plotted for the two sectors show little difference in the strut wakes with or without isotropic equilibrium. The main discrepancies are observed at $h/H = 50\%$ and $h/H = 90\%$, where the Mach number is underestimated in the non-cardinal direction. For the rest of the profiles, the intensity and width of the wake are similar. The difference of Mach number reached in the wake at the different h/H using the isotropic-equilibrium or not are summarized in Table 5.7:

h/H	25%	50%	75%	90%
No-Iso	4.4e-05	0.016225	0.010435	0.025611
Iso	0.000126	0.01508	0.011906	0.02633

Table **(5.7)** – Difference of Mach number in the wake between the cardinal and non-cardinal direction.

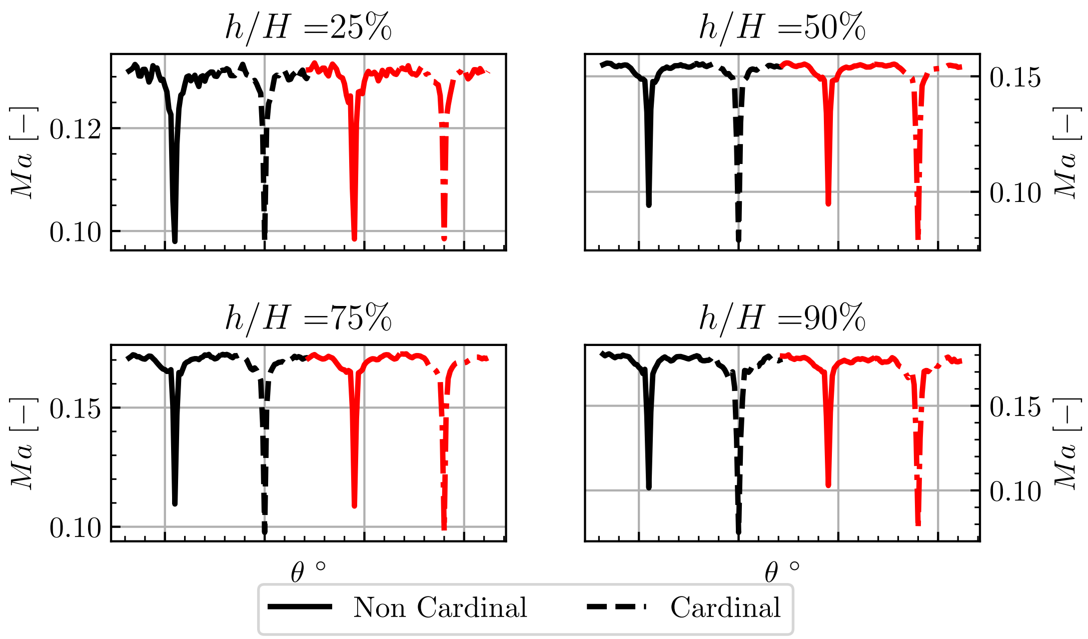

Figure **(5.22)** – Comparison of the Mach number profiles in the azimuthal direction at different h/H with (black) or without (red) isotropic equilibrium.

To further validate the isotropic behavior, static pressure contour maps on the strut blade are presented in Fig. 5.23. The pressure distributions on the strut blade are compared between sectors 1 and 2 and show an identical flow development.

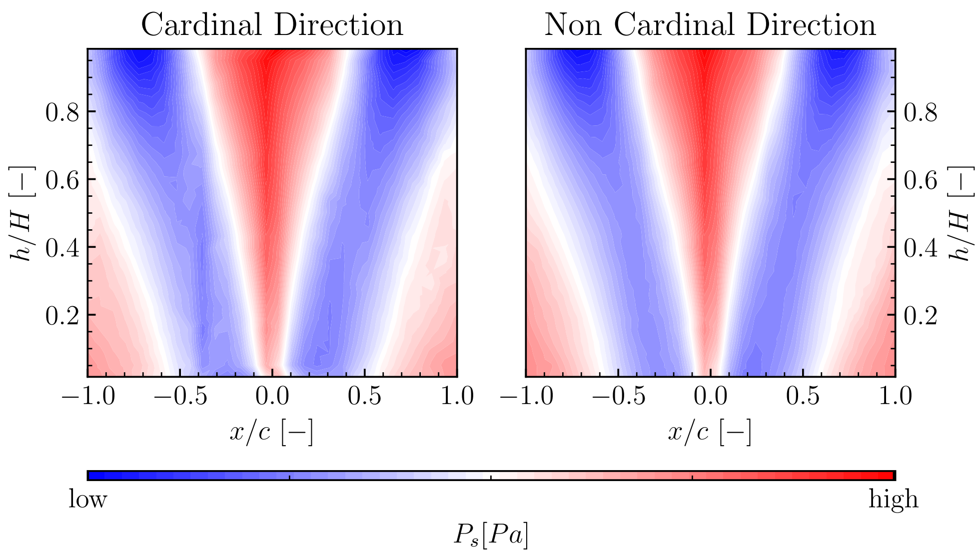

Figure **(5.23)** – Contour map of static pressure on the strut blade in the cardinal and non-cardinal direction.

To illustrate the differences in flow development, contour maps of Mach number in the cardinal and non-cardinal directions are presented in Fig. 5.24. It visually confirms that the two sectors' flow field differences are minor.

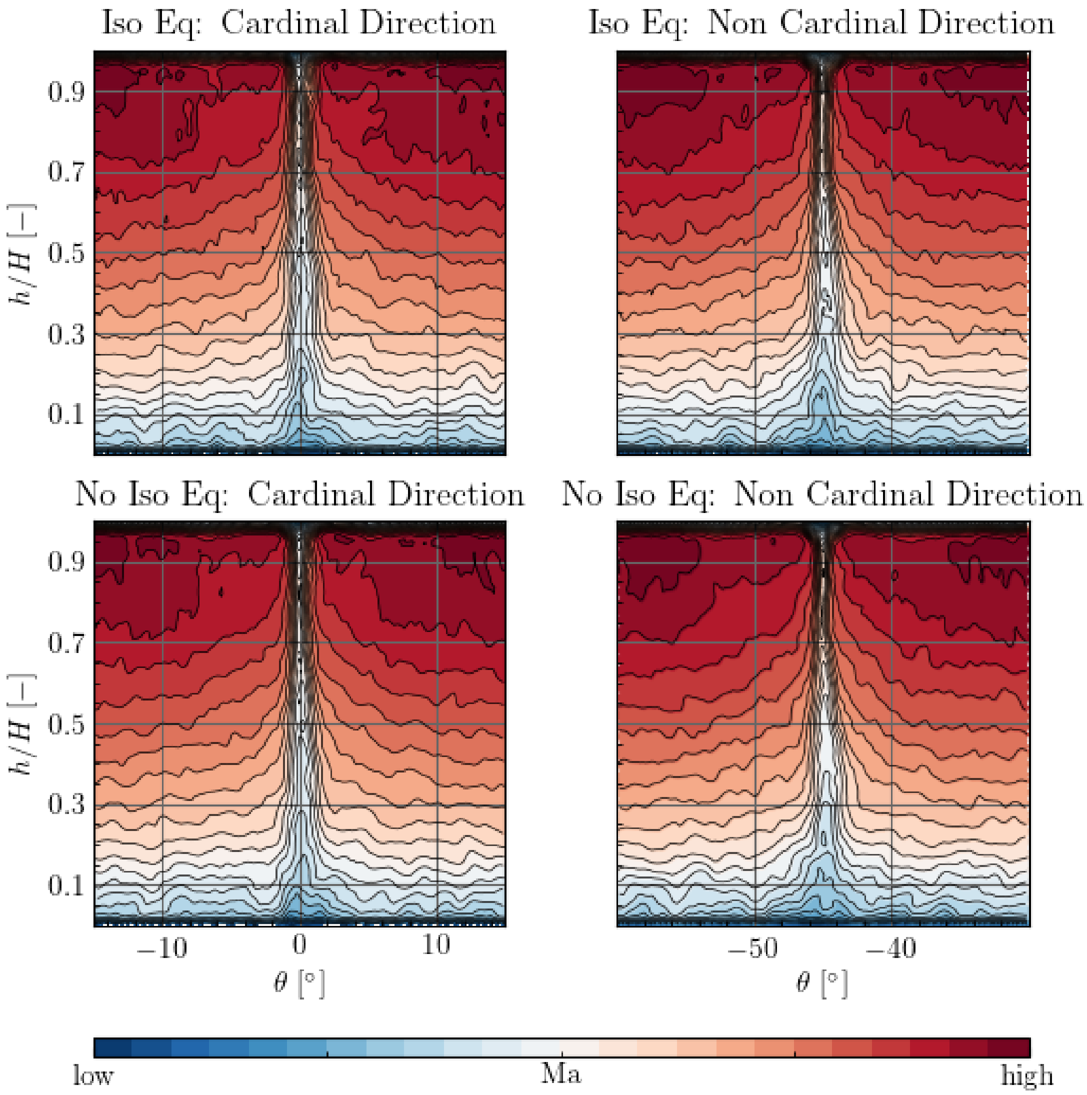

Figure **(5.24)** – Comparison of the Mach number contour map in the cardinal and non-cardinal directions at the duct exit with or without isotropic equilibrium.

This study illustrated that no major isotropy issues were found in this case. Differences between the cardinal and non-cardinal directions appear with a variation of at most 0.02 in terms of Mach number in the wakes. Moreover, the influence of the isotropic equilibrium correction has been evaluated and shown to be minor. In the following computations, the isotropic equilibrium correction is kept by security as no detrimental impact on the results was observed.

5.7 Primary Validation of the Rotating Domains

This section presents the work performed to validate the rotating domains used in the following. The properties of the rotating domains using the Hybrid Recursive Regularized (HRR) collision operator have been studied previously [121] on some test cases. This section aims to verify that the additional interpolations introduced by the rotating domains do not deteriorate the stationary wakes and azimuthal profiles that are going through it. Here, a more complex and representative test case for turbomachinery is set up. For this study, the rows considered are taken from the High Pressure Compressor (HPC) stage of CAM1 as they include fewer blades, thus reducing the computational time, and include the rotor with the highest rotational speed.

5.7.1 Wakes Traversing a Rotational Domain

Two simplified test cases are built from the CAM1 geometry. First, a computational domain is fixed to contain the 360° IGV2 stator row, followed by a long annulus region where a rotating region can be imposed in the fluid zone. This way, the IGV2 blades generate wakes, and they will cross either a stationary fluid domain (case A) or a rotating one (case B) (see Fig. 5.25). Comparisons are made downstream of the fluid zone to compare the wake evolution. At the inlet, experimental radial profiles of total pressure, temperature, and flow angles from the duct exit are imposed. Static pressure is dynamically adjusted at the outlet to match the target mass flow.

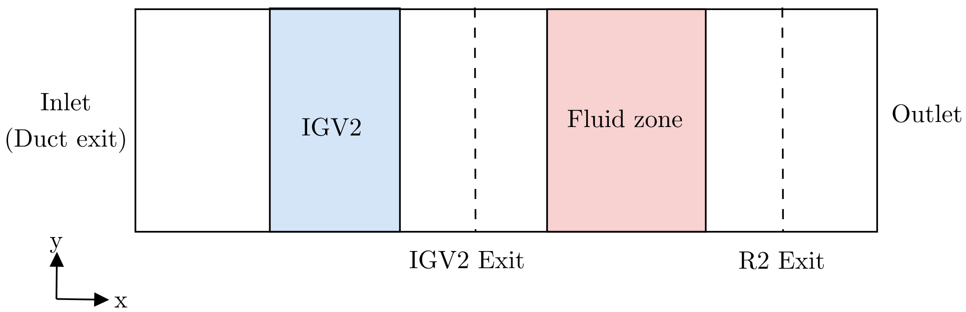

Figure **(5.25)** – Scheme of the domain including the IGV2 blades and the fluid zone that is either stationary (case A) or rotating (case B).

For the two cases, radial profiles at the R2 exit are presented in Fig. 5.26. Radial profiles of total pressure, azimuthal angle, and Mach number are strictly conserved through the rotating domain. Concerning the total temperature, a disparity is observed in the first 25% of vein height. This is attributed to a slight mass-flow difference during the averaging period as illustrated in Fig. 5.27 and also visible on the 20Pa difference of static pressure. This confirms a first property of the rotating domain to conserve the information going through it.

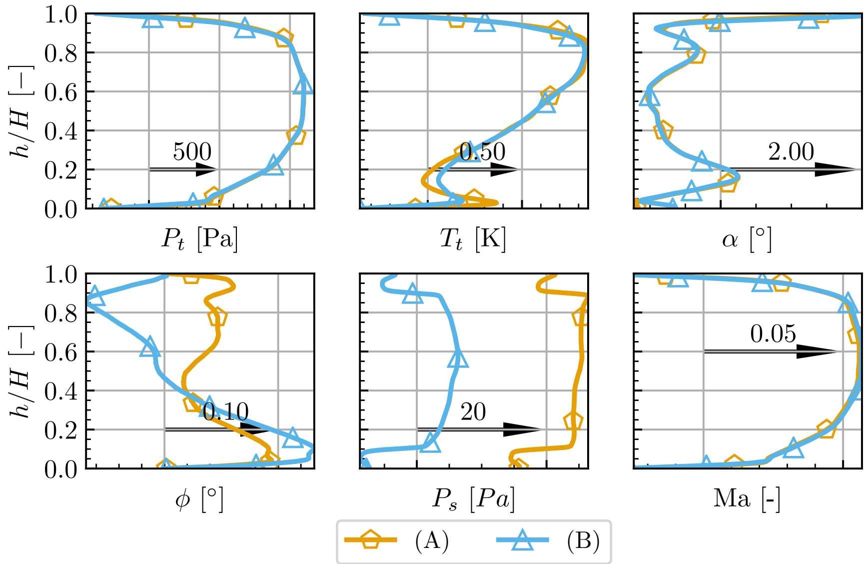

Figure **(5.26)** – Radial profiles for cases (A) and (B) at the R2 exit.

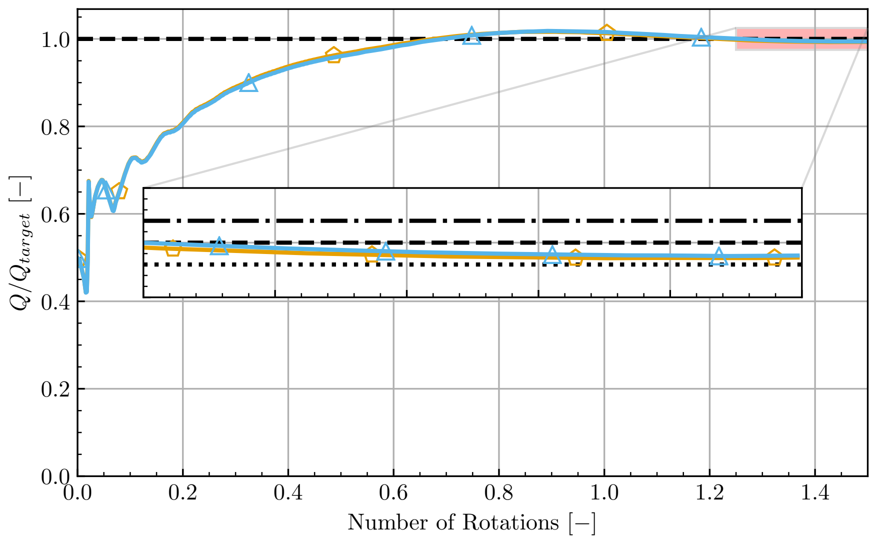

Figure **(5.27)** – Mass flow convergence for cases (A) and (B) at the R2 exit.

Next, contour maps of the Mach number at the IGV2 exit are represented in Fig. 5.28 and compared at the R2 exit. The general shape of the wakes coming from the IGV2 is conserved through the rotating domain. However, it is slightly diffused for both cases.

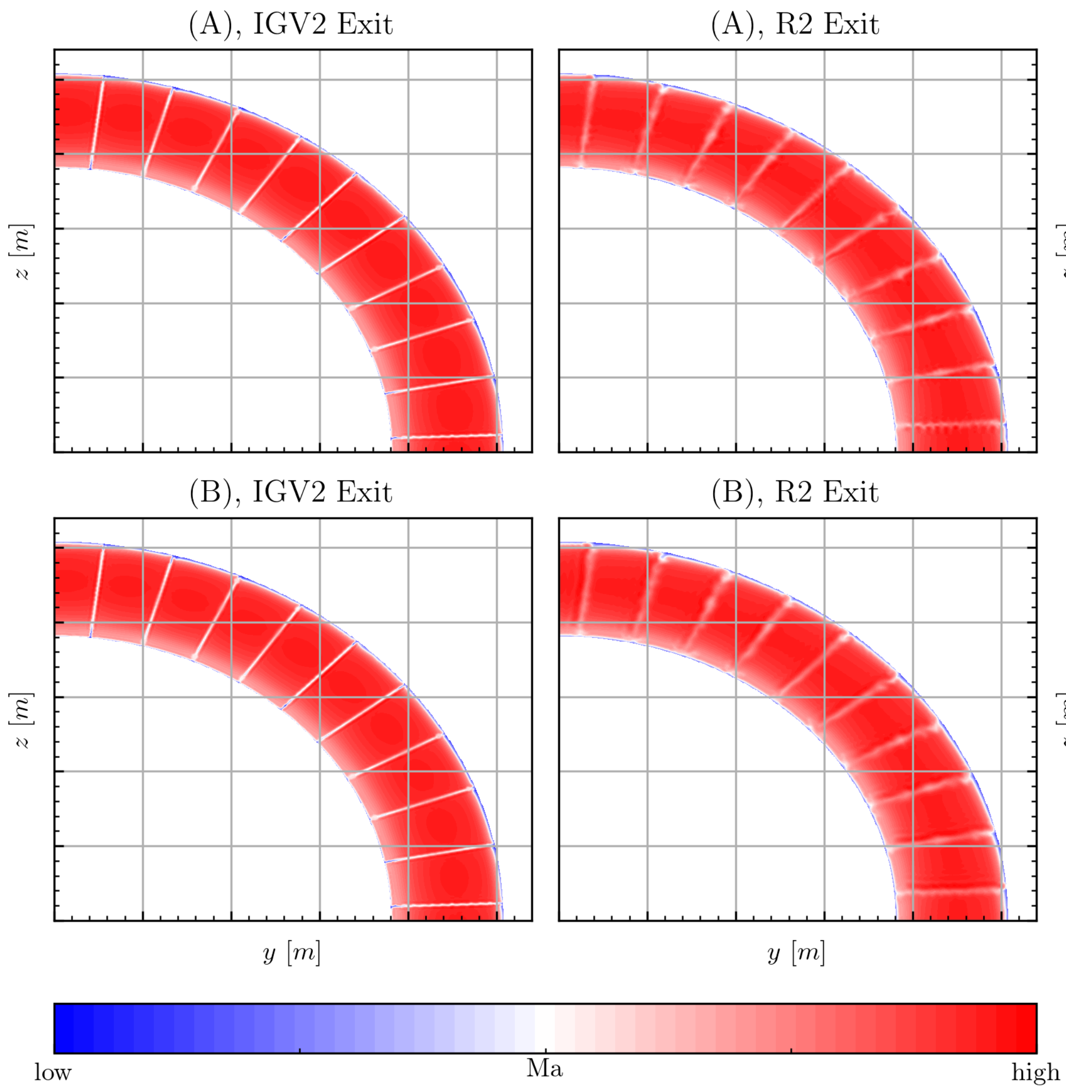

Figure **(5.28)** – Contour map of Mach number for cases (A) and (B) at the IGV2 and R2 exit.

To evaluate the level of dissipation at the comparison plane, the $L2$ error defined as $L2 = \sum_i (Ma_{after,i} - Ma_{before,i})^2$ is computed for cases (A) and (B). The contour map is represented in Fig. 5.29. After integration over the domain, the results give $L2_A = 0.2545$ while $L2_B = 0.2613$, meaning that the rotational domain introduces around 2.58% more numerical error.

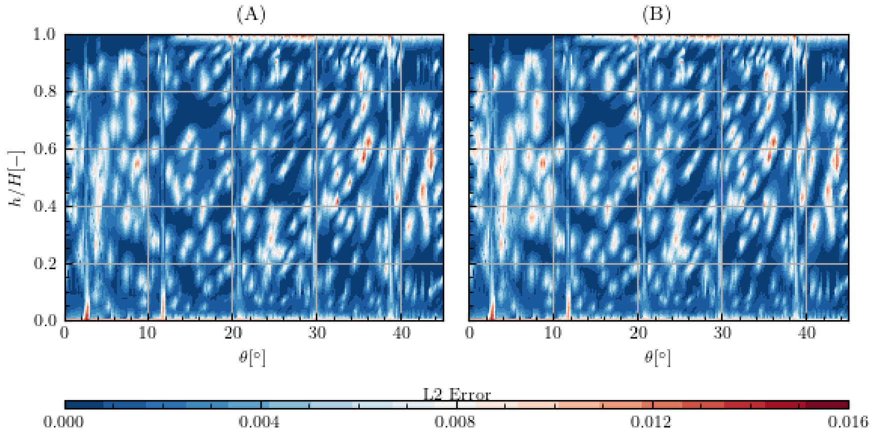

Figure **(5.29)** – Contour map of L2 error for cases (A) and (B) at the R2 exit.

From this study, it can be concluded that using rotating domains does not introduce significant numerical errors or distortion to the radial profiles and traversing wakes so that it can be applied to future simulations.

5.7.2 Operating Rotor, Taking Into Account the Tip Gap

This section evaluates the tip gap resolution necessary to capture its effect correctly. To do so, a test case is built that includes only the R2 row. The inlet corresponds to the IGV2 exit, and a long annulus section is defined after the R2 exit, where static pressure is imposed at the outlet to match the target mass flow. Several cases are considered where the tip gap is first neglected (extrusion of the blade to touch the shroud), then discretized with 4 and 10 cells (see Fig. 5.30). Comparisons are made on the radial profiles at the rotor exit for this different number of cells in the tip gap.

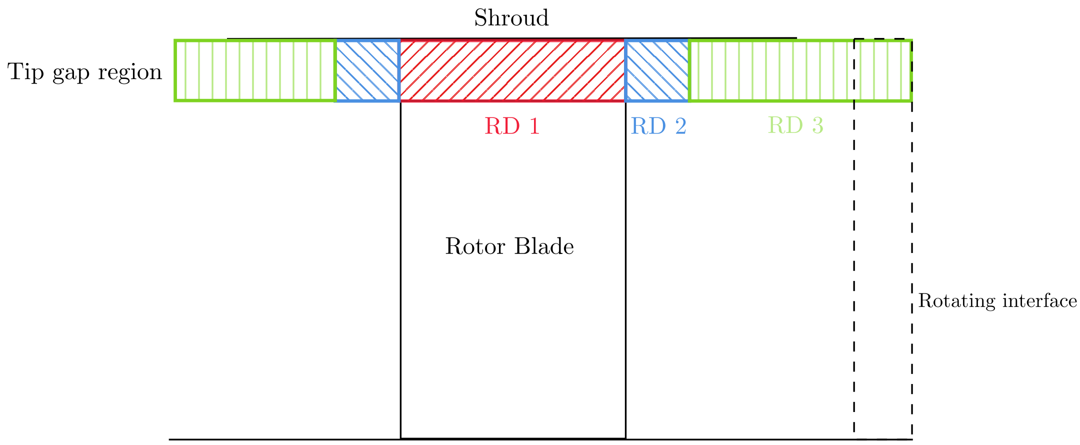

Figure **(5.30)** – Scheme of the rotor tip gap region and meshing strategy.

Radial profiles at the rotor exit are plotted in Fig. 5.31. It shows that as the tip is considered, the radial profile at the shroud is getting closer to the experimental values. The improvement is slight on the total pressure and Mach number, and no significant change is captured when using ten cells instead of four. This is attributed to a global lack of resolution at the shroud that does not allow propagation of the tip gap effect downstream properly. The shroud region should be refined to retrieve the tip gap effect. However, the mesh between the rotating and stationary regions must be uniform at the interface (limitation of ProLB). Concerning the azimuthal angle, a significant improvement is observed when refining the tip gap resolution. This is explained by more realistic flow velocity in this region that can not be retrieved when neglecting the tip gap.

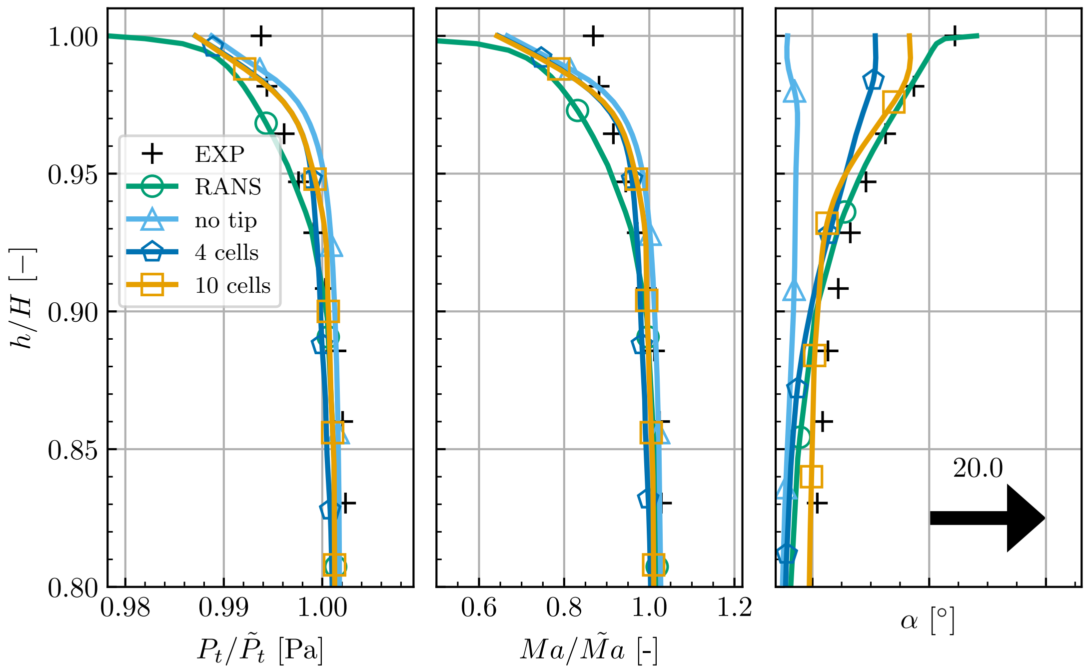

Figure **(5.31)** – Radial profiles at the R2 for different tip gap resolutions.

This study showed that only a fraction of the tip gap physics could be propagated downstream of the rotor. This is explained by a mesh resolution that is too coarse in the shroud region, and that can not be solved with the current solver functionality. In the following, it is thus recommended to include at least four cells in the tip gap to obtain the best quality solution in this zone at a minimal cost knowing that a slight discrepancy will remain above $h/H = 0.9$.

5.8 Chapter Summary

Several functionalities necessary to conduct the physical investigation of the CAM1 configuration have been validated. They concern:

- Accurate mass flow computation,
- meshing strategy in the wake region using the LIKE criterion,
- wall resolution using a y^+ criterion,
- proper turbulence injection,
- validation of the isotropic behavior,
- introduction of rotating domains and investigation of the tip gap resolution effects.

The mass flow can be computed during the computation using the functionalities of the ProLB solver with a satisfactory precision level for turbomachinery applications. This, coupled with the valve law formulation introduced before, allows for easy convergence of the computations toward the operating point.

For the meshing strategy, best practices have been defined on a simplified test case to properly mesh the wake region of the different blade rows of the CAM1 configuration and the wall region. This was done using the LIKE criterion to define the wake region properly and evaluate the mesh resolution needed. On the walls, arbitrary surfaces can be defined to adjust the y^+ to ensure the best application of the wall law.

Different setups of turbulence injection have been tested in terms of turbulence intensity, length scale, and turbulence spectrum. It is concluded that a level of 10% needs to be injected at the inlet to reach the appropriate level of 5% at the blade LE with an integral length scale of $h/5$. The choice of the turbulence spectrum was shown to have a negligible impact on the results.

The isotropic behavior of the D3Q19 lattice has been evaluated using the CAM1 geometry allowing for a comparison of the wakes and the blade static pressure distribution between two struts placed in the cardinal or non-cardinal directions. Small differences of about $5\,\mathrm{m \cdot s^{-1}}$ in the wakes are observed and the isotropic equilibrium formulation could not improve. This discrepancy is explained by the difference in mesh density in the non-cardinal direction when using an octree mesh.

Finally, a study was conducted to evaluate the possibility of considering the rotors' tip gap. It was shown that even though ten cells could be placed inside the gap region, the propagation of the effect was limited by the shroud resolution that could not be set fine enough. Indeed, no mesh transitions can be placed at the rotating interface, leading to inappropriate computational times for an industrial application. The best compromise was found by placing four cells in the tip gap region.

Chapter 6: Physical Analysis of the CAM1 Configuration

This chapter is a retranscription of the submitted article:

Gianoli, T., Boussuge, J. F., Sagaut, P., de Laborderie, J. (2023). Investigation of an Inter-Compressor S-duct using the Lattice Boltzmann Method., Journal of Turbomachinery.

Some notations have been modified to stay consistent with the rest of the manuscript. The LBM presentation has been removed as they are redundant with Chapter 3. The article has the following abstract:

This article presents the study of an inter-compressor annular S-duct. Numerical simulations are performed using a compressible hybrid thermal lattice Boltzmann method (LBM) implemented within the ProLB solver. Comparisons are made between the LBM results, Reynolds Averaged Navier-Stokes (RANS) computations, and experimental measurements on a representative S-duct taken from the European project AIDA. Several cases of increasing complexity are considered where the different rows surrounding the duct are gradually included in the computations. This allows to study the effect of each row on the flow field development and on the loss level. The goal is to evaluate the ability of the LBM to recover the aerodynamic behavior and the total pressure loss evolution within the duct. Results show that the LBM retrieves the correct flow evolution inside the S-duct compared to the experiment and previous RANS results. The case where the upstream stator row or the Low-Pressure Compressor (LPC) stage is integrated shows an increase in total pressure loss, as previously observed in the literature, and a more developed flow field with complex flow features contributing to the loss generation. To further analyze the loss mechanism, an entropy-based approach is presented and highlights that most losses are generated close to the hub wall due to the migration of the upstream stator wakes.

Contents

6.1 Goal of the Study

This study investigates the ability of the LBM to recover the main physical phenomenon described during the literature review on an academic configuration. This configuration is less critical than a real industrial S-duct regarding Mach number and inlet mass flow, but the S-duct aerodynamic loading is still considered representative. Moreover, the experimental data available are abundant, as well as RANS results to allow a complete comparison and analysis.

6.2 Setup

6.2.1 Geometry Reduction

The complete geometry is quite complex, so the best approach consists of starting from the simplest geometry and progressively adding the different rows. This allows for establishing guidelines and a methodology to perform S-duct aerodynamic simulations, and, moreover, this grants the possibility to compare the flow physics evolution for every additional component included in the simulation. This chapter focuses on the numerical validation of the different simulations and the physical analysis of the flow field using comparisons between the cases, RANS results, and experimental data.

Six different configurations can be examined by separating the full CAM1 geometry into sub-configurations. They are referred to in the following:

- Duct
- S1-Duct
- LPC
- HPC
- S1-HPC
- Full

For clarity, the computational domain associated with each case is represented in Fig. 6.1.

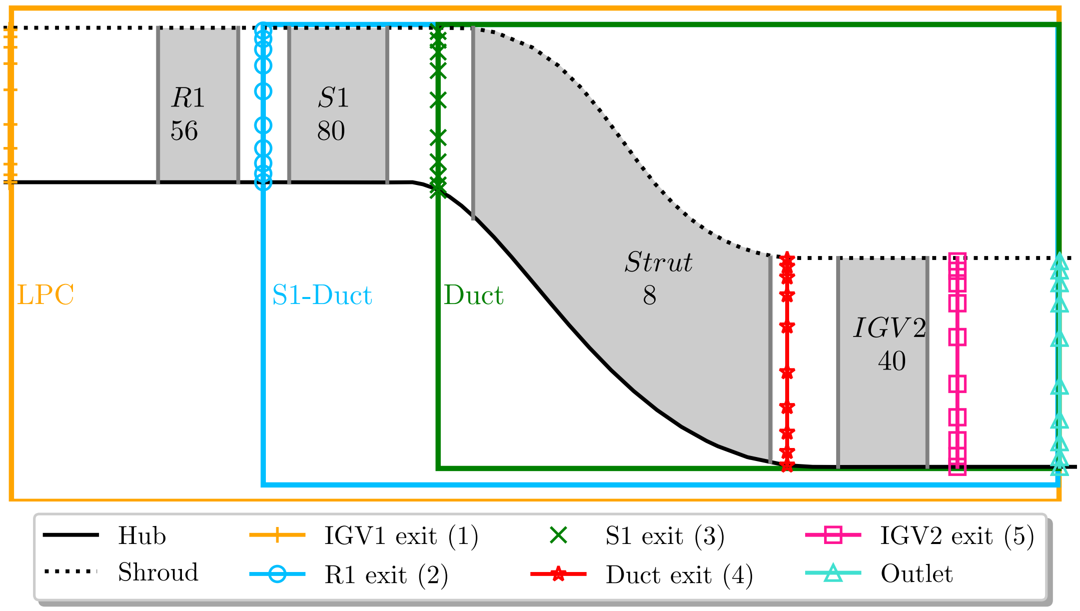

(a) Scheme and highlight of the cases Duct, S1-Duct and LPC.

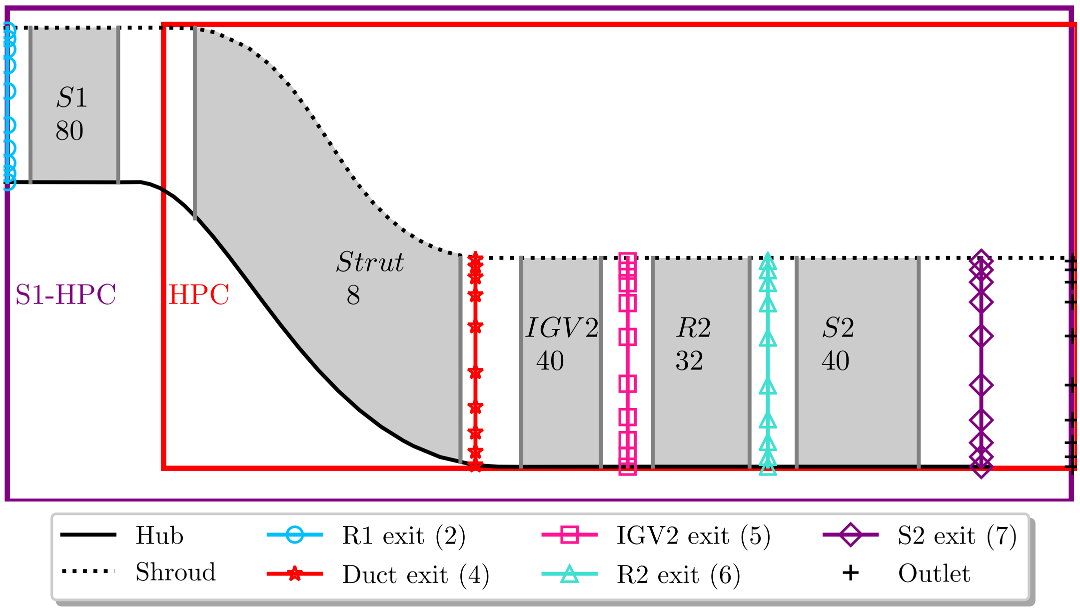

(b) Scheme and highlight of the (HPC) case.

Figure **(6.1)** – Illustration of the computational domain for the different cases.

6.2.2 Boundary Conditions

The working fluid has a specific gas constant set to $R_g = 287.15\,\mathrm{J \cdot kg^{-1} \cdot K^{-1}}$ corresponding to the experimental conditions. The dynamic viscosity is imposed as $\mu_{ref} = 1.49 \times 10^{-5}\mathrm{kg \cdot m^{-1} \cdot s^{-1}}$. It varies according to Sutherland's law with a reference temperature fixed to $T = 291\,\mathrm{K}$ corresponding to the inlet static temperature.

At the inlet, an azimuthal averaging of the experimental data is performed to impose radial profiles of total pressure, total temperature, and flow angles using a LODI formulation as presented in Chapter 4. Moreover, turbulence injection is set at the inlet with an intensity of 5% and a turbulent length scale $l = H_{in}/5$. At the outlet, uniform static pressure is taken from the experimental data and will be dynamically adjusted to match the correct mass flow [152, 89]. The outlet condition uses a LODI formalism that naturally respects the radial equilibrium assumption [161]. Concerning the rest of the boundaries, adiabatic walls are imposed in association with a wall law.

6.2.3 Wall Law

The wall law applied for the computations is derived from the classical wall (Eq.6.1) onto which additional correction terms to take into account curvature $F_c(y^+)$, pressure gradient $F_p(y^+)$ and near-wall damping $F_d(y^+)$ are added to construct a more elaborated wall law [119] (Eq.6.2).

$$U_0^+(y^+) = \frac{1}{\kappa}\log\left(y^+\right) + B \tag{6.1}$$

$$U^+(y^+) = (U_0^+(y^+) + F_c(y^+) + F_p(y^+)).F_d(y^+) \tag{6.2}$$

6.2.4 Subgrid Scale Model

An additional subgrid viscosity is added to consider the unresolved turbulent structures in the bulk flow. This study tested both the Shear-Improved Smagorinsky's Model (SISM) and the Vreman model. No significant differences in the results between the two models have been observed. In the following, the Vreman model is kept. This modeling, coupled with the Lattice-Boltzmann approach, has already been demonstrated on complex applications that deal with turbulent flows [162].

6.2.5 Meshing Strategy

The conclusions extracted from the simplified study presented in Chapter 5 are used to generate a mesh for the different cases. However, the mesh size recommended in Chapter 5 leads to too heavy mesh, thus forcing a coarsening of the smallest mesh size imposed in RD1 to $\Delta x = 0.188\,\mathrm{mm}$ and imposed on all the blades. This ensures that at least four cells are put in the rotor tip gaps when rotors are considered. Then RD2 is applied to the hub, shroud, and blade wake regions highlighted by the LIKE criteria. Finally, RD3 with a size of $0.753\,\mathrm{mm}$ is applied to the rest of the fluid domain (see Fig. 6.2).

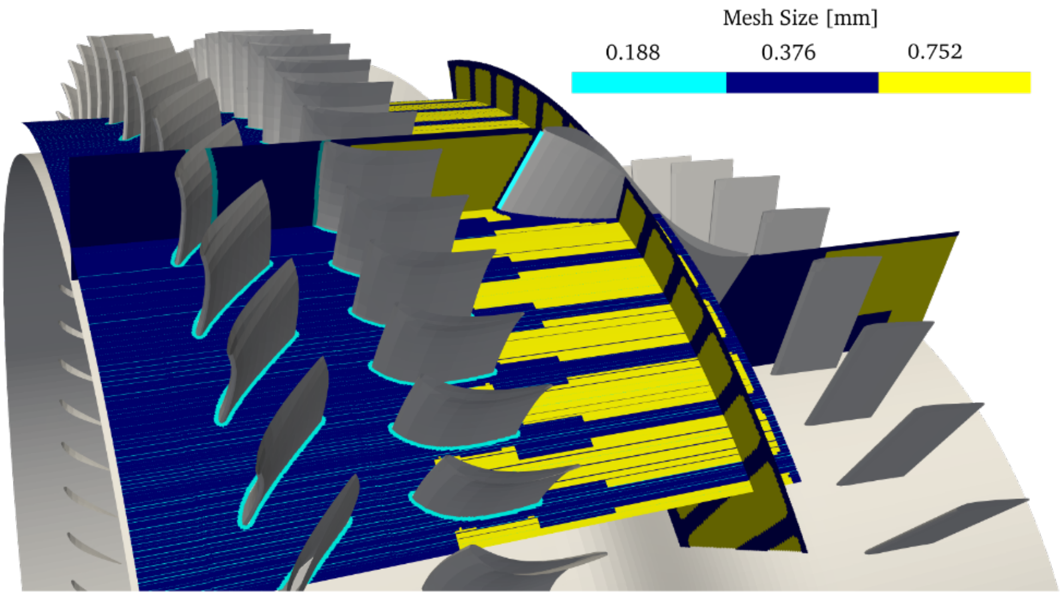

Figure **(6.2)** – Illustration of the mesh refinement domains (RD).

The mesh characteristics and computational times are presented in Table 6.1.

Case	Equivalent Fine Points	Total Nb. Points	CPU.h
Duct	112×10^6	202×10^6	12160
S1-Duct	254×10^6	413×10^6	28000
LPC	359×10^6	570×10^6	58710
HPC	267×10^6	448×10^6	41070

Table **(6.1)** – Summary of the mesh properties for the different cases.

Blade	R1	S1	Strut	IGV2	R2	S2
Cells / chord	165	210	350	200	225	284

Table **(6.2)** – Cells per chord for the different blades.

6.2.6 LBM Model Parameters

The free HRR parameter is set to $\sigma = 0.99$ for all cases. The reference temperature is set as $T_0 = 291K$ leading to a time step computed from the formula $\Delta t = \frac{\Delta x c_s^*}{\sqrt{R_g T_0}} = 3.69813 \times 10^{-7}$s. The resulting bulk Courant-Friedrichs-Lewy (CFL) number obtained is $CFL = \frac{U_{bulk}+c}{\Delta x/\Delta t} = 0.74$ with U_{bulk} taken as the mean velocity through the S-duct.

6.2.7 Simulation and Averaging Time

The simulations are initialized from a uniform flow field with a velocity half of the mean one expected and corresponding density and static temperature. The simulations are run for a physical time corresponding to three rotations of the rotor R1, and the averaging is performed on the last rotation. The time evolution of the mass flow rate at the duct exit for the different cases is presented in Fig. 6.3. It shows that all cases converge in about two rotations towards the target and that, during the averaging period, no mass flow oscillations are observed.

6.3 Results and Discussion

This section presents the numerical results of the different cases defined in Fig. 6.1a and 6.1b. First, the convergence of the simulations towards the correct operating point will be illustrated before analyzing the radial profiles of macroscopic quantities of interest. A closer inspection of the results in terms of flow physics and their impact on the radial profiles is conducted by studying two-dimensional contour maps.

6.3.1 Convergence of the Simulations

First, the convergence towards the target mass flow is validated by plotting the mass flow time evolution at the duct exit for the different cases in Fig. 6.3. It shows a similar mass flow evolution for the different cases towards the target in about two rotations. No significant oscillations are observed during the averaging period highlighted in red.

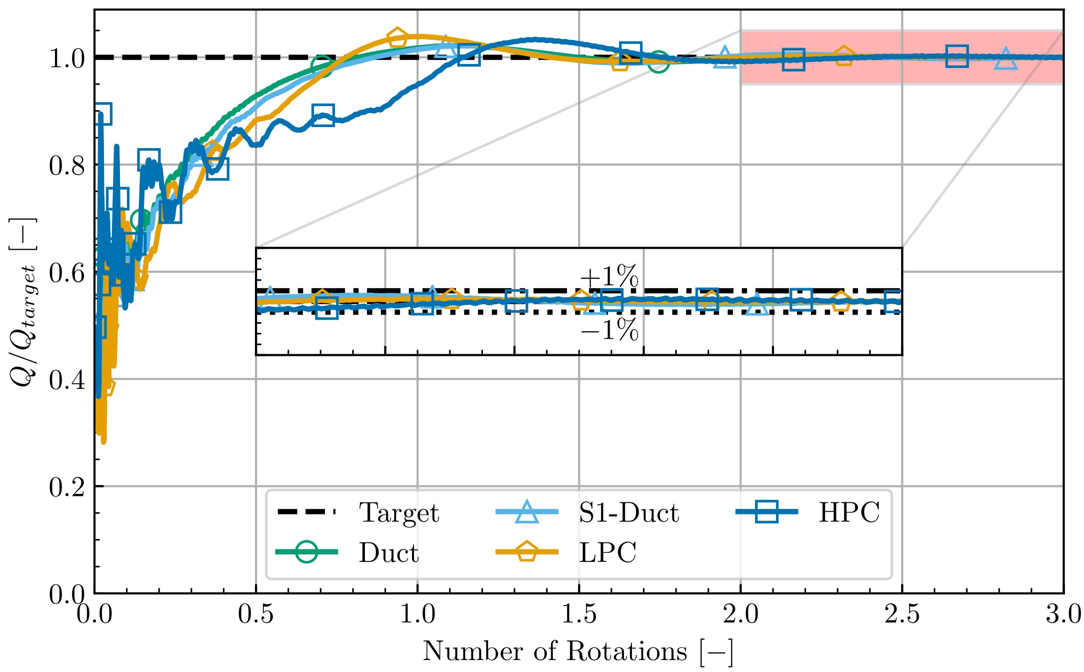

Figure **(6.3)** – Validation of the mass flow convergence for all cases at the Duct exit plane.

Additionally, to corroborate the convergence, plots of averaged total pressure and total temperature time evolution at the duct exit are shown in Fig. 6.4. It confirms that during the averaging period, these quantities are constant.

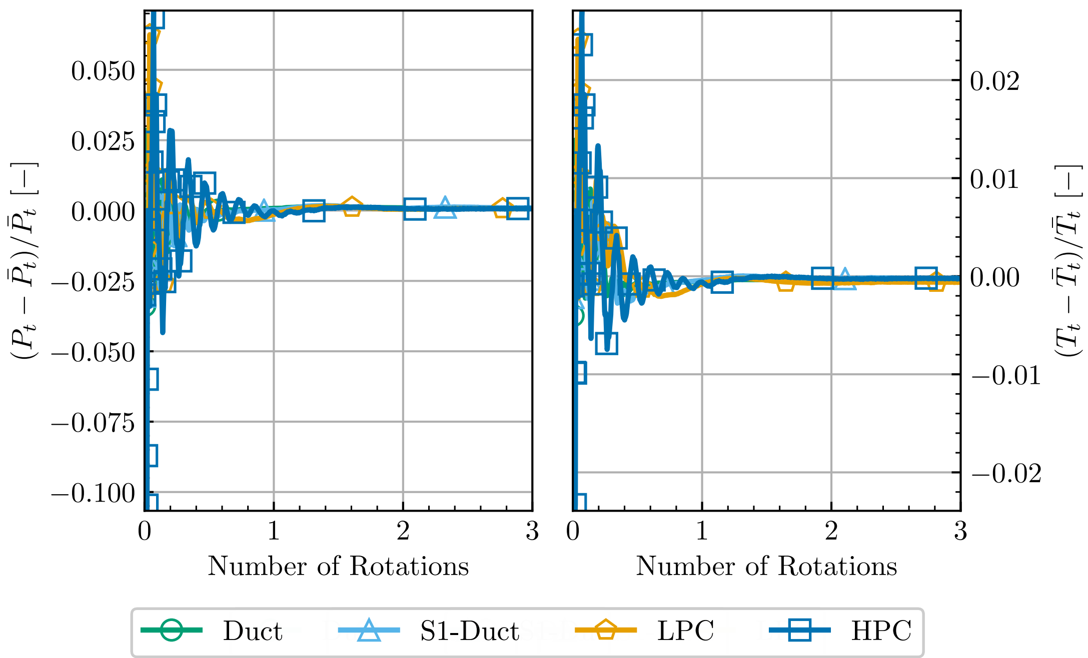

Figure **(6.4)** – Plots of averaged total pressure and total pressure time evolution.

From these two figures, it can be concluded that all the simulations have reached a satisfying convergence around the target mass flow in the time needed to perform three rotations of the rotor R1. In the following, results will be analyzed and discussed at the different comparison planes going downstream of the machine.

6.3.2 IGV1 Exit

First, at the IGV1 exit corresponding to the inlet of the (LPC) case, it is checked that the boundary condition correctly imposes radial profiles of total pressure, total temperature, and azimuthal angle and matches the experimental ones. The resulting Mach number is also found close to the experiment. Due to some experimental incertitude, radial profiles are plotted in distortion, looking at the relative variation of the quantity around its mean value. Only the azimuthal angle α is not plotted in distortion. In the following plots, the radial profiles corresponding to the inlet of the case will be omitted for clarity.

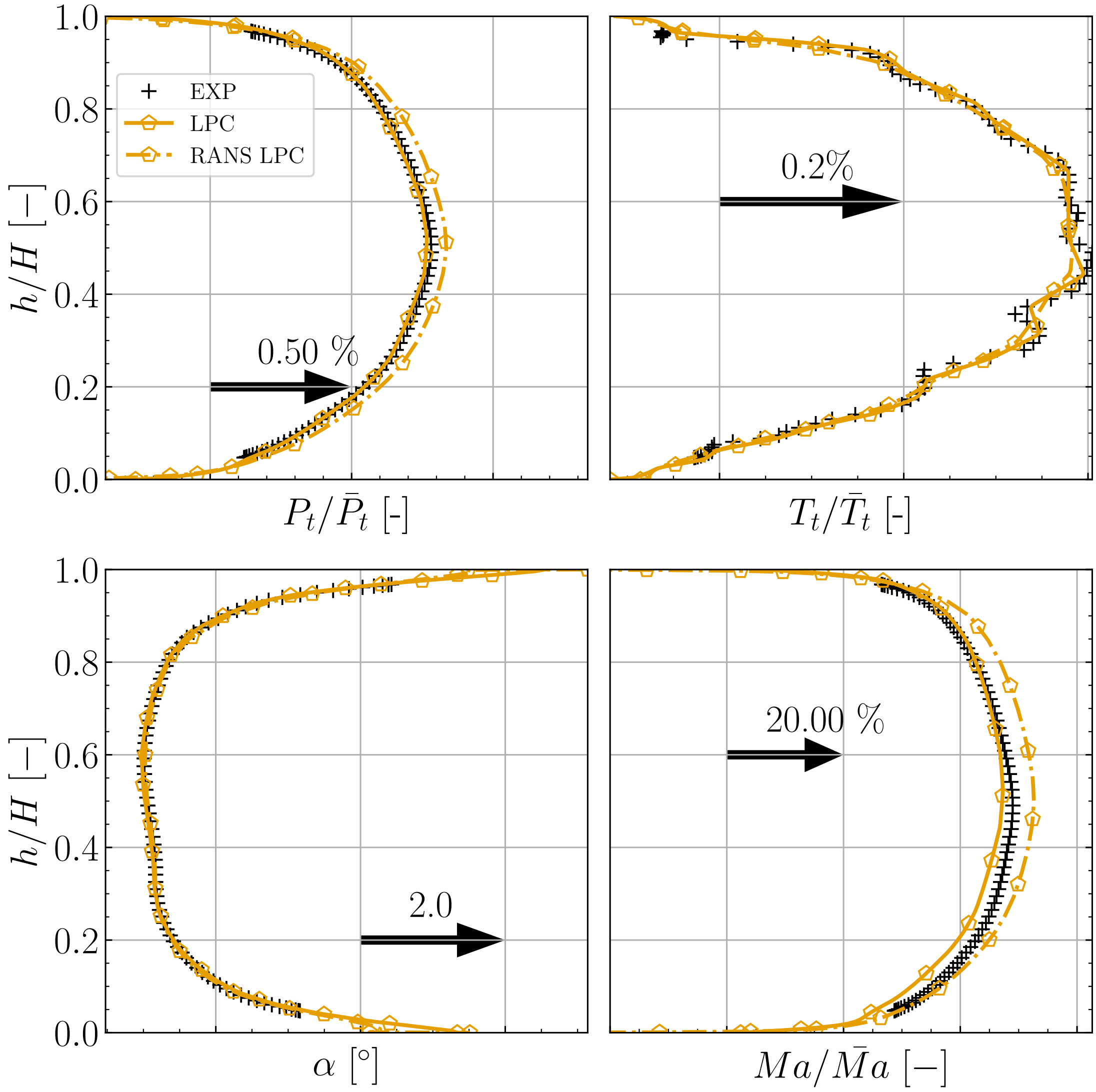

Figure **(6.5)** – Radial profiles at the IGV1 exit plane (1).

6.3.3 R1 Exit

Going downstream of the machine, at the R1 exit, it can be observed in Fig. 6.6 that the radial profiles predict the experimental trend of the different quantities correctly and even show some improvements compared to the RANS. However, a main zone of discrepancy can be observed at the shroud region, where an overestimation of total pressure and an inaccurate angle prediction are found. This is linked to the tip gap mesh resolution being too coarse, as previously observed in Chapter 5. Moreover, a slight break in the trend prediction of total pressure is observed at $h/H = 20\%$, corresponding to a flow separation occurring on the R1 blade in this region (see Fig. 6.7). Unfortunately, no information about the flow field in this region is available in the experiment.

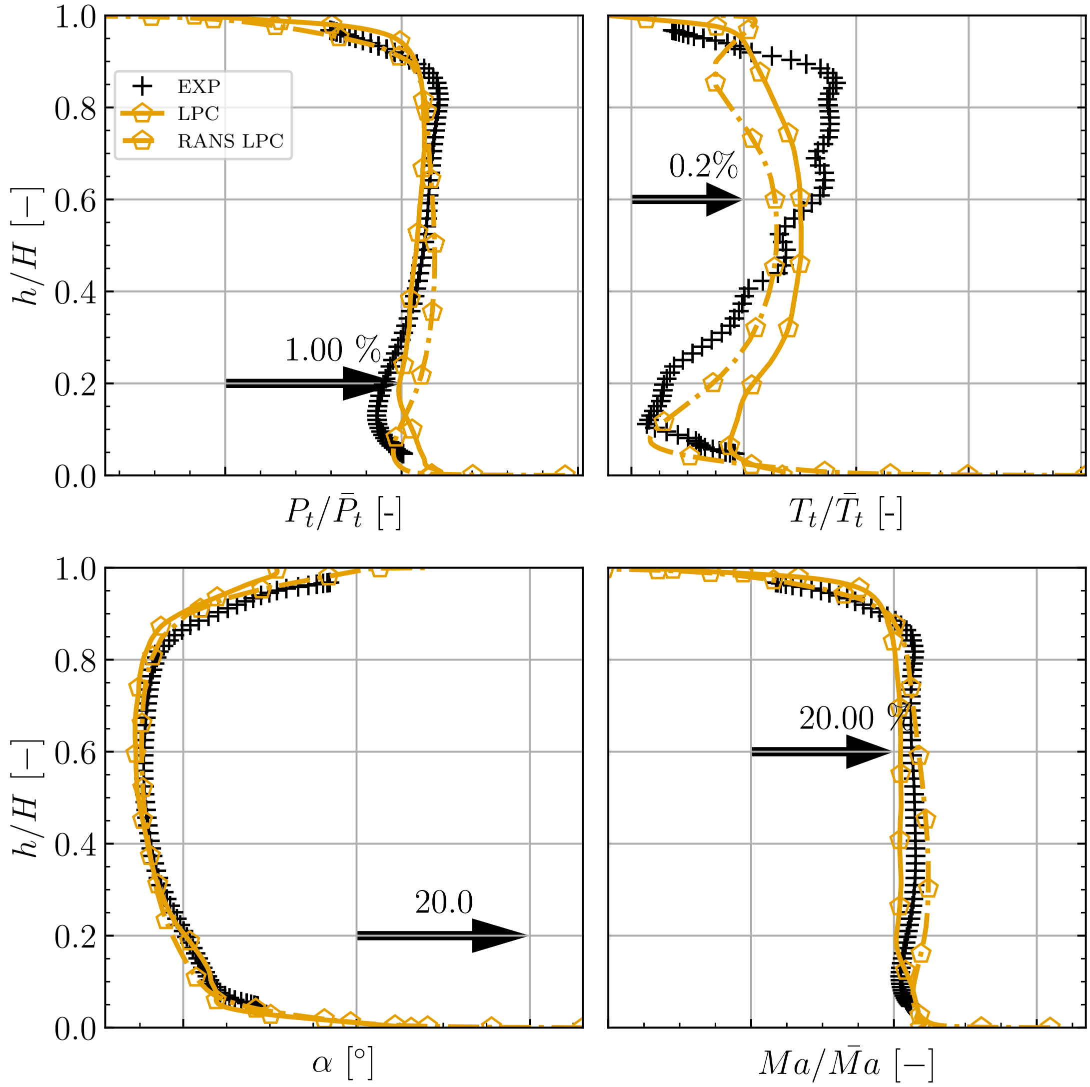

Figure **(6.6)** – Radial profiles at the R1 exit plane (2).

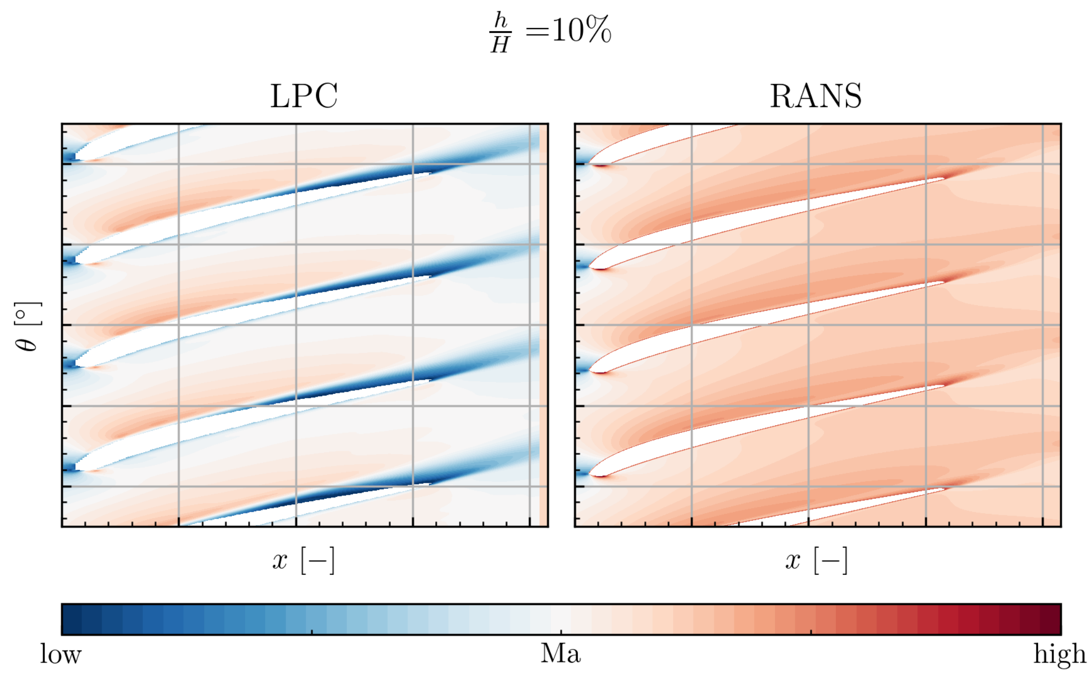

Figure **(6.7)** – Comparison between (LBM) and (RANS) of Mach number contour map at $h/H = 10\%$ around the R1 blade.

6.3.4 S1 Exit

At the S1 exit (see Fig. 6.8), radial profiles show good agreement with the experiment, and improvements compared to the RANS are noticeable. For the (LPC) case, the overestimation of the total pressure near the hub and shroud is transported from the previous plane through the stator. The total pressure trend is well captured on the remaining vein height. Concerning the Mach number, the trend corresponds well to the experiment except in the first 20%. Moreover, the azimuthal angle is especially well recovered compared to the RANS computations. Finally, the total temperature evolution is close to the RANS one but comparison to the experiment is difficult as the measurements appear particularly noisy. It should be noted that for the (S1-Duct) case, the results are very similar to the (LPC) case meaning that the turbulent inlet placed upstream is representative of the rotor R1. For both cases, the results show smaller relative error compared to the experimental profiles and better retrieval of their shape than the RANS. This is especially visible around $h/H = 20\%$, where the RANS retrieves a pretty flat profile of total pressure, whereas the LBM captures this specific inflection point in this zone. This is due to a better capture of the secondary flows created by the stator wakes in this region.

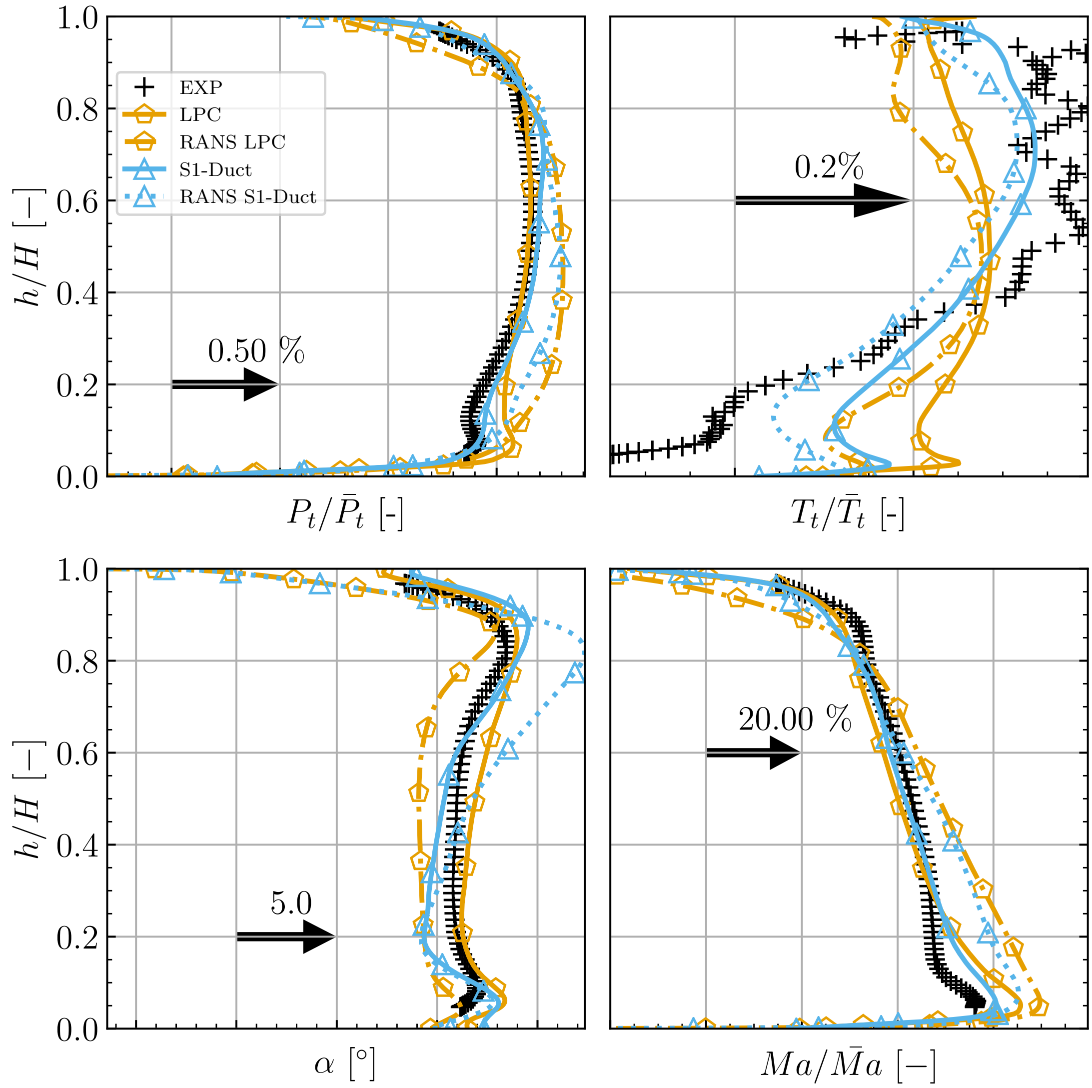

Figure **(6.8)** – Radial profiles at the S1 exit plane (3).

To explain the differences observed on the radial profiles, Fig. 6.9a illustrates the Mach number taken across a 15° azimuthal sector at different h/H and Fig. 6.9b compares the contour map of Mach number between the experiment and the computations at the S1 exit plane. For the (S1-Duct) case, the S1 stator wakes obtained match the experimental ones in terms of shape, direction, and peak level of Mach number with however a discrepancy in terms of thickness and a corner separation at 10% not found in the computation. This issue concerning thickness can be linked to a lack of resolution on the blade wall. Indeed, as the mesh uses the cut-cell approach, it is not body-fitted, leading to a boundary layer development on the blade surface too large that produces a thicker wake downstream. Finally, for the (LPC) case, it can be observed that the prediction of the wakes is similar to the (S1-Duct) case meaning that the turbulence injection for this case is representative of the actual rotor. Indeed, the wake thickness and peak level are pretty well captured compared to the experiment. The thickness of the wakes is still not precisely recovered as the boundary layer developing on the blades is too thick.

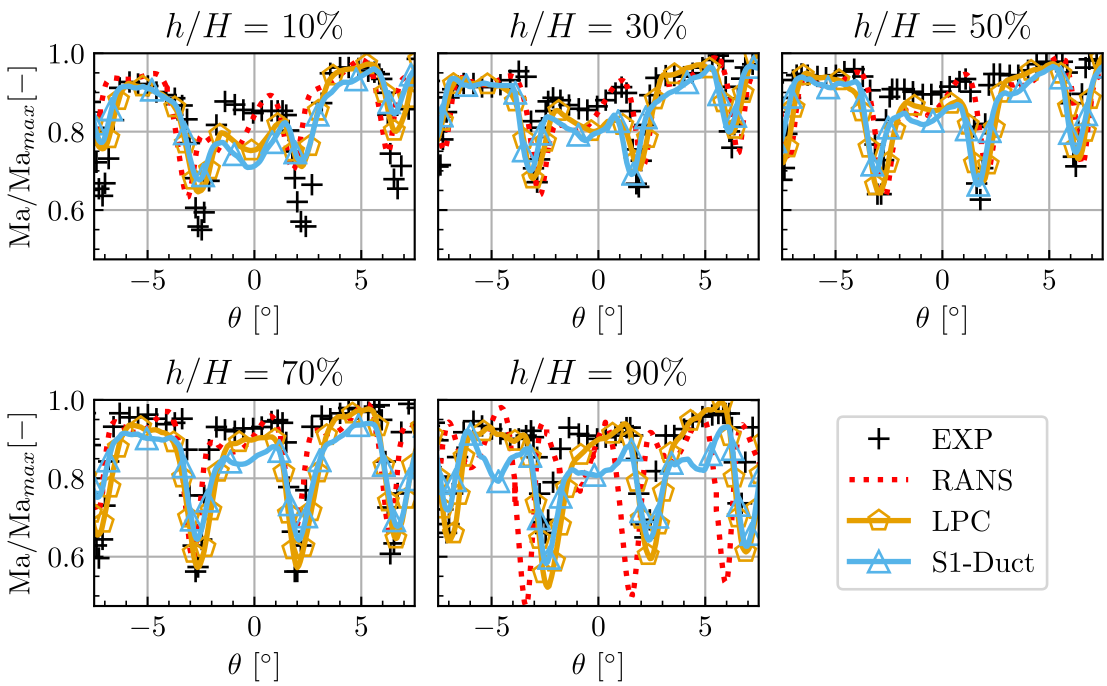

(a) Azimuthal profiles at the S1 exit plane (3).

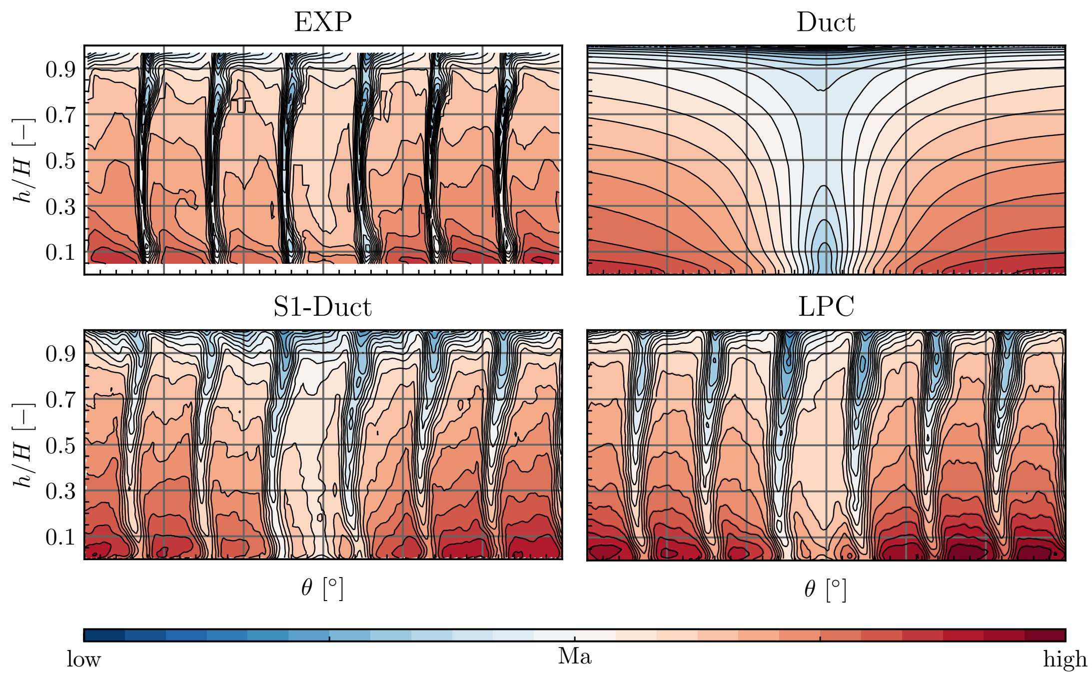

(b) 2D map of Mach number at the S1 exit plane (3) for case (Duct).

Figure **(6.9)** – Flow analysis at the S1 exit plane (3).

Additionally, Fig. 6.10 compares the contour map of the Mach number between the experiment, the RANS, and the LBM. It can be seen that the LBM retrieves slightly larger and more diffused wakes. Indeed, the octree mesh does not allow it to be body-fitted, introducing a loss of geometrical fidelity in this thin region. However, the flow topology is still close to the experiment and the RANS using a body-fitted mesh.

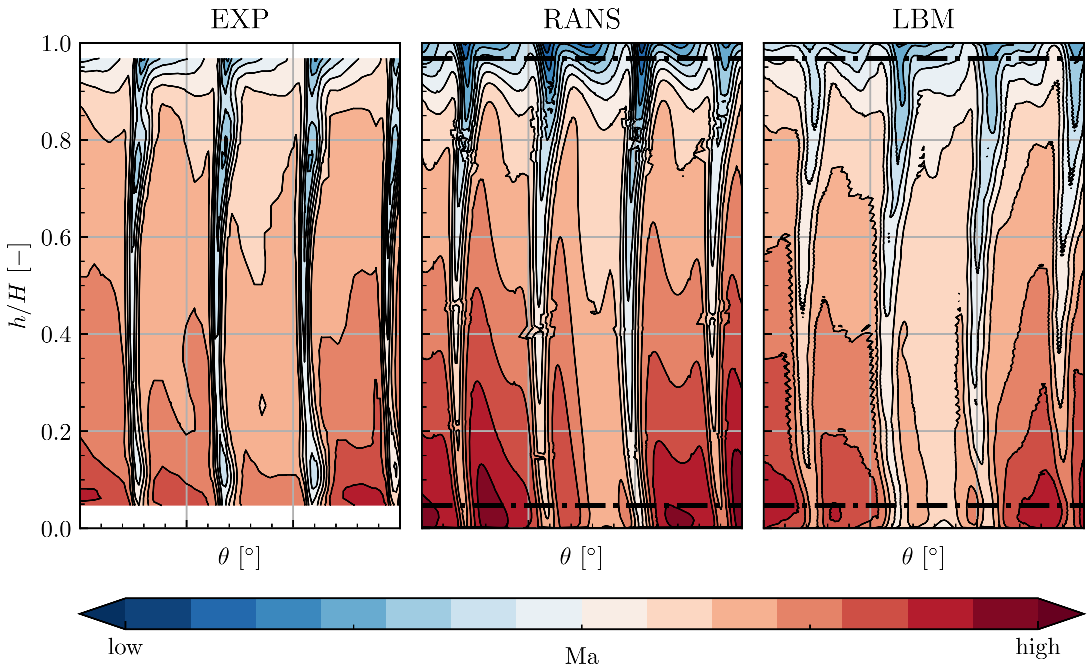

Figure **(6.10)** – Comparison of Mach number contour map between LBM and RANS at the S1 exit.

Fig. 6.11 illustrates the flow evolution around the S1 blade for cases (S1-Duct) and (LPC) at $h/H = 50\%$ compared to the RANS results. It shows that even though the flow remains attached on the suction side of the blade, the wake generated at the trailing edge is thicker than for the RANS. This is caused by a thicker boundary layer and difficulty in properly capturing the thin geometry of the trailing edge using Cartesian mesh.

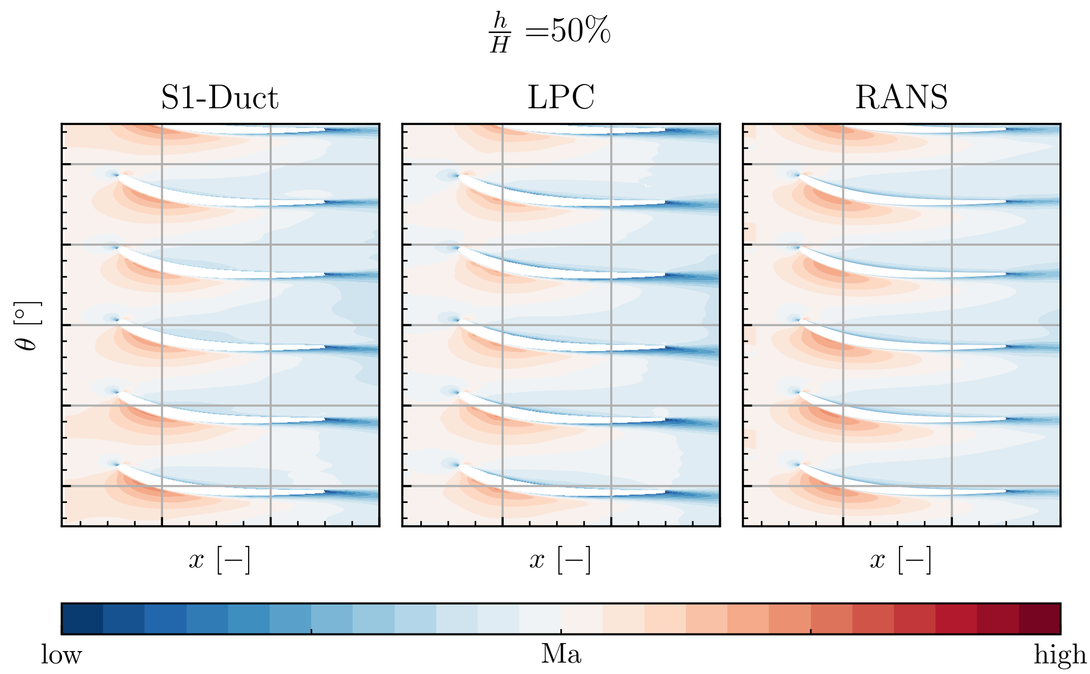

Figure **(6.11)** – Mach number contour map around the S1 blade at $h/H = 50\%$ for the different cases.

6.3.5 Duct Exit

Then, at the duct exit, several comments can be drawn on the radial profiles (see Fig. 6.12). For the (Duct) case, the profile trends are already in good agreement with the experiment in the mid-section of the vein but the major discrepancy is observed at $h/H = 20\%$. Indeed, an overestimation of the Mach number and total pressure, as well as a trend not corresponding to the experiment are observed in this zone. This trend was also found with the RANS computations. Moreover, the same results are obtained for the (HPC) case meaning that the downstream compressor does not influence the flow at this position. For clarity, the plots of the (HPC) case are withdrawn but presented in Appendix 8.2. It is interesting to observe that for the (S1-Duct) and (LPC) cases, the behavior is corrected at the hub, and the experimental trend is retrieved for the Mach number and total pressure. This means that it is necessary to take into account at least the upstream stator row to obtain the correct flow physic in the S-duct. These trends are closer to the experiment than the RANS results. For all cases, the LBM predicts a similar azimuthal angle evolution with less deviation from the experiment than the RANS. Concerning the total temperature, all the simulations give similar results.

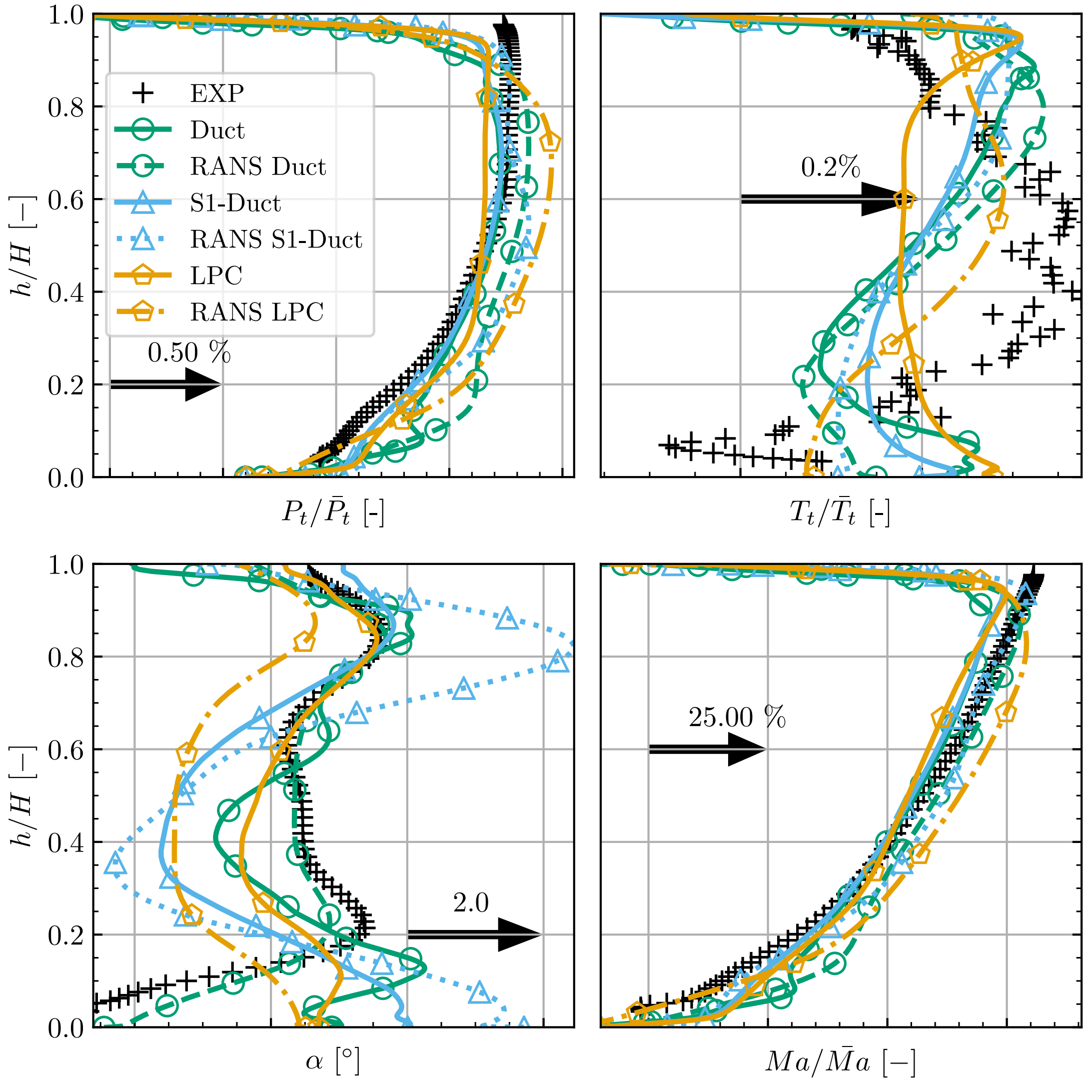

Figure **(6.12)** – Radial profiles at the Duct exit plane (4).

Additional results at the duct exit are illustrated in Figs 6.13a-6.13b. It shows that all the cases predict the same thickness and peak Mach number of the strut wake. However, the peak Mach number in the wake is generally overestimated compared to the experiment. At 10%, this can be explained by the absence of the corner separation on the S1 blades compared to the experimental observations. This will affect the flow structures and their migration along the hub wall. For the (Duct) case, the wake seems destabilized compared to the others. This is explained by the difference in inlet flow perceived by the strut blade where, for the other cases, S1 wakes are impacting it with a specific clocking, creating a difference in terms of the azimuthal angle at the leading edge. When upstream rows are included, it is clear that a higher level of turbulence is developing in the duct. A zone of low momentum fluid has accumulated at the hub, explaining the total pressure change observed on the radial profiles in this part of the vein. Moreover, it should be noted that the RANS computation failed to predict the correct direction of the strut wake.

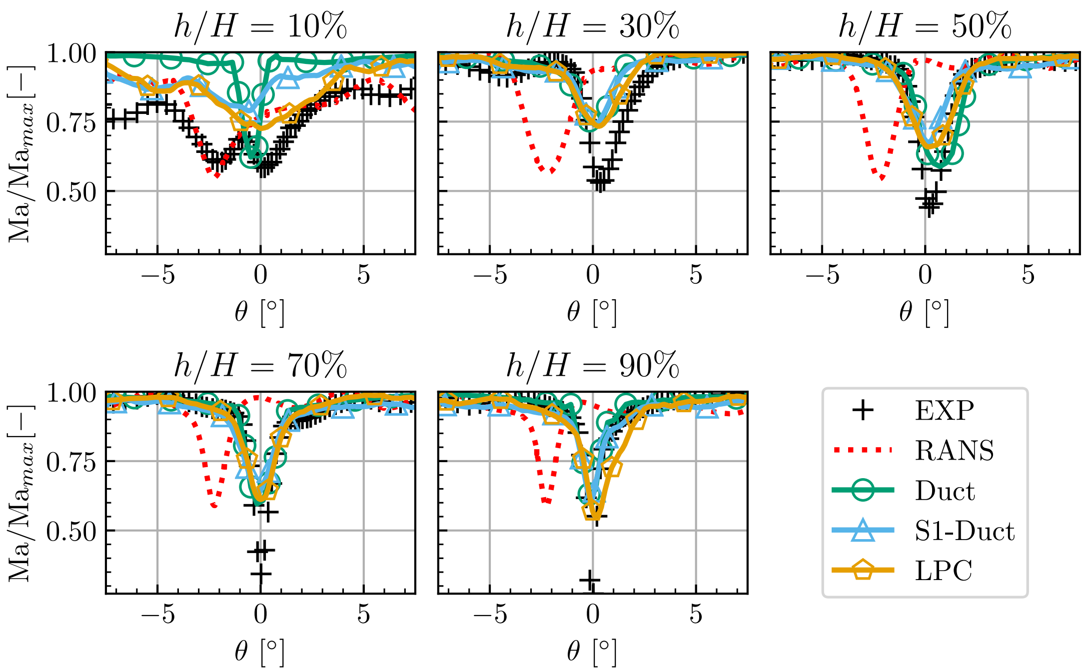

(a) Azimuthal profiles at the Duct exit plane (4) for case (Duct).

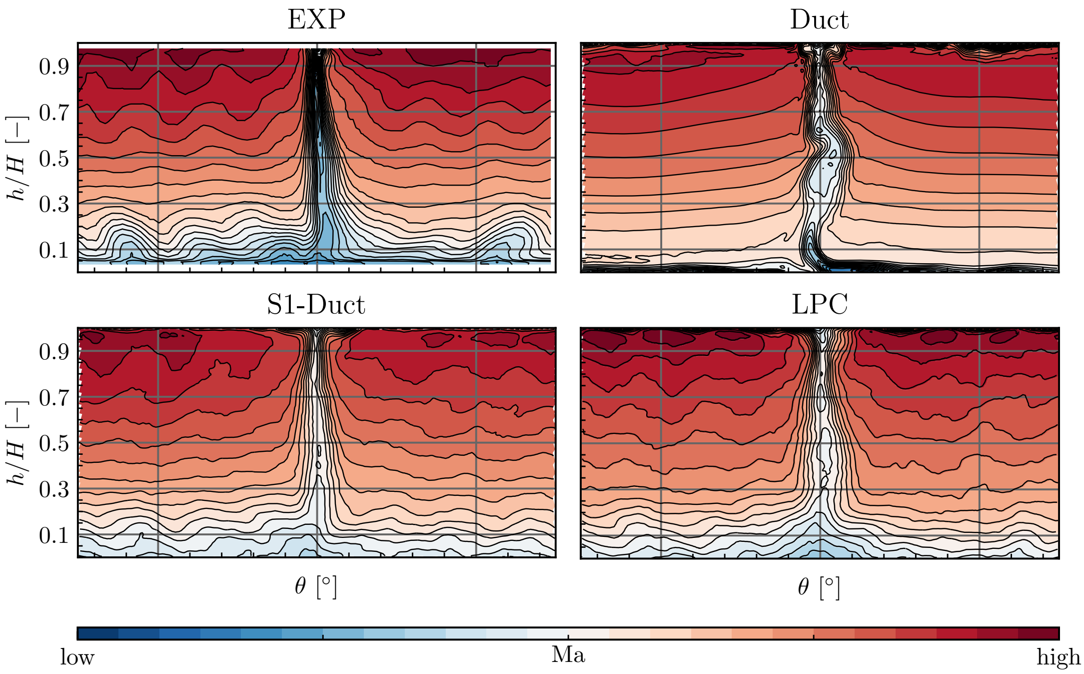

(b) 2D map of Mach number at the Duct exit plane (4) for case (Duct).

Figure **(6.13)** – Flow analysis at the Duct exit plane (4).

The RANS computations were also found to have difficulty predicting the strut wake direction. Moreover, Fig. 6.14 illustrates that even though the LBM does not capture the correct Mach number in the strut wake, the flow structures correspond well to the experiment.

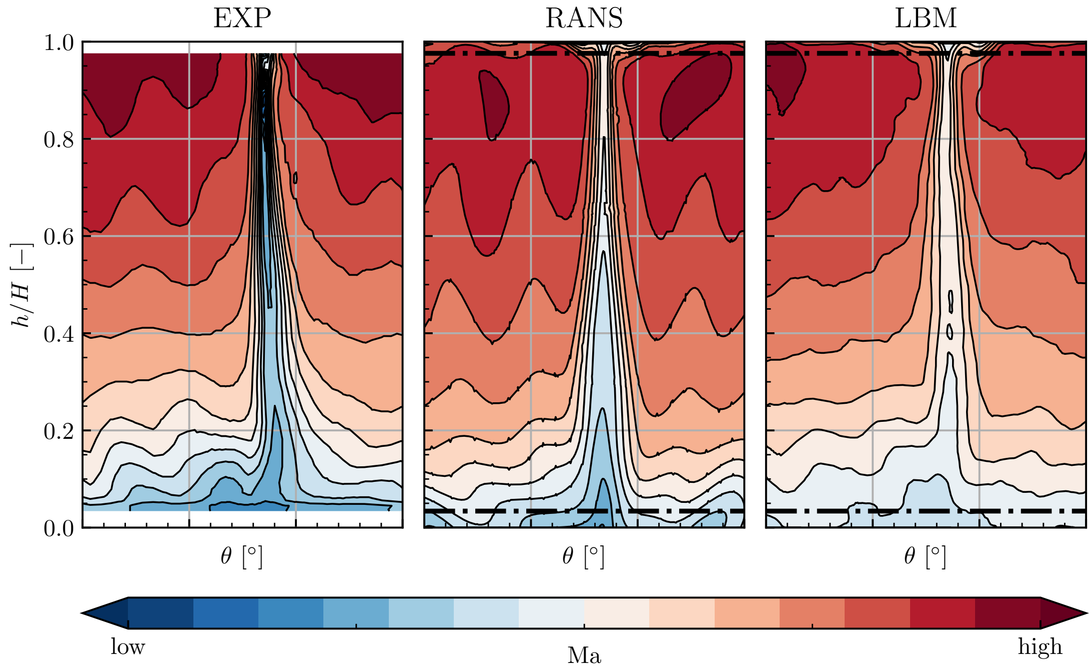

Figure **(6.14)** – Comparison of Mach number contour map between LBM and RANS at the Duct exit.

6.3.6 IGV2 Exit

Next, at the IGV2 exit (Fig. 6.15), it is illustrated that for the Mach number and total pressure profiles, the LBM results recover a trend closer to the experiment than the RANS. For the (S1-Duct) and (LPC) cases, the same improvement near the hub due to the upstream wake introduction is also found. Finally, all simulations closely predict azimuthal angle and total temperature. At this plane, the influence of the HPC stage was also negligible, with almost identical results between the (Duct) and (HPC) cases.

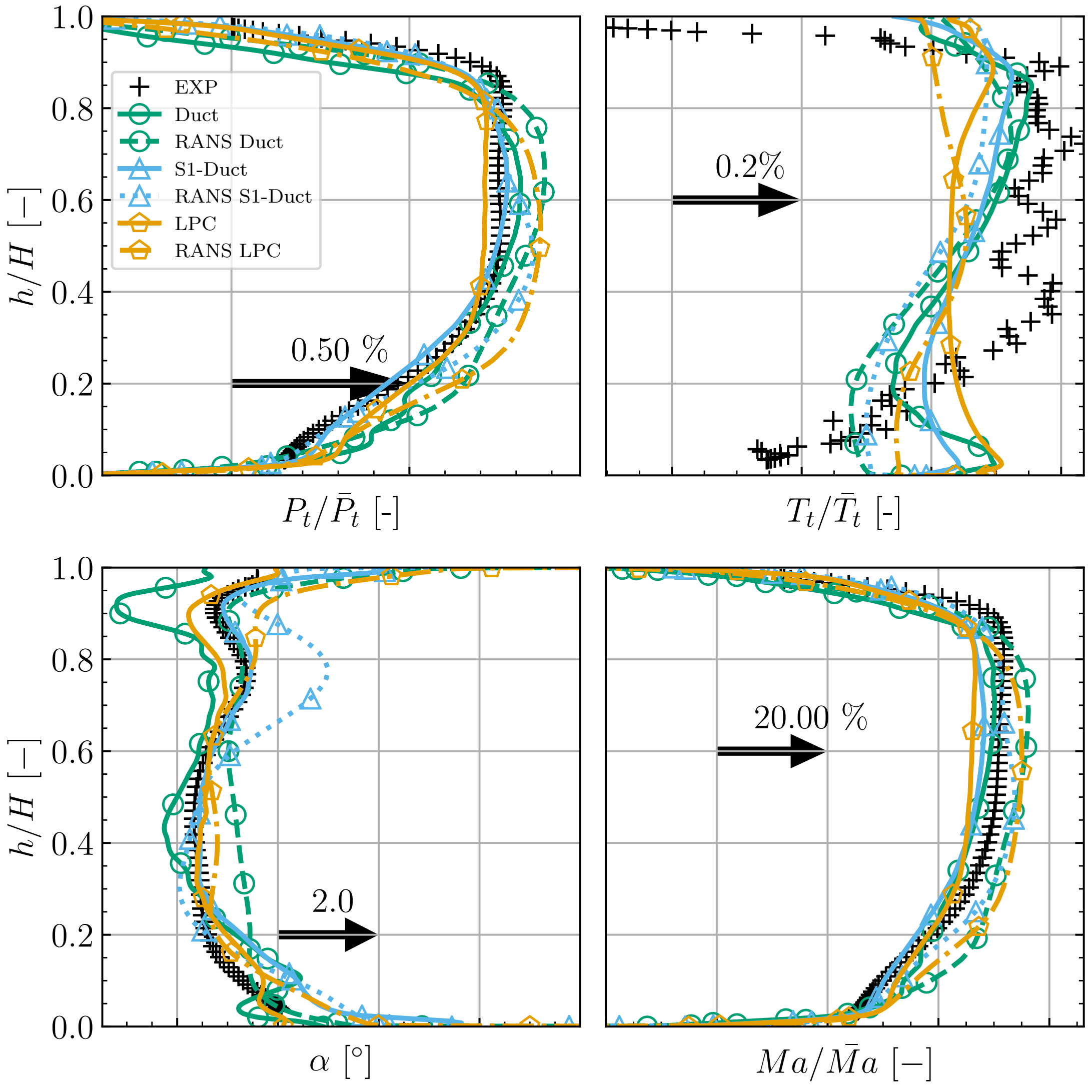

Figure **(6.15)** – Radial profiles at the IGV2 exit plane (5).

Figs 6.16a- 6.16b illustrates that the wake direction is well matched as well as the peak values in the wakes for all cases but are predicted a bit too thick. This is caused by an especially thin trailing edge difficult to capture with the octree elements. Finally, the trace of the strut wake of the previous plane is also well captured as well as the pair of vortex near the shroud generated by a strut-shroud corner separation.

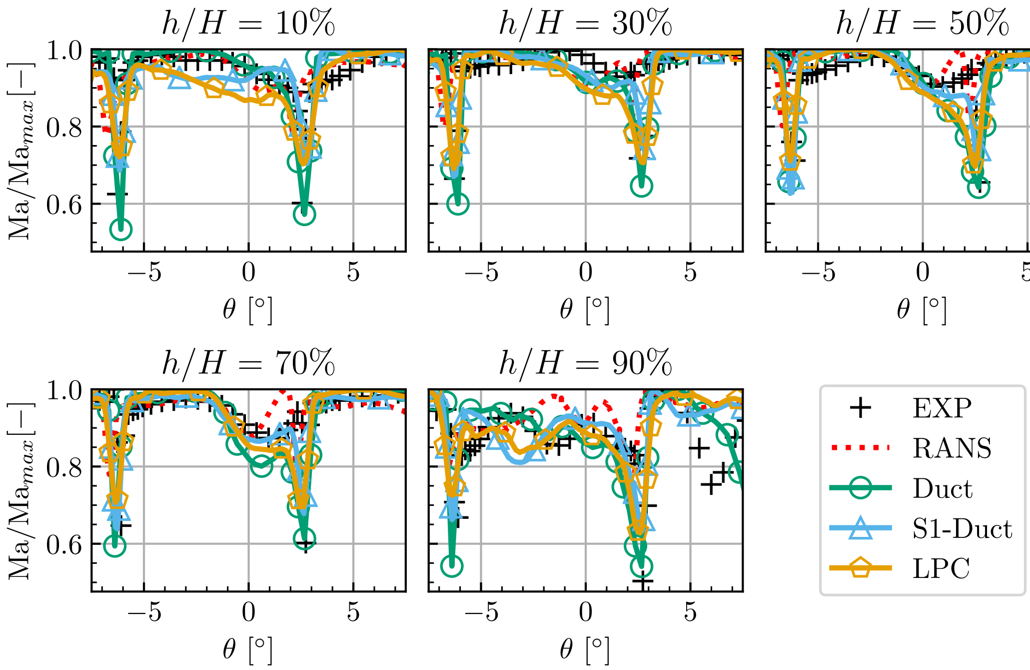

(a) Azimuthal profiles at the IGV2 exit plane (5).

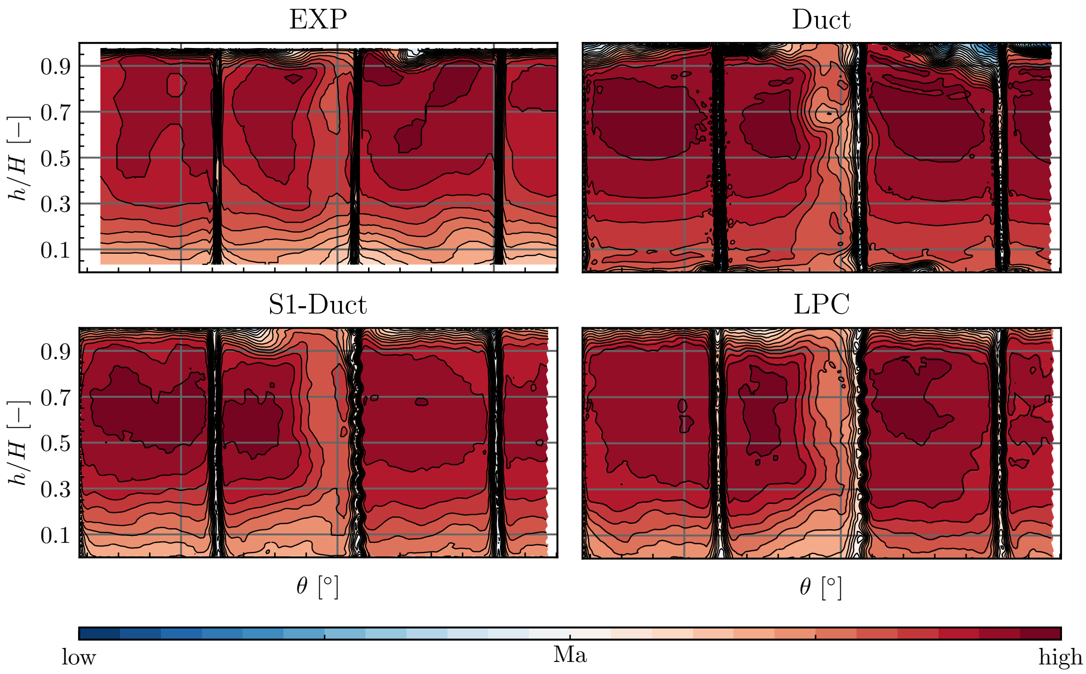

(b) 2D map of Mach number at the IGV2 exit plane (5) for case (Duct).

Figure **(6.16)** – Flow analysis at the IGV2 exit plane (5).

6.3.7 R2 Exit

For the (HPC) case, results at the R2 exit are illustrated in Fig. 6.17. The trend of total pressure is especially well retrieved compared to the experiment and shows a large improvement compared to the RANS. For the azimuthal angle, a result similar to the one obtained at the R1 exit is observed with a discrepancy around $h/H = 90\%$ due to the difficulty of properly capturing the tip gap effect. Finally, the LBM is closer to the experimental profile for the Mach number than RANS, showing a better capture of secondary flows exiting the rotor.

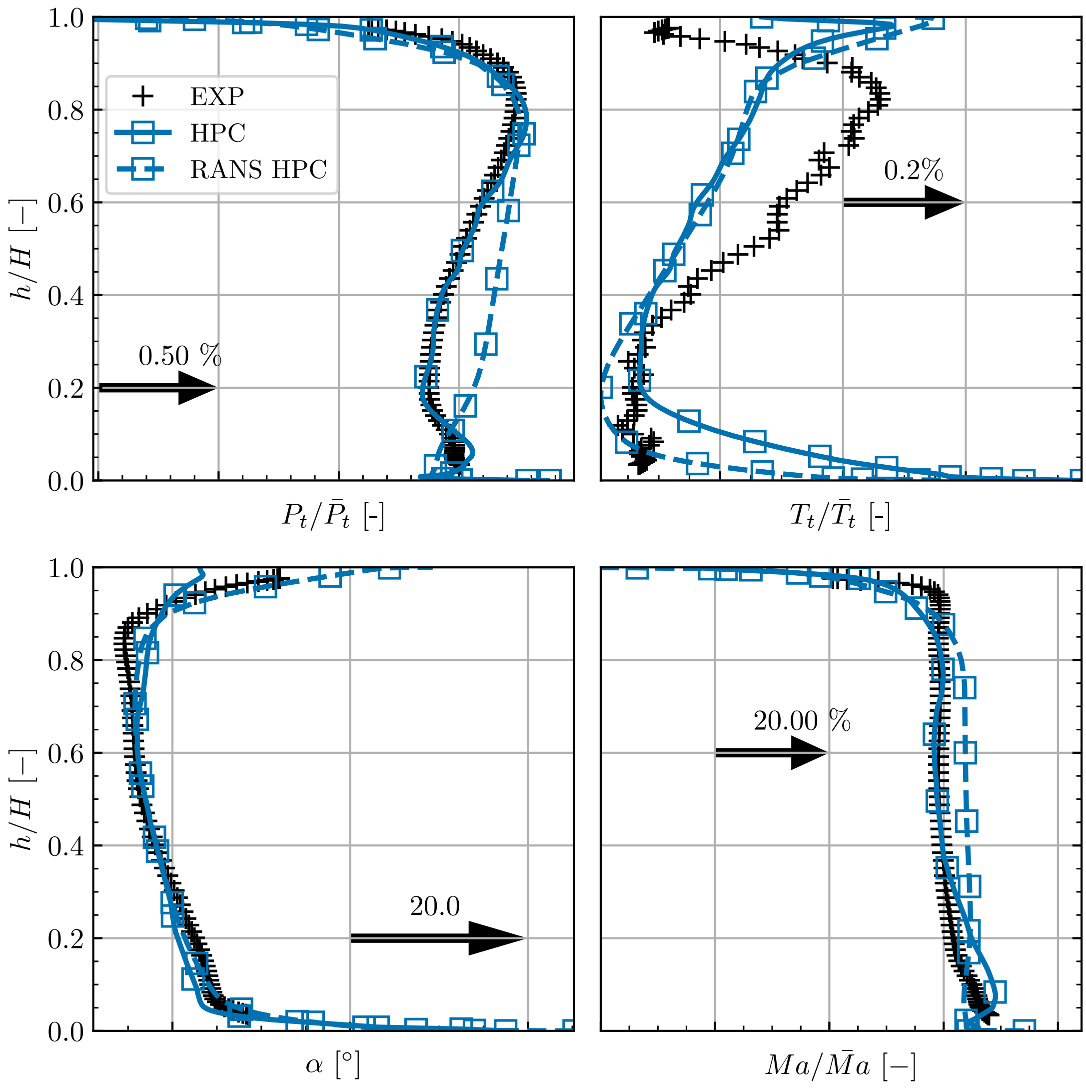

Figure **(6.17)** – Radial profiles at the R2 exit plane (6).

6.3.8 S2 Exit

Finally, at the S2 exit (Fig. 6.18, the trend of total pressure, azimuthal angle, and Mach number are especially well recovered with the LBM. RANS and LBM give similar results for the total temperature, which deviate from the experiment. Considering the variations previously observed on this quantity and the experimental uncertainties, the measurements are considered as not representative.

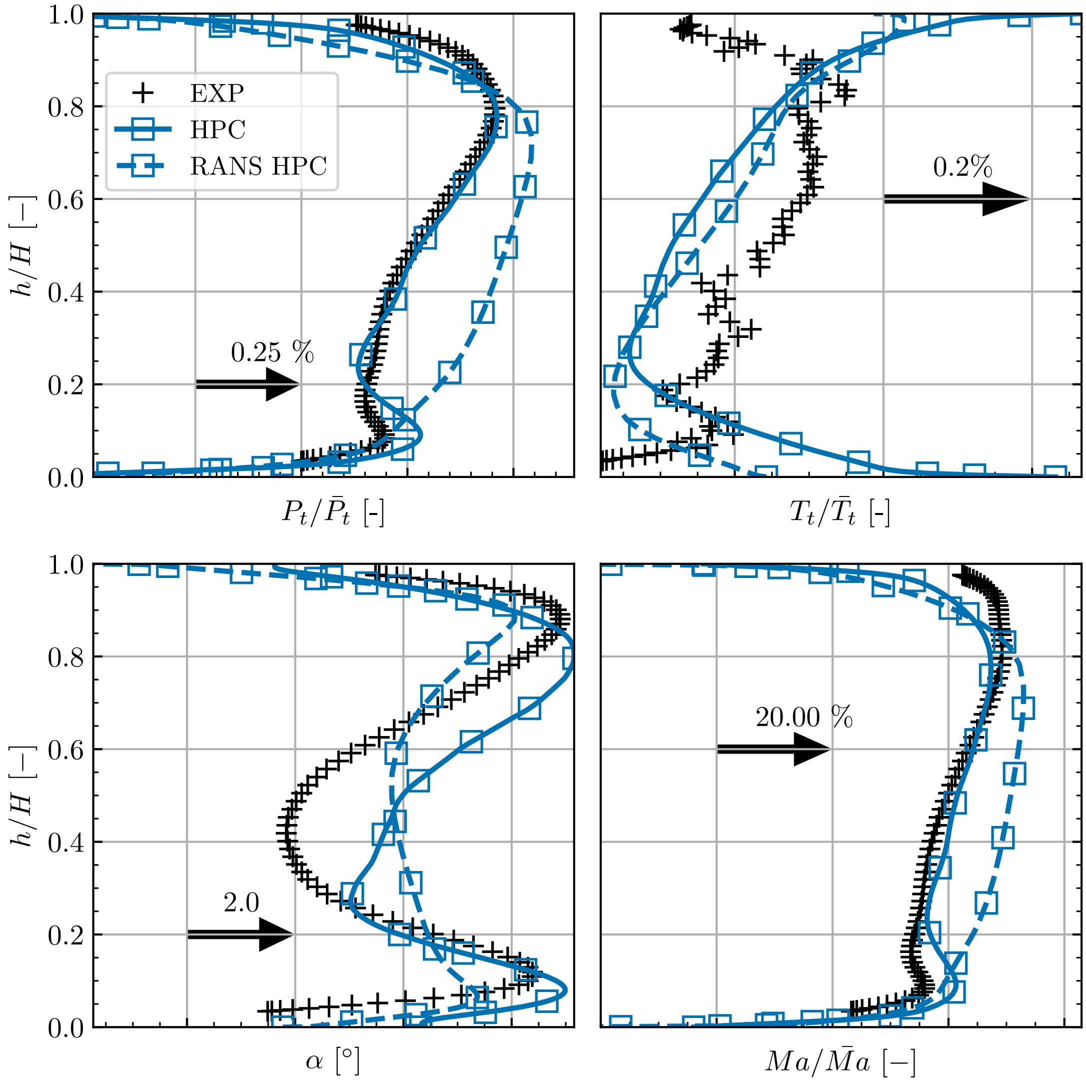

Figure **(6.18)** – Radial profiles at the S2 exit plane (7).

Finally, at the S2 exit plane, it can be observed a similar result to the one at the S1 exit plane. The wake direction and peak Mach number level are well captured unless at 50% and 70% where the wakes are too large and too slow down.

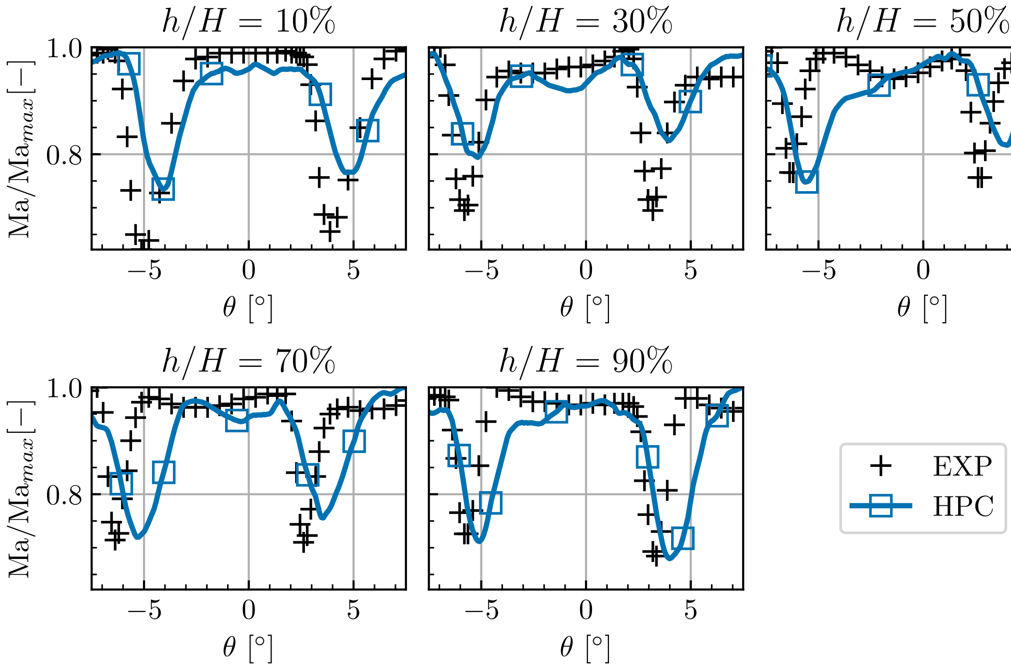

(a) Azimuthal profiles at the S2 exit plane (7).

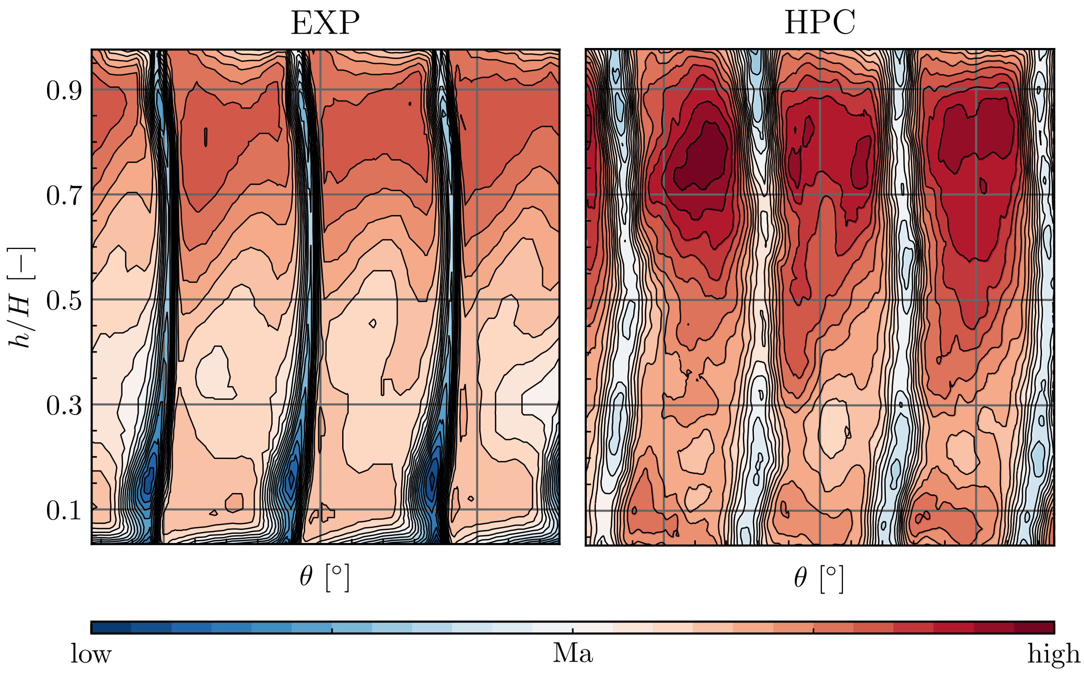

(b) 2D map of Mach number at the S2 exit plane (5) for case (Duct).

Figure **(6.19)** – Flow analysis at the S2 exit plane (5).

6.4 Loss Generation Mechanism

6.4.1 Total Pressure Losses

The total pressure loss is defined as $Y_{pt} = \frac{P_{t,out}-P_{t,in}}{P_{t,in}-P_{s,in}}$ with the inlet plane located at the plane (3) and the outlet at the plane (4). Radial profiles of this loss coefficient are represented in Fig. 6.20 for all cases and compared to RANS. As the radial profiles of the (Duct) and (HPC) cases are almost identical, the loss profile of the (HPC) case has been omitted for clarity here. The figure highlights that for the (Duct) case, the loss level is largely underestimated compared to the experiment. The RANS computation recovers a similar result with a larger loss level close to the hub. Additionally, for the (S1-Duct) and (LPC) cases, the prediction is improved with the best match obtained for the (S1-Duct) case. The same conclusion is reached for RANS with still an underestimation compared to the experiment. This observation is coherent with the literature [23] and confirms the necessity to include at least the upstream stator row to capture the full physic developing in the S-duct. The best agreement of the (S1-Duct) case is explained by the more realistic S1 wakes entering the duct as shown previously in Fig. 6.9a. However, the global level is still underestimated compared to the experiment. It can be explained by the over-prediction of the Mach number in the strut wake. Indeed, the flow is not as slow as in the experiment, leading to lower loss generation. Finally, the predicted loss level is especially low, requiring an accuracy on the total pressure variations of around 100 Pa, around the experimental accuracy.

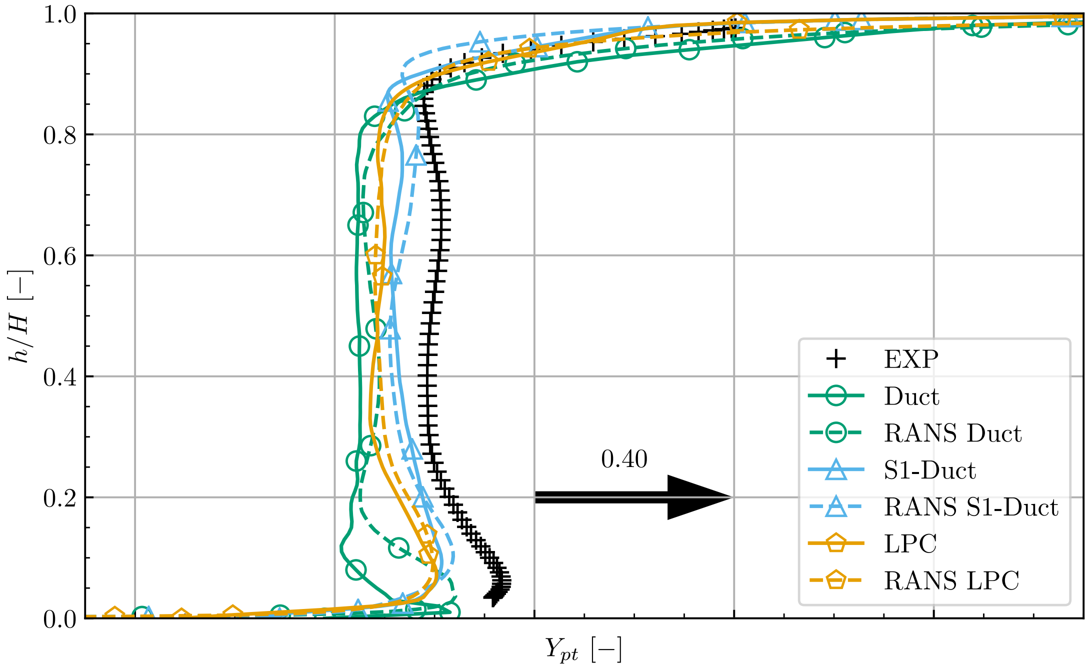

Figure **(6.20)** – Plots of the total pressure loss for the different cases.

6.4.2 Extension of the Loss Analysis using an Entropy Formulation

This section presents the work performed to deepen the analysis of the loss generation mechanism occurring in an S-duct. In the previous section, losses were assessed using a total pressure coefficient. This corresponds to a usual practice when studying S-duct losses [23, 27, 12]. This approach is especially convenient as the required quantities are easily obtained during the experiment. However, previous studies have shown that the stagnation loss coefficient can misrepresent the overall loss distributions, particularly when secondary flows are involved [163]. An entropy formulation has been applied to avoid these issues and gain additional insight into the loss generation mechanism. The same approach as the one presented in [164] has been used. A volumetric entropy source term, denoted S, is defined as:

$$S = S_{Visc} + S_{Therm} \tag{6.3}$$

$$S_{Visc} = \frac{1}{T}\tau_{ij}\frac{\partial V_i}{\partial x_j} \tag{6.4}$$

$$S_{Therm} = \frac{k_{eff}}{T^2}\left(\frac{\partial T}{\partial x_j}\right)^2 \tag{6.5}$$

with k_{eff} being the effective thermal conductivity and τ_{ij} the shear stress tensor. S_{Visc} is the entropy generation rate per unit volume due to viscous effects, and S_{therm} is the entropy generation rate per unit volume due to thermal mixing. The entropy generation rate is computed by accumulation across the duct by integrating the volume between the inlet plane and the following plane at $x_{in} + d$. The distance d corresponded to the coarsest grid size encountered in the fluid domain. Figs. 6.21-6.22 show the accumulated entropy terms S_{Visc} and S_{Therm} through the S-duct for the (Duct) and (S1-Duct) cases. For the (Duct) case, the entropy is progressively generated along the duct with a slightly more pronounced increase close to the Duct outlet due to the strut wake at the trailing edge. However, a low level of entropy is generated across the duct compared to the (S1-Duct) case, which is in agreement with the evolution of the loss pressure coefficient (Fig 6.20). Moreover, as expected for this configuration, the S_{Therm} part remains negligible, considering that the walls are adiabatic and no major temperature gradients exist in the machine.

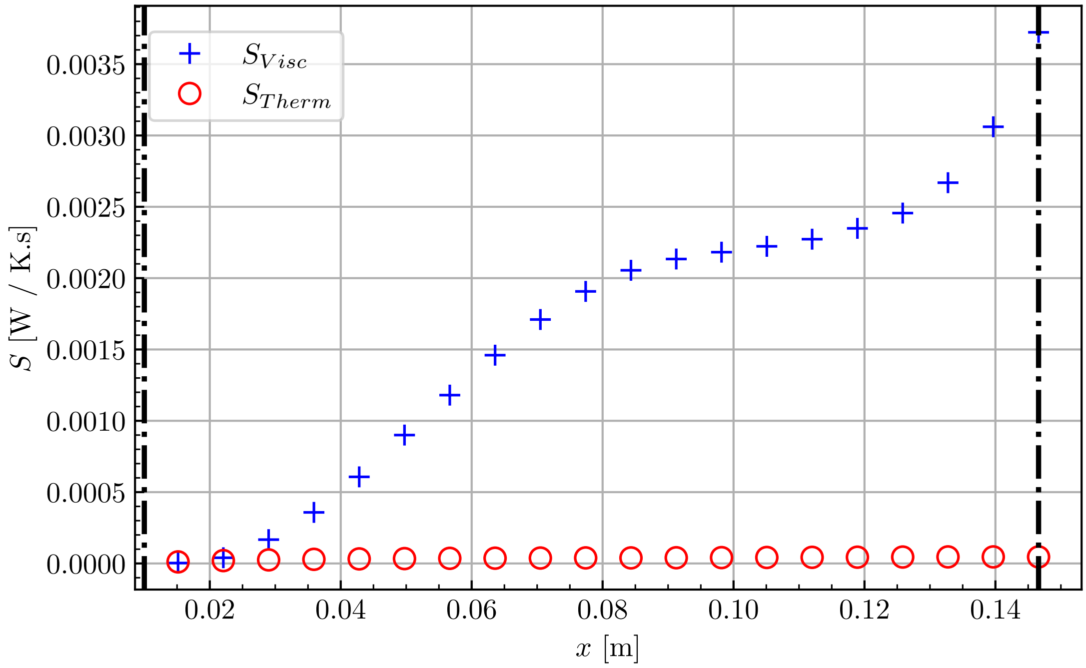

Figure **(6.21)** – Plot of accumulated S_{visc} and S_{therm} terms through the S-duct for case (Duct).

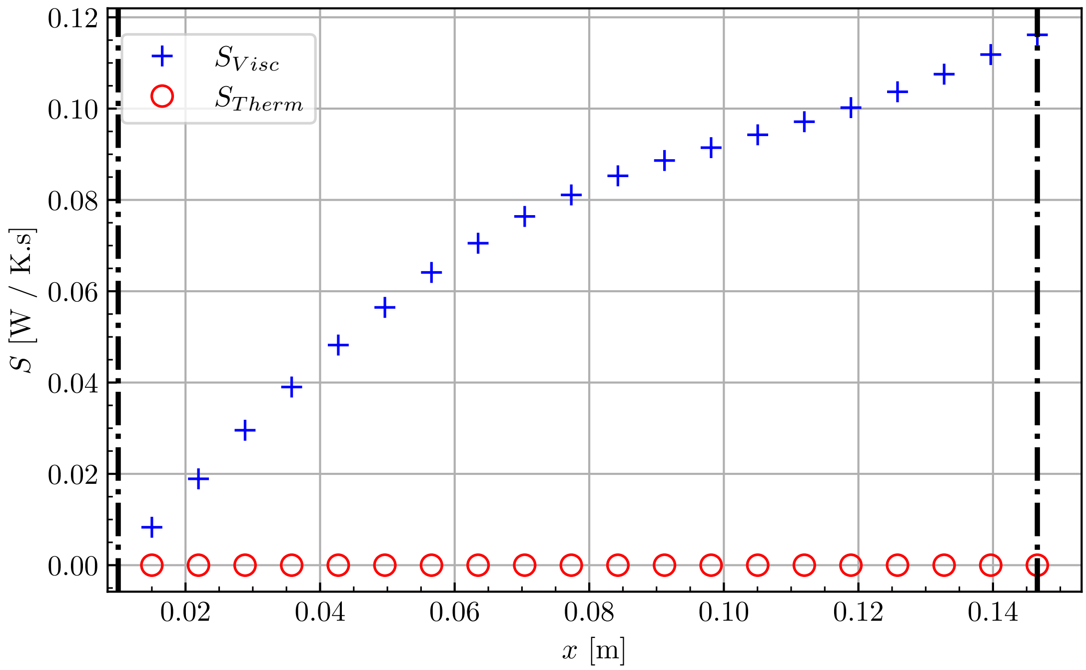

Figure **(6.22)** – Plot of accumulated S_{visc} and S_{therm} terms through the S-duct for case (S1-Duct).

To further analyze the results, the Duct geometry is divided into three zones see Fig.

(6.23):

- Hub 25% that encompasses the region from the hub to 25% of height.
- Shroud 75% that includes the region from the shroud to 75% height.
- Mid 50% that comprises the region between the hub 25% and the shroud 75%.

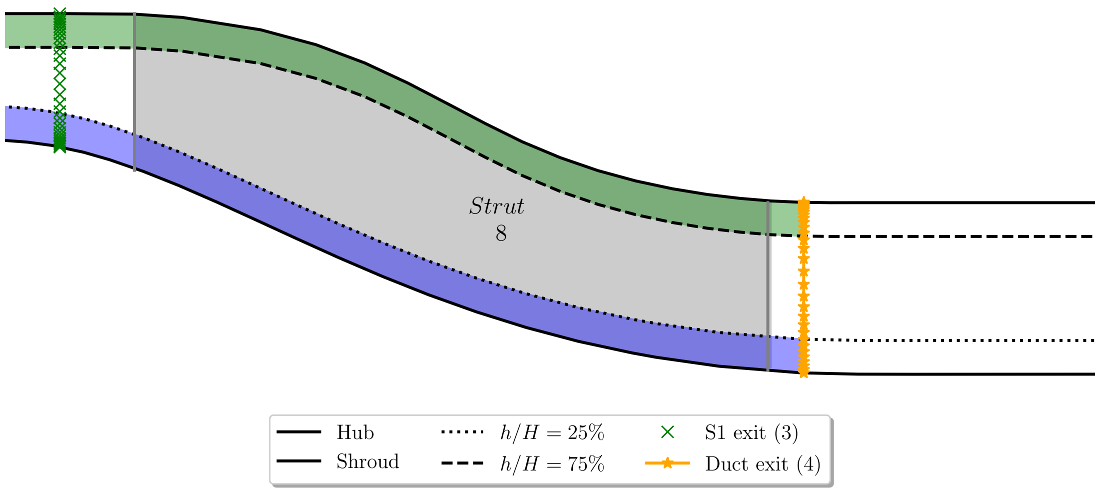

Figure **(6.23)** – Illustration of the Duct vein zone separation.

Considering that the thermal contribution is negligible in this case, only S_{visc} is included for clarity in the following plots. Figs. 6.24-6.25 present the accumulated entropy generation through the duct for the (Duct) and (S1-Duct) cases, respectively. For the (Duct) case, the entropy is quickly generated in the first half of the duct at the shroud due to the boundary layer development. Then, an additional contribution is produced at the strut trailing edge, leading to a similar level at the end of the duct for the three zones. However, a discrepancy is observed for S_{50} as a negative value is obtained in this duct part. This is due to the difficulty of accurately computing the velocity gradients in the middle of the vein where the fluid has the largest mesh size. Moreover, as the entropy values involved are especially small, the numerical errors introduced by the coarse gradient computations are of the same order of magnitude.

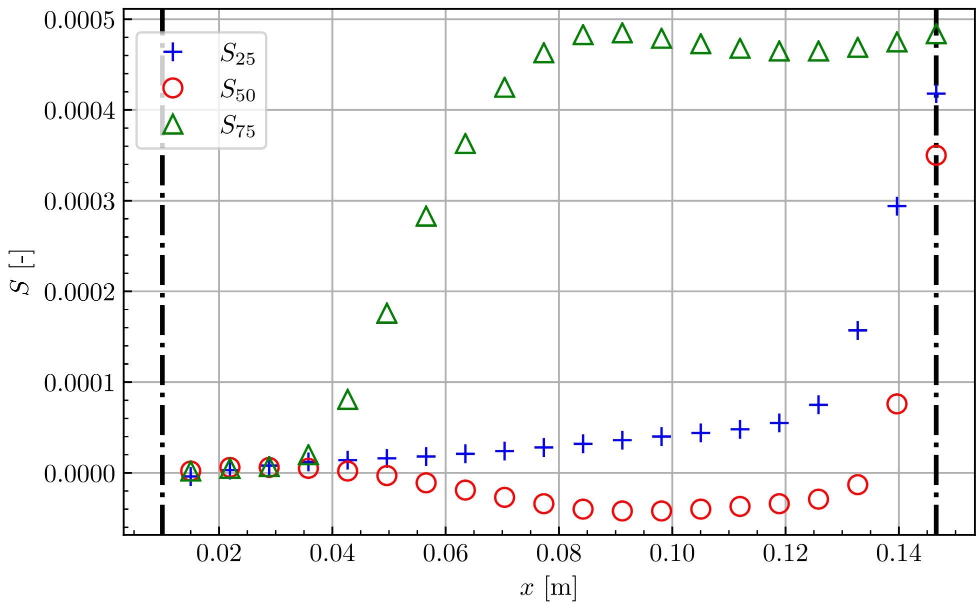

Figure **(6.24)** – Plot of accumulated entropy through the S-duct in the different zones for case (Duct).

On the other hand, for the (S1-Duct) case, a rapid and larger entropy growth is seen through the S-duct. Moreover, it shows that a more significant entropy generation is happening in the hub 25% zone compared to the others. This is coherent with observing the low momentum zone accumulating in this area.

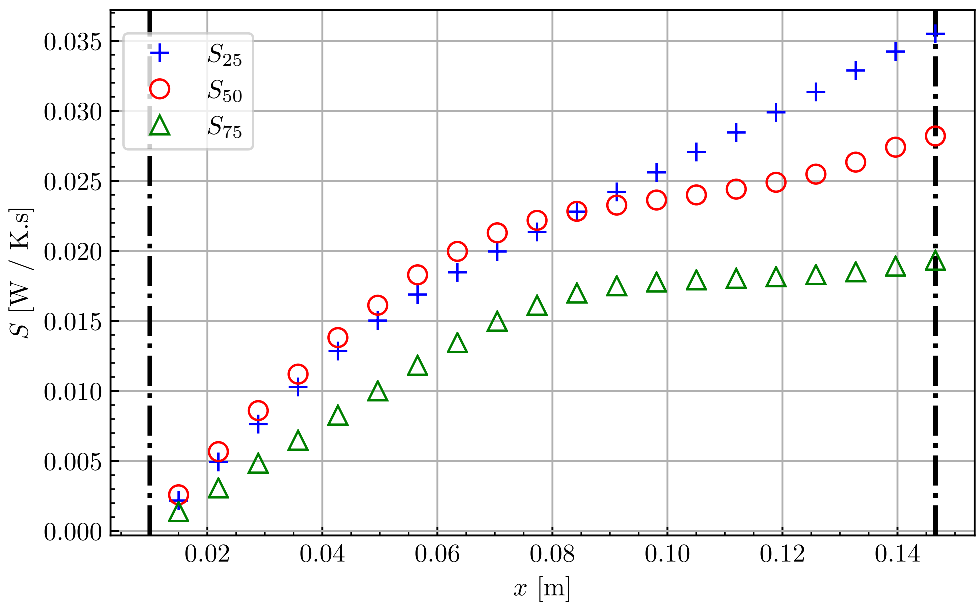

Figure **(6.25)** – Plot of accumulated entropy through the S-duct in the different zones for case (S1-Duct).

Fig. 6.26 compares the contour map of Mach number at the duct exit with a contour of entropy generation rate. It shows that zones of high entropy generation are found in the boundary layer at the shroud, in the strut wake, and a zone taking around 20% of the vein near the hub corresponding to the stator wake migration towards the hub.

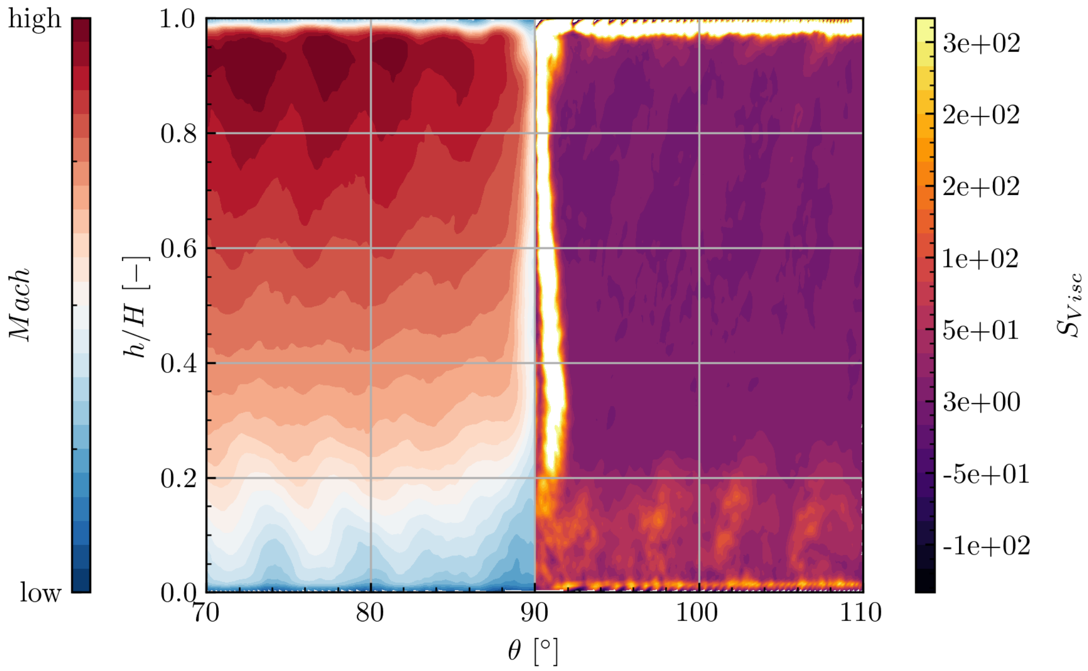

Figure **(6.26)** – Contour plot of entropy generation rate and Mach number at the duct exit for case (S1-Duct).

To further illustrate this high loss generation near the hub, contour maps of entropy generation rate and Mach number are shown at two different h/H in Figs. 6.27-6.28. For $h/H = 5\%$, zones of high entropy are found across all the duct length and correspond to the decelerating wakes due to the strong adverse pressure gradient and friction at the wall. However, at $h/H = 50\%$, entropy loss is generated at the duct inlet due to the entering wakes, but the effect is quickly suppressed as the flow is accelerated in this region.

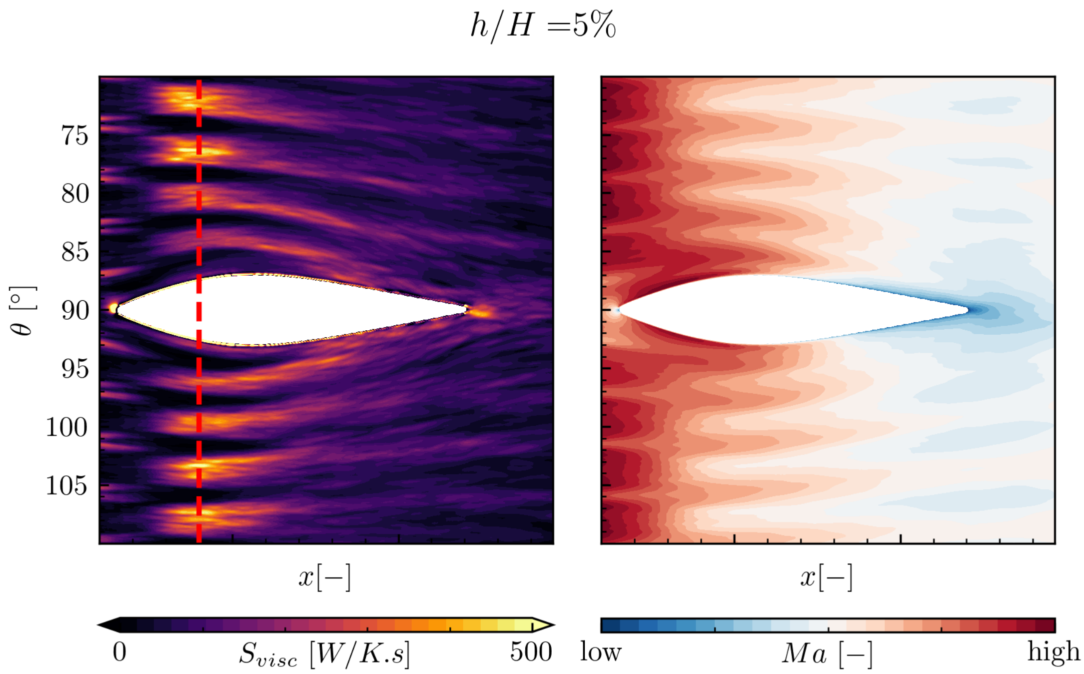

Figure **(6.27)** – Contour plot of entropy generation rate and Mach number at $h/H = 5\%$.

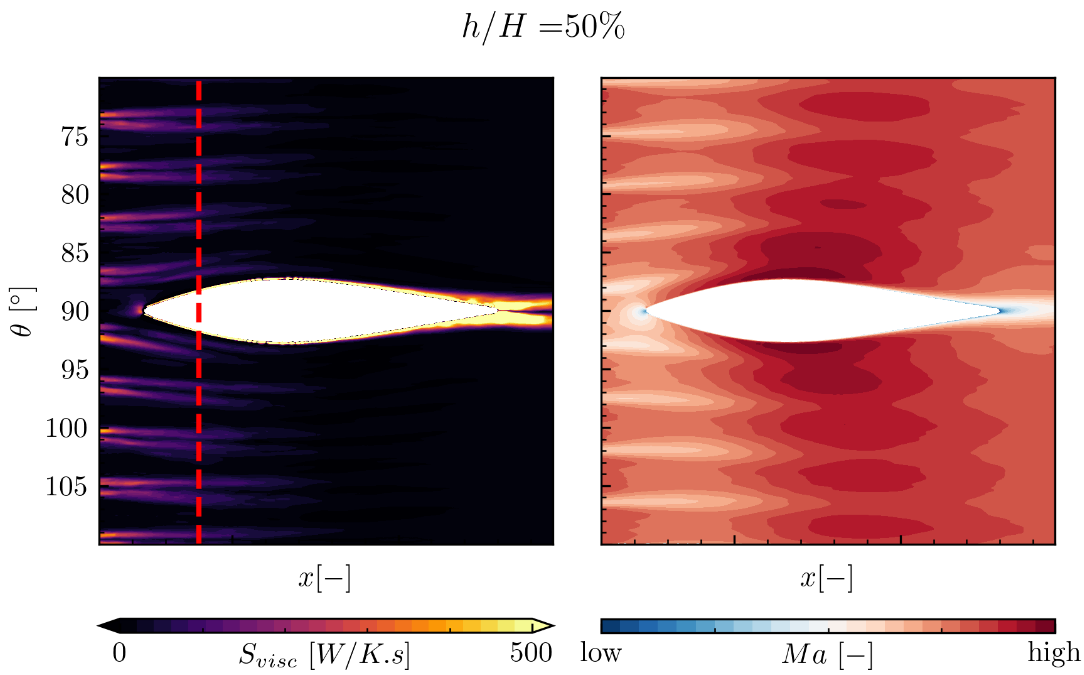

Figure **(6.28)** – Contour plot of entropy generation rate and Mach number at $h/H = 50\%$.

Fig. 6.29 illustrates the contour map of the entropy generation rate, Mach number, and radial velocity taken in the zone of high value as shown on the red dashed line of Fig.

6.27. It shows that the zones of high losses correspond to several spots of low-velocity fluid between the wakes propagating across the duct. Moreover, in these particular zones, a high radial velocity is found, and the streamlines illustrate that the fluid is pumped from the hub boundary layer to the free stream.

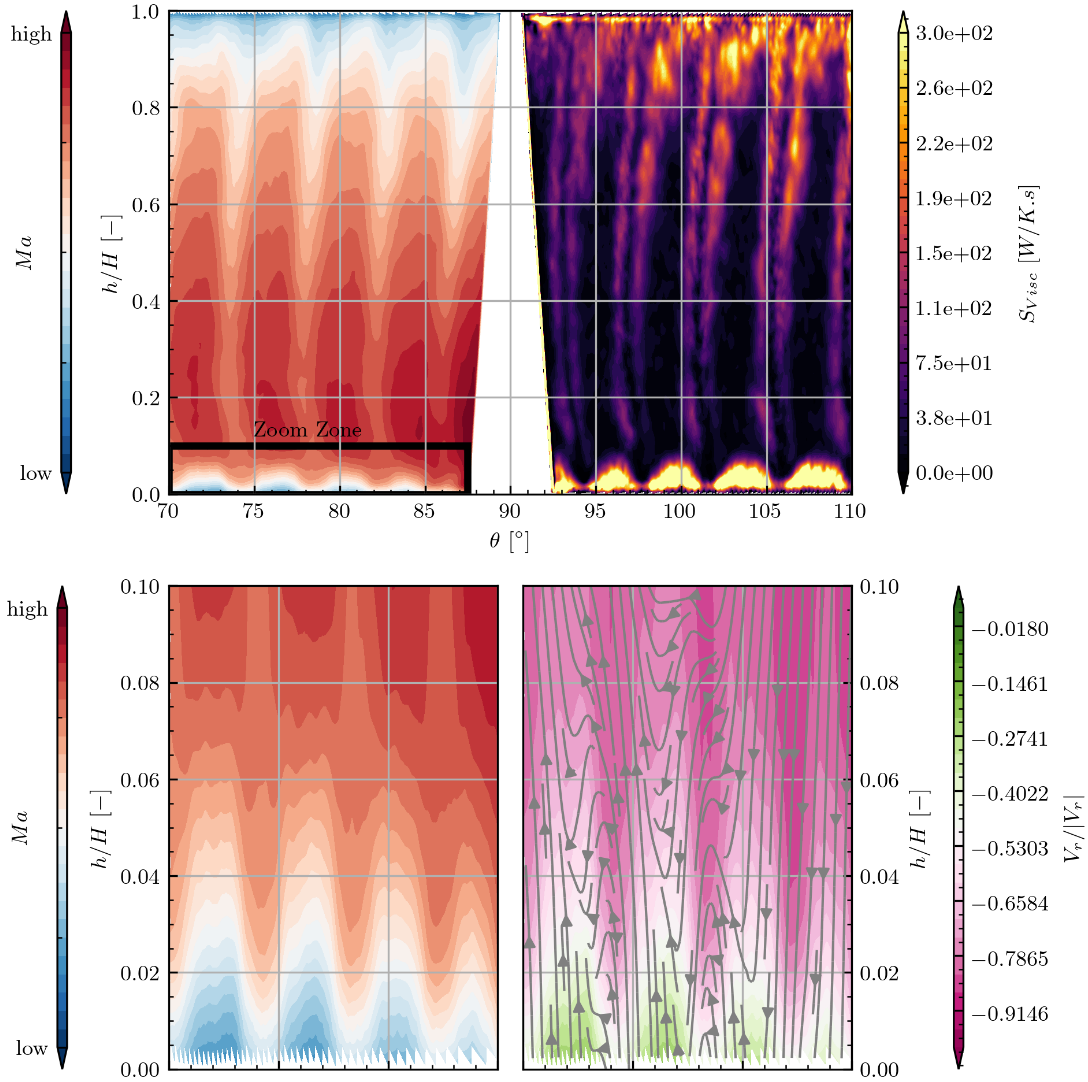

Figure **(6.29)** – Contour plot of entropy generation rate, Mach number, and radial velocity taken at the position highlighted by the red dashed line in Figs. 6.28-6.27.

6.5 Chapter Summary

Simulations of the CAM1 experimental facility have been performed where the surrounding rows were gradually included. The results for all configurations have been examined in terms of mass flow convergence, radial profiles, loss level, and flow phenomenology using two-dimensional contour maps. This study's primary results are:

- The successful application of ProLB to a representative S-duct that correctly retrieves the mean radial profiles at several control planes.
- Additionally, it shows that it is necessary to consider engine realistic inlet conditions upstream of the duct as this entering flow has a major influence on the flow evolution and, thus, the loss level of the duct.
- On the other hand, the downstream HPC stage can be neglected, considering that no influence on the duct flow physics was detected.
- Finally, an entropy-based approach has been applied to study the loss evolution and highlighted the hub and the first 25% of vein height as a critical zone of loss generation.
- This represents, to the best of the author's knowledge, the first compressible LBM simulation of a 360° multi-stage turbomachinery.

Chapter 7: Application and Evaluation of the LBM Methodology to an Industrial Configuration

This chapter presents the study of an S-duct configuration representative of an actual aircraft engine in terms of geometry and operating conditions. The different developments and guidelines established on the CAM1 *configuration are used to treat this case.*

Contents

7.1 Description of the Configuration

The configuration studied in this chapter called INDUS, corresponds to a representative industrial S-duct linking two compressor stages. The geometry considered here comprises a stator row, S1, and a strutted S-duct. A scheme of the vein geometry and the blade positions are drawn in Fig. 7.1.

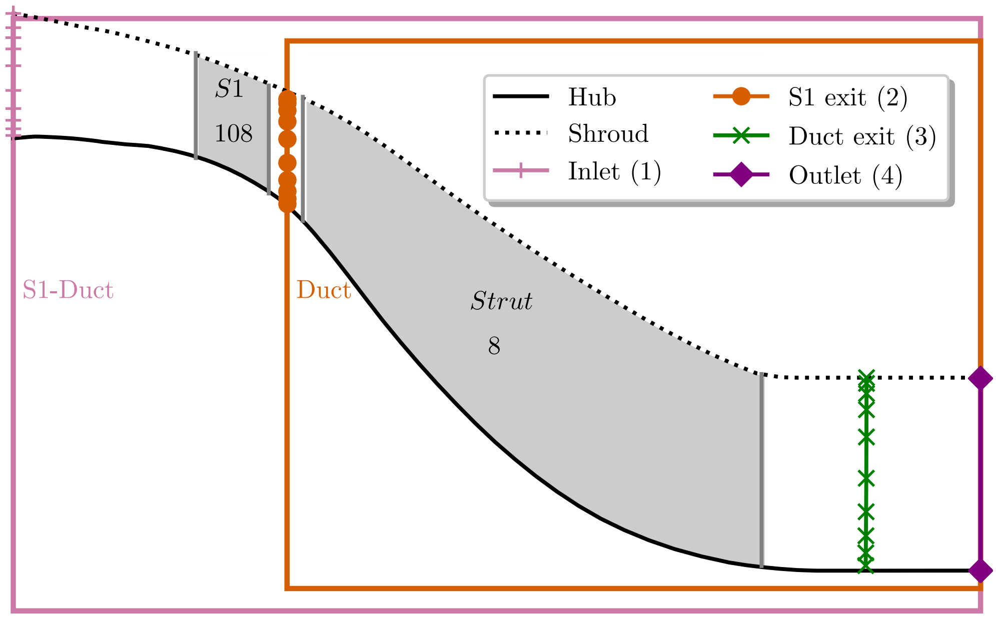

Figure **(7.1)** – Computational domains of the INDUS configuration.

The Aerodynamic Duct Loading (ADL) coefficient is computed using Eq. 2.12 and compared to the CAM1 value in Fig. 7.2. It can be seen that the INDUS case has a value close to modern aircraft engines, which is smaller than CAM1. Considering the approach of Britchford [19], this means that INDUS should be a priori less critical than CAM1. Based on the inlet velocity and vein height, the Reynolds number is 7×10^5, which is way above the CAM1 value of 1.55×10^5.

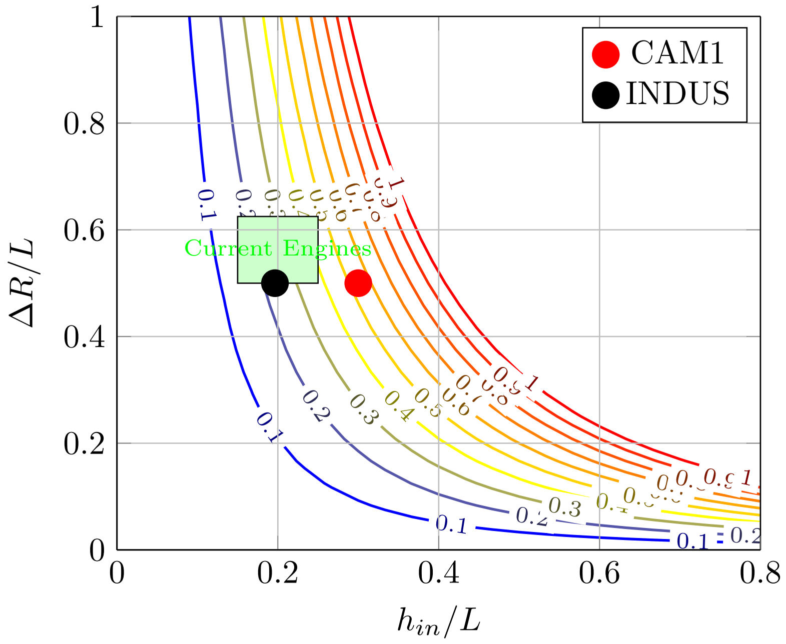

Figure **(7.2)** – Duct loading of the INDUS configuration.

To further illustrate the differences in terms of geometry between the two configurations, a scheme of the vein is shown in Fig. 7.3. It can be observed that the slope of the INDUS case is indeed less pronounced than for CAM1, and the duct length is greater. However, the INDUS case has an increase of its cross-section area with the axial position adding a diffusive effect that CAM1 did not have.

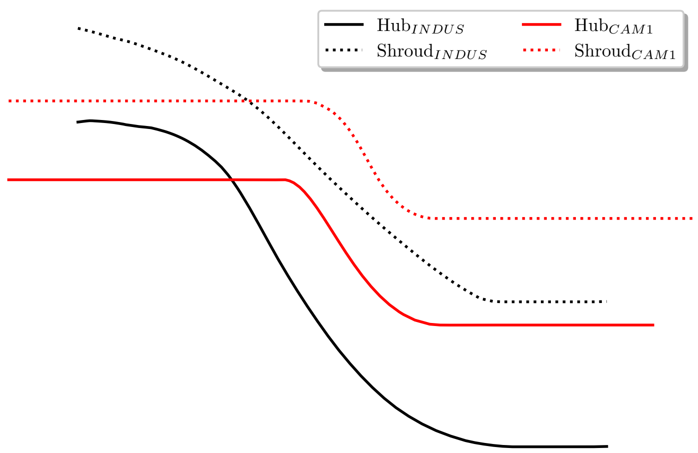

Figure **(7.3)** – Comparison of the hub and shroud lines between the INDUS and CAM1 configurations.

Moreover, eight struts are installed but are not uniform due to their different thicknesses depending on their azimuthal position. Four struts have the same thickness and are denoted *std*. The other four struts are thicker, leading to the largest azimuthal passage between the struts of 35° and the smallest one of 32°.

Finally, the major difference concerns the operating point. The Mach number for this configuration is two times larger than CAM1, around 0.6, placing the flow in the mid/high compressible regime where the LBM must be evaluated.

7.2 Setup

7.2.1 Definition of the Cases

The same methodology as for CAM1 is applied to treat this INDUS configuration. Two cases, namely (Duct) and (S1-Duct), are defined as represented in Fig. 7.1.

7.2.2 Fluid Properties and Boundary Conditions

The physical parameters of the simulation are chosen to match the experimental conditions. The working fluid has a specific gas constant of $R_g = 287.15\,\mathrm{J}\cdot\mathrm{kg}^{-1}\cdot\mathrm{K}^{-1}$. The dynamic viscosity is imposed as $\mu_{ref} = 2.89\times10^{-5}\mathrm{kg}\cdot\mathrm{m}^{-1}\cdot\mathrm{s}^{-1}$ and varies according to the Sutherland's law.

The inlet and outlet boundary conditions are similarly imposed for the CAM1 configuration. At the inlet of the simulation domain, radial profiles of P_t, T_t, and flow angles taken from the experiment are imposed. At the outlet, static pressure is, by default, set to the one given by the experiment but is dynamically adjusted during the computation to converge toward the target mass flow. The inlet and outlet use Locally One-Dimensional Inviscid (LODI) relations as presented in Chapter 4. The walls are considered adiabatic, and a wall law is applied. It should be noted that the same values of relaxation parameters as for CAM1 have been used at the inlet and outlet. Higher values of relaxation coefficients have been tested, but a similar behavior in terms of convergence has been observed. This validates the methodology concerning the application of LODI conditions and the choice of relaxation parameters for turbomachinery applications.

7.2.3 Meshing Strategy

The LIKE criterion defines Refinement Domains (RD) in the wake region of the strut and S1 blades. This is especially useful here for the S1 blades that don't have a uniform clocking and are highly twisted, leading to specific wake directions. The smallest mesh size imposed in RD1 is set as $\Delta x = 0.15\,\mathrm{mm}$. It is applied uniformly on the S1 blades, leading to a mean y^+ of 120. A specific patch is also applied near the leading edge of the struts where a zone of high y^+ was observed. Then RD2 is applied at the hub, shroud, and blade wake regions highlighted by the LIKE criterion. This results in a mean y^+ of 150 on the hub and shroud walls. Finally, on the rest of the fluid domain, RD3 is imposed with a size of 0.6 mm, putting at least 140 points in the vein height (see Fig. 7.4).

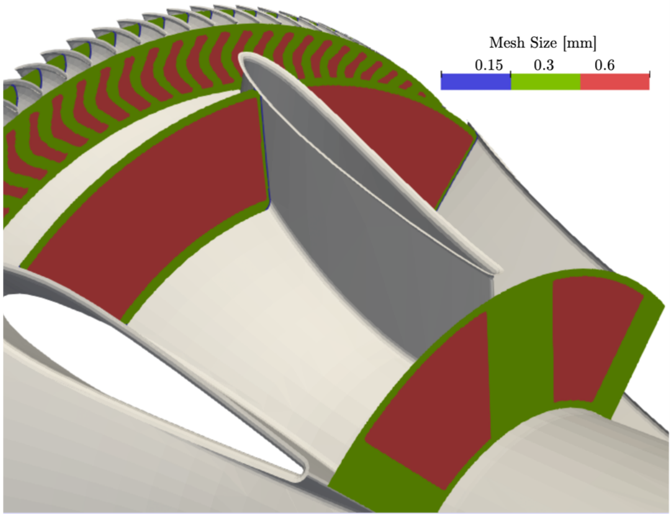

Figure **(7.4)** – Illustration of the mesh refinement domains (RD) for the INDUS case.

Case	Equivalent Fine Points	Total Nb. Points	$CPU.h$
Duct	188×10^6	475×10^6	73728
S1-Duct	368×10^6	655×10^6	109098

Table **(7.1)** – Summary of the mesh properties for the different cases.

Blade	S1	Strut
Cells / chord	270	875

Table **(7.2)** – Cells per chord for the different blades.

7.2.4 LBM Model Parameters

The free HRR parameter is set to $\sigma = 0.99$ for all computations. The time step is $\Delta t = \frac{\Delta x c_s^*}{\sqrt{R_g T_0}} = 1.46 \times 10^{-7}$s. The resulting bulk Courant-Friedrichs-Lewy (CFL) number obtained is $CFL = \frac{U_{bulk}+c}{\Delta x/\Delta t} = 0.52$, slightly lower than the CAM1 value that was fixed at 0.74.

7.2.5 Simulation and Averaging Time

For this case, no rotating component is present within the configuration to determine the simulation and averaging time as performed for CAM1. The physical time and averaging period of CAM1 is thus expressed in terms of flow through the duct, $\tau_{conv} = \frac{L}{U_{bulk}}$, with L being the S-duct length and U_{bulk} the average velocity in the Duct. For CAM1, this represented a running time of 12 convective flows for an averaging time of 4 convective flows. The same guideline will be used for the INDUS simulations to have a fair comparison in terms of convergence and averaging time.

7.2.6 Previous RANS Computation

A RANS computation was performed at Safran Aircraft Engines on this configuration. The elsA software [153, 154] was used with the RANS model on a structured mesh with an appropriate mesh resolution near the wall. A main difference with our current case is that the RANS study considered the full machine, adding compressor stages upstream of the S-duct. For the boundary conditions, radial profiles of total pressure, temperature, and flow angles have been imposed at the inlet. At the outlet, a radial equilibrium was set. The computations were run on a periodic sector representing $1/8^{th}$ of the geometry. Considering that the different struts installed in the duct differ by thickness, a simplification is made by choosing a strut of average thickness. Mixing planes were used between each row, including the interface between the stator and the duct passage, leading to only one stator blade passage included in the simulation. This leads to a mesh of 19×10^6 points total. **However, the RANS computation did not reach the same operating point at the end of the simulation, with a mass flow superior by 3% of the true one. This will limit the quantitative comparisons of the results, and only qualitative conclusions can be drawn.**

7.3 Preliminary Studies and Mesh Convergence

7.3.1 Issues Concerning the Total Temperature and Implementation of a Crocco-Busemann Approach

The radial profile of the total temperature obtained at the duct exit during the first (Duct) case simulation is presented in Fig. 7.5. It can be seen that the temperature matches the experimental one in terms of trend and absolute value except close to the hub and shroud, where a major underestimation is found. This is explained by the viscous heating that is not properly captured by the method. Indeed, even though a wall law is used on the velocity, only a Dirichlet condition on the temperature is used at the wall. However, with a mean y^+ around 150 at the hub and shroud walls and strong temperature gradients, this approach is not satisfactory for properly predicting the wall temperature.

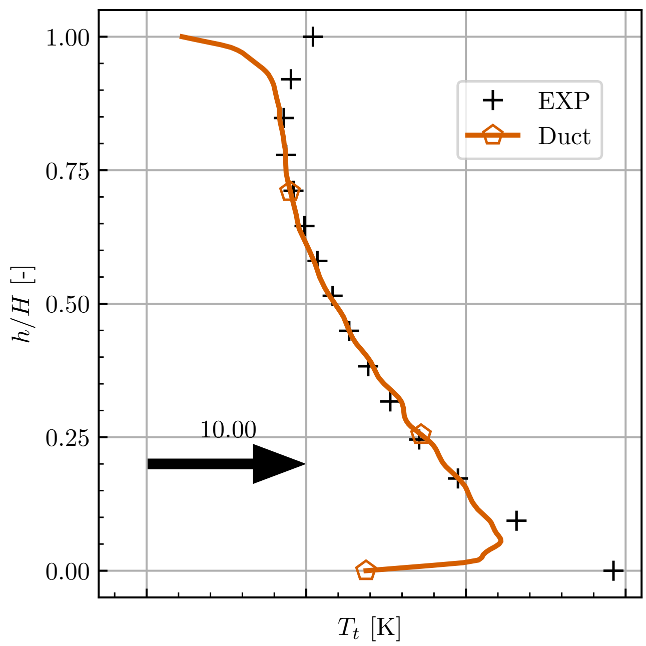

Figure **(7.5)** – Illustration of the first issue observed on the T_t at the duct exit.

A Crocco-Busemann approach [165] has been implemented in the solver to improve the results. The analogy between the conservation equations for momentum and energy has derived several algebraic relations between temperature and velocity. Walz's equation [166] (also known as the modified Crocco-Busemann relation) leverages the analogy between the conservation equations for momentum and energy to arrive at an algebraic relation between mean temperature and velocity. This relation accounts for non-unity Pr effects via a recovery factor, which is taken as $r = (Pr)^{1/3}$.

The temperature at the No Fully Fluid (NFF) node, T_{NFF}, is given using Eq. 7.1:

$$T_{NFF} = T_{REF1} + \frac{\sqrt[3]{Pr}}{2Cp}(u^2_{t,REF1} - u^2_{t,NFF}) \tag{7.1}$$

where Pr is the Prandtl number, Cp is the specific heat coefficient at constant pressure, and u_t is the tangential velocity the wall law gives at the corresponding points.

The improvement brought by this implementation is presented in Fig. 7.6. The case *Std* is the reference where the Crocco-Busemann is deactivated. It should be noted that this issue did not appear on the CAM1 simulations as the temperature gradient near the wall was less pronounced, combined with a smaller velocity and thus smaller viscous heating. Moreover, the y^+ at the wall was also lower for CAM1, reducing the error of applying a Dirichlet condition on the temperature in the wall law.

Δx [mm]		0.5	0.25
Hub	y^+_{min}	70	30
	y^+_{mean}	170	109
	y^+_{max}	250	200
Shroud	y^+_{min}	70	30
	y^+_{mean}	212	121
	y^+_{max}	250	200

Table **(7.3)** – Definition of the cases for the Crocco-Busemann validation.

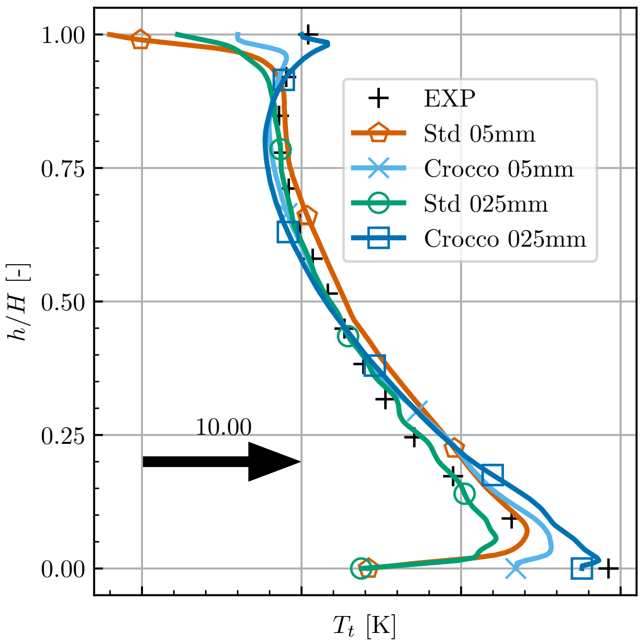

Figure **(7.6)** – Comparison of the total temperature profile with the Crocco-Busemann approach for different y^+ values.

It can be observed that as the mesh is refined, the total temperature is progressively improved at the hub and shroud walls. For the finest case *Crocco 025mm*, this leads to an error under $1K$ at the hub and shroud. A small discrepancy remains as the y^+ is too large to properly estimate the tangential velocities used in Eq. 7.1. The Crocco-Busemann formulation will be used on all the walls in the following.

7.3.2 Mesh Convergence

This section illustrates the mesh convergence study performed on the (S1-Duct) case. Three minimal mesh sizes have been tested, 0.5mm, 0.3mm, 0.15mm, called Mesh 1, Mesh 2 and Mesh 3. The refinement domain size and position are not changed between the cases. The numbers of equivalent fine and total number of nodes are presented in Table 7.4.

	Mesh1	Mesh 2	Mesh 3
$\Delta(x, y, z)_{RD1}$ [mm]	0.5	0.3	0.15
Total Points (M)	80	181	655
Eq. Fine Points (M)	60	98	368
Δt [s]	4.48×10^{-7}	2.92×10^{-7}	1.46×10^{-7}
N_{iter} for τ_{conv}	8640	14400	28800
CPU time for τ_{conv} $[CPU.h]$	2727	4545	9091

Table **(7.4)** – Summary of the properties of the different meshes.

Fig. 7.7 illustrates the radial profiles obtained at the S1 exit for the different mesh sizes. It shows that the total pressure prediction is close for all three meshes above $h/H = 60\%$ while it is progressively improved under. A similar conclusion is reached on the Mach number profile. On the total temperature, small improvements can be noticed, especially at the hub wall, while in the rest of the vein height, no major differences can be observed. Finally, concerning the azimuthal angle, the results are progressively improved in the lower half of the vein, but even with the finest mesh, a deviation remains. Moreover, above 50%, the angle is also diminishing and does not match the experiment.

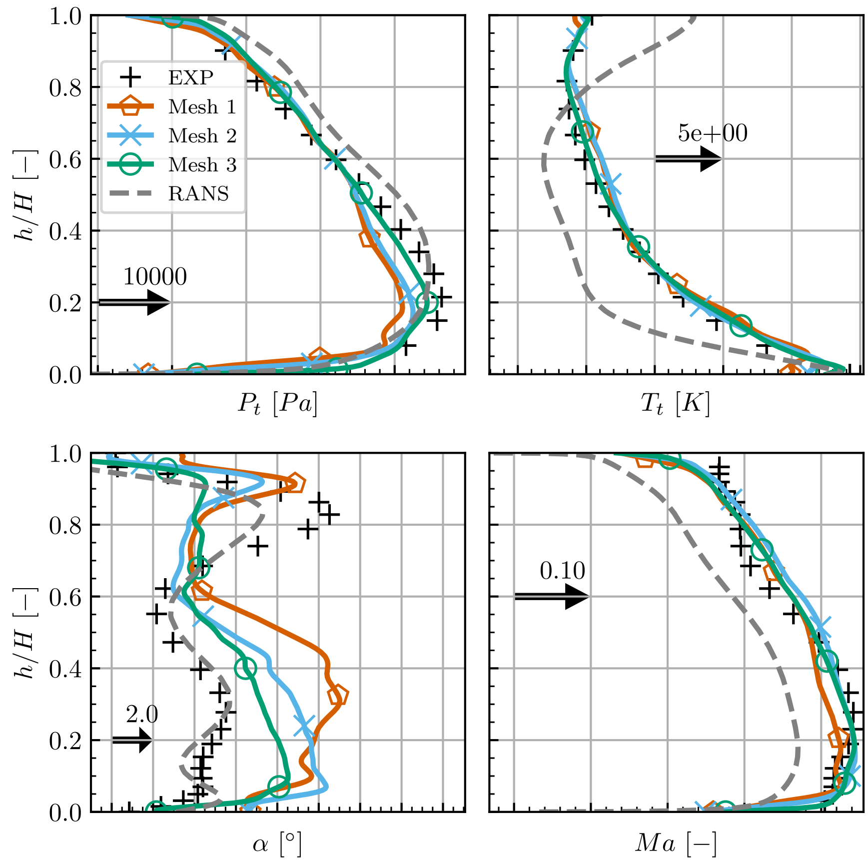

Figure **(7.7)** – Radial profiles at the S1 exit for the different mesh sizes.

Fig. 7.8 presents the radial profiles at the duct exit for the different mesh sizes. The total pressure prediction is progressively improved, especially under 60%. The different profiles of total temperature are in close agreement with a particular improvement for Mesh 3 at the hub. Finally, all three meshes predict the same Mach number evolution under 50%. However, only Mesh 3 can recover the Mach number profile in the upper part of the vein.

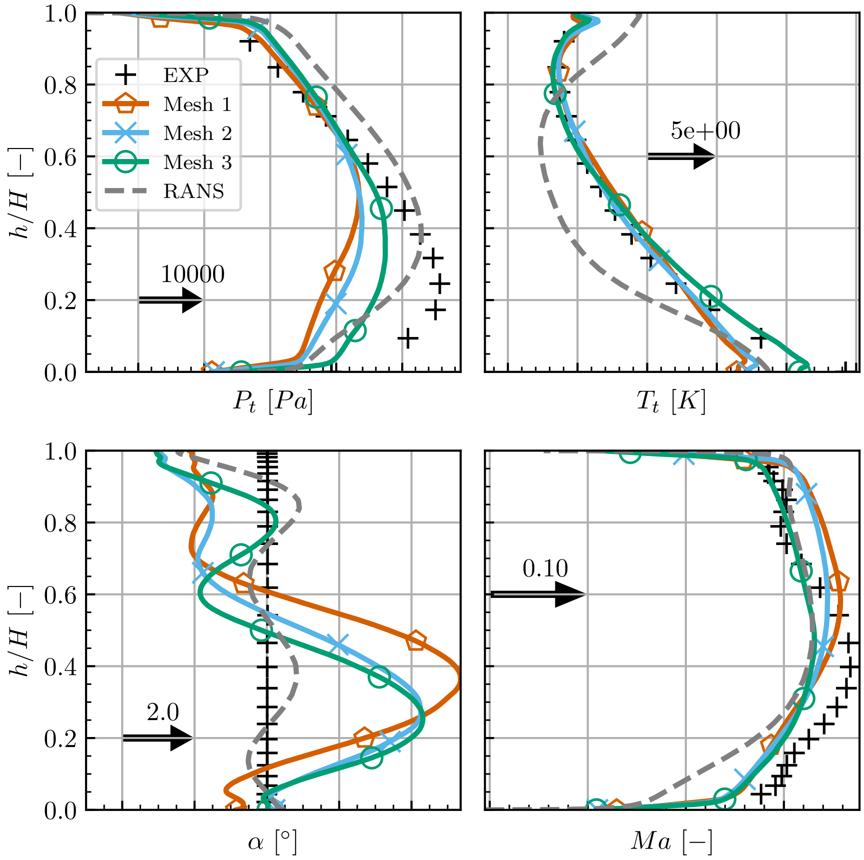

Figure **(7.8)** – Radial profiles at the duct exit for the different mesh sizes.

As previously observed on the CAM1 configuration, the flow development around the upstream stator is heavily mesh-dependent. Fig. 7.9 illustrates the contour map of the Mach number taken across the stator blades near the Trailing Edge (TE). It shows that as the wall resolution is refined, the separation observed especially under 60% is reduced. However, even with the finest mesh used, a separation remains, leading to thicker wakes downstream as shown in Fig. 7.9 and explaining the differences observed on the radial profiles.

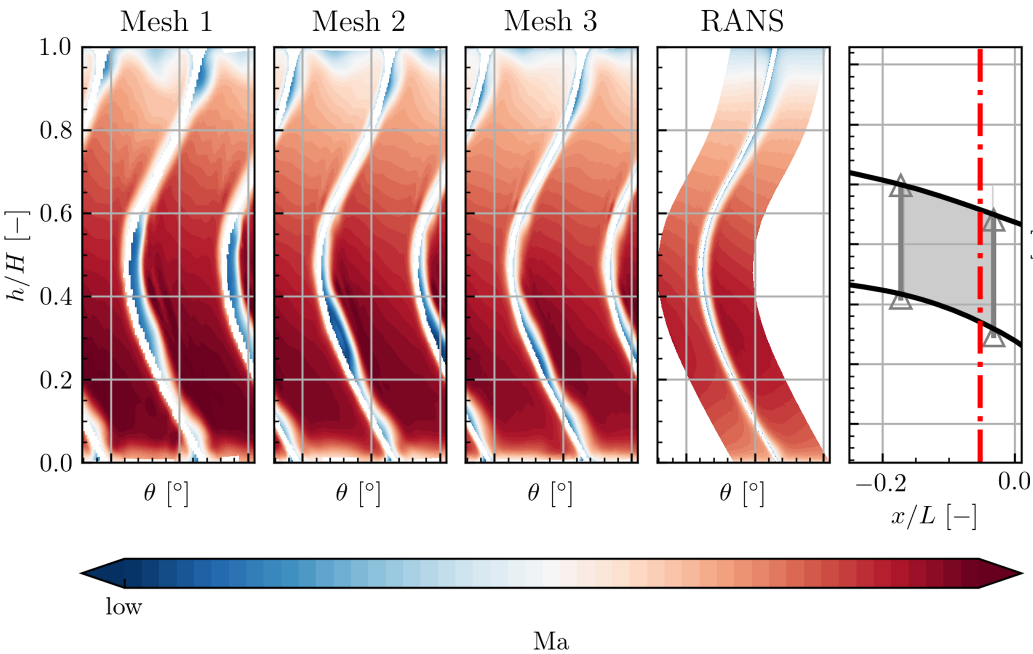

Figure **(7.9)** – Contour plot of Mach number across the S1 blades for the different meshes.

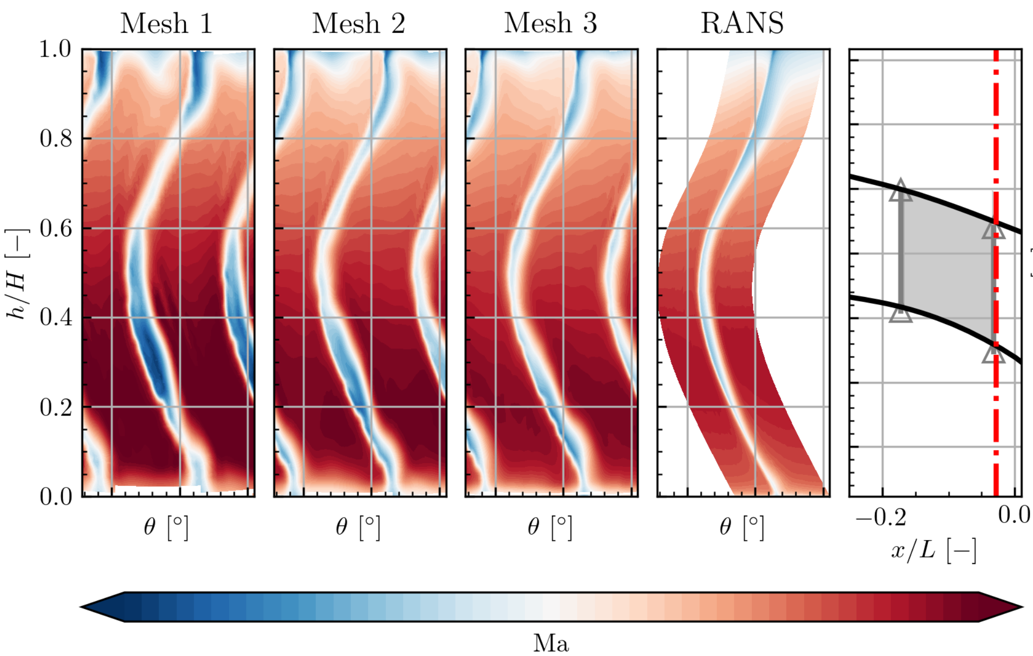

Figure **(7.10)** – Contour plot of Mach number at the S1 exit for the different meshes.

7.3.3 Influence of Strut Thickness

Considering that the struts installed for the INDUS case have varying thicknesses, it is desired to know if this impacts the radial profiles downstream. Azimuthal averaging is performed on each 45° sector, and results are presented in Fig. 7.11. It shows that only minor variations are found between the different sectors, meaning that the different strut profiles do not significantly influence the flow downstream.

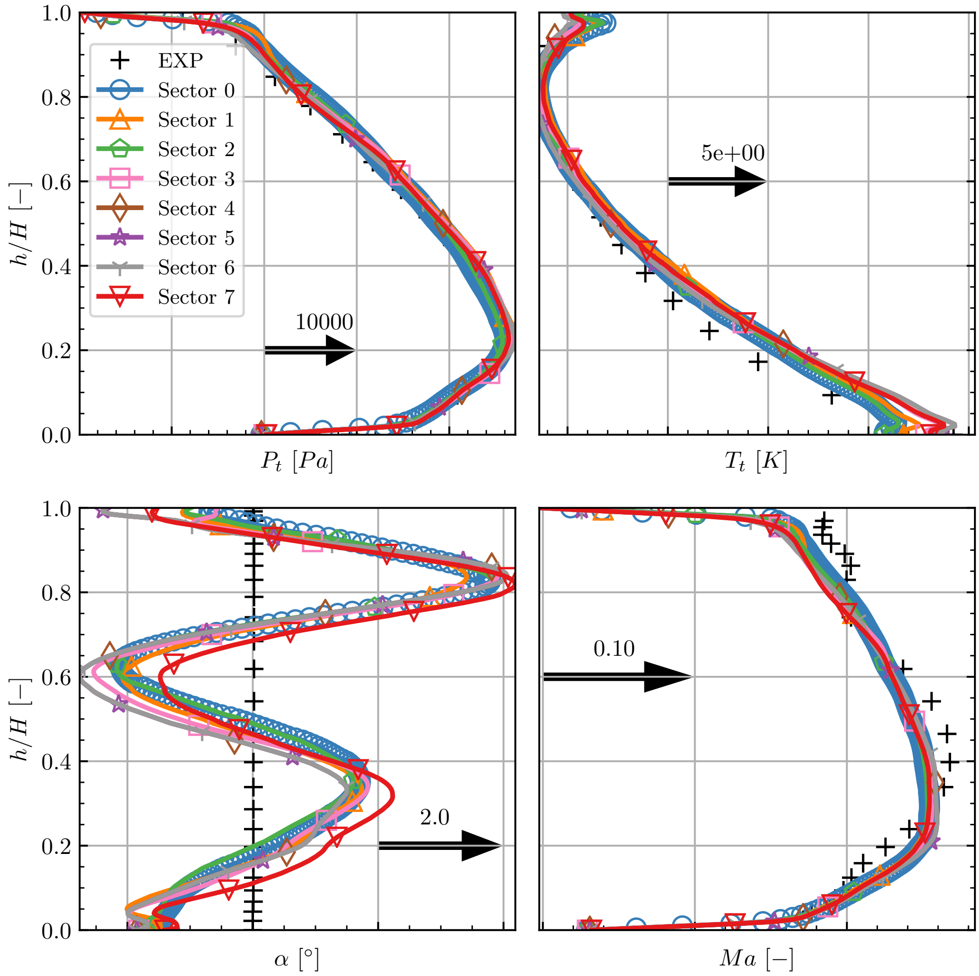

Figure **(7.11)** – Radial profiles for the different sectors at the Duct exit plane (3).

From this mesh convergence study, it is retained that a minimal mesh size of 0.15 mm is recommended on the blade walls even though some discrepancies are observed on the radial profiles and a small separation is occurring on the S1 blade for $h/H \leq 50\%$. A finer mesh size on the wall could not be tested due to the resulting number of elements but it would certainly be beneficial to improve the results. RD2 on the hub and shroud walls appears to be sufficient to capture the correct total temperature in these zones using the Crocco-Busemann relation implemented previously.

7.4 Results

7.4.1 Convergence and 0D Values

First, the convergence towards the target mass flow is illustrated in Fig. 7.12. It shows that around four convective times are needed to evacuate the transient part of the simulation. Then, the mass flow approaches the target value, but a small overshoot is observed and is corrected thanks to the valve law at the outlet. On the last four convective times, the mass flow at the duct exit is close to the operating point without any significant oscillations during the averaging period (highlighted in red).

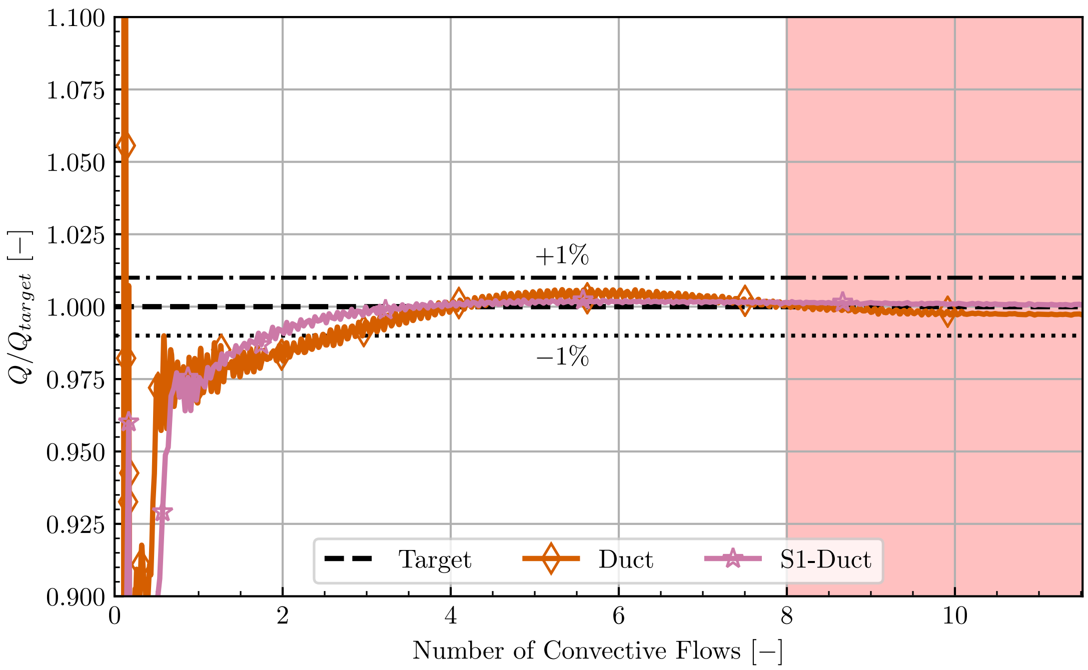

Figure **(7.12)** – Mass flow convergence for cases (Duct) and (S1-Duct) at the duct exit.

Plots of total pressure and total temperature time evolution at the duct exit are shown in Fig. 7.13. It confirms that during the averaging period, these quantities are constant. All the simulations have reached a satisfying convergence around the target mass flow in 12 convective flows, and no oscillations are observed during the averaging period.

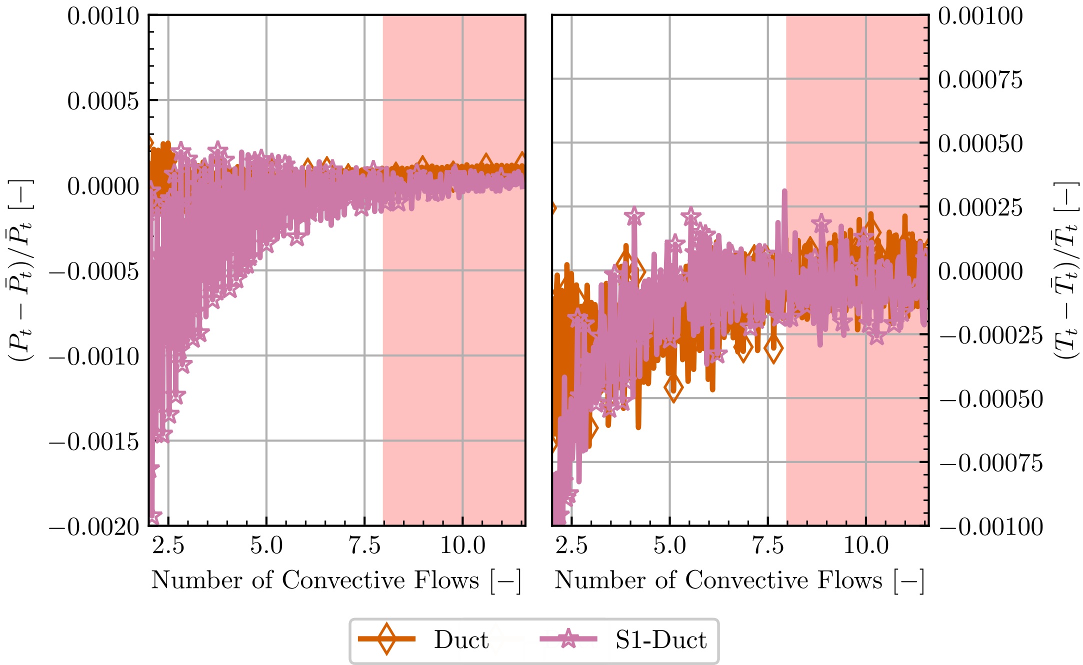

Figure **(7.13)** – Total pressure and total temperature convergence for cases (Duct) and (S1-Duct) at the duct exit.

7.4.2 Inlet plane

Fig. 7.14 shows the radial profiles at the inlet of the S1-Duct case, confirming that the boundary imposes the correct values and the resulting Mach number is close to the experiment. Some discrepancies with the RANS computation are noticeable. This is explained by the fact that the RANS simulated the full machine, with additional compressor stages upstream at a slightly higher operating point, leading to distortion of the radial profiles at the R3 exit plane.

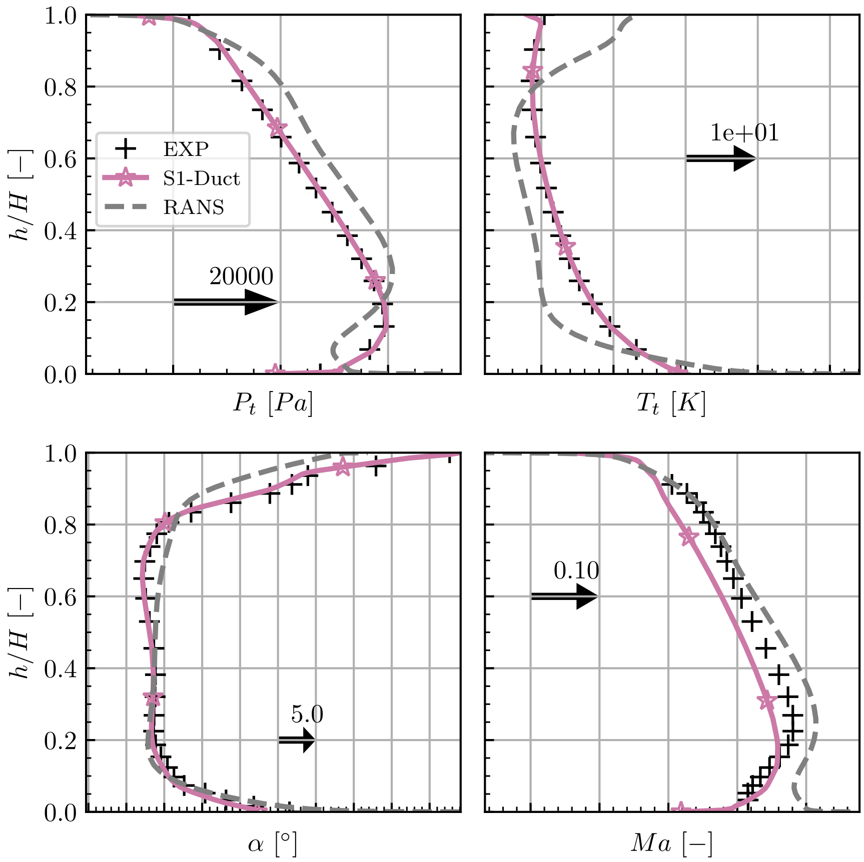

Figure **(7.14)** – Radial profiles at the R3 exit plane (1).

7.4.3 S1 Exit

7.4.3.1 Radial Profiles

Radial profiles at the S1 exit are illustrated in Fig. 7.15. It can be observed that the total pressure is well recovered above $h/H = 50\%$ but is, however, underestimated on the rest of the vein height. Concerning the azimuthal angle, it is observed that above $h/H = 50\%$, a similar prediction to the RANS one is obtained that underestimates slightly the value compared to the experiment. On the other hand, under 50%, an overestimation of the angle by 2° is found. The total temperature matches the experiment well. Finally, the LBM computation retrieves the Mach number trend and absolute value measured experimentally. To explain these variations with the experiment and the RANS results, contour maps at the S1 exit and around the stator blades are presented in the following.

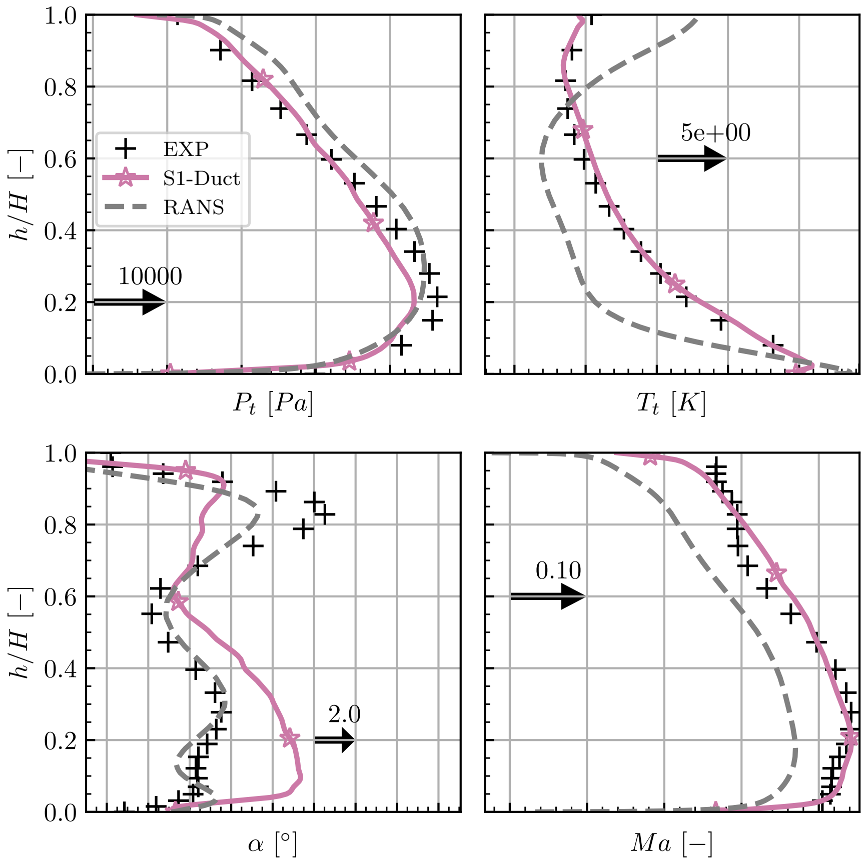

Figure **(7.15)** – Radial profiles at the S1 exit plane (2).

7.4.3.2 Contour Maps

Fig. 7.16 illustrates the flow field obtained in the middle of an S1 blade and shows that a thickening of the Boundary Layer (BL) near the hub and around $h/H = 50\%$ for the LBM computation. Negative values of axial velocity in these regions indicate that a separation is occurring. The rest of the flow structure is well retrieved, especially above 80%.

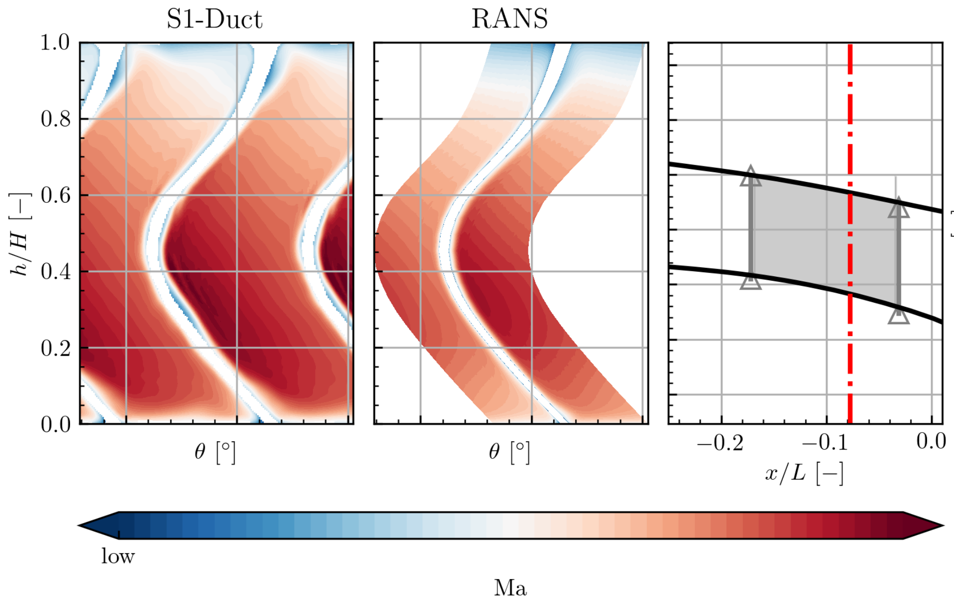

Figure **(7.16)** – Contour plot of Mach number on the S1 blade.

At the S1 exit (see Fig 7.17), this leads to a wider wake in the first half of the vein. This explains the underestimation of total pressure and the azimuthal angle deviation observed previously. The results could be improved by refining the S1 blade, especially on the suction side, to reduce the separation.

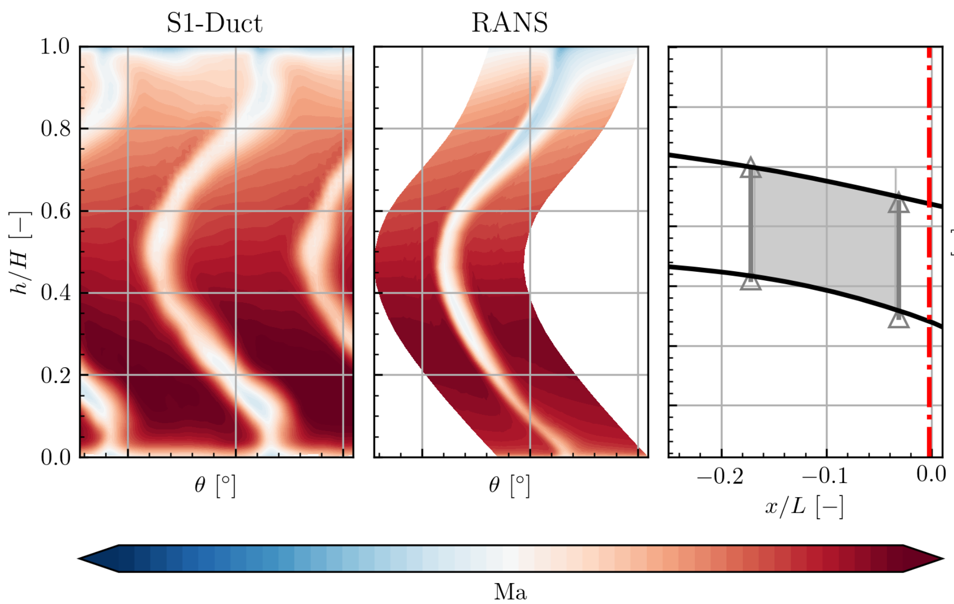

Figure **(7.17)** – Contour plot of Mach number at the S1 exit plane.

7.4.4 Duct Exit

7.4.4.1 Radial Profiles

Fig. 7.18 illustrates radial profiles at the Duct exit plane. It shows that for the (S1-Duct) case, a large underestimation of the total pressure is found under $h/H = 60\%$. This is linked to the losses induced by the entering wakes that are too thick in this region since the S1 exit plane. Another consequence of the upstream wakes is observed on the azimuthal angle where a larger variation of about 2° is found at 30%. The total temperature is well recovered with a similar prediction as the (Duct) case. Finally, the Mach number trend is recovered under 50%, with a lower absolute value than in the experiment. Meanwhile, a good agreement is found above 60%. On the other hand, for the (Duct) case, the total pressure is almost exactly recovered, and a better agreement of the azimuthal angle is retrieved. Still, variations of the azimuthal angle are observed along the vein height, similarly to the RANS, which are not found in the experiment. The experiment predicts a uniform outflow angle, which seems unlikely considering that a tangential component is introduced at the duct inlet and that flow separation happens inside the duct. Finally, the total temperature and the Mach number are close to the experiments for this case. This illustrates that the LBM computations retrieve quantitatively good results on the isolated configuration (Duct) when exact profiles are imposed at the duct inlet plane.

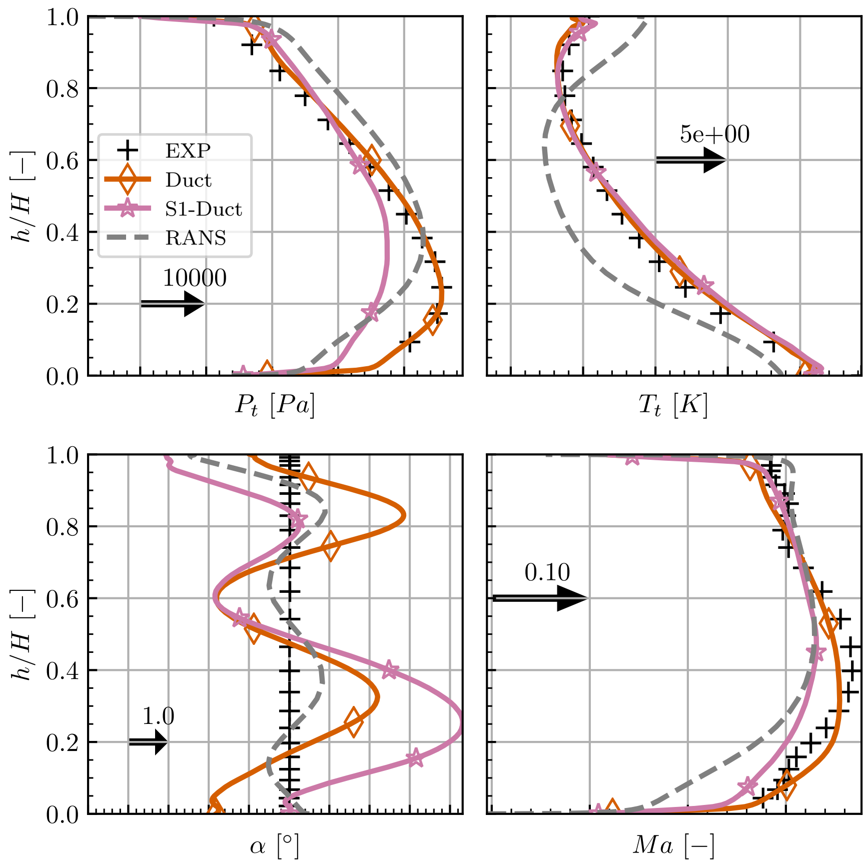

Figure **(7.18)** – Radial profiles at the Duct exit plane (3).

7.4.4.2 Contour Maps

Fig 7.19 illustrates the Mach number contour map taken at the duct exit. The two cases (Duct) and (S1-Duct) show a similar fine strut wake slightly destabilized compared to the one obtained by the RANS. Concerning the differences, the (Duct) case retrieves a large zone of deceleration near the shroud similar to the RANS one that is not found in the (S1-Duct) case. Moreover, the two cases retrieve a zone of low Mach number in the first 20% of vein height less pronounced than in the RANS computation. The flow structure in this zone is also slightly different from the RANS computation, where the flow is slowed down by a pair of vortices developing uniformly on each side of the strut blade.

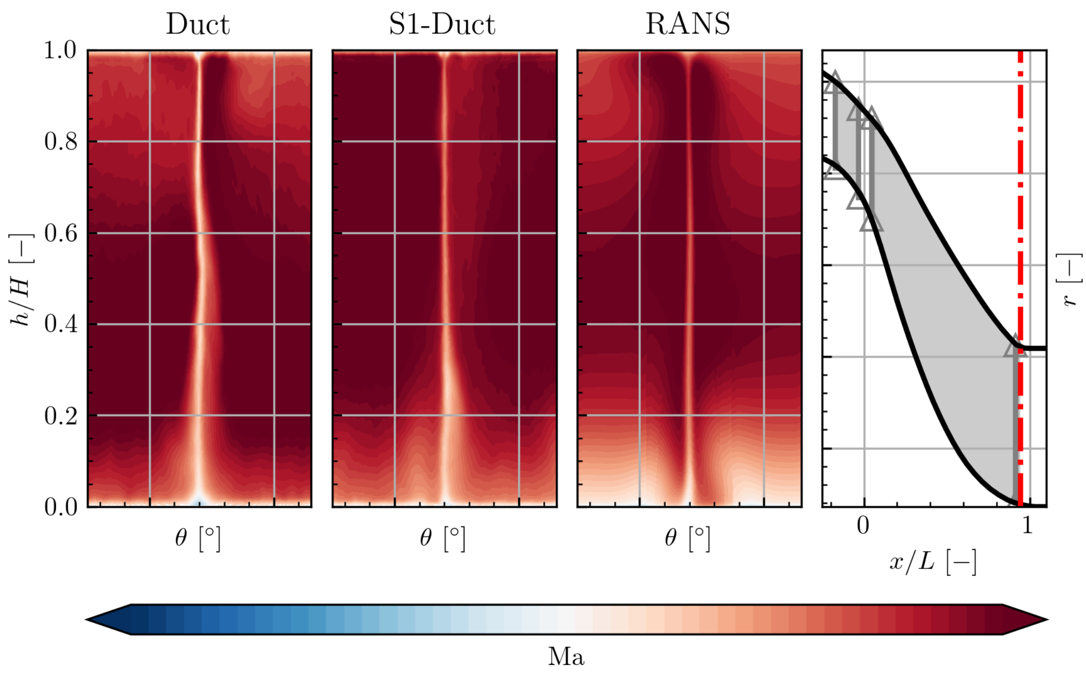

Figure **(7.19)** – Contour plot of Mach number at the duct exit.

Fig. 7.20 illustrates the difference of flow development at $h/H = 50\%$. It shows that when no upstream wakes are injected ((Duct) case) or a mixing plane is used (RANS), the potential effect of the strut generates a large deviation of the flow around the strut. This deviation is symmetrical for the RANS computation, whereas it is not for the (Duct) case, explaining the difference observed on the strut wake and flow structures at the duct exit plane. On the other hand, when wakes are impacting the strut, the potential effect is limited, and the flow appears more symmetrical.

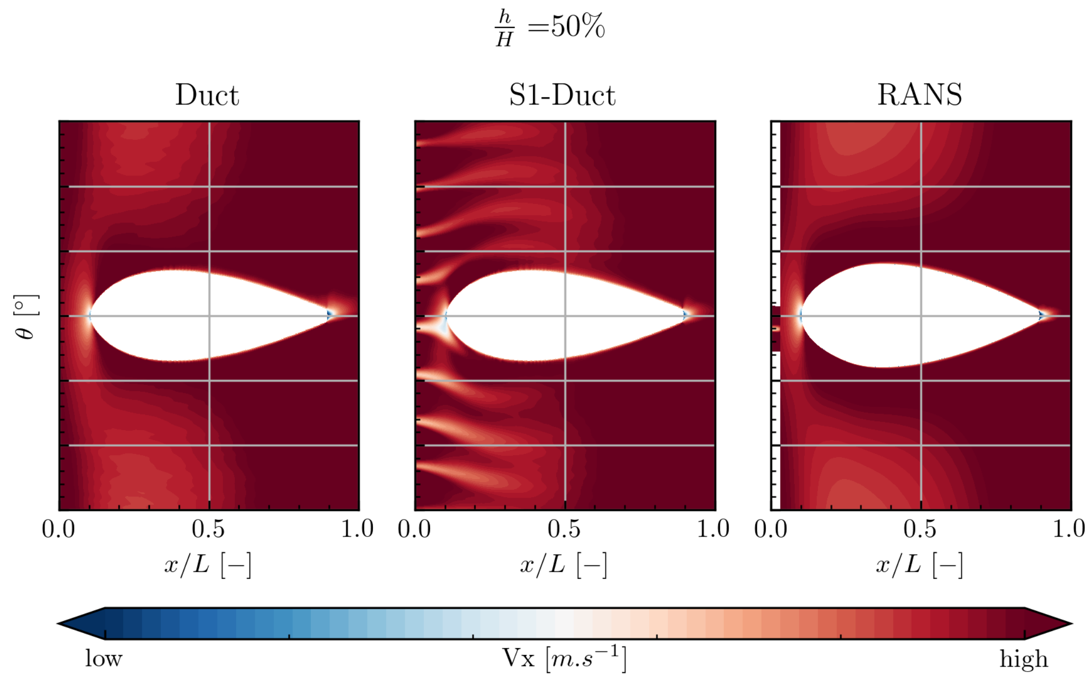

Figure **(7.20)** – Contour plot of axial velocity at $h/H = 50\%$.

7.4.5 Total Pressure Losses

The total pressure loss for the different cases is illustrated in Fig. 7.21. No experimental data are plotted on this figure as the experimental accuracy on the pressure measurements necessary to compute the pressure loss coefficient was judged unsatisfactory according to Safran experts. For the (S1-Duct) case, an increase in pressure losses can be seen under $h/H = 50\%$, which is coherent with the different observations made on the radial profiles and contour maps in this region. However, above $h/H = 50\%$, a close agreement with the (Duct) case is found.

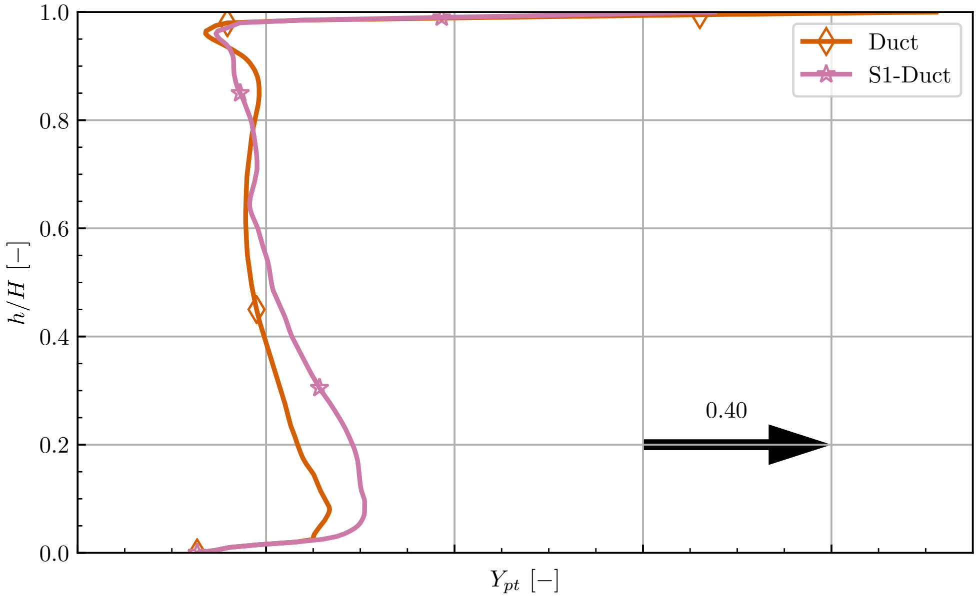

Figure **(7.21)** – Radial profile of total pressure loss for the different cases.

7.4.6 Entropy Loss

This section presents a similar approach as developed in Chapter 6 to study the losses using an entropy formulation. The entropy generation rate per unit volume due to viscous effects (S_{Visc}) and the entropy generation rate per unit volume due to thermal mixing (S_{therm}) are computed. The entropy generation rate is calculated by accumulation across the duct by integrating the volume between the inlet plane (S1 exit) and the following plane at $x_{in} + d$. The distance d corresponded to the coarsest grid size encountered in the fluid domain. This leads to the results presented in Fig. 7.22. The entropy production rate (S_{Prod}) is computed by integrating (S_{Visc}) between the axial position x and the following one at $x + d$. This production rate highlights specific zones where entropy is being created (see Fig. 7.23).

The integrated values of S_{Visc} and S_{therm} have been computed on the full domain for the (Duct) case and give $S_{Visc} = 4.907$, $S_{therm} = 0.0911$. This confirms that even with stronger temperature gradients compared to the CAM1 configuration, entropy generation due to thermal mixing is negligible and will not be included in the following.

Fig. 7.22 shows that for the (Duct) case, linear growth of entropy is observed throughout the duct between the strut LE and TE. A slight slope break near the TE is also found due to the strut wake in this zone. On the other hand, for case (S1-Duct), a larger entropy value is found at the end of the duct, which is coherent with the overpredicted pressure loss illustrated in the previous section. Moreover, it can be seen that the growth rate of entropy in the first half of the duct ($0 \leq x/L \leq 0.5$) is larger than for the (Duct) case before retrieving a similar slope with the same tendency near the strut TE.

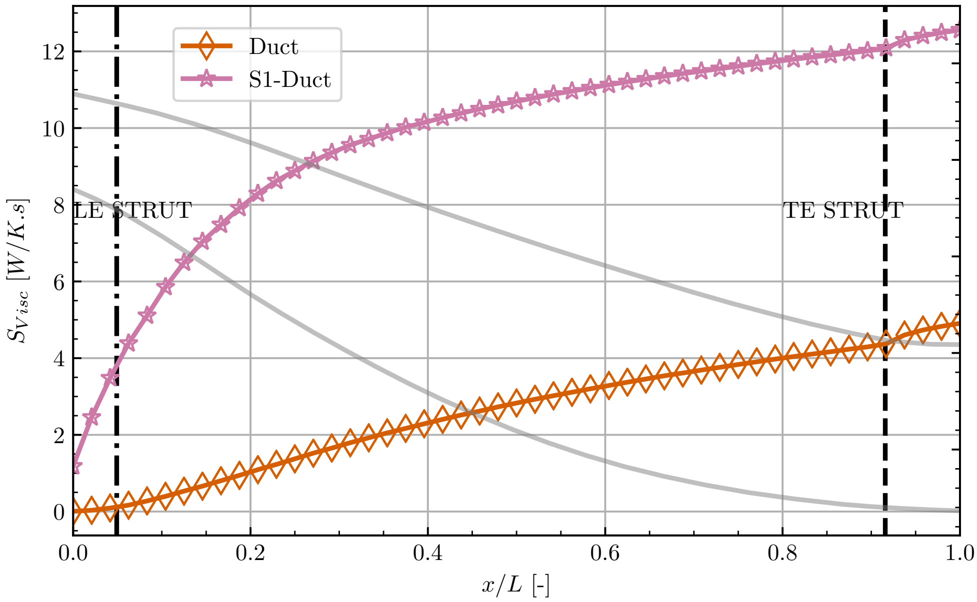

Figure **(7.22)** – Plot of accumulated S_{Visc} through the S-duct for both cases.

Fig. 7.23 compares the entropy production rate between the two cases. It shows that for the (Duct) case, entropy is being slowly produced before reaching the strut LE. After the LE, the production rate increases slightly and remains uniform until $x/l = 0.4$. It then decreases slowly until reaching another production peak at the strut TE. For the (S1-Duct) case, a large level of losses is produced at the duct inlet due to the entering wakes but is progressively reducing until $x/l = 0.4$, where the same behavior as for the (Duct) case is retrieved.

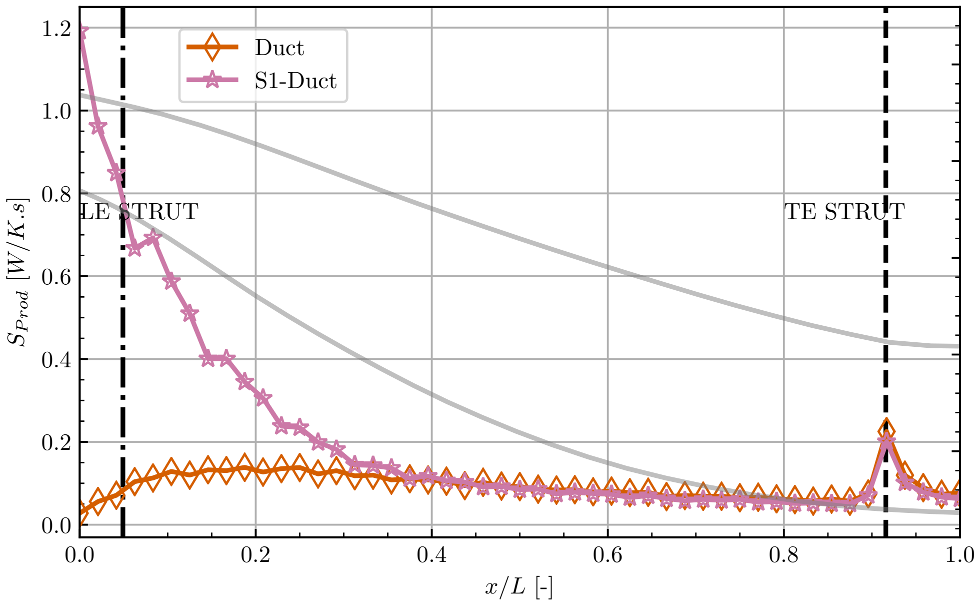

Figure **(7.23)** – Plot of S_{Visc} production through the S-duct for both cases.

To further analyze the results, the duct vein geometry is divided into three zones:

- Hub 25% that encompasses the region from the hub to 25% of height.

- Shroud 75% that includes the region from the shroud to 75% height.

- Mid 50% that comprises the region between the hub 25% and the shroud 75%.

The decomposition for the (Duct) case is illustrated in Fig. 7.24. All three zones produce a similar entropy level until $x/L = 0.25$. Then, most of the losses are created in the Hub 25% zone, while the Shroud 75% and Mid 50% have the same contribution overall.

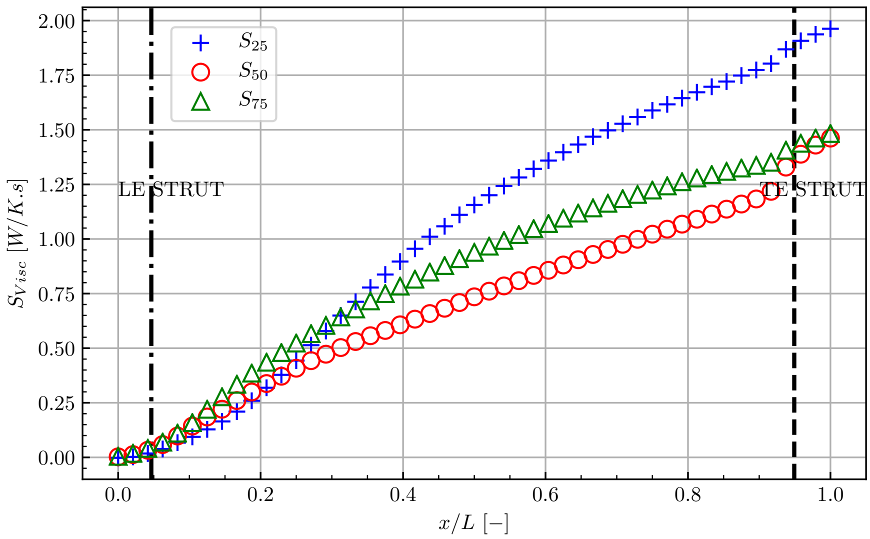

Figure **(7.24)** – Plot of accumulated entropy through the S-duct in the different zones for case (Duct).

For the (S1-Duct) case (see Fig. 7.25), most of the losses are produced in the Mid 50% due to the thick wakes in this region created by the blade flow separation. However, the Hub 25% loss contribution is close at the duct exit, and both zones vastly exceed the Shroud 75% zone.

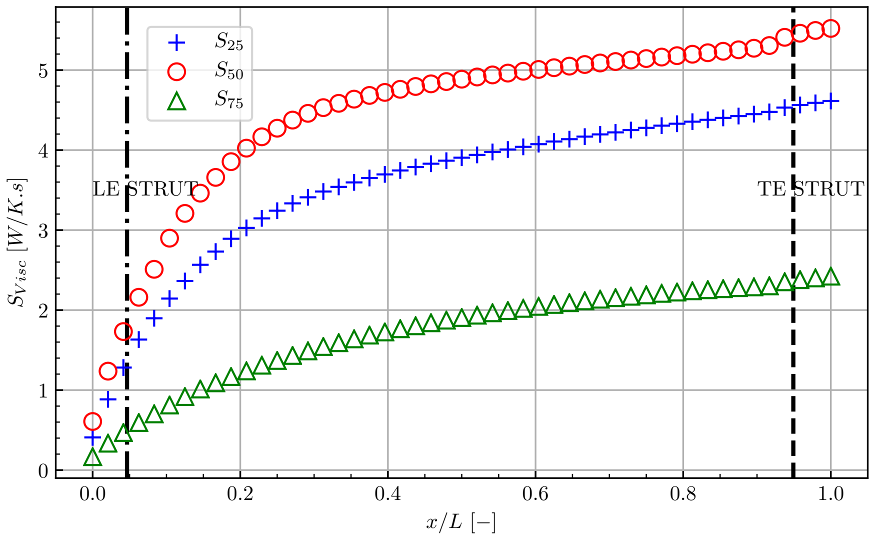

Figure **(7.25)** – Plot of accumulated entropy through the S-duct in the different zones for case (S1-Duct).

Different contour maps are presented in the following to analyze the entropy loss further. First, Fig. 7.26 illustrates contour plots of entropy for both cases at $h/H = 5\%$. It shows that for the (Duct) case, a zone of high entropy can be found across the duct width between $x/L = 0.2$ and $x/L = 0.4$ as well as a peak at the strut TE. For the (S1-Duct) case, high entropy loss is introduced by the wakes at the inlet of the duct. This slightly changes the high entropy zone for $0.2 \leq x \leq 0.4$, where the distribution is not as uniform as for the (Duct) case but is concentrated around streaks formed by the S1 wakes.

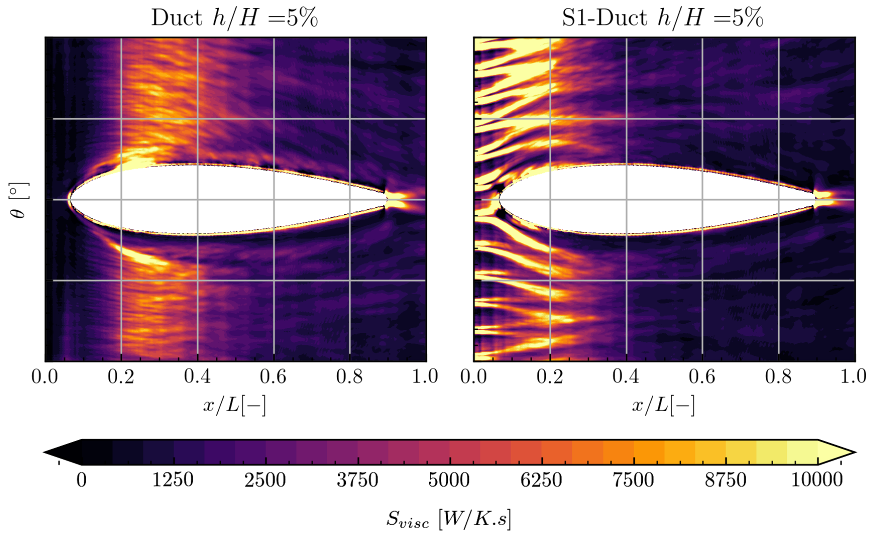

Figure **(7.26)** – Contour plot of entropy at $h/H = 5\%$ for cases (Duct) and (S1-Duct).

Fig. 7.27 compares the Mach number and entropy contours for the two cases at a cut situated at $x/L = 0.2$. For the (Duct) case, a uniform separation is found at the hub leading to the corresponding high entropy zone. Another zone of relatively low Mach number is present at the shroud but responsible for less entropy creation. On the other hand, for the (S1-Duct) case, a slightly larger separation is found at the hub with structures matching the introduced upstream wakes. It is also observed that these wakes leave a trace in the rest of the vein height, explaining the higher entropy loss found in the mid 50% zone.

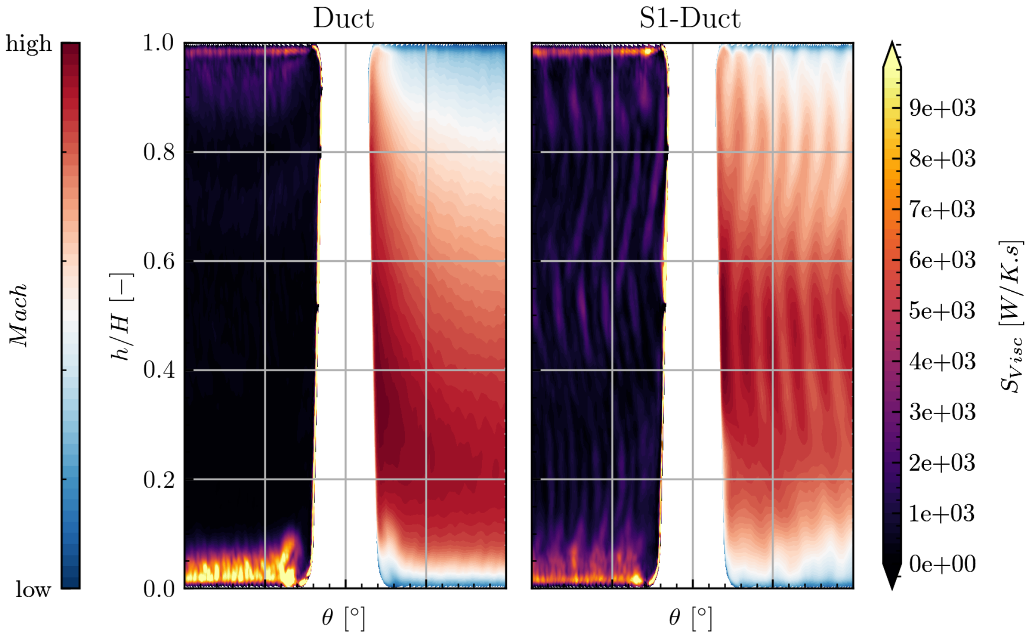

Figure **(7.27)** – Comparison of Mach number and entropy contours for the two cases at $x/L = 0.3$

The separation occurring in the duct is illustrated in Fig 7.28, which shows Mach number contours on a cut taken in the $x - z$ direction across the duct. It can be seen that in both cases, the separation is developing at the hub from $x/L = 0.2$. For both cases, similar flow field development is found across the S-duct except at the shroud for the (Duct) case, where a larger zone of low Mach number is found until $x/L = 0.8$.

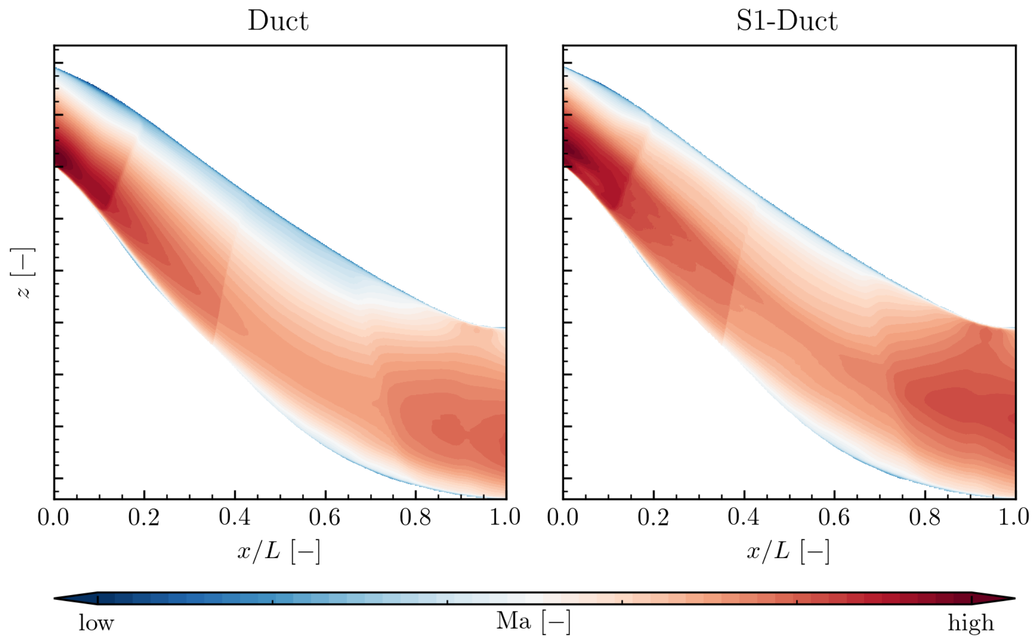

Figure **(7.28)** – Comparison of Mach number contours on a $x-z$ plane for both cases.

At the duct exit plane (see Fig. 7.29), similar results are obtained for both cases with a fine strut wake concentrating high level of entropy and an additional zone of low momentum fluid below $h/H = 20\%$ contributing to the losses.

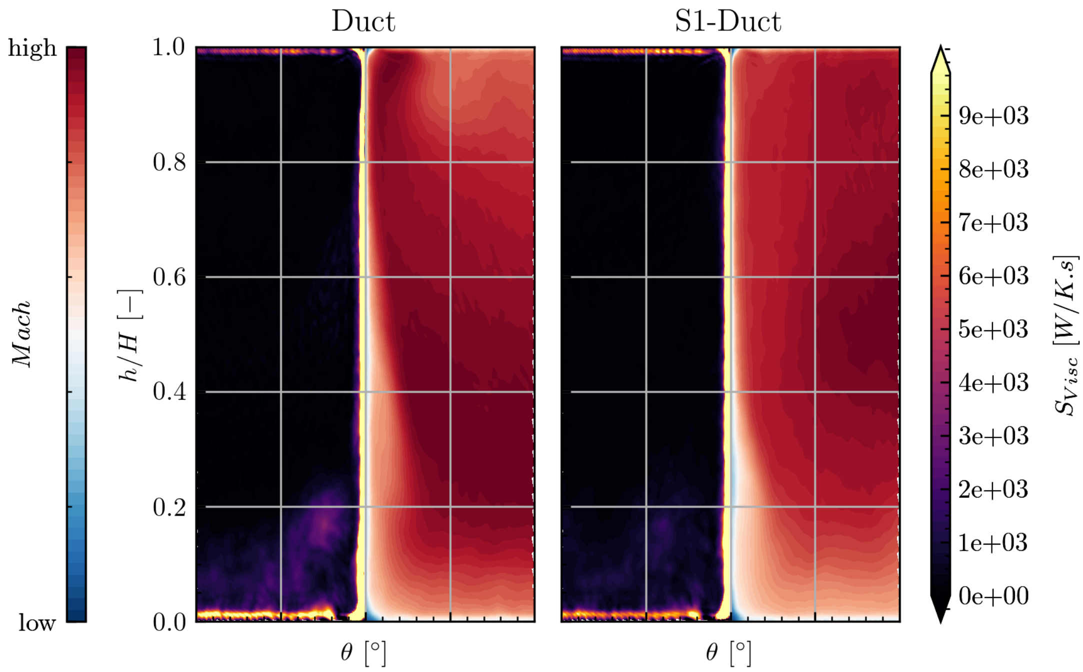

Figure **(7.29)** – Comparison of Mach number and entropy contours for the two cases at the duct exit $(x/L = 1)$

7.5 Chapter Summary

The primary conclusions to retain from the study presented in this chapter are:

- The successful application of the ProLB solver on an S-duct of industrial complexity at high Mach and Reynolds numbers. Two configurations have been examined and compared to experimental and RANS data. Results regarding radial profiles are close to the experiment.
- An entropy formulation to characterize the losses has been applied and showed similar physical phenomena compared to the CAM1 configuration with a zone of high entropy situated close to the hub. However, the effect of the upstream stator on the radial profiles is not as visible as in the CAM1 case. Indeed, even though the loss level increases when the S1 is installed, the level is slightly overestimated due to inaccurate prediction of the wakes. This is explained by a separation that is developing at the first bend of the duct, with or without the stator row, contributing to the losses.
- Some difficulties concerning the prediction of separations have been observed, especially on the S1 blades that are highly loaded and curved.

Chapter 8: Conclusions and Perspectives

Recalling the Objectives

Developing new, more aggressive designs of Intermediate Compressor Duct (ICD) is essential for an aircraft manufacturer as they allow substantial gains in engine weight. However, the flow field evolution has not been investigated as extensively as other engine components and experimental measurements are challenging to achieve. The use of Computational Fluid Dynamic (CFD) is thus of primary importance during the design phase, where numerous geometries can be evaluated and compared at a reduced cost. Nonetheless, CFD can be expensive, so the computational time must be contained and the accuracy evaluated.

8.1 Conclusions

To answer these issues, this Ph.D. thesis focused on developing and validating the Lattice Boltzmann Method for accurate turbomachinery simulation of a representative S-duct.

- During this Ph.D. thesis, the development and validation of several features that would be useful for complex industrial turbomachinery test cases have been performed and include:
  - The development and validation of a non-reflecting total pressure, total temperature, and flow angle inlet boundary condition on a wide range of test cases.
  - The validation of a non-reflecting static pressure outlet boundary condition that verifies the radial equilibrium assumption and can be coupled with an adaptive mass flow condition.
- The thermal compressible version of the solver was used to perform several Large Eddy Simulation (LES) on an academic S-duct configuration of increasing complexity. The results generally agreed with the experiment and showed improvements compared to the previous Reynold Averaged Navier-Stokes (RANS) simulations. This case served as a validation of the ProLB solver on a configuration that includes several rows. Then, a physical analysis of the flow field was performed to study the loss generation mechanism. It was observed that the upstream stator row of the duct significantly influenced the flow development and loss level produced across the duct. Indeed, the upstream stator wakes were shown to migrate along the hub wall, creating patches of flow separation and, ultimately, raising the overall level of losses.
- In terms of design philosophy, this means that if the S-duct is designed in isolation from the surrounding modules and is separating, adding an upstream stator does

not further increase the separation and the loss level. However, the CAM1 case illustrated that adding an upstream row creates flow separation at the hub for a duct that did not separate when studied in isolation. This confirms the need to move towards an integrated design that considers the stator row installed at the duct inlet.

- ProLB was finally applied on a realistic industrial S-duct operating at a compressible operating point. The results were found to be in good agreement with the experimental results. The flow field developing inside the duct slightly differs from the academic case. The impact of introducing an upstream stator is less visible on the radial profiles and loss level. This is explained by a separation that is already occurring with the isolated duct at this operating point. The addition of migrating wakes at the hub thus does not significantly modify the flow field. This illustrates the capability of the code to treat configurations of high complexity encountered in the industry.

8.2 Perspectives

The Lattice Boltzmann Method (LBM) solver ProLB has shown itself capable of accurately conducting S-duct turbomachinery simulations. However, numerous subjects could be improved in the future:

- The results in the tip gap region were shown to be limited by the number of cells that could be placed in this zone and the limited resolution that could be applied on the shroud to propagate the effects downstream. This was imposed by the solver functionality that can not deal with mesh transitions at the rotating interface.

- All the simulations performed during this Ph.D. included a 360° computational domain. This increased the computational cost unnecessarily, considering that the geometry of the academic case showed a periodicity of $1/8^{th}$. Being able to perform simulations with azimuthal periodicity offers a major reduction of the already competitive computational cost.

- As illustrated during the simulations of the industrial case, the prediction of the total temperature near the hub and shroud walls lacks precision due to the actual implementation of the wall law. A first correction was introduced with the Crocco-Busemann approach. However, despite improving the results, some discrepancies are still observed. It would be beneficial to implement and validate a thermal wall law and compare it to the current results of the solver.

- The current thermal scheme is based on the primitive entropy variable and was shown to be satisfactory for the test cases considered during this manuscript. However, this formulation is limited to high-subsonic regimes and could limit the application of the method to turbomachinery configurations where transonic or supersonic phenomena must be considered. A possible solution is implementing a conservative total energy scheme, leading to a more versatile formulation that solves the equivalent macroscopic equations of most compressible Navier-Stokes solvers.

Appendix

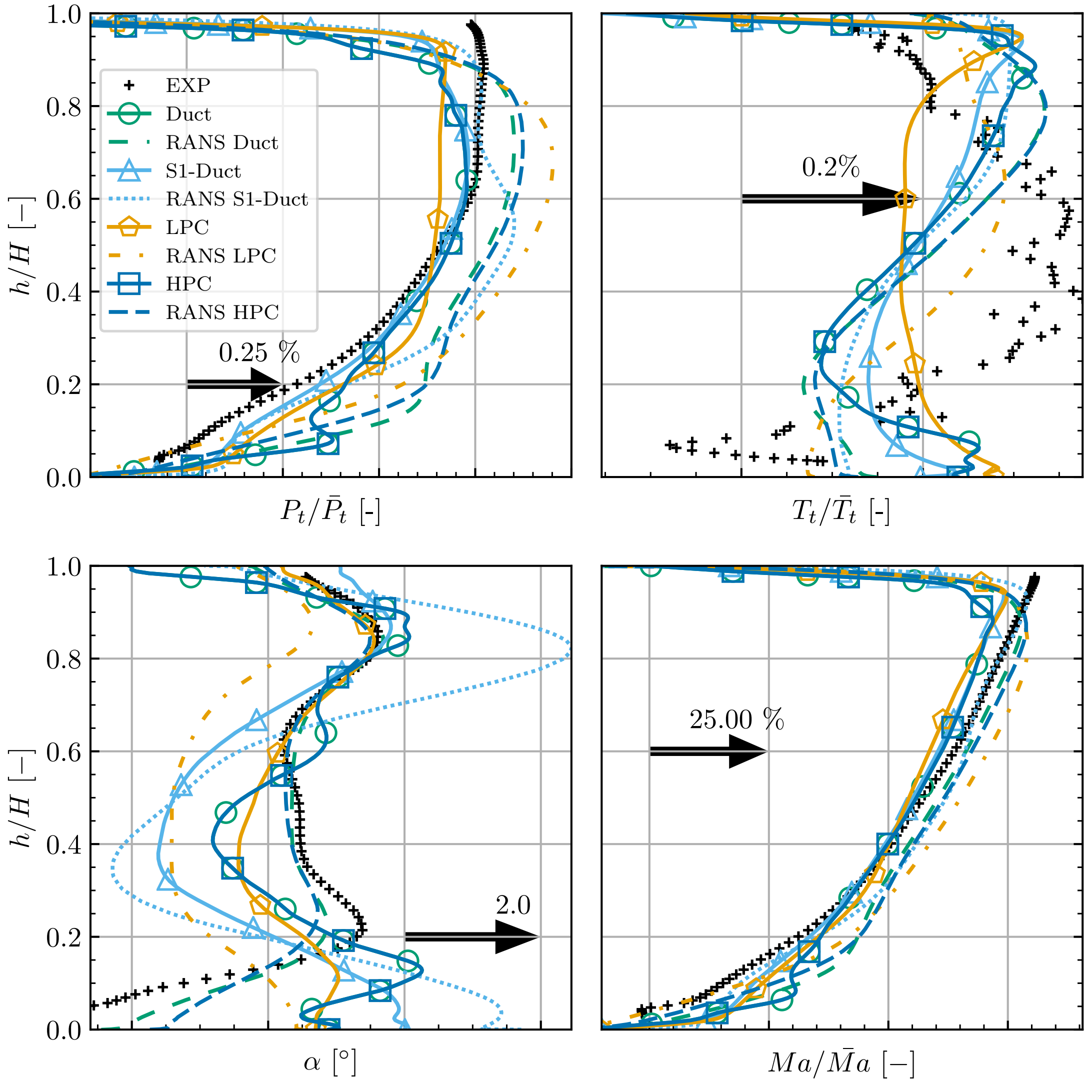

Figure **(.1)** – Radial profiles at the Duct exit plane (4).

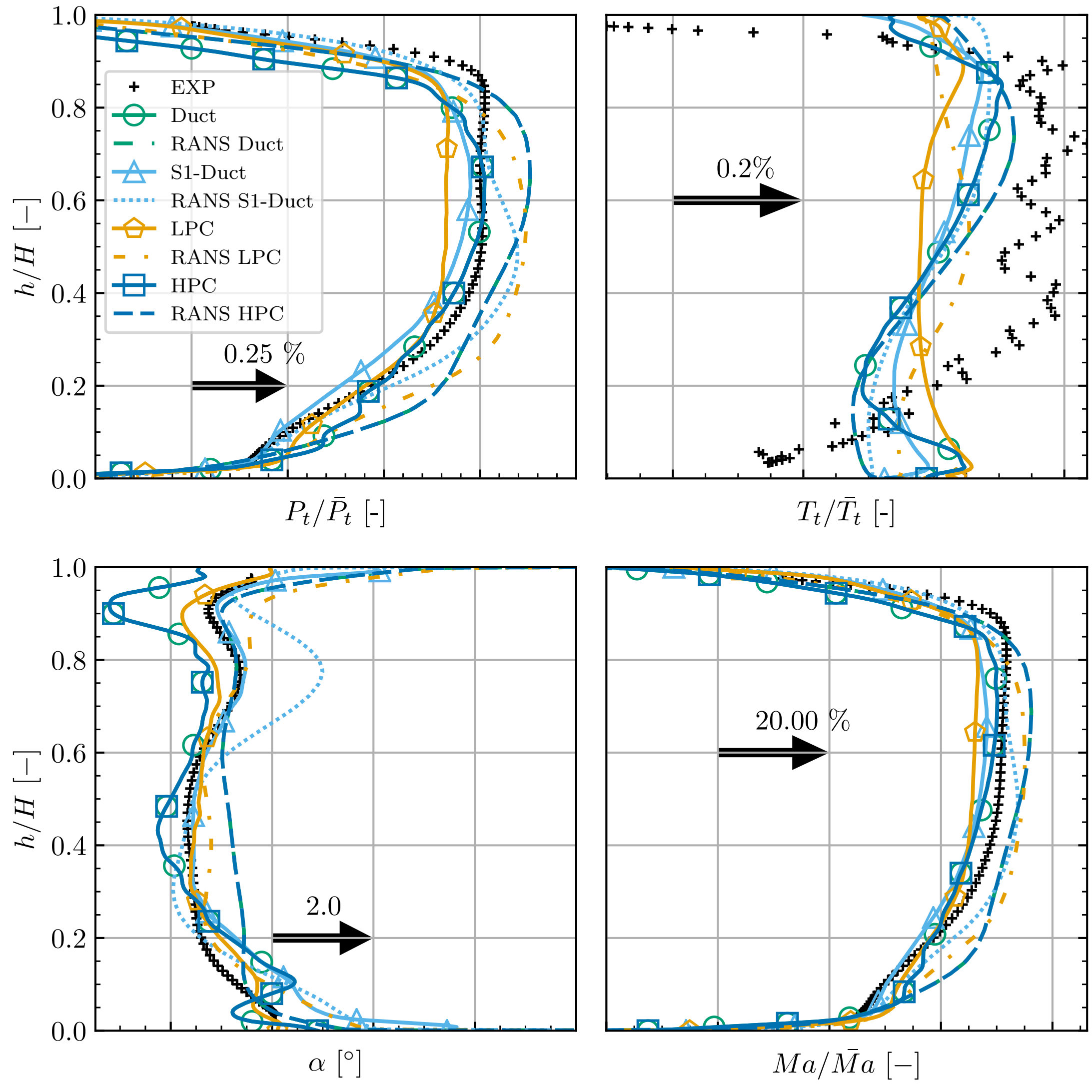

Figure **(.2)** – Radial profiles at the IGV2 exit plane (5).

Bibliography

[1] M Klöwer, M R Allen, D S Lee, et al. "Quantifying aviation's contribution to global warming". In: *Environmental Research Letters* 16.10 (Oct. 2021), p. 104027. DOI: 10.1088/1748-9326/ac286e. URL: https://dx.doi.org/10.1088/1748-9326/ac286e (cit. on p. 17).

[2] McKinsey. *Hydrogen-powered aviation. A fact-based study of hydrogen technology, economics, and climate impact by 2050.* 2020, pp. 20740–20764. URL: https://www.euractiv.com/wp-content/uploads/sites/2/2020/06/20200507_Hydrogen-Powered-Aviation-report_FINAL-web-ID-8706035.pdf (cit. on p. 17).

[3] Vedant Singh and Somesh Kumar Sharma. "Fuel consumption optimization in air transport: a review, classification, critique, simple meta-analysis, and future research implications". In: *European Transport Research Review* 7.2 (2015), p. 12. DOI: 10.1007/s12544-015-0160-x. URL: https://doi.org/10.1007/s12544-015-0160-x (cit. on p. 17).

[4] J. A. Jupp. "The design of future passenger aircraft – the environmental and fuel price challenges". In: *The Aeronautical Journal* 120.1223 (2016), 37–60. DOI: 10.1017/aer.2015.4 (cit. on p. 17).

[5] P.P Walsh and P. Fletcher. *Gas Turbine Performance*. Second Edi. June. 2014, pp. 1–542. ISBN: 978-0-582-41483-9 (cit. on p. 18).

[6] Jack D Mattingly, William H Heiser, and David T Pratt. *Aircaft Engine Design*. 1801. ISBN: 1563475383 (cit. on p. 18).

[7] Saravanamutoo, Cohen H., and GFC Rogers. *Gas Turbine Theory*. 2013, p. 283. ISBN: 9788177589023 (cit. on p. 18).

[8] Tiziano Ghisu, Geoffrey T. Parks, Jerome P. Jarrett, et al. "An integrated system for the aerodynamic design of compression systems-part I: Development". In: *Journal of Turbomachinery* 133.1 (2011). ISSN: 0889504X. DOI: 10.1115/1.4000534 (cit. on p. 19).

[9] Tiziano Ghisu, Geoffrey T. Parks, Jerome P. Jarrett, et al. "An integrated system for the aerodynamic design of compression systems-part II: Application". In: *Journal of Turbomachinery* 133.1 (2011). ISSN: 0889504X. DOI: 10.1115/1.4000535 (cit. on p. 19).

[10] A. D. Walker, A. G. Barker, J. F. Carrotte, et al. "Integrated Outlet Guide Vane Design for an Aggressive S-Shaped Compressor Transition Duct". In: *Journal of Turbomachinery* 135.1 (2012), pp. 1–11. ISSN: 0889504X. DOI: 10.1115/1.4006331 (cit. on pp. 19, 34).

[11] Pedro Alves, Miguel Silvestre, and Pedro Gamboa. "Aircraft propellers—Is there a future?" In: *Energies* 13.6 (2020), pp. 1–17. ISSN: 19961073. DOI: 10.3390/en13164157 (cit. on p. 20).

[12] C Ortiz Dueñas, R J Miller, H P Hodson, et al. *Effect of Length on Compressor Inter-Stage Duct Performance*. Tech. rep. 2007 (cit. on pp. 21, 32, 34, 44, 46, 55, 167).

[13] Osborne Reynolds. "IV. On the dynamical theory of incompressible viscous fluids and the determination of the criterion". In: *Philosophical Transactions of the Royal Society of London. (A.)* 186 (1895), pp. 123–164. DOI: 10.1098/rsta.1895.0004. URL: https://royalsocietypublishing.org/doi/abs/10.1098/rsta.1895.0004 (cit. on p. 21).

[14] J Smagorinsky. "General Circulation Experiments with the Primitive Equations". In: *Monthly Weather Review* 91.3 (Jan. 1963), p. 99. DOI: 10.1175/1520-0493(1963)091<0099:GCEWTP>2.3.CO;2 (cit. on p. 21).

[15] Haecheon Choi and Parviz Moin. "Grid-point requirements for large eddy simulation: Chapman's estimates revisited". In: *Physics of Fluids* 24.1 (2012), p. 11702. DOI: 10.1063/1.3676783. URL: https://doi.org/10.1063/1.3676783 (cit. on p. 21).

[16] Alexandre Suss, Ivan Mary, Thomas Le Garrec, et al. "Comprehensive comparison between the lattice Boltzmann and Navier–Stokes methods for aerodynamic and aeroacoustic applications". In: *Computers and Fluids* 257 (2023), p. 105881. ISSN: 0045-7930. DOI: https://doi.org/10.1016/j.compfluid.2023.105881. URL: https://www.sciencedirect.com/science/article/pii/S0045793023001068 (cit. on p. 22).

[17] J P Longley and E. M. Greitzer. *Inlet Distortion Effects in Aircraft Propulsion System Integration* (cit. on p. 26).

[18] Muhammad Sahidin Rizal Maulana. "Experimental and Numerical Investigation of an S-duct Diffuser that is Designed for a Micro Trubine Engine Powered Aircraft". In: *Ekp* 13.3 (2017), pp. 1576–1580 (cit. on p. 26).

[19] K.M. Britchford. "The Aerodynamic Behaviour of an Annular S-shaped Duct". PhD thesis. Loughborough University, 1998, p. 463. ISBN: 0415782228. URL: https://dspace.lboro.ac.uk/ (cit. on pp. 28, 32, 176).

[20] K. M. Britchford, A. P. Manners, J. J. McGuirk, et al. "Measurement and prediction of Flow in annular S-shaped ducts". In: *Experimental Thermal and Fluid Science* 9.2 (1994), pp. 197–205. ISSN: 08941777. DOI: 10.1016/0894-1777(94)90112-0 (cit. on pp. 28, 44, 50).

[21] Fredrik Wallin, Jörgen Olsson, Peter Bv Johansson, et al. *High Speed Testing and Numerical Validation of an Aggressive Intermediate Compressor Duct*. Tech. rep. 2013 (cit. on pp. 30, 34, 52, 55).

[22] Michael M. Wojewodka, Craig White, Shahrokh Shahpar, et al. "A review of flow control techniques and optimisation in s-shaped ducts". In: *International Journal of Heat and Fluid Flow* 74.June (2018), pp. 223–235. ISSN: 0142727X. DOI: 10.1016/j.ijheatfluidflow.2018.06.016. URL: https://doi.org/10.1016/j.ijheatfluidflow.2018.06.016 (cit. on p. 30).

[23] Marios K Karakasis, Edward M J Naylor, Robert J Miller, et al. *The Effect of an Upstream Compressor on a Non-Axisymmetric S-Duct*. Tech. rep. 2010 (cit. on pp. 30, 32, 34, 50–52, 112, 122, 130, 166, 167).

[24] John C. Vaccaro, Yossef Elimelech, Yi Chen, et al. "Experimental and numerical investigation on the flow field within a compact inlet duct". In: *International Journal of Heat and Fluid Flow* 44 (2013), pp. 478–488. ISSN: 0142727X. DOI: 10.1016/j.ijheatfluidflow.2013.08.004. URL: http://dx.doi.org/10.1016/j.ijheatfluidflow.2013.08.004 (cit. on p. 30).

[25] Rajesh K. Singh, S. N. Singh, and V. Seshadri. "Performance and flow characteristics of double-offset Y-shaped aircraft intake ducts". In: *Journal of Aircraft* 45.4 (2008), pp. 1230–1243. ISSN: 15333868. DOI: 10.2514/1.34137 (cit. on p. 31).

[26] Titiksh Patel, S. N. Singh, and V. Seshadri. "Characteristics of Y-Shaped rectangular diffusing duct at different inflow conditions". In: *Journal of Aircraft* 42.1 (2005), pp. 113–120. ISSN: 15333868. DOI: 10.2514/1.4690 (cit. on p. 31).

[27] Edward M.J. Naylor, Cecilia Ortiz Dueñas, Robert J. Miller, et al. "Optimization of non-axisymmetric endwalls in compressor S-shaped ducts". In: *Journal of Turbomachinery* 132.1 (Jan. 2010). ISSN: 0889504X. DOI: 10.1115/1.3103927 (cit. on pp. 31, 32, 34, 38, 167).

[28] Durham. "Flows Through S-Shaped Annular , Inter-Turbine Diffusers". In: (1998) (cit. on p. 33).

[29] Toyotaka Sonoda, Toshiyuki Arima, and Mineyasu Oana. *The Effect of Inlet Boundary Layer Thickness on the Flow within an Annular S-Shaped Duct*. Tech. rep. 1998. URL: https://proceedings.asmedigitalcollection.asme.org (cit. on pp. 34, 46, 47).

[30] A D Walker, A G Barker, and J F Carrotte. *Numerical Design and Experimental Evaluation of an Aggressive S-Shaped Compressor Transition Duct with Bleed*. Tech. rep. 2011. URL: http://asmedigitalcollection.asme.org/GT/proceedings-pdf/GT2011/54679/151/2761274/151_1.pdf (cit. on p. 34).

[31] Fredrik Wallin, Mark H Ross, Max Rusche, et al. *Investigation of Loss Impact from Production-like Features in a Compressor Duct under Engine Realistic Conditions*. Tech. rep. 2017 (cit. on pp. 34, 39).

[32] Robin Bergstedt. *Aero-Design of Aerodynamically Lifting Struts for Intermediate Compressor Ducts*. Tech. rep. 2014 (cit. on pp. 34, 52).

[33] T StürzebecherSt, G Goinis, C Voss, et al. *Automated Aerodynamic Optimization of an Aggressive S-Shaped Intermediate Compressor Duct*. Tech. rep. 2018 (cit. on pp. 34, 44, 45, 52).

[34] Courtney Rider, Grant Ingram, and Robert Stowe. "Investigation of a Passive Flow Control Device in an S-Duct Inlet at High Subsonic Flow". In: (2021), pp. 1–17 (cit. on p. 34).

[35] Asad Asghar, Robert Stowe, William D.E. Allan, et al. "S-duct diffuser offset-to-length ratio effect on aerodynamic performance of propulsion-system inlet of high speed aircraft". In: *Proceedings of the ASME Turbo Expo* 1.November 2020 (2018). DOI: 10.1115/GT2018-76661 (cit. on p. 34).

[36] Sebastian Brehm, Thomas Kächele, and Reinhard Niehuis. “CFD investigations on the influence of varying inflow conditions on the aerodynamics in an s-shaped inlet duct”. In: *50th AIAA/ASME/SAE/ASEE Joint Propulsion Conference 2014* (2014), pp. 1–14. DOI: 10.2514/6.2014-3595 (cit. on p. 34).

[37] Anne Laure Delot and Richard K. Scharnhorst. “A comparison of several CFD codes with experimental data in a diffusing S-Duct”. In: *49th AIAA/ASME/SAE/ASEE Joint Propulsion Conference* 1 PartF (2013), pp. 1–25. DOI: 10.2514/6.2013-3796 (cit. on p. 34).

[38] Geoffrey Tanguy, David G Macmanus, Pavlos Zachos, et al. “Passive Flow Control Study in an S-Duct Using Stereo Particle Image Velocimetry”. In: *AIAA Journal* 55.6 (2017), pp. 1862–1877. DOI: 10.2514/1.J055354Ãŕ. URL: https://hal.archives-ouvertes.fr/hal-01719894 (cit. on p. 34).

[39] D. W. Bailey, K. M. Britchford, J. F. Carrotte, et al. “Performance assessment of an annular S-shaped duct”. In: *Proceedings of the ASME Turbo Expo* 1.January 1997 (1995). DOI: 10.1115/95-GT-242 (cit. on pp. 36, 37).

[40] B. Majumdar, S. N. Singh, and D. P. Agrawal. “Flow characteristics in S-shaped diffusing duct”. In: *International Journal of Turbo and Jet Engines* 14.1 (1997), pp. 45–57. ISSN: 03340082. DOI: 10.1515/TJJ.1997.14.1.45 (cit. on p. 37).

[41] Manoj Kumar Gopaliya, Mahesh Kumar, Shailendra Kumar, et al. “Analysis of performance characteristics of S-shaped diffuser with offset”. In: *Aerospace Science and Technology* 11.2-3 (2007), pp. 130–135. ISSN: 12709638. DOI: 10.1016/j.ast.2006.11.003 (cit. on p. 37).

[42] Y. T. Ng, S. C. Luo, T. T. Lim, et al. “On the relation between centrifugal force and radial pressure gradient in flow inside curved and S-shaped ducts”. In: *Physics of Fluids* 20.5 (2008). ISSN: 10706631. DOI: 10.1063/1.2926759 (cit. on p. 37).

[43] G. Norris, R. G. Dominy, and A. D. Smith. “Strut influences within a diffusing annular S-shaped duct”. In: *Proceedings of the ASME Turbo Expo* 1 (1998). DOI: 10.1115/98-GT-425 (cit. on p. 38).

[44] T. Sonoda, T. Arima, and M. Oana. “The influence of downstream passage on the flow within an annular s-shaped duct”. In: *Journal of Turbomachinery* 120.4 (1998), pp. 714–722. ISSN: 15288900. DOI: 10.1115/1.2841782 (cit. on p. 38).

[45] Fredrik Wallin and Lars Erik Eriksson. “Response surface-based transition duct shape optimization”. In: *Proceedings of the ASME Turbo Expo* 6 PART B (2006), pp. 1465–1474. DOI: 10.1115/GT2006-90978 (cit. on p. 38).

[46] Ivana Milanovic, John Whiton, Razvan Florea, et al. “RANS simulations for sensitivity analysis of compressor transition duct”. In: *50th AIAA/ASME/SAE/ASEE Joint Propulsion Conference 2014* (2014), pp. 1–9. DOI: 10.2514/6.2014-3631 (cit. on pp. 38, 55).

[47] H. X. Bu, H. J. Tan, H. Chen, et al. “Investigation on Secondary Flow Characteristics in a Curved Annular Duct with Struts”. In: *Flow, Turbulence and Combustion* 97.1 (2016), pp. 27–44. ISSN: 15731987. DOI: 10.1007/s10494-015-9674-5 (cit. on p. 38).

[48] Beena D. Baloni, Kadiyam Vijay Kumar, and S. A. Channiwala. "Study and numerical analysis of compressor transition duct". In: *International Conference on Fluid Flow, Heat and Mass Transfer* 108 (2017), pp. 1–10. ISSN: 23693029. DOI: 10.11159/ffhmt17.108 (cit. on p. 38).

[49] P. K. Sinha, A. N. Mullick, B. Halder, et al. "Flow investigation through annular curved diffusing duct". In: *AIP Conference Proceedings* 1298 (2010), pp. 80–90. ISSN: 0094243X. DOI: 10.1063/1.3516429 (cit. on pp. 42–44).

[50] P. K. Sinha, A. N. Mullick, B. Halder, et al. "Numerical investigation of flow through a curved annular diffuser". In: *AIP Conference Proceedings* 1440.Imat 2011 (2012), pp. 799–805. ISSN: 0094243X. DOI: 10.1063/1.4704290 (cit. on pp. 42, 43).

[51] O. E. Abdellatif, M. Abd Rabbo, M. Abd Elganny, et al. "Area ratio effect on the turbulent flow through a diffusing S-duct using large-eddy simulation". In: *6th International Energy Conversion Engineering Conference, IECEC* July (2008), pp. 28–30. DOI: 10.2514/6.2008-5726 (cit. on p. 43).

[52] Asad Asghar, Robert A. Stowe, William D.E. Allan, et al. "Entrance Aspect Ratio Effect on S-Duct Inlet Performance at High-Subsonic Flow". In: *Journal of Engineering for Gas Turbines and Power* 139.5 (2017), pp. 1–11. ISSN: 15288919. DOI: 10.1115/1.4035206 (cit. on p. 43).

[53] Jinhan Kim, Chang Ho Choi, Jungu Noh, et al. "Numerical Flow Investigation of an annular S-Shaped-Duct". In: (2004) (cit. on pp. 44, 52).

[54] T. Dygutsch, A. Kasper, and C. Voss. "On the effect of inter compressor duct length on compressor performance". In: *The Aeronautical Journal* (2022), pp. 1–18. ISSN: 0001-9240. DOI: 10.1017/aer.2022.51 (cit. on pp. 45, 55).

[55] Limin Gao, Xiaoming Deng, Xudong Feng, et al. "Effect of inlet conditions on compressor intermediate duct". In: *Proceedings of the Institution of Mechanical Engineers, Part G: Journal of Aerospace Engineering* 229.6 (2015), pp. 1154–1168. ISSN: 20413025. DOI: 10.1177/0954410014542624 (cit. on pp. 47–49).

[56] R. P. Lohmann, S. J. Markowski, and E. T. Brookman. "Swirling flow through annular diffusers with conical walls". In: *Journal of Fluids Engineering, Transactions of the ASME* 101.2 (1979), pp. 224–249. ISSN: 1528901X. DOI: 10.1115/1.3448939 (cit. on p. 48).

[57] D. W. Bailey and J F Carrotte. "The Influence of Inlet Swirl on the Flow within an Annular S-Dhaped Duct". In: *Proceedings of the ASME Turbo Expo* 1 (1996), pp. 1–11. DOI: https://doi.org/10.1115/96-GT-060 (cit. on p. 49).

[58] A. Duncan Walker, Ian Mariah, Dimitra Tsakmakidou, et al. "The Influence of Fan Root Flow on the Aerodynamic of a Low-Pressure Compressor Transition Duct". In: *Journal of Turbomachinery* 142.1 (2020). ISSN: 0889-504X. DOI: 10.1115/1.4045272 (cit. on pp. 49, 50, 53–55).

[59] D. W. Bailey. "The Aerodynamic Performance of an Annular S-Shaped Duct". In: (1997), p. 372 (cit. on p. 50).

[60] K. M. Britchford, J. F. Carrotte, J. H. Kim, et al. "The effect of operating conditions on the aerodynamic performance of an integrated OGV and S-shaped duct". In: *Proceedings of the ASME Turbo Expo* 1.1994 (2001), pp. 1–12. DOI: 10.1115/2001-GT-0347 (cit. on p. 50).

[61] Lakshya Kumar, Dilipkumar B Alone, and A M Pradeep. "Aerodynamics of inter-spool duct under the influence of an upstream transonic compressor stage". In: *Aerospace Science and Technology* (2023), p. 108282. ISSN: 1270-9638. DOI: https://doi.org/10.1016/j.ast.2023.108282. URL: https://www.sciencedirect.com/science/article/pii/S1270963823001797 (cit. on p. 52).

[62] Simão Rodrigues and Andre Marta. "DISCRETE ADJOINT MIXING-PLANE FORMULATION FOR MULTI-STAGE TURBOMACHINERY DESIGN". In: June 2015 (cit. on p. 52).

[63] Alastair Duncan Walker, Fredrik Wallin, Robin Bergstedt, et al. "Aerodesign and validation of turning struts for an intermediate compressor duct". In: *proceedings of the 22nd International Symposium on Air Breathing Engines.* (2015), pp. 1–8 (cit. on pp. 52, 53, 55).

[64] Elias Mikael Vagn Siggeirsson. *Aerodynamics of an Aeroengine Intermediate Compressor Duct : Effects from an Integrated Bleed System.* 2020. ISBN: 9789179053215 (cit. on p. 54).

[65] Elias M.V. Siggeirsson, Niklas Andersson, and Markus Burak Olander. "Numerical and Experimental Aerodynamic Investigation of an S-Shaped Intermediate Compressor Duct with Bleed". In: *Journal of Turbomachinery* 143.10 (2021), pp. 1–12. ISSN: 15288900. DOI: 10.1115/1.4050670 (cit. on pp. 54, 55).

[66] Manish Sharma and Beena D. Baloni. "Design optimization of S-shaped compressor transition duct using particle swarm optimization algorithm". In: *SN Applied Sciences* 2.2 (2020), pp. 1–17. ISSN: 25233971. DOI: 10.1007/s42452-020-1972-4. URL: https://doi.org/10.1007/s42452-020-1972-4 (cit. on p. 55).

[67] Timm Kruger, Halim Kusumaatmaja, Alexandr Kuzmin, et al. *The lattice boltzmann method, principles and practice.* 207. 2017, pp. 1–705. ISBN: 9783319446479. DOI: 10.1191/0265532206lt326oa. arXiv: arXiv:1011.1669v3 (cit. on pp. 57, 63, 84).

[68] J. Hardy, Y. Pomeau, and O. de Pazzis. "Time Evolution of a Two-Dimensional Classical Lattice System". In: *Phys. Rev. Lett.* 31 (5 July 1973), pp. 276–279. DOI: 10.1103/PhysRevLett.31.276. URL: https://link.aps.org/doi/10.1103/PhysRevLett.31.276 (cit. on p. 57).

[69] Zhi Gang Feng and Efstathios E. Michaelides. "The immersed boundary-lattice Boltzmann method for solving fluid-particles interaction problems". In: *Journal of Computational Physics* 195.2 (2004), pp. 602–628. ISSN: 00219991. DOI: 10.1016/j.jcp.2003.10.013 (cit. on pp. 57, 84).

[70] T. Krüger, F. Varnik, and D. Raabe. "Efficient and accurate simulations of deformable particles immersed in a fluid using a combined immersed boundary lattice Boltzmann finite element method". In: *Computers and Mathematics with Applications* 61.12 (2011), pp. 3485–3505. ISSN: 08981221. DOI: 10.1016/j.camwa.2010.03.057. arXiv: 1004.2416. URL: http://dx.doi.org/10.1016/j.camwa.2010.03.057 (cit. on pp. 57, 84).

[71] Julien Favier, Alistair Revell, Alfredo Pinelli, et al. "A Lattice Boltzmann - Immersed Boundary method to simulate the fluid interaction with moving and slender flexible objects To cite this version : HAL Id : hal-00822044 A Lattice Boltzmann - Immersed Boundary method to simulate the fluid interaction with mo". In: (2014) (cit. on pp. 57, 84).

[72] Guo Qing Chen, Xiao Huang, A. Man Zhang, et al. "Three-dimensional simulation of a rising bubble in the presence of spherical obstacles by the immersed boundary-lattice Boltzmann method". In: *Physics of Fluids* 31.9 (2019). ISSN: 10897666. DOI: 10.1063/1.5115097 (cit. on pp. 57, 84).

[73] J. M. Buick, C. A. Greated, and D. M. Campbell. "Lattice BGK simulation of sound waves". In: *Europhysics Letters* 43.3 (1998), pp. 235–240. ISSN: 02955075. DOI: 10.1209/epl/i1998-00346-7 (cit. on pp. 57, 84).

[74] Simon Marié, Denis Ricot, and Pierre Sagaut. "Comparison between lattice Boltzmann method and Navier-Stokes high order schemes for computational aeroacoustics". In: *Journal of Computational Physics* 228.4 (2009), pp. 1056–1070. ISSN: 10902716. DOI: 10.1016/j.jcp.2008.10.021. URL: http://dx.doi.org/10.1016/j.jcp.2008.10.021 (cit. on pp. 57, 84).

[75] Kun Xu and Chang Liu. "A paradigm for modeling and computation of gas dynamics". In: *Physics of Fluids* 29.2 (2017), pp. 1–17. ISSN: 10897666. DOI: 10.1063/1.4974873. arXiv: 1608.00303 (cit. on pp. 57, 84).

[76] Yipei Chen, Yajun Zhu, and Kun Xu. "A three-dimensional unified gas-kinetic wave-particle solver for flow computation in all regimes". In: *Physics of Fluids* 32.9 (2020). ISSN: 10897666. DOI: 10.1063/5.0021199. arXiv: 2007.13091. URL: https://doi.org/10.1063/5.0021199 (cit. on pp. 57, 84).

[77] Omar Es-Sahli, Adrian Sescu, Mohammed Z. Afsar, et al. "Investigation of wakes generated by fractal plates in the compressible flow regime using large-eddy simulations". In: *Physics of Fluids* 32.10 (2020). ISSN: 10897666. DOI: 10.1063/5.0018712. arXiv: 2009.03814. URL: https://doi.org/10.1063/5.0018712 (cit. on pp. 57, 84).

[78] Thomas Astoul, Gauthier Wissocq, Jean François Boussuge, et al. "Analysis and reduction of spurious noise generated at grid refinement interfaces with the lattice Boltzmann method". In: *Journal of Computational Physics* 418 (2020). ISSN: 10902716. DOI: 10.1016/j.jcp.2020.109645. arXiv: 2004.11863 (cit. on pp. 57, 84).

[79] Yuan Ma and Zhigang Yang. "Simplified and highly stable thermal Lattice Boltzmann method simulation of hybrid nanofluid thermal convection at high Rayleigh numbers". In: *Physics of Fluids* 32.1 (2020). ISSN: 10897666. DOI: 10.1063/1.5139092. URL: https://doi.org/10.1063/1.5139092 (cit. on pp. 57, 84).

[80] S. A. Hosseini, A. Abdelsamie, N. Darabiha, et al. "Low-Mach hybrid lattice Boltzmann-finite difference solver for combustion in complex flows". In: *Physics of Fluids* 32.7 (2020), pp. 1–13. ISSN: 10897666. DOI: 10.1063/5.0015034 (cit. on pp. 57, 84).

[81] Linlin Fei, Jingyu Du, Kai H. Luo, et al. "Modeling realistic multiphase flows using a non-orthogonal multiple-relaxation-time lattice Boltzmann method". In: *Physics of Fluids* 31.4 (2019). ISSN: 10897666. DOI: 10.1063/1.5087266 (cit. on pp. 57, 84).

[82] Yongliang Feng, Pierre Sagaut, and Wenquan Tao. "A three dimensional lattice model for thermal compressible flow on standard lattices". In: *Journal of Computational Physics* 303.September (2015), pp. 514–529. ISSN: 10902716. DOI: 10.1016/j.jcp.2015.09.011. URL: http://dx.doi.org/10.1016/j.jcp.2015.09.011 (cit. on pp. 57, 84).

[83] Dominik Wilde, Andreas Krämer, Dirk Reith, et al. "Semi-Lagrangian lattice Boltzmann method for compressible flows". In: *Physical Review E* 101.5 (2020). ISSN: 24700053. DOI: 10.1103/PhysRevE.101.053306. arXiv: 1910.13918 (cit. on pp. 57, 84).

[84] M. H. Saadat and I. V. Karlin. "Arbitrary Lagrangian-Eulerian formulation of lattice Boltzmann model for compressible flows on unstructured moving meshes". In: *Physics of Fluids* 32.4 (2020). ISSN: 10897666. DOI: 10.1063/5.0004024. arXiv: 2002.04353. URL: https://doi.org/10.1063/5.0004024 (cit. on pp. 57, 84).

[85] E. Reyhanian, B. Dorschner, and I. V. Karlin. "Thermokinetic lattice Boltzmann model of nonideal fluids". In: *Physical Review E* 102.2 (2020). ISSN: 24700053. DOI: 10.1103/PhysRevE.102.020103 (cit. on pp. 57, 84).

[86] Romana Begum and M. Abdul Basit. "Lattice Boltzmann method and its applications to fluid flow problems". In: *European Journal of Scientific Research* 22.2 (2008), pp. 216–231. ISSN: 1450202X (cit. on pp. 57, 84).

[87] L. Boltzmann. "Weitere Studien über das Wärmengleichgewicht unter Gasmolekülen". In: (1872), pp. 275–370 (cit. on p. 58).

[88] M. Bhatnagar, P. L. and Gross, E. P. and Krook. "A Model for Collision Processes in Gases. I. Small Amplitude Processes in Charged and Neutral One-Component Systems". In: *Phys. Rev* 94.3 (1954), pp. 511–525. DOI: 10.1103/PhysRev.94.511. URL: https://link.aps.org/doi/10.1103/PhysRev.94.511 (cit. on p. 59).

[89] M. Nguyen. "Investigation of the Lattice Boltzmann Method for the Simulation of Turbine Active Clearance Control Systems". PhD thesis. 2023, pp. 1–273 (cit. on pp. 62, 101, 132, 133, 147).

[90] Martin Geier and Andrea Pasquali. "Fourth order Galilean invariance for the lattice Boltzmann method". In: *Computers & Fluids* 166 (2018), pp. 139–151. ISSN: 0045-7930. DOI: https://doi.org/10.1016/j.compfluid.2018.01.015. URL: https://www.sciencedirect.com/science/article/pii/S0045793018300239 (cit. on p. 63).

[91] Xiaowen Shan. “The mathematical structure of the lattices of the lattice Boltzmann method”. In: *Journal of Computational Science* 17 (2016), pp. 475–481. ISSN: 1877-7503. DOI: https://doi.org/10.1016/j.jocs.2016.03.002. URL: https://www.sciencedirect.com/science/article/pii/S1877750316300163 (cit. on p. 63).

[92] Gauthier Wissocq, Nicolas Gourdain, Orestis Malaspinas, et al. “Regularized characteristic boundary conditions for the Lattice-Boltzmann methods at high Reynolds number flows”. In: *Journal of Computational Physics* 331 (2017), pp. 1–18. ISSN: 10902716. DOI: 10.1016/j.jcp.2016.11.037. arXiv: 1701.07734. URL: http://dx.doi.org/10.1016/j.jcp.2016.11.037 (cit. on pp. 64, 85, 94).

[93] Florian Renard. “Hybrid Lattice Boltzmann Method for Compressible Flows”. In: (2021) (cit. on pp. 64, 84).

[94] Florian Renard, Gauthier Wissocq, Jean François Boussuge, et al. “A linear stability analysis of compressible hybrid lattice Boltzmann methods”. In: *Journal of Computational Physics* 446.2 (2021). ISSN: 10902716. DOI: 10.1016/j.jcp.2021.110649. arXiv: 2006.08477 (cit. on pp. 64, 71).

[95] G. Farag, S. Zhao, G. Chiavassa, et al. “Consistency study of Lattice-Boltzmann schemes macroscopic limit”. In: *Physics of Fluids* 33.3 (2021), p. 037101. DOI: 10.1063/5.0039490. eprint: https://doi.org/10.1063/5.0039490. URL: https://doi.org/10.1063/5.0039490 (cit. on p. 69).

[96] Gabriel Farag. “Modélisation des écoulements compressibles via les méthodes Lattice-Boltzmann”. In: (2022) (cit. on pp. 69, 71).

[97] Yongliang Feng, Pierre Boivin, Jérôme Jacob, et al. “Hybrid recursive regularized lattice Boltzmann simulation of humid air with application to meteorological flows”. In: *Physical Review E* 100.2 (2019). ISSN: 24700053. DOI: 10.1103/PhysRevE.100.023304 (cit. on p. 70).

[98] S. Guo, Y. Feng, and P. Sagaut. “Improved standard thermal lattice Boltzmann model with hybrid recursive regularization for compressible laminar and turbulent flows”. In: *Physics of Fluids* 32.12 (2020). ISSN: 10897666. DOI: 10.1063/5.0033364 (cit. on pp. 70, 71).

[99] Florian Renard, Yongliang Feng, Jean-François Boussuge, et al. “Improved compressible hybrid lattice Boltzmann method on standard lattice for subsonic and supersonic flows”. In: *Computers and Fluids* 219 (2021), p. 104867. ISSN: 0045-7930. DOI: https://doi.org/10.1016/j.compfluid.2021.104867. URL: https://www.sciencedirect.com/science/article/pii/S0045793021000335 (cit. on pp. 70, 71).

[100] G. Farag, T. Coratger, G. Wissocq, et al. “A unified hybrid lattice-Boltzmann method for compressible flows: Bridging between pressure-based and density-based methods”. In: *Physics of Fluids* 33.8 (2021). ISSN: 10897666. DOI: 10.1063/5.0057407 (cit. on pp. 70, 71, 73).

[101] G. Wissocq, T. Coratger, G. Farag, et al. "Restoring the conservativity of characteristic-based segregated models: Application to the hybrid lattice Boltzmann method". In: *Physics of Fluids* 34.4 (Apr. 2022), p. 046102. ISSN: 1070-6631. DOI: 10.1063/5.0083377. eprint: https://pubs.aip.org/aip/pof/article-pdf/doi/10.1063/5.0083377/16614498/046102_1_online.pdf. URL: https://doi.org/10.1063/5.0083377 (cit. on p. 71).

[102] Kyu Hong Kim, Chongam Kim, and Oh Hyun Rho. "Methods for the accurate computations of hypersonic flows. II. Shock-aligned grid technique". In: *Journal of Computational Physics* 174.1 (2001), pp. 81–119. ISSN: 00219991. DOI: 10.1006/jcph.2001.6896 (cit. on p. 71).

[103] Yongliang Feng, Pierre Boivin, Jérôme Jacob, et al. "Hybrid recursive regularized thermal lattice Boltzmann model for high subsonic compressible flows". In: *Journal of Computational Physics* 394 (Oct. 2019), pp. 82–99. ISSN: 0021-9991. DOI: 10.1016/J.JCP.2019.05.031 (cit. on pp. 71, 77, 94).

[104] S. Guo, Y. Feng, and P. Sagaut. "Improved standard thermal lattice Boltzmann model with hybrid recursive regularization for compressible laminar and turbulent flows". In: *Physics of Fluids* 32.12 (2020). ISSN: 10897666. DOI: 10.1063/5.0033364 (cit. on p. 71).

[105] G. Farag, S. Zhao, T. Coratger, et al. "A pressure-based regularized lattice-Boltzmann method for the simulation of compressible flows". In: *Physics of Fluids* 32.6 (2020). ISSN: 10897666. DOI: 10.1063/5.0011839 (cit. on pp. 71–73).

[106] Pierre Lallemand and Li-Shi Luo. "Theory of the lattice Boltzmann method: Dispersion, dissipation, isotropy, Galilean invariance, and stability". In: *Phys. Rev. E* 61 (6 June 2000), pp. 6546–6562. DOI: 10.1103/PhysRevE.61.6546. URL: https://link.aps.org/doi/10.1103/PhysRevE.61.6546 (cit. on p. 72).

[107] C. Coreixas. "High-order extension of the recursive regularized lattice Boltzmann method". PhD Thesis. Université de Toulouse, INP Toulouse - Ecole doctorale MEGeP, Feb. 2018 (cit. on p. 72).

[108] Christophe Coreixas, Bastien Chopard, and Jonas Latt. "Comprehensive comparison of collision models in the lattice Boltzmann framework: Theoretical investigations". In: *Phys. Rev. E* 100 (3 Sept. 2019), p. 033305. DOI: 10.1103/PhysRevE.100.033305. URL: https://link.aps.org/doi/10.1103/PhysRevE.100.033305 (cit. on p. 72).

[109] "Generalized Lattice-Boltzmann Equations". In: *Rarefied Gas Dynamics: Theory and Simulations*. 1992, pp. 450–458. DOI: 10.2514/5.9781600866319.0450.0458. eprint: https://arc.aiaa.org/doi/pdf/10.2514/5.9781600866319.0450.0458. URL: https://arc.aiaa.org/doi/abs/10.2514/5.9781600866319.0450.0458 (cit. on p. 72).

[110] Bruce M Boghosian, Jeffrey Yepez, Peter V Coveney, et al. "Entropic lattice Boltzmann methods". In: *Proceedings of the Royal Society of London. Series A: Mathematical, Physical and Engineering Sciences* 457.2007 (2001), pp. 717–766. DOI: 10.1098/rspa.2000.0689. eprint: https://royalsocietypublishing.org/doi/pdf/10.1098/rspa.2000.0689. URL: https://royalsocietypublishing.org/doi/abs/10.1098/rspa.2000.0689 (cit. on p. 72).

[111] Jonas Latt and Bastien Chopard. "Lattice Boltzmann method with regularized pre-collision distribution functions". In: *Mathematics and Computers in Simulation* 72.2-6 (2006), pp. 165–168. ISSN: 03784754. DOI: 10.1016/j.matcom.2006.05.017. arXiv: 0506157 [physics] (cit. on pp. 72, 94).

[112] Jérôme Jacob, Orestis Malaspinas, and Pierre Sagaut. "A new hybrid recursive regularised bhatnagar–gross–krook collision model for lattice boltzmann method-based large eddy simulation". In: *Journal of Turbulence* 19.11 (2019), pp. 1051–1076. ISSN: 14685248. DOI: 10.1080/14685248.2018.1540879 (cit. on p. 72).

[113] S. Guo, Y. Feng, J. Jacob, et al. "An efficient lattice Boltzmann method for compressible aerodynamics on D3Q19 lattice". In: *Journal of Computational Physics* 418.May (2020). ISSN: 10902716. DOI: 10.1016/j.jcp.2020.109570 (cit. on p. 73).

[114] Martin Bauer, Goncalo Silva, and Ulrich Rüde. "Truncation errors of the D3Q19 lattice model for the lattice Boltzmann method". In: *Journal of Computational Physics* 405 (2020), p. 109111. ISSN: 0021-9991. DOI: https://doi.org/10.1016/j.jcp.2019.109111. URL: https://www.sciencedirect.com/science/article/pii/S0021999119308162 (cit. on pp. 73, 74, 133).

[115] E. Lévêque, F. Toschi, L. Shao, et al. "Shear-improved Smagorinsky model for large-eddy simulation of wall-bounded turbulent flows". In: *Journal of Fluid Mechanics* 570 (2007), 491–502. DOI: 10.1017/S0022112006003429 (cit. on p. 76).

[116] BERT VREMAN, BERNARD GEURTS, and HANS KUERTEN. "Large-eddy simulation of the turbulent mixing layer". In: *Journal of Fluid Mechanics* 339 (1997), 357–390. DOI: 10.1017/S0022112097005429 (cit. on p. 76).

[117] Y. Feng, S. Guo, J. Jacob, et al. "Solid wall and open boundary conditions in hybrid recursive regularized lattice Boltzmann method for compressible flows". In: *Physics of Fluids* 31.12 (2019). ISSN: 10897666. DOI: 10.1063/1.5129138. URL: https://doi.org/10.1063/1.5129138 (cit. on pp. 76, 85, 94, 95).

[118] Donald Shepard. "A Two-Dimensional Interpolation Function for Irregularly-Spaced Data". In: *Proceedings of the 1968 23rd ACM National Conference*. ACM '68. New York, NY, USA: Association for Computing Machinery, 1968, 517–524. ISBN: 9781450374866. DOI: 10.1145/800186.810616. URL: https://doi.org/10.1145/800186.810616 (cit. on p. 78).

[119] J. Boudet, E. Lévêque, and H. Touil. "Unsteady Lattice Boltzmann Simulations of Corner Separation in a Compressor Cascade". In: *Journal of Turbomachinery* 144.1 (2022), pp. 1–12. ISSN: 0889-504X. DOI: 10.1115/1.4052017 (cit. on pp. 79, 147).

[120] Stephen B. Pope. *Turbulent Flows*. Cambridge University Press, 2000 (cit. on p. 79).

[121] H. Yoo, M. L. Bahlali, J. Favier, et al. "A hybrid recursive regularized lattice Boltzmann model with overset grids for rotating geometries". In: *Physics of Fluids* 33.5 (2021), p. 057113. DOI: 10.1063/5.0045524. eprint: https://doi.org/10.1063/5.0045524. URL: https://doi.org/10.1063/5.0045524 (cit. on pp. 79, 80, 137).

[122] Zhaoli Guo, Chuguang Zheng, and Baochang Shi. "Discrete lattice effects on the forcing term in the lattice Boltzmann method". In: *Phys. Rev. E* 65 (4 2002), p. 046308. DOI: 10.1103/PhysRevE.65.046308. URL: https://link.aps.org/doi/10.1103/PhysRevE.65.046308 (cit. on p. 80).

[123] Heesik Yoo. "Lattice Boltzmann method for rotating geometries at high Reynolds number and high Mach number conditions". In: (2022) (cit. on p. 80).

[124] Y. H. Qian, D. D'Humières, and P. Lallemand. "Lattice bgk models for navier-stokes equation". In: *Epl* 17.6 (1992), pp. 479–484. ISSN: 12864854. DOI: 10.1209/0295-5075/17/6/001 (cit. on p. 84).

[125] Sharath Girimaji. *Lattice Boltzmann Method: Fundamentals and Engineering Applications with Computer Codes*. Vol. 51. 1. 2013, pp. 278–279. ISBN: 9780857294548. DOI: 10.2514/1.j051744 (cit. on p. 84).

[126] Kurnchul Lee Girimaji, Dazhi Yu, and Sharath S. "Lattice Boltzmann DNS of decaying compressible isotropic turbulence with temperature fluctuations". In: *International Journal of Computational Fluid Dynamics* 20 (2006), pp. 401–413. DOI: 10.1080/10618560601001122. URL: https://doi.org/10.1080/10618560601001122 (cit. on p. 84).

[127] Phoi Tack Lew, Anastasios Lyrintzis, Bernd Crouse, et al. "Noise prediction of a subsonic turbulent round jet using the lattice-Boltzmann method". In: *13th AIAA/CEAS Aeroacoustics Conference (28th AIAA Aeroacoustics Conference)* September (2007). ISSN: 00014966. DOI: 10.1121/1.3458846 (cit. on p. 84).

[128] A. Scagliarini, L. Biferale, M. Sbragaglia, et al. "Lattice Boltzmann methods for thermal flows: Continuum limit and applications to compressible Rayleigh-Taylor systems". In: *Physics of Fluids* 22.5 (2010), pp. 1–21. ISSN: 10706631. DOI: 10.1063/1.3392774. arXiv: 1005.3639 (cit. on p. 84).

[129] T. J. Poinsot and S. K. Lele. "Boundary conditions for direct simulations of compressible viscous flows". In: *Journal of Computational Physics* 101.1 (1992), pp. 104–129. ISSN: 10902716. DOI: 10.1016/0021-9991(92)90046-2 (cit. on pp. 84, 86).

[130] C. D. Rakopoulos, A. M. Dimaratos, E. G. Giakoumis, et al. "Study of turbocharged diesel engine operation, pollutant emissions and combustion noise radiation during starting with bio-diesel or n-butanol diesel fuel blends". In: *Applied Energy* 88.11 (2011), pp. 3905–3916. ISSN: 03062619. DOI: 10.1016/j.apenergy.2011.03.051. URL: http://dx.doi.org/10.1016/j.apenergy.2011.03.051 (cit. on p. 84).

[131] G. Daviller, G. Oztarlik, and T. Poinsot. "A generalized non-reflecting inlet boundary condition for steady and forced compressible flows with injection of vortical and acoustic waves". In: *Computers and Fluids* 190.June 2019 (2019), pp. 503–513. ISSN: 00457930. DOI: 10.1016/j.compfluid.2019.06.027 (cit. on p. 84).

[132] C. Koupper, T. Poinsot, L. Gicquel, et al. "Compatibility of characteristic boundary conditions with radial equilibrium in turbomachinery simulations". In: *AIAA Journal* 52.12 (2014), pp. 2829–2839. ISSN: 00011452. DOI: 10.2514/1.J052915 (cit. on pp. 85, 104, 105).

[133] Nicolas Odier, Marlène Sanjosé, Laurent Gicquel, et al. "A characteristic inlet boundary condition for compressible, turbulent, multispecies turbomachinery flows". In: *Computers and Fluids* 178 (2019), pp. 41–55. ISSN: 00457930. DOI: 10.1016/j.compfluid.2018.09.014 (cit. on pp. 85, 90, 95, 102).

[134] J. S. Carullo, S. Nasir, R. D. Cress, et al. "The effects of freestream turbulence, turbulence length scale, and exit reynolds number on turbine blade heat transfer in a transonic cascade". In: *Journal of Turbomachinery* 133.1 (2011), pp. 1–11. ISSN: 0889504X. DOI: 10.1115/1.4001366 (cit. on p. 85).

[135] Mohsen Jahanmiri. "Boundary Layer Transitional Flow in Gas Turbines". In: (2011), pp. 1–51. ISSN: 1652-8549 (cit. on p. 85).

[136] E. Collado Morata, N. Gourdain, F. Duchaine, et al. "Effects of free-stream turbulence on high pressure turbine blade heat transfer predicted by structured and unstructured les". In: *International Journal of Heat and Mass Transfer* 55.21-22 (2012), pp. 5754–5768. ISSN: 00179310. DOI: 10.1016/j.ijheatmasstransfer.2012.05.072 (cit. on p. 85).

[137] Jan G. Wissink, Tamer A. Zaki, Wolfgang Rodi, et al. "The effect of wake turbulence intensity on transition in a compressor cascade". In: *Flow, Turbulence and Combustion* 93.4 (2014), pp. 555–576. ISSN: 15731987. DOI: 10.1007/s10494-014-9559-z (cit. on p. 85).

[138] Vittorio Michelassi, Li-wei Chen, Richard Pichler, et al. "GT2014-25689". In: (2014) (cit. on p. 85).

[139] Ashley D. Scillitoe, Paul G. Tucker, and Paolo Adami. "Numerical investigation of three-dimensional separation in an axial flow compressor: The influence of free-stream turbulence intensity and Endwall boundary layer state". In: *Proceedings of the ASME Turbo Expo* 2D-2016.September 2020 (2016). DOI: 10.1115/GT2016-57241 (cit. on p. 85).

[140] Kevin W. Thompson. "Time dependent boundary conditions for hyperbolic systems". In: *Journal of Computational Physics* 68.1 (1987), pp. 1–24. ISSN: 10902716. DOI: 10.1016/0021-9991(87)90041-6 (cit. on p. 86).

[141] Nicolas Guézennec and Thierry Poinsot. "Acoustically nonreflecting and reflecting boundary conditions for vorticity injection in compressible solvers". In: *AIAA Journal* 47.7 (2009), pp. 1709–1722. ISSN: 00011452. DOI: 10.2514/1.41749 (cit. on pp. 86, 101).

[142] Sergio Pirozzoli and Tim Colonius. "Generalized characteristic relaxation boundary conditions for unsteady compressible flow simulations". In: *Journal of Computational Physics* 248 (2013), pp. 109–126. ISSN: 10902716. DOI: 10.1016/j.jcp.2013.04.021 (cit. on p. 94).

[143] Laurent Selle, Franck Nicoud, Thierry Poinsot, et al. "Actual impedance of nonreflecting boundary conditions : Implications for computation of resonators To cite this version : HAL Id : hal-00910165 Actual Impedance of Nonreflecting Boundary Conditions : Implications for Computation of Resonators". In: (2013) (cit. on p. 94).

[144] Salvador Izquierdo and Norberto Fueyo. "Characteristic nonreflecting boundary conditions for open boundaries in lattice Boltzmann methods". In: *Physical Review E - Statistical, Nonlinear, and Soft Matter Physics* 78.4 (2008), pp. 1–7. ISSN: 15393755. DOI: 10.1103/PhysRevE.78.046707 (cit. on p. 94).

[145] Daniel Heubes, Andreas Bartel, and Matthias Ehrhardt. "Characteristic boundary conditions in the lattice Boltzmann method for fluid and gas dynamics". In: *Journal of Computational and Applied Mathematics* 262 (2014), pp. 51–61. ISSN: 03770427. DOI: 10.1016/j.cam.2013.09.019. URL: http://dx.doi.org/10.1016/j.cam.2013.09.019 (cit. on p. 94).

[146] O. Malaspinas, B. Chopard, and J. Latt. "General regularized boundary condition for multi-speed lattice Boltzmann models". In: *Computers and Fluids* 49.1 (2011), pp. 29–35. ISSN: 00457930. DOI: 10.1016/j.compfluid.2011.04.010 (cit. on p. 94).

[147] Jonas Latt, Bastien Chopard, Orestis Malaspinas, et al. "Straight velocity boundaries in the lattice Boltzmann method". In: *Physical Review E - Statistical, Nonlinear, and Soft Matter Physics* 77.5 (2008). ISSN: 15393755. DOI: 10.1103/PhysRevE.77.056703 (cit. on p. 94).

[148] Yongliang Feng, Pierre Boivin, Jérôme Jacob, et al. "Hybrid recursive regularized thermal lattice Boltzmann model for high subsonic compressible flows". In: *Journal of Computational Physics* 394 (2019), pp. 82–99. ISSN: 10902716. DOI: 10.1016/j.jcp.2019.05.031 (cit. on p. 94).

[149] Xiaohua Wu. "Inflow Turbulence Generation Methods". In: *Annual Review of Fluid Mechanics* 49.1 (2017), pp. 23–49. DOI: 10.1146/annurev-fluid-010816-060322. eprint: https://doi.org/10.1146/annurev-fluid-010816-060322. URL: https://doi.org/10.1146/annurev-fluid-010816-060322 (cit. on pp. 100, 101).

[150] G. I. Taylor. "The Spectrum of Turbulence". In: *Proceedings of the Royal Society of London. Series A - Mathematical and Physical Sciences* 164.919 (1938), pp. 476–490. DOI: 10.1098/rspa.1938.0032. eprint: https://royalsocietypublishing.org/doi/pdf/10.1098/rspa.1938.0032. URL: https://royalsocietypublishing.org/doi/abs/10.1098/rspa.1938.0032 (cit. on p. 101).

[151] Jr. Smith L. H. "The Radial-Equilibrium Equation of Turbomachinery". In: *Journal of Engineering for Power* 88.1 (Jan. 1966), pp. 1–12. ISSN: 0022-0825. DOI: 10.1115/1.3678471. eprint: https://asmedigitalcollection.asme.org/gasturbinespower/article-pdf/88/1/1/5667488/1_1.pdf. URL: https://doi.org/10.1115/1.3678471 (cit. on p. 104).

[152] Florent Duchaine and Laurent Gicquel. "Inlet and Outlet Characteristics Boudary Conditions For Large Eddy Simulations of Turbomachinery". In: (2019) (cit. on pp. 109, 147).

[153] Laurent Cambier, Sébastien Heib, and Sylvie Plot. "The Onera elsA CFD software: Input from research and feedback from industry". In: *Mechanics and Industry* 14.3 (2013), pp. 159–174. ISSN: 22577777. DOI: 10.1051/meca/2013056 (cit. on pp. 115, 180).

[154] Frédéric Sicot, Adrien Gomar, Guillaume Dufour, et al. "Time-Domain Harmonic Balance Method for Turbomachinery Aeroelasticity". In: *AIAA Journal* 52.1 (2014), pp. 62–71. DOI: 10.2514/1.J051848. eprint: https://doi.org/10.2514/1.J051848. URL: https://doi.org/10.2514/1.J051848 (cit. on pp. 115, 180).

[155] Ignacio Gonzalez-martino. "Design Sensitivity of a 1-1/2 Stage Unshrouded High Work Turbine Using Very-Large Eddy Simulations". In: (2022), pp. 1–16 (cit. on p. 115).

[156] Guillaume Daviller, Maxence Brebion, Pradip Xavier, et al. "A Mesh Adaptation Strategy to Predict Pressure Losses in LES of Swirled Flows". In: *Flow, Turbulence and Combustion* 99.1 (2017), pp. 93–118. DOI: 10.1007/s10494-017-9808-z. URL: https://doi.org/10.1007/s10494-017-9808-z (cit. on pp. 120, 124, 125).

[157] A. Aniello, D. Schuster, P. Werner, et al. "Comparison of a finite volume and two Lattice Boltzmann solvers for swirled confined flows". In: *Computers and Fluids* 241 (2022), p. 105463. ISSN: 0045-7930. DOI: https://doi.org/10.1016/j.compfluid.2022.105463. URL: https://www.sciencedirect.com/science/article/pii/S0045793022001128 (cit. on p. 121).

[158] T. Passot and A. Pouquet. "Numerical simulation of compressible homogeneous flows in the turbulent regime". In: *Journal of Fluid Mechanics* 181 (1987), 441–466. DOI: 10.1017/S0022112087002167 (cit. on p. 132).

[159] Walid Bechara, Christophe Bailly, Philippe Lafon, et al. "Stochastic approach to noise modeling for free turbulent flows". In: *AIAA Journal* 32.3 (1994), pp. 455–463. DOI: 10.2514/3.12008. eprint: https://doi.org/10.2514/3.12008. URL: https://doi.org/10.2514/3.12008 (cit. on p. 132).

[160] M. Nguyen, J. F. Boussuge, P. Sagaut, et al. "Large eddy simulation of a thermal impinging jet using the lattice Boltzmann method". In: *Physics of Fluids* 34.5 (2022), p. 055115. ISSN: 1070-6631. DOI: 10.1063/5.0088410 (cit. on p. 133).

[161] Thomas Gianoli, Pierre Sagaut, Jean François Boussuge, et al. "S-Duct Turbomachinery Simulations using the Lattice Boltzmann Method". In: March (2022) (cit. on p. 147).

[162] T Coratger, G Farag, S Zhao, et al. "Large-eddy lattice-Boltzmann modeling of transonic flows". In: *Physics of Fluids* 33.11 (2021), p. 115112. DOI: 10.1063/5.0064944. URL: https://doi.org/10.1063/5.0064944 (cit. on p. 147).

[163] *Impact of Time-Resolved Entropy Measurement on a One-and-1/2-Stage Axial Turbine Performance*. Vol. Volume 6: Turbomachinery, Parts A, B, and C. Turbo Expo: Power for Land, Sea, and Air. June 2008, pp. 1289–1300. DOI: 10.1115/GT2008-50807. eprint: https://asmedigitalcollection.asme.org/GT/proceedings-pdf/GT2008/43161/1289/4578850/1289_1.pdf. URL: https://doi.org/10.1115/GT2008-50807 (cit. on p. 167).

[164] Metodi Zlatinov. "Secondary Air Interaction with Main Flow in Axial Turbines". In: (Nov. 2011) (cit. on p. 167).

[165] Benjamin Constant, Stéphanie Péron, Héloïse Beaugendre, et al. "An improved immersed boundary method for turbulent flow simulations on Cartesian grids". In: *Journal of Computational Physics* 435 (2021), p. 110240. ISSN: 0021-9991. DOI: https://doi.org/10.1016/j.jcp.2021.110240. URL: https://www.sciencedirect.com/science/article/pii/S0021999121001352 (cit. on p. 181).

[166] Alfred Walz. "Compressible turbulent boundary layers with heat transfer and pressure gradient in flow direction". In: *Journal of Research of the National Bureau of Standards Section B Mathematics and Mathematical Physics* 63B.1 (1959), p. 53. ISSN: 0022-4340. DOI: 10.6028/jres.063b.008 (cit. on p. 181).